Carbon Mineralization in Fractured Basalt

by

Anne H. Menefee

A dissertation submitted in partial fulfillment
of the requirements for the degree of
Doctor of Philosophy
(Environmental Engineering)
in the University of Michigan

2020

Doctoral Committee:

Assistant Professor Brian Ellis, Chair
Dr. J. William Carey, Los Alamos National Laboratory
Professor Daniel Giammar, Washington University
Professor Kim Hayes
Professor Steven Skerlos

Anne Menefee
amenefee@umich.edu
ORCID iD: 0000-0003-2740-3208

DEDICATION

For my family, here and gone. I love you more than you'll ever know.

ACKNOWLEDGEMENTS

Wow. “The nights are long but the years are short” has never felt more accurate. A PhD really takes a village and I could fill another (even longer) dissertation trying to properly thank everyone who has guided and supported me throughout this crazy journey – I owe every aspect of my grad school experience, in and out of this document, to the incredible people I’ve been able to work, teach, learn, serve, run, and live alongside every day. With that said, I want to personally thank:

My committee: I am so grateful for all of your time and feedback and have benefited immensely from your diverse perspectives. Kim, your expertise in aquatic chemistry is unparalleled and I really appreciate your attention to detail that has helped me to formulate key research questions. Steve, I equally appreciate your focus on the ‘bigger picture’ and have learned so much from you with respect to teaching, research, and critically evaluating sustainability. Dan, you are the most organized person I’ve ever met and it was such a privilege to work with you in my first 2 years – I am incredibly thankful you’ve remained invested in my work and have greatly appreciated all of your career advice and support. And Bill, I can’t thank you enough for the opportunity to work with your group and for being such an enthusiastic mentor from the start – I learned so much during our time trying to crack the precipitation cold case and am so excited to go back to Los Alamos.

Brian: I really don’t have words for what your mentorship has meant to me. I could never thank you enough for giving me the opportunity to come to Michigan and for all the opportunities you’ve given me since. I was really naïve coming in from undergrad and you’ve gone far above and beyond to teach me the ins and outs of academia. We’ve been through so much from mailing in proposals at the eleventh hour to adventuring through the Australian bush... I’m actually impressed you didn’t buckwash me there after spending 9+ hours together on reversed roads. I could write a novel on everything you’ve taught me and how much of an asset you are to the department. But on a personal note, I’ve most valued how much you’ve genuinely cared about me as a person – often more than I cared about myself. And I can’t really articulate the impact that’s had on my life. Thank you for all you’ve invested in trying to build my confidence. Thank you for letting me help write proposals and preparing me for a faculty position I couldn’t have attained without you. Thank

you for your time, energy, positivity, and generosity. And thank you for setting the bar so high. You are everything I aspire to be in a mentor and I'm so excited to see what you'll accomplish as a tenured professor. It's been an honor and a privilege to work with you during this stage of your career and it's amazing to reflect on how far we've both come. Thank you for all the laughs through the highs and lows. Thank you for all of the invaluable life advice and countless conversations that meant more than you could know. And thank you – above all – for always having my back.

Jubilee Adeoye: Thank you for being the most genuine, wise, hard-working, and hilarious lab brother ever. There's nobody else I'd rather battle reactors with at 4am and I'm beyond grateful for all of the antics, conversations, and adventures from the classroom to Alabama and Japan. I miss you so much but I know your best is yet to come. It's been a true blessing to be your friend.

I wouldn't be here without the people at UVa who had far more confidence in me than I did:

Andres Clarens: You have been my academic role model since I was 18 (!!) and I wouldn't have applied to PhD programs – especially Michigan – without your influence and encouragement. Thank you for sparking my desire to pursue research, for showing me the ropes, for believing in my potential, and for everything you've invested in me. Thank you for remaining such a strong mentor throughout grad school – I've really appreciated all of our interactions at conferences and your on-point career advice. Oh and thanks for not holding the donkey video against me – that's a hard one to live down. I'm so psyched to see how you keep advancing our field as a full professor.

Buddy Wilkins: You said you wouldn't have made it through your PhD without me but that goes both ways. I grew so much in publishing our first paper (and more importantly in the trenches we went through to get there). Thank you for always treating me as an equal, despite what our age and experience gap might imply. Thank you for your steady stream of wisdom, advice, and support. And thank you for teaching me the most valuable life skills like driving tractors and picking locks.

I also want to recognize all of the amazing people I met during my time at national labs:

LANL: I'm so grateful for all the friends and mentors who made Los Alamos a hard place to leave and an easy place to return to. A special thanks to Margaret and the Wiens family for your hospitality and to Chris for all the adventures in the mountains (plus the crash - kind of literally - courses in sailing and snowmobiling). I also want to thank Luke Frash for generously sharing his wisdom and proficiency in experimental design and coding. And Nathan, thank you for your constant jokes and positivity, "Welch's wealth," and letting me commandeer your desk on the reg.

NETL: Many thanks to Dustin, John, and Bryan for hosting me in WV on multiple counts – I learned so much from working with you all, even if our primary result was a geyser of DowTherm.

And I want to acknowledge everyone else in the academic community who has generously advised me on careers and research, especially Jeff Bielicki and Dave Goldberg.

I want to express my sincere gratitude to everyone who has made Ann Arbor a home, including:
The runner gang(s): especially Nicole, Seth, Jamie, Andrew, Ben G, other Ben G, Juanita, Lexi, and the goats Calli and Louisa – thanks for all the miles, smiles, and sunrises over Bird Hills. And also for validating that running 8-12 miles a day might be the least insane thing about me.
GradCru: Thank you all, especially my co-leaders Katie and Danielle and all of my Bible study members through the years, for keeping me grounded in faith and community.
Michigan CEE: I'm so thankful for all of the friendships, in and out of work; for all of the students who made my first teaching experiences so rewarding; for all of the faculty who have given me advice and feedback; and for the staff who were always willing to assist with logistics. I also want to thank all of our amazing technicians – especially Steve Donajkowski, Tom Yavaraski, and Rick Burch – for all of their help, no matter how unusual the task. Thank you all for creating such a strong sense of community. Many thanks to my labmates over the years, especially Yuqiang, Wenjia, and Ivan for setting such a great example. And Wenjia, without you I'd probably still be lost in a Japanese train station. I also want to thank all of my officemates, especially Ellen and Liz for their camaraderie (and for putting up with excessive office temperatures when desperate times drove me to take control of the thermostat during frigid graveyard shifts). And Liz, your company during many of those late shifts meant more than you know. Lastly, a special shoutout to the OG's Emily, Sara, and Nicole who have been there since our recruitment days. Emily, I'm so lucky to be quarantined with you and Jimmy – thank you for the years of friendship and making a falling-apart house at 1520 Jones a home. And Sara, I'll really miss our drives to church. Thank you both for the Google chats and real life hangouts – you've gifted me with so many positive memories and our Poldark and Balderdash nights with Allison really lit up some dark times back in the day.

Last but definitely not least - I want to thank all my friends and family back in Virginia, especially:

Coach L: Thanks for always reminding me that working hard and being a good person would carry me far beyond running. You were right about many things, but #1 – I finally made it to Iowa.

Emily Seay: Thank you for your friendship, fellowship, and moral support since our Civil days.

Lynn and Phil: Thank you for loving me as the goofball I have always been and reminding me to never lose it. And for providing me with the timeless knee-slapping joke of the nevergreen tree.

My brother, Bill: my best friend forged in fire. I know you definitely won't read this dissertation but thank you for being a continual source of comedic relief. You have no idea how many times your (overly sarcastic) responses to my random 2 am texts gave me life. I can't believe we've made it a quarter century but couldn't imagine it without you. And I'm so freaking proud of you.

My parents: I'm eternally grateful for your unwavering love and support since Day 1, even when you don't get what I'm doing. You were probably confused why the smallest kid in fifth grade was aspiring to the NFL or why the most cold-averse person you know thought it'd be a great idea to move to Michigan, but you've always let me chase my dreams and had more confidence than me that I could reach them. Ok.. maybe not the NFL. But I can't thank you enough for working so hard to give us opportunities to get an education and for raising us to value good character, which will always be worth more than any level of success. I could never repay all the sacrifices you've made for us but will forever strive to pay them forward. And I love you guys beyond words.

And finally, my grandparents: Granny, our weekly phone calls were as valuable to me as they were to you and I wish you were still here to hear I'm finally out of school. Grandma, thank you for epitomizing the human spirit – you and Grandpa were second parents growing up and I'll never forget all our adventures in the woods and good times in Rocky Mount. And to my grandfather, who was my biggest fan and wanted more than anything to see the first Dr. Menefee – I know you're still watching from somewhere above and hope I can make you and the whole family proud.

This dissertation was supported in part by a National Science Foundation Graduate Research Fellowship and a Department of Energy Office of Science Graduate Student Research Award. Additional funding was provided by the National Science Foundation (via Award CBET-1214416), the Department of Energy (under Award DE-FE0023382), and the Department of Civil and Environmental Engineering at the University of Michigan.

TABLE OF CONTENTS

LIST OF FIGURES

LIST OF TABLES

LIST OF APPENDICES

ABSTRACT

The need to meet rising energy demands while mitigating climate change driven by associated CO_2 emissions has motivated the development of geologic carbon storage systems. Until recently, most research has focused on sedimentary reservoirs that rely primarily on short-term solubility and physical trapping mechanisms, where CO_2 can migrate if the structural integrity of the caprock or wellbore is compromised. This inherent leakage risk could be eliminated by leveraging the natural reactivity of basalt reservoirs, which are abundant in silicate minerals that dissolve rapidly under acidic conditions and can ultimately trap dissolved CO_2 as solid carbonate minerals. Given the significant advantage of mineral trapping for long-term storage security, basalts may be the most readily deployable CO_2 repositories in the near term. However, our fundamental understanding of the conditions under which this CO_2 mineralization process occurs and its viability as a permanent carbon sequestration pathway remain limited. This dissertation highlights multiple series of high-pressure core flooding experiments and coupled reactive transport models designed to evaluate the effects of temperature, fluid chemistry, and flow regimes on basalt dissolution and CO_2 trapping through carbonate precipitation. Results indicate that basalts can effectively mineralize CO_2 at representative subsurface stress conditions, but mineralization predominantly occurred within buffered diffusion-limited zones (e.g. dead-end fractures) where reaction fronts have developed from competing geochemical gradients. Carbonate precipitation was highly localized on the reactive silicate minerals contributing key divalent cations and was significantly enhanced by elevated temperature and alkalinity. Complementary triaxial direct shear fracturing experiments with carbonate-rich shales revealed that spatial distributions of precipitates may be more significant than the total amount, as small volumes at critical fracture contact points can dramatically restrict flow. In combination, this work demonstrates how complex interactions between reservoir geochemistry and transport conditions drive the extent and location of carbon mineralization reactions in basalt fractures, which will inform selection of storage sites and injection schemes that optimize long-term CO_2 trapping efficiency.

CHAPTER 1
Introduction

1.1. BACKGROUND AND MOTIVATION

According to the National Academy of Sciences, tempering the impacts of climate change is one of the most pressing global challenges environmental engineers must address in the coming decades.[1] Anthropogenic CO_2 emissions are dominated by the combustion of fossil fuels, which currently meet over 80% of global energy demands and are expected to remain a significant source of base power for the foreseeable future.[2] While some renewable technologies are gaining traction, this continued dependence on fossil energy compels the development of large-scale carbon mitigation strategies to meet rising energy demands while limiting irreversible environmental damage. Stationary sources (e.g. power plants and industrial facilities) account for around 60% of total carbon emissions associated with fossil fuels,[3] presenting opportunities to significantly curb global emissions through carbon capture, utilization, and storage (CCUS) systems. Here, CO_2 is separated from flue gases at the source and either utilized to produce a commodity (e.g. in enhanced oil recovery) or injected deep underground and permanently sequestered in subsurface reservoirs through geologic carbon storage (GCS).[4] CCUS is considered an integral component of efforts to prevent global temperature rise exceeding the 2˚C threshold set in recent international climate agreements, but commercial-scale development has been limited by economic and political barriers largely involving risk.[4]

Geologic carbon storage research has traditionally focused on sedimentary formations such as deep saline aquifers or depleted oil and gas fields due to their ubiquity, high permeability, extensive capacity, and general familiarity to the energy industry from decades of extensive exploration and production.[6,7] However, sedimentary formations rely primarily on short-term physical or solubility trapping mechanisms that present risks of CO_2 leakage and groundwater contamination if CO_2 is not structurally secured.[6] At injection depths, supercritical CO_2 is buoyant with respect to reservoir brines and could migrate through fractures if caprock or wellbore integrity is compromised.[8] Additionally, because most sedimentary basins amenable to CO_2 injection have

been extensively developed for oil and gas production, CO_2 can escape through abandoned or poorly plugged wells. This potential limitation with conventional sedimentary basins has motivated recent interest in alternative formations enriched in reactive silicate minerals that could permanently sequester CO_2 through physical and geochemical trapping.[6] Basalt and ultramafic formations are particularly attractive host reservoirs, as reactive minerals such as olivine ($(Mg,Fe)_2SiO_4$) and pyroxene ($(Ca,Mg,Fe)_2Si_2O_6$) promote *in situ* mineral carbonation. Here, CO_2 injection drives rapid mineral dissolution, releasing divalent metal cations (e.g. Ca^{2+}, Mg^{2+}, Fe^{2+}) that can combine with CO_2 in resident brines to form stable carbonate minerals such as calcite ($CaCO_3$), magnesite ($MgCO_3$), and siderite ($FeCO_3$) through the following general reaction:[9]

$$(\mathrm{Fe, Ca, Mg})^{2+} + \mathrm{CO_2} + \mathrm{H_2O} = (\mathrm{Fe, Ca, Mg})\mathrm{CO_3} + 2\mathrm{H}^{+} \qquad \textbf{(Eqn. 1.1)}$$

Continued dissolution of the host rock provides the necessary acid neutralization capacity to drive the reaction to the right. For example, Ca-pyroxene (wollastonite) consumes H^+ produced in the dissociation of carbonic acid and releases Ca^{2+} according to the reaction:

$$\mathrm{CaSiO_{3(s)}} + 2\mathrm{H}^{+} + \mathrm{H_2O} = \mathrm{Ca}^{2+} + \mathrm{H_4SiO_4} \qquad \textbf{(Eqn. 1.2)}$$

Under suitable pH conditions, dissolved calcium ions then combine with carbonate ions to form calcite in accordance with Eqn. 1.1. Of the silicate minerals present in mafic and ultramafic rocks, olivine has the highest cation:silica ratio and thus has the greatest potential for CO_2 fixation.[6] While ultramafic rocks such as peridotites are most abundant in reactive minerals, consisting primarily of pyroxene and up to 98% olivine,[10] mafic formations such as basalts are more ubiquitous.[6] Compared with peridotites, basalt reservoirs also typically have higher porosity and permeability along with alternating permeable and dense layers that may favor secure CO_2 trapping.[11]

While natural weathering and low-temperature alteration processes are known to induce mineral carbonation in mafic and ultramafic rocks over geologic time scales, silicate reaction rates increase dramatically with increasing temperature and CO_2 partial pressure (P_{CO2}).[12] In combination, elevated temperatures and pressures at typical injection depths along with CO_2-driven acidification of formation fluids should inherently accelerate mineral dissolution and carbonation reactions that can permanently trap dissolved CO_2,[13] but the long-term impacts of carbonate precipitation on reservoir permeability and continued CO_2 injectivity remain poorly understood. In larger fracture networks, carbonates could simply coat fracture surfaces without compromising fluid transport. However, given the low intrinsic permeability of most basalt reservoirs, precipitates are more likely to clog pores, block fractures, and ultimately self-limit CO_2

storage potential unless the associated increase in solids volume (during the conversion of silicate to carbonate minerals) is sufficient to fracture the surrounding rock.[6,10] In theory, this "reactive cracking" or "reaction-induced fracturing" process could allow CO_2 mineralization to become inherently self-sustaining by continually generating new flow paths and reactive surface area. Reactive cracking is held as the key to maximizing carbon storage capacities in basalt, but has not been demonstrated under relevant CO_2 injection conditions in natural systems. Figure 1.1 below provides a schematic overview of CO_2-driven basalt carbonation and resulting positive or negative feedback mechanisms that could control fracture permeability evolution.

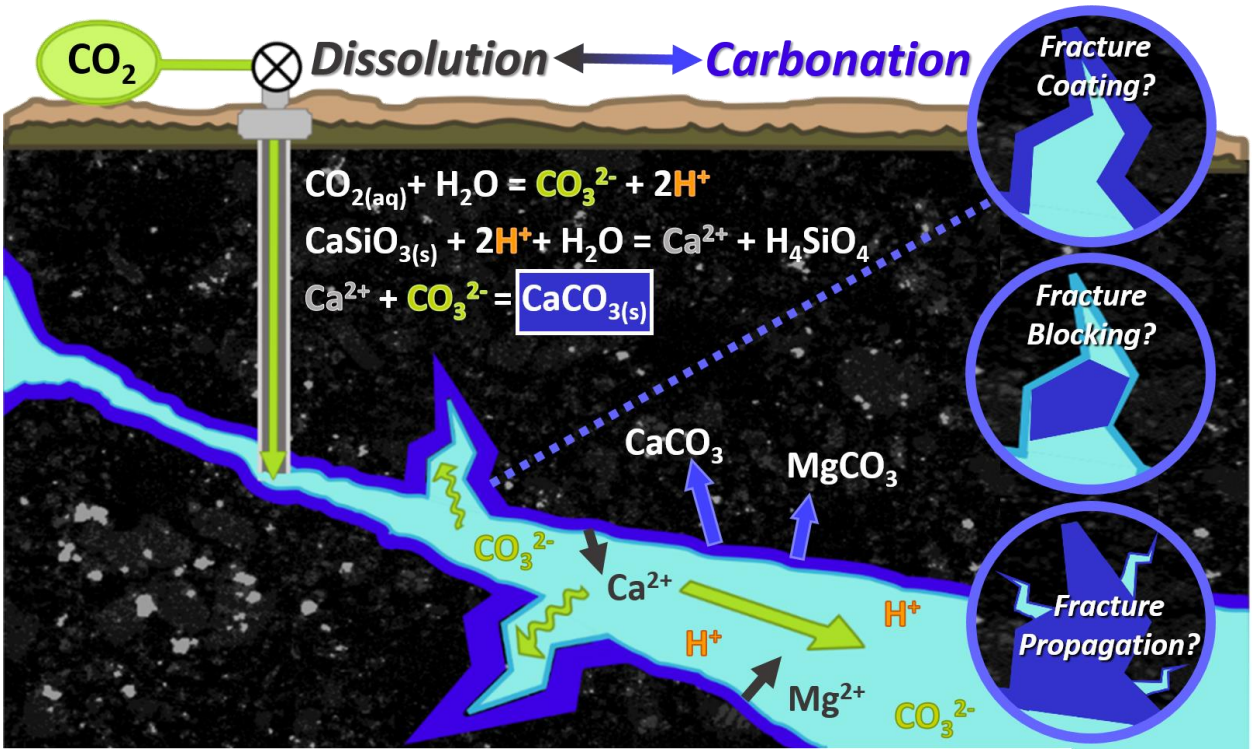

Figure 1.1. Schematic overview of CO_2 mineralization in basalt. Silicate mineral dissolution releases divalent cations (e.g. Ca^{2+}) that react with injected CO_2 to form stable carbonate precipitates (e.g. $CaCO_3$), which can coat or block existing fractures or potentially propagate new fractures in the surrounding rock.

Given the inherent advantages of mineral trapping for long-term storage security, basalts may be the most readily deployable CO_2 repositories. The National Academies recently reported that carbon mineralization could enable large-scale implementation of negative emissions technologies (NETs) but remains underdeveloped,[14] motivating systematic efforts to understand factors controlling the rate and extent of CO_2 mineralization in natural basalts as well as opportunities to strategically select and engineer systems to optimize CO_2 trapping potential. More broadly, sustainable subsurface development for large-scale carbon mitigation strategies including CO_2

mineralization requires a fundamental understanding of the long-term impacts of mineral dissolution-precipitation reactions induced by reactive fluid injection. Most target reservoirs for emerging low-carbon energy technologies (e.g. enhanced geothermal systems) or CO_2 utilization and storage (e.g. CO_2-enhanced shale oil recovery) are characterized by low permeability, where fracture systems control the injection, extraction, or leakage of fluids. Fracture permeability can be critically altered by geochemical reactions between injected fluids, resident brines, and the host rock that are challenging to predict *a priori*. In particular, mineral precipitation can have significant positive or negative impacts on reservoir performance. Precipitation is generally desirable during CO_2 sequestration, where CO_2 is trapped in the form of carbonate minerals, or in operations where fluid migration needs to be actively controlled, where targeted precipitation can create natural seals. However, precipitates may adversely affect long-term CO_2 injectivity or the performance of subsurface energy systems when they deposit as scale in wellbores or block critical flow paths. Predicting when and where precipitation reactions will impact long-term fluid injectivity remains an open research challenge but is critical to minimizing risks while optimizing the efficiency of emerging subsurface technologies aiming to decarbonize the energy sector.

1.2. RESEARCH OBJECTIVES

This work aims to define conditions that drive the extent and distribution of mineral dissolution-precipitation reactions and understand their long-term implications for fluid transport in subsurface systems. While most of this dissertation will focus specifically on CO_2 mineralization in basalt, the last component addresses the impacts of geochemical reactions more generally with application to low-permeability reservoirs targeted for emerging carbon utilization and energy production technologies. The primary research objectives seek to:

1. Evaluate the impacts of reservoir temperature, fluid chemistry, transport limitations, and mineral heterogeneity on silicate mineral dissolution and carbonate precipitation in basalt fractures exposed to CO_2-acidified fluids.
2. Improve predictive capabilities for the spatial distribution of carbonate precipitation based on initial reservoir chemistry and mineralogy.
3. Identify reservoir and injection conditions that limit or enhance the extent of permanent CO_2 trapping through mineralization in basalts.
4. Determine conditions under which mineral precipitation induced by fluid-rock interactions can seal existing fractures, maintain fracture permeability, or propagate new fractures.

1.3. DISSERTATION OVERVIEW

This dissertation is organized into four chapters of content addressing the research questions outlined above. Chapters 2-4 specifically focus on CO_2 mineralization in basalt, while Chapter 5 explores rapid carbonate precipitation in shales as an analog for reactive fluid injection into low-permeability subsurface systems. Chapter summaries are provided here along with citations for corresponding manuscripts, as the majority of this work has already been published or submitted.

Chapter 2 presents results from initial experimental and modeling efforts focused on the role of transport limitations and mineral heterogeneities on basalt dissolution and carbonation under relevant CO_2 injection and storage conditions. 2D reactive transport models were developed based on data from high-temperature, high-pressure core flooding experiments where CO_2-acidified brines were injected through saw-cut basalt cores with milled fracture patterns. Both experimental and modeling results revealed that advection-dominated transport (e.g. regions near wellbores or well-connected fractures) will drive net dissolution, while diffusion-dominated regimes create sufficient fluid residence time to promote carbonate precipitation. Elevated temperature and salinity enhanced basalt dissolution, which also became more congruent (i.e. stoichiometric) at higher temperatures. Given equivalent bulk mineral compositions, mineral heterogeneities impacted the spatial distribution of dissolution-precipitation reactions but negligibly affected the extent. Beyond direct applications to carbon mineralization, the predictive modeling framework developed in this chapter can be applied to a range of reactive subsurface systems to extend experimental observations over greater spatial and temporal scales. Work presented in this chapter has been published in two manuscripts (referenced below). Note that in the first, J.T. Adeoye and A.H. Menefee contributed equally to first authorship.

> Adeoye, J.T.; **Menefee, A.H.;** Xiong, W.; Wells, R.K.; Skemer, P.; Giammar, D.E.; Ellis, B.R. Effect of transport limitations and fluid properties on reaction products in fractures of unaltered and serpentinized basalt exposed to high P_{CO2} fluids. *International Journal of Greenhouse Gas Control* **2017**, *63*, 310–320.
>
> **Menefee, A.H.**; Li, P.; Giammar, D.E.; Ellis, B.R. Roles of transport limitations and mineral heterogeneity in carbonation of fractured basalts. *Environmental Science & Technology* **2017**, *51* (16), 9352–9362.

Building on the coupled experimental and modeling efforts to isolate advection- and diffusion-controlled transport conditions in Chapter 2, **Chapter 3** presents a series of experiments designed to evaluate both transport regimes in a single core flooding system along with the impacts of reservoir temperature and brine alkalinity. Basalt core samples were milled to create a primary advection-dominated flow channel connected to four dead-end fractures where transport was

limited to diffusion. Whereas the advection-dominated experiments in Chapter 2 resulted in net dissolution, carbonate precipitation occurred in all of these tests but was limited to diffusion-limited zones. At 100°C and 6.3 mM $NaHCO_3$, representative of potential GCS reservoir temperatures and brine alkalinity, carbonate precipitates were highly localized on reactive mineral grains contributing key divalent cations. Increasing the concentration of $NaHCO_3$ to 640 mM dramatically enhanced carbonation in dead-end fractures, but an associated increase in clay minerals that filled advection-controlled flow paths could ultimately obstruct flow and limit sequestration capacity over multi-year injection operations. Raising the temperature to 150°C increased both carbonate and clay precipitation, which reduced the total pre-reaction fracture volume by 48% compared to a 35% reduction at 100°C. In combination, the results were consistent with field tests indicating that carbon mineralization will predominate in buffered diffusion-limited zones adjacent to bulk flow paths and indicated that alkaline reservoirs with strong geothermal gradients will enhance the ultimate extent of CO_2 trapping. The work presented in this chapter has been published in the following manuscript:

> **Menefee, A.H.;** Giammar, D.E.; Ellis, B.R. Permanent CO_2 trapping through localized and chemical gradient-driven basalt carbonation. *Environmental Science & Technology* **2018**, *52* (15), 8954–8964.

Chapter 4 investigates CO_2 mineralization patterns in diffusion-limited zones of reactive minerals where the bulk of carbonate precipitation is expected to occur. Core flooding experiments were designed to optimize the likelihood of achieving rapid and near-complete carbonation by creating packed beds of reactive mineral powders (olivine and wollastonite) within flood basalt cores. All of the packed beds evidenced conversion of silicates to carbonate minerals with up to 58% carbonation efficiency. Consistent with complementary reactive transport model predictions and prior work on packed beds in static systems, carbonation reached a local maximum near the center due to opposing geochemical gradients as CO_2 diffused into and dissolved cations (Ca, Mg) diffused out of the system. Despite equivalent initial amounts of Ca- and Mg-silicate powders, Ca-carbonates were the predominant reaction product as Mg-carbonate precipitation was kinetically limited and was also competing with more favorable Mg-silicate hydration (i.e. serpentinization) processes. While dissolution has been commonly held as the rate-limiting step for silicate carbonation, the strong favorability of Ca- over Mg-carbonates in these tests and the experiments conducted in Chapter 3 indicate that precipitation will be rate-limiting under subsurface conditions

relevant to GCS. Additionally, while the volume expansion associated with carbonation reactions has been considered critical to optimizing carbonation efficiency through continual renewal of reactive surface area, no evidence of reaction-induced fracturing was observed in these tests as precipitates were accommodated by available pore space and simultaneous dissolution of the packed beds. This work has not been previously published.

More broadly, the sustainable development of CO_2 storage repositories and related low-permeability reservoirs where significant flow is confined to fracture systems requires a deeper understanding of how fractures respond to the penetration of reactive fluids under confining stress. In **Chapter 5**, a series of triaxial direct shear experiments was designed to evaluate how geochemical reactions between pore fluids and the host rock impact fracture permeability and microstructure with a focus on the role of mineral precipitation. Experiments were conducted within an x-ray computed tomography (xCT) scanner to capture the spatial and temporal evolution of fracture geometry and precipitate growth. Calcite-rich shale cores were directly sheared using $BaCl_2$-rich solutions as a surrogate working fluid to improve x-ray contrast. Three shear tests evidenced non-uniform precipitation of barium carbonates ($BaCO_3$) along through-going fractures, where the extent of precipitation increased with increasing calcite content in the shale cores. Precipitates were strongly localized within fracture networks due to mineral, geochemical, and structural heterogeneities and generally concentrated in smaller apertures where rock:water ratios were highest. The combination of elevated fluid saturation and reactive surface area created in freshly activated fractures drove near-immediate precipitation that led to an 80% permeability reduction and significant flow obstruction in the most reactive core. While most previous studies have focused on mixing-induced precipitation, this work demonstrates that fluid-rock interactions can trigger precipitation-induced permeability alterations that can either initiate or mitigate risks associated with subsurface energy systems. This work was conducted at Los Alamos National Laboratory through a Department of Energy Office of Science Graduate Student Research Award and is published in the following manuscript:

> **Menefee, A.H.;** Welch, N.J.; Frash, L.P.; Hicks, W.; Carey, J.W.; Ellis, B.R. Rapid mineral precipitation during shear fracturing of carbonate-rich shales. *Journal of Geophysical Research: Solid Earth* **2020,** *125* (6).

Finally, **Chapter 6** discusses overarching conclusions from this dissertation and directions for future work. Supplemental data associated with Chapters 2-5 are included in the appendices, along with additional unpublished experiments and a list of all other work published during this PhD.

REFERENCES

(1) National Academies of Sciences, Engineering, and Medicine. *Environmental Engineering for the 21st Century: Addressing Grand Challenges*; DOE-NASEM-0016218, 1494822; 2018; p DOE-NASEM-0016218, 1494822. https://doi.org/10.2172/1494822.

(2) Olajire, A. A. A Review of Mineral Carbonation Technology in Sequestration of CO2. *J. Pet. Sci. Eng.* **2013**, *109*, 364–392. https://doi.org/10.1016/j.petrol.2013.03.013.

(3) *Global Energy Assessment (GEA)*; Johansson, T. B., Patwardhan, A., Nakićenović, N., Gomez-Echeverri, L., International Institute for Applied Systems Analysis, Eds.; Cambridge University Press ; International Institute for Applied Systems Analysis: Cambridge : Laxenburg, Austria, 2012.

(4) Cuéllar-Franca, R. M.; Azapagic, A. Carbon Capture, Storage and Utilisation Technologies: A Critical Analysis and Comparison of Their Life Cycle Environmental Impacts. *J. CO2 Util.* **2015**, *9*, 82–102. https://doi.org/10.1016/j.jcou.2014.12.001.

(5) Celia, M. A. Geological Storage of Captured Carbon Dioxide as a Large-Scale Carbon Mitigation Option: GEOLOGICAL STORAGE FOR CARBON MITIGATION. *Water Resour. Res.* **2017**. https://doi.org/10.1002/2017WR020841.

(6) Matter, J. M.; Kelemen, P. B. Permanent Storage of Carbon Dioxide in Geological Reservoirs by Mineral Carbonation. *Nat. Geosci.* **2009**, *2* (12), 837–841. https://doi.org/10.1038/ngeo683.

(7) McGrail, B. P.; Schaef, H. T.; Ho, A. M.; Chien, Y.-J.; Dooley, J. J.; Davidson, C. L. Potential for Carbon Dioxide Sequestration in Flood Basalts: SEQUESTRATION IN FLOOD BASALTS. *J. Geophys. Res. Solid Earth* **2006**, *111* (B12), n/a-n/a. https://doi.org/10.1029/2005JB004169.

(8) Harvey, O. R.; Qafoku, N. P.; Cantrell, K. J.; Lee, G.; Amonette, J. E.; Brown, C. F. Geochemical Implications of Gas Leakage Associated with Geologic CO_2 Storage— A Qualitative Review. *Environ. Sci. Technol.* **2013**, *47* (1), 23–36. https://doi.org/10.1021/es3029457.

(9) Gislason, S. R.; Wolff-Boenisch, D.; Stefansson, A.; Oelkers, E. H.; Gunnlaugsson, E.; Sigurdardottir, H.; Sigfusson, B.; Broecker, W. S.; Matter, J. M.; Stute, M. Mineral Sequestration of Carbon Dioxide in Basalt: A Pre-Injection Overview of the CarbFix Project. *Int. J. Greenh. Gas Control* **2010**, *4* (3), 537–545. https://doi.org/10.1016/j.ijggc.2009.11.013.

(10) Power, I. M.; Harrison, A. L.; Dipple, G. M.; Wilson, S. A.; Kelemen, P. B.; Hitch, M.; Southam, G. Carbon Mineralization: From Natural Analogues to Engineered Systems. *Rev. Mineral. Geochem.* **2013**, *77* (1), 305–360. https://doi.org/10.2138/rmg.2013.77.9.

(11) Schaef, H. T.; McGrail, B. P.; Owen, A. T. Carbonate Mineralization of Volcanic Province Basalts. *Int. J. Greenh. Gas Control* **2010**, *4* (2), 249–261. https://doi.org/10.1016/j.ijggc.2009.10.009.

(12) Kelemen, P. B.; Matter, J. In Situ Carbonation of Peridotite for CO_2 Storage. *Proc. Natl. Acad. Sci.* **2008**, *105* (45), 17295–17300.

(13) Olsson, J.; Bovet, N.; Makovicky, E.; Bechgaard, K.; Balogh, Z.; Stipp, S. L. S. Olivine Reactivity with CO2 and H2O on a Microscale: Implications for Carbon Sequestration. *Geochim. Cosmochim. Acta* **2012**, *77*, 86–97. https://doi.org/10.1016/j.gca.2011.11.001.

(14) National Academies of Sciences, Engineering, and Medicine. *Negative Emissions Technologies and Reliable Sequestration: A Research Agenda*; National Academies Press: Washington, D.C., 2019.

CHAPTER 2

Controls on Basalt Dissolution-Carbonation Reactions

2.1. BACKGROUND AND MOTIVATION

The drive to mitigate anthropogenic CO_2 emissions associated with rising energy demands has motivated research efforts on an array of carbon capture, utilization, and storage strategies. Research in geologic carbon storage (GCS) has centered on ubiquitous and well-characterized sedimentary formations that primarily rely on physical containment of injected CO_2. Associated leakage risks (e.g., through breached caprocks or abandoned wells)[1] have prompted interest in utilizing alternative reservoirs with higher abundances of reactive minerals that could provide secure long-term carbon trapping.[2] Flood basalts are particularly attractive, as rapid mineral dissolution promoted by CO_2 injection releases divalent metal cations that can then combine with CO_2 to form stable carbonates.[3] Despite investigations at both lab[4,5] and pilot[6,7] scales, our understanding of the fundamental controls on this process along with its viability as a permanent sequestration option remain limited.

Because transport limitations likely dictate both the speed and extent of mineral carbonation, characterizing basalt alterations resulting from CO_2 injection under different flow regimes is crucial to predicting microstructural changes that impact sustained CO_2 injection and trapping rates. Through a series of reactive percolation experiments in sintered magmatic olivine cores, Peuble et al.[8] concluded that higher flow rates result in greater carbonation efficiency because permeability reductions can block transport in low-flow regions. In addition, they confirmed that secondary precipitates controlled by rock dissolution formed in diffusion-dominated paths, while those limited by influent fluid composition formed along advective paths. Andreani et al.[9] also conducted percolation experiments on sintered dunite and only observed significant carbonate-induced porosity alterations in dead-end zones, whereas high-flow zones promoted rapid dissolution followed by the formation of a passivating Si-rich surface layer that created a barrier between fluids and reactive surfaces. Such studies highlight the need to optimize injection

strategies that promote basalt mineral dissolution while maintaining adequate conditions for mineral carbonation.

The effects of mineral spatial distributions on the extent of CO_2 mineralization in basalts are less established but are likely coupled with the effects of transport limitations. Peuble et al.[8] noted that carbonation rates were a function of complex interactions between flow conditions, kinetics, and mineral heterogeneities. Due to these complexities, secondary carbonate precipitation was localized and subsequently inhibited flow. Conversely, Andreani et al.[9] observed that localized precipitation along preferential flow paths resulting from mineral heterogeneities generated simultaneous increases in permeability and rock volume that would support continued CO_2 trapping. Xiong and Giammar[10] attributed localized carbonate formation in packed forsterite beds to geochemical gradients induced by diffusion-limited transport, while Giammar et al.[11] showed that magnesite can form in diffusive regions before volume-averaged properties reach saturation. Several studies have also demonstrated the influence of heterogeneities on mineral dissolution, an anticipated rate-limiting factor for mineral carbonation. Salehikhoo et al.[12] found that magnesite dissolution rates varied by no more than 14% under different spatial distributions of magnesite within quartz samples, but that variations in rates due to heterogeneities were most pronounced under mixed flow conditions compared with advection- and diffusion-limiting regimes. Li et al.[13] extended this work, confirming modeling indications that random mineral distributions with smaller clustering result in greater dissolution than distributions with larger discrete mineral zones. Similarly, Molins et al.[14] concluded that given the same average geochemical parameters, different mineral spatial patterns resulted in different pore-scale flow patterns and concentration gradients that impacted bulk dissolution rates. Heterogeneities in both reactive mineral distributions and the locations of advection- and diffusion-controlled zones relative to CO_2 injection sites are expected to be key drivers of permeability and porosity changes governing long-term injectivity.

Reactive transport models have been applied extensively to study CO_2 storage in sedimentary basins in the context of caprock stability, CO_2 plume migration, permeability evolution, and wellbore integrity.[e.g., 15–22] Such models are critical to advancing experimental findings given the time and spatial constraints of lab-scale studies.[21] Because CO_2 storage in basalt is a relatively new pursuit compared with storage in deep saline aquifers, most research efforts have yet to substantially integrate numerical modeling. Several studies have included reaction path models, which capture a sequence of chemical or mineralogical states and may incorporate kinetics but do

not explicitly consider transport processes.[23] For instance, Marini et al.[24] carried out reaction path modeling of CO_2 injection in continental flood basalt aquifers, predicting dramatic porosity reductions due to sequential precipitation of chalcedony, kaolinite, minor amounts of goethite, and carbonates dominated by dolomite. In reaction path models of volcanic flood basalts, Schaef et al.[25] found that precipitation of clays and chalcedony preceded carbonate formation, which was delayed by reductions in available reactive surface area led by basaltic glass and clinopyroxene dissolution. The authors further noted that carbonate accumulation may affect *in situ* mineralization efficiency by limiting mass transport across mineral interfaces.[25] More recently, Paukert et al.[26] developed reaction path models for peridotites and demonstrated that anthropogenic CO_2 injection significantly enhanced both the amount of CO_2 mineralized *in situ* and carbonation efficiency relative to natural systems.

Batch experiments on olivines and basalts have also been supplemented with reaction path models to predict geochemical alterations and reaction product formation,[27,28,29] but few experimental or modeling efforts have incorporated transport components. Giammar et al.[11] created a reactive transport code to simulate chemical gradients resulting from dissolved inorganic carbon diffusion into packed beds of forsterite. At field scale, Aradottir et al.[30] built 2D and 3D reservoir models for the CarbFix pilot project in Iceland, where CO_2 from the Hellisheidi power plant has been co-injected with formation waters in a nearby basalt flow since 2012.[30] The results indicate mineral carbonation in basalts represents a viable CO_2 sequestration option and provide valuable feedback to optimize injection site management.[30] However, simplifications necessary to run efficient field-scale models such as the use of volume-averaged subsurface properties preclude the isolation of parameters governing carbonation reactions at local scales.

The specific objective of this work was to develop a predictive framework for evaluating the roles of transport limitations and mineral spatial distributions on the location and extent of mineral carbonation reactions under conditions relevant to CO_2 injection in basalts. A series of core flooding experiments was conducted on serpentinized and unaltered basalt cores under advection-dominated transport regimes at representative GCS temperatures and pressures. Effluent chemistry data from these tests served as a benchmark for the development of complementary 2D reactive transport models using the multicomponent code CrunchTope,[31] which has recently been applied to simulate flow of CO_2-acidified fluids through fractures in carbonates,[32] sedimentary host rocks,[16,33] and wellbore cements.[22,34] The fracture surfaces from these reacted cores were

segmented into discrete mineral grids aligning with the dimensions of model domains in CrunchTope through a series of imaging techniques. Simulated injection of CO_2-acidified brine was compared between this mineral distribution from an actual basalt sample and random spatial distributions of the same volume-averaged composition to assess whether mineral heterogeneities directly impact carbonation efficiency. Advection- and diffusion-controlled systems were modeled to decouple the influence of transport regimes on basalt dissolution and carbonation reactions. This integrated experimental and modeling approach creates a framework for identifying key controls on the favorability of secondary mineral precipitation in a given system and extending lab-scale results to elucidate implications for long-term CO_2 storage.

2.2. Experimental Methods

2.2.1. Sample preparation and characterization

Core flooding experiments were conducted on two different basalts, an unaltered flood basalt from the Columbia River flood basalt near Pullman, Washington and a serpentinized basalt from a basalt dike near Valmont Butte, Colorado (hereafter referred to as FB and CB, respectively). Several cores (2.54 cm diameter) were taken from 42-45 mm thick slabs of each bulk sample material using a diamond core drill. Each core was divided in half length-wise using a precision saw with a diamond blade. The surface of one half of the split core was polished flat with 400-grit sandpaper, while the other half was etched with a meandering 1-mm wide fracture (Figure 2.1) using a CNC milling machine (Roland Model MDX-40a) with a 0.5 mm diamond bur. The etched surface was polished with 400 grit sandpaper until the pattern depth reached the target of 95-105 μm, which was determined by comparing the z-value of the spots on the groove and the spots on the closest polished surface in an optical microscope (ZEISS, Observer.Z1). This milled fracture served as the primary flow path for injected fluids and was designed to increase fluid residence time, as this pattern increased the flow path to ~6 times the length of the core. Assembled core halves were coated with epoxy on the sides parallel to the direction of flow and encased in chemical-resistant heat-shrink tubing.

Table 2.1. Advection-controlled experimental conditions

Experiment	Influent Composition	T (°C)	pCO_2 (MPa)
CB/FB-1	DI water	45	10
CB/FB-2	DI water	100	10
CB/FB-3	1.2 mM $NaHCO_3$ 13.8 mM NaCl	100	10

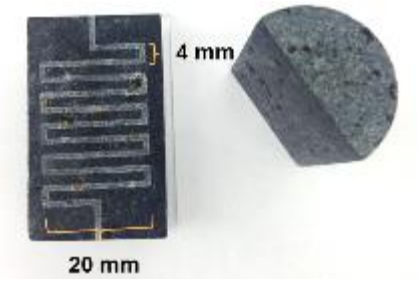

Figure 2.1. CB/FB core design

Samples of both basalts were analyzed with wavelength dispersive spectroscopy (WDS) to obtain bulk compositional data. The Colorado basalt was heavily serpentinized, containing 14% serpentine and only 1% unaltered Mg-rich olivine. The samples were rich in plagioclase (28% labradorite) and pyroxene (21% diopside) as well as a potassium-rich matrix (32%). Mineral grains were coarse and accessory minerals including apatite and chromite occurred as inclusions in larger silicate grains. In contrast, the flood basalt was fine-grained and was mostly unserpentinized (9% olivine and 1% serpentine). Plagioclase (31% labradorite), pyroxene (22% diopside), and a potassium-rich matrix (33%) still comprised the majority of the sample. The porosity of both samples was low (~1%). Additional details on material composition are provided in the Sample Library developed at Washington University.[35]

2.2.2. Advection-controlled basalt core flooding experiments

A series of six flow-through experiments was conducted in a customized biaxial core flooding system (Appendix A, Figure A1). In each test, water was first saturated with CO_2 within a 600-mL stainless steel batch reactor (Parr Instrument) under a constant CO_2 pressure of 10 MPa and the experimental temperature for at least 24 hours prior to initiating flow through the fractured basalt samples. Epoxy was applied to the sides of the two halves of the basalt cores (Figure 2.1) to prevent shifting post-reaction. The assembled cores were then secured in chemical–resistant heat shrink tubing and placed in a viton sleeve within a biaxial core holder (Core Laboratories). CO_2-acidified water was injected at a constant rate of 5 mL/hr, corresponding to a residence time of approximately 16s in the etched channel. Confining pressure was maintained at 20 MPa with a high-pressure syringe pump, while a back pressure regulator was used downstream of the core to prevent *in situ* degassing of CO_2 and to maintain a constant system pressure of 10 MPa. Differential pressure was monitored throughout the experiment by pressure transducers installed upstream and

downstream of the biaxial reactor. Note that a schematic overview of the core flooding system and additional details on its design and operation are provided in Appendix A.

Two sets of experiments were conducted, where 3 sets of conditions were tested for both the serpentinized Colorado basalt (CB) and unaltered flood basalt (FB) cores (Table 2.1). The first two experiments injected CO_2-saturated deionized (DI) water (with resistivity greater than 18.2 MΩ-cm), but temperature was raised from 45 °C to 100 °C in the second. In actual systems, temperature depends on the geothermal gradient and storage depth; injection sites are typically selected to exceed the critical point of CO_2 (31.6˚C, 7.31 MPa) so that it remains supercritical downhole.[36] Higher temperatures were applied in these experiments to enhance reactivity over shorter time scales. The third flow-through experiment was also run at 100ºC and used a solution with salinity and alkalinity representative of a typical basalt reservoir in the U.S. Pacific Northwest, based on hydrochemical data for Pasco Basin basalt aquifers collected at depths relevant to CO_2 storage (greater than 800 m) with reported charge balances within 10% error. Because Na^+ and Cl^- were the dominant cations and anions in these samples, the average Na^+ concentration was selected along with the average alkalinity (as HCO_3^-) to create a simplified representative brine for this study. These levels of salinity and alkalinity were matched by adding 1.2 mM of $NaHCO_3$ and 13.8 mM of NaCl to DI water prior to brine equilibration in the batch reactor.

2.2.3. Post-reaction analyses

Discrete effluent samples were aggregated over 1-2 hr intervals for the 120-hr duration of the experiments. Major cations (Ca, Mg, Fe, Si, Na, K, and Al) were analyzed via ICP-MS and pH was calculated at each sampling point based on the data with the constraint of electroneutrality (see Appendix A). Effluent chemistry was also used in mass balance calculations to estimate net changes in mineral content and fracture volume along the flow pathway. Because measured Na concentrations were significantly higher than could be accounted for with congruent plagioclase dissolution, the corresponding amount of Ca released assuming all Na dissolved stoichiometrically would result in little to no pyroxene dissolution based on the Ca balance. Sodium was thus assumed to dissolve incongruently from the plagioclase or from trace reactive glass phases and excluded from mass balance calculations. All Al dissolution was attributed to plagioclase given a lack of information on the Al content of the K-rich groundmass. The difference between the Ca that would have dissolved stoichiometrically from this calculated amount of dissolved plagioclase and the

total measured moles of Ca in the effluent was attributed to pyroxene, which was then assumed to dissolve stoichiometrically per the molar ratios identified via WDS. Finally, olivine dissolution was estimated from an Mg balance with pyroxene, assuming any olivine that dissolved was primarily in its more reactive unserpentinized state. Mineral densities and molar weights from WDS-derived stoichiometry were used to convert moles to mineral volumes. Other trace minerals (e.g. chromite, apatite) were excluded from calculations due to their low reactivity.

Core samples were scanned post-reaction at the University of Michigan to infer dissolution patterns along the fracture pathway. Scans were collected in a micro-CT scanner (XTH225, Nikon Metrology, Inc.) and reconstructed using CT Pro (XT5.1.3, Nikon Metrology, Inc). A beam energy of 190 kV and current of 134 μA were applied to take 3141 projections at 0.11˚ steps integrating 4 frames per projection. The scans were processed and analyzed in ImageJ.[37]

2.3. MODELING METHODS

2.3.1. Reactive transport code

All models were developed in CrunchTope, a multicomponent reactive transport code that has been applied to a variety of environmental problems involving flow through porous media.[31] Simulations were conducted using the global implicit approach, where time steps are extended as the system approaches steady state to enhance computational efficiency.[31] Additional details on the code's capabilities, limitations, and governing equations are available in the user's manual (available for download from www.csteefel.com).

Mineral reactions are modeled based on transition state theory assuming continuous reversibility between dissolution and precipitation at equilibrium. Reaction rate constants at 100°C, the temperature applied in all models considered here, were calculated based on selected literature values for the reaction rate constant at 25°C and activation energy according to the Arrhenius relationship:

$$k = k_{25} \exp\left[\frac{-E_a}{R}\left(\frac{1}{T} - \frac{1}{298.15}\right)\right] \quad (1)$$

Reaction pH dependence was incorporated by summing adjusted rate constants for acid (H), neutral (neu), and basic (OH) mechanisms, where *n* and *m* are the partial orders of reaction with respect to H^+ and OH^-, respectively:

$$k_{rxn} = {a_H}^n k_H + k_{neu} + {a_{OH}}^m k_{OH} \quad (2)$$

For each mineral included in the system (Section 2.3.3), the reaction rate constant, total surface area (A), and saturation index are then used to calculate the overall reaction rate at each time step:

$$r = -Ak_{rxn}\left[1 - \frac{Q}{K}\right] \quad (3)$$

While extrapolating to high temperatures may introduce errors in mineral reactivities, specific surface areas are likely the main source of uncertainty in this formulation. Calculated reaction rate constants and literature-reported pH and pOH dependence for all primary (i.e., initially present) and secondary (i.e., formed by reaction) minerals are summarized in Table 2.2. Note that dolomite was intentionally excluded as a secondary mineral due to its well-established disinclination to precipitate under modern natural conditions despite thermodynamic favorability.[38,39] Quartz was also suppressed due to its slow precipitation kinetics. Under the conditions in this study, solutions supersaturated with respect to SiO_2 would predominantly precipitate amorphous silica, which has a lower interfacial energy and faster nucleation rate than crystalline forms.[40]

Table 2.2. Summary of primary and secondary mineral kinetic data and reactive surface areas.

Mineral	Initial Volume Fraction (%)	Acid mechanism		Neutral	Basic mechanism		SSA (m^2/g)	
		log k, 100°C ($mol/m^2/s$)	n^{H+}	log k, 100°C ($mol/m^2/s$)	log k, 100°C ($mol/m^2/s$)	n^{OH-}	Calculated (geometric)*	Selected**
Primary Minerals								
Diopside	22	-2.97[41]	0.71[41]	-9.68[41]	--	--	0.0148	0.0034[+]
Albite	12	-6.47[42]	0.50[42]	-9.66[41,42]	--	--	0.0225	0.0225
Anorthite	18	-6.47[42]	0.50[42]	-9.66[42]	--	--	0.0225	0.0225
Antigorite	11	-7.54[43]	0.45[43]	-10.1[44]	--	--	0.0165	0.18
Forsterite	1	-4.48[41]	0.47[41]	-7.85[41]	--	--	0.0148	0.018
Fayalite	3	-3.53[++]	0.47[41]	-9.48[41]	--	--	0.0148	0.0018
K-feldspar	33	-7.63[41,42]	0.50[41]	-11.29[41]	-17.9[41]	-0.823[41]	0.019	0.019
Secondary Minerals								
Calcite	0	0.21[41]	1.0[41]	-4.98[41]	--	--	--	0.037[45]
Magnesite	0	-5.87[41]	1.0[41]	-8.51[41]	--	--	--	0.0662[45]
Siderite	0	-1.76[46]	0.90[46]	-6.69[42]	--	--	--	0.105[47]
SiO_2(am)	0	--	--	-6.92[48]	--	--	--	0.0225[49]
Kaolinite	0	-8.99[41]	0.777[41]	-12.4[41]	-16.4[41]	-0.472[41]	--	8.16[50]

*Geometric surface areas calculated as smooth spheres based on average phenocryst grain sizes (see Appendix B)

**Some SSA values were tuned from the calculated geometric values to optimize fit to experimental effluent data.

[+]In the initial calibration, 18% of the diopside was added with a higher SSA of 0.11 m^2/g to match rapid initial dissolution from finer surface particles (see Appendix B).

[++]Reaction rate adjusted to fit Fe data by setting k_{25} to that of forsterite (see Appendix B).

2.3.2. Model benchmarking

An initial model was developed to simulate experiment CB-2 in Table 2.1 (Section 2.2.2), where CO_2-acidified brine was injected through a serpentinized basalt core under high temperature (100°C) and pressure (10 MPa P_{CO2}). In the experiment, the core was divided into two halves with one containing a 100 μm-deep etched fracture pathway designed to extend fluid residence time (Figure 2.1). To create the model domain the surface of this fractured half was discretized into a grid of 48x80 cells, each 0.5x0.5 mm. The height of each cell (0.011 mm) was calculated to match the residence time of the flow-through experiments (0.0046 hr). Although the actual physical domain consists of an open fracture between two basalt surfaces, 2D models consider each cell as a porous media with bulk volumes of mineral and void space. To simulate the fracture walls and provide sufficient mineral for reaction, the fracture porosity was set to 90% in the code.[33] Some prior studies have assigned fracture porosities of 100% to examine fracture cross-sections,[16,22] but the incorporation of minerals in the fracture here was necessary to simulate a 2D plane of fluid surrounded by reactive surface area. While the actual porosity of the basalt samples is low (~1%),[35] the modeled matrix porosity was set to 5% to prevent rapid pore clogging. Porosity is allowed to evolve during simulations in accordance with changes in mineral volume fractions. The initial mineral volume fractions listed in Table 2.2 were set based on bulk sample characterization (Section 2.2.1), as detailed in Appendix B (Section B2). To match experimental conditions, water equilibrated with 10 MPa CO_2 was injected into the fracture pathway at a rate of 5 mL/h. CO_2 fugacity was computed directly in the code using the empirical formulation provided by Duan and Sun.[51] Longitudinal and transverse dispersivity values were set to 10% of the flow path length (0.023 m). The diffusion coefficient was fixed at $7.5*10^{-9}$ m^2/s, corresponding to the mean value for CO_2 in water at 100°C reported by Cadogan et al.[52]

Experimental effluent chemistry data served as a benchmark for adjusting uncertain model input parameters. Because reactive transport models are highly sensitive to mineral reactive surface areas, which are also generally the source of greatest uncertainty,[53] values are typically adjusted from calculated geometric or measured BET surface areas to fit experimental data.[16,30] Here, specific surface area (SSA) for each mineral was first calculated assuming spherical geometry, using average diameters corresponding to phenocryst grain size distributions from preliminary characterization of the reacted cores.[54,35] These geometric SSA values were then fine-tuned where necessary to match effluent chemistry for divalent cations (Ca^{2+}, Mg^{2+}, Fe^{2+}) at the

outlet of the model domain. Aligning model outputs with experimental silica and minor cation (Na^+, K^+) concentrations required altering mineral stoichiometry and reaction rates and was ultimately neglected to avoid over-constraining the model. Initial primary mineral volume fractions were adjusted to within 2% of values derived from previously reported wavelength dispersive spectroscopy analyses[35] to optimize the fit.

While Steefel and Van Cappellen[40] developed a reactive flow model incorporating expressions for heterogeneous nucleation, growth, and Ostwald ripening, nucleation has not been fully coupled with reactive transport codes. Fritz et al.[55] modeled clay nucleation and growth but acknowledged that significant uncertainties in input parameters such as interfacial free energies and pre-exponential constants in the nucleation rate equation limit the application of quantitative results. In the absence of sufficient nucleation kinetic data for the secondary mineral phases in our system, precipitation is initiated through a threshold volume fraction. All secondary minerals are assigned initial volume fractions of 0 and volume fraction thresholds of 10^{-5} to calculate bulk surface area until the volume fraction threshold is exceeded; thereafter, the precipitate's surface area is updated according to its calculated volume fraction and reported BET surface areas. SSA values for all minerals used in the models are included in Table 2.2, while additional details regarding the calculation and selection of input parameters are provided in Appendix B (Section B1).

After achieving calibration using data from a flow-through experiment with a serpentinized basalt (CB-2), the model was validated using data from a flow-through experiment conducted under the same temperature, pressure, and flow conditions (100 °C; 10 MPa CO_2; 5 mL/hr) but with an unserpentinized flood basalt core (i.e. experiment FB-2 in Table 2.1). Mineral volume fractions of pyroxene and olivine were altered to account for slight differences in bulk mineralogy, and the reactive surface areas of diopside and forsterite were reduced by half to match lower effluent Ca and Mg concentrations. Appendix B includes a full accounting of the model inputs and results. Because both samples produced similar experimental effluent data and the effect of bulk composition was not the focus of this work, the mineralogy of the serpentinized basalt used in the initial calibration is applied for all models presented in this chapter.

2.3.3. Mapping mineral spatial distributions

Discretized mineral grids were developed for heterogeneous models using an approach similar to that demonstrated by Ellis and Peters,[56] which is detailed in Appendix B (Section B4) and summarized here. Energy-dispersive spectroscopy (EDS) was coupled with back-scattered

electron (BSE) images to identify specific minerals in a reacted basalt core, which were then mapped to features in x-ray computed tomography (xCT) scans. Mineral spatial distributions along the fracture path were obtained by first coarsening an image of the fracture to align with the model domain by assigning one average pixel intensity to each 0.5x0.5mm block. This image was segmented into four discrete mineral phases (pyroxene; plagioclase; serpentinized and unserpentinized olivine; and K-feldspar) based on ranges in pixel intensities corresponding to each mineral identified in the xCT/EDS analysis. Conditions for each mineral group were created in CrunchTope to match the specific minerals selected in the uniform 'calibration' models (Table 2.1), and each cell was assigned one of four mineral conditions based on the processed CT image. Relative fractions of each mineral aligned well with those applied in the uniform model based on WDS analyses. Example BSE/EDS images and a schematic overview of the segmentation process are also provided in Appendix B.

2.3.4. Hypothesis-driven model development

Previous flow-through experiments served as an effective benchmark but were not intended to constrain modeling efforts. To this end, an idealized uniform fracture was taken as the domain for subsequent models designed to isolate the roles of transport and mineral heterogeneities in controlling dissolution and precipitation reactions. Because the small volume of the domain used in calibration induced rapid mineral dissolution and exhaustion due to low mineral volumes, all cells were scaled up to 0.5x0.5x0.5cm, effectively increasing the domain volume by 3 orders of magnitude, to facilitate comparisons over longer time frames.

Two models were developed to investigate the role of transport limitations: one considering pure advection and one with pure diffusion. The segmented mineral distribution based on an actual core sample was used for these models to explore coupled effects of transport and mineral heterogeneities. The mineralogy, domain setup, and boundary conditions are illustrated in Figure 2.2. Both conditions allowed free flow at the lower boundary, while the upper boundary supplied CO_2-saturated water (equilibrated at 10 MPa P_{CO2}) through constant injection for the advection model and a Dirichlet (fixed concentration) boundary for diffusion. Pure advection models were developed by setting the injection rate to achieve each of 8 selected residence times (6, 12, 24, 48, 96, 144, 192, and 288 hr) in the fixed domain volume. The fixed diffusion coefficient used in calibration ($7.5*10^{-9}$ m^2/s) was applied for pure diffusion. Each grid cell was assigned a porosity of 60% to provide sufficient mineral volumes in the domain for continued reaction over longer

time frames. The remaining mineral fraction (40%) essentially consisted of two "layers": 70% contains only the mineral allocated to that cell in the segmentation, and 30% is comprised of an underlying uniform mineral distribution corresponding to the bulk mineralogy. This approach reasonably captures mineral heterogeneities while allowing for continued dissolution of the underlying rock matrix if reactive mineral cells are depleted during simulations. As previously noted, a cell containing both mineral and fracture is viewed as a porous medium in 2D modeling; thus, applying a lower porosity to the fracture than that used in model calibration essentially increases the amount of surrounding rock captured by the domain. Note that in contrast to the dual porosity models developed for calibration with zones of fracture and matrix, the models developed here to investigate the roles of transport limitations and heterogeneities have a single uniform porosity of 60% to simulate a fracture surrounded by reactive surface area.

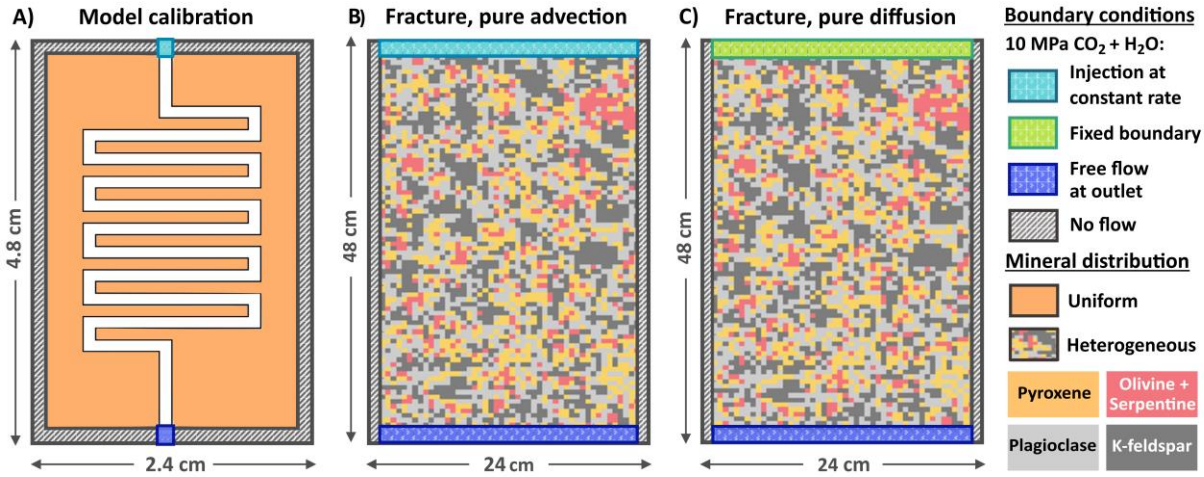

Figure 2.2. Conceptual model domains for A) initial calibration simulating flow-through experiments with uniform mineralogy; B) pure advection in a heterogeneous open fracture; and C) pure diffusion in a heterogeneous open fracture.

To isolate the effects of mineral heterogeneity on the extent and location of carbonation, transport conditions were held constant while additional simulations were run using random mineral grids with comparable domain-averaged compositions. These models were set up identically to those in Figures 2.2b and 2.2c with varying realizations of mineral spatial distributions, including models with larger clusters of reactive minerals to evaluate whether highly localized concentrations of certain minerals affect the extent of carbonation compared with more even allocation across the domain. A summary of transport conditions and mineral distributions applied to each model included in this study is provided in Table 2.3. Segmented mineral

distributions refer to those obtained by segmenting the fracture surface of the serpentinized basalt core in experiment CB-2 (see Appendix B, Section B4), while random distributions were generated in MATLAB using the same volume-averaged fractions of primary minerals. Two types of "random" grids were tested: grids where the mineral assigned to every cell was truly random and grids where larger mineral clusters were randomly generated within the domain to emphasize preferential precipitation of certain secondary minerals on specific primary sites. Because simulations with these random distributions resulted in negligible differences in the total volume of carbonates formed at a given time step, only one of these grids is presented in the results for comparison with the segmented grid from the actual serpentinized basalt sample. Results for other selected random grids are included in Appendix B.

Table 2.3. Summary of key conditions for models discussed in this chapter.

Model*	Transport conditions	Mineral distribution
TA1	Pure advection with τ = 6, 12, 24, 48, 96, 144, 192, and 288 h	Segmented (1)
TD1	Pure diffusion	Segmented (1)
SA1	Pure advection with τ = 288h	Segmented (1)
SA2	Pure advection with τ = 288h	Random (2)
SD2	Pure diffusion	Random (2)

*First letter corresponds to the model purpose: investigating transport conditions (T) or mineral spatial distributions (S); second reflects transport conditions (advection or diffusion); and third indicates the spatial distribution used (1 for the segmented grid from an actual core and 2 for a random distribution with the same volume-averaged mineralogy).

2.3.5. Simulations with additional secondary silicates

Previous work has suggested secondary silicate precipitation may limit carbonation efficiency. Experimental and modeling studies have demonstrated precipitation of clays and zeolites over a range of conditions relevant to CO_2 storage that could compete with carbonates for divalent cations.[e.g. 30,57–60] In packed bed experiments with the same basalts and similar conditions as this study, siderite, zeolite, lizardite, and trace amounts of amorphous silica were observed.[61] To evaluate the influence of Ca-, Mg-, and Fe-bearing secondary silicates, the advection and diffusion models developed to investigate transport limitations were run with additional secondary minerals: smectite (modeled as 4 montmorillonite end-members); biotite (annite and phlogopite); and zeolite (laumontite). Further details on modeling inputs and results from these simulations are provided in Appendix B (Section B6), while the implications are presented in Section 2.4.4.

2.4. Results and Discussion

2.4.1. Advection-controlled flow drives net basalt dissolution

Figure 2.3 presents effluent cation concentrations over time for each set of core flooding experiments. Note that Ca, Mg, and Fe are the major released cations capable of forming carbonate minerals. In the CB runs, calcium and magnesium exhibited similar early spikes in concentration that peaked around 6 hours followed by a decline toward quasi-steady-state conditions. Similar trends were observed for the FB cores with Ca and Mg peaking after 2-3 hours. In all six experiments, Fe increased most rapidly over the first 3-6 hours but leveled off after 20 hours.

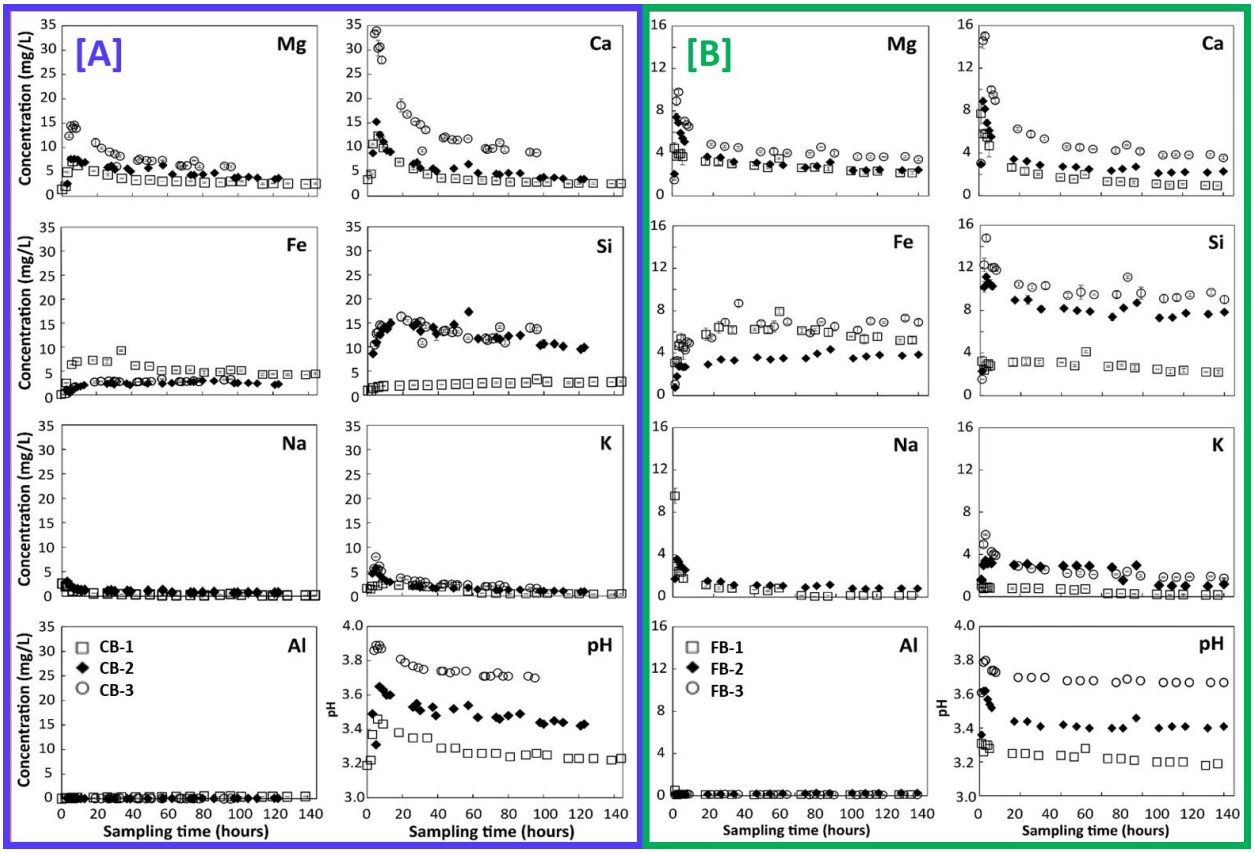

Figure 2.3. Effluent chemistry data for each set of advection-controlled flow-through experiments using the [A] serpentinized Colorado basalt (CB) and [B] unaltered flood (FB) basalt cores. For each set, experiments were conducted at 45˚C (CB/FB-1) or 100˚C (CB/FB-2 and -3) with pure DI water (CB/FB-1 and -2) or DI with 13.8 mM NaCl and 1.2 mM $NaHCO_3$ (CB/FB-3). Error bars correspond to relative standard deviations from 3 replicate measurements on ICP-MS.

Concentrations of the remaining cations analyzed were consistently lower than Ca, Mg, and Fe. Na and K leaching exhibited similar trends to those of Ca and Mg, while Al concentrations were about an order of magnitude lower than Ca and Mg with inconsistent trends across different experimental conditions. For all cations, changes in temperature had little effect on the time

required to reach quasi-steady-state conditions. Dissolved Ca and Mg concentrations were increased to a greater degree with the addition of salinity and alkalinity in the influent fluid than with an increase in temperature from 45 to 100°C. The influence of temperature and fluid chemistry are discussed in more detail in Section 2.4.2.

The evolution of pH was similar for all three experiments conducted for each material, but quasi steady-state conditions were achieved faster for the FB (~20 h) than for the CB (40-60 h) cores. The early-stage pH was slightly higher in the CB cores, corresponding to a greater amount of initial mineral dissolution, but final pH values were comparable for both samples. Greater initial dissolution for the CB tests may be partially due to the larger grains that may have been more readily mobilized upon CO_2 exposure. The pH increased at 100°C due to reduced CO_2 solubility at higher temperatures and was also elevated in experiments with added $NaHCO_3$.

Carbonate saturation indices (SI), calculated from the effluent solution chemistry and estimated *in situ* pH conditions presented in Figure 2.3, indicate that all carbonate minerals were undersaturated throughout all advection-controlled core flooding experiments, consistent with the lack of observed carbonate precipitation. Although more Ca and Mg dissolved than Fe, the systems were closest to saturation with respect to siderite as opposed to calcite or magnesite, as exemplified by the SI trends for the third experiments (CB/FB-3) presented in Figure 2.4 below. Under the low pH conditions of the experiments, the solubility product of siderite is roughly two orders of magnitude smaller than that of the other carbonate minerals, and siderite saturation would be achieved first given the similar concentrations of major divalent cations (Fe^{2+}, Ca^{2+}, Mg^{2+}).

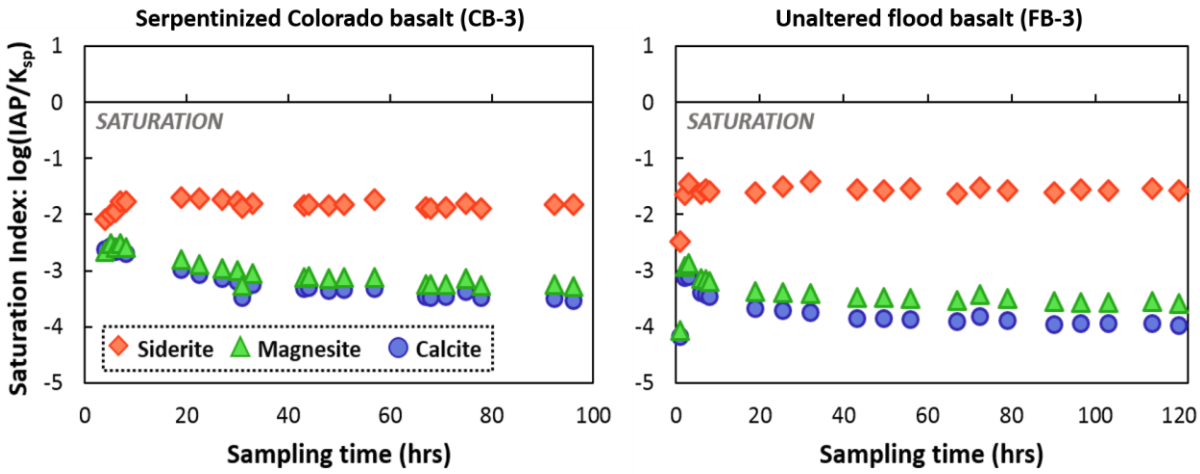

Figure 2.4. Carbonate saturation indices for CB-3 and FB-3 experiments, which were conducted at 100˚C with representative reservoir brine (13.8 mM NaCl and 1.2 mM $NaHCO_3$).

Net dissolution was corroborated by mass balance calculations based on effluent chemistry and relative mineral reactivity (Section 2.2.3), which are summarized in Table 2.4. Of the major primary mineral phases, pyroxene contributed most to dissolution in all experiments, but released Ca, Mg, and Fe cations were transported out of the system before they could precipitate out of solution as carbonate minerals. The lack of precipitation is further supported by measured pressure differentials below the tolerance of the transducers (5-10 psi), which suggests little change in permeability. These analyses indicate the short residence time of the system under advection-dominated flow promoted net dissolution, while carbonation was limited by the low pH with continued CO_2 injection and insufficient mineral buffering.

Table 2.4. Calculated mineral dissolution volumes based on mass balance calculations.

Experiment	Pyroxene (mm^3)	Olivine (mm^3)	Plagioclase (mm^3)	Total (mm^3)
CB-1	5.03	1.16	0.997	7.19
CB-2	6.66	1.37	0.139	8.17
CB-3	12.9	--	0.102	13.0
FB-1	2.48	1.43	0.258	4.17
FB-2	2.33	1.85	0.511	4.68
FB-3	7.58	0.433	0.249	8.26

2.4.2. Temperature and salinity enhance basalt dissolution

In all core flooding experiments, the effect of temperature was most pronounced for dissolved silica, where concentrations were roughly four to five times higher at 100°C than at 45°C (Figure 2.3). Molar ratios of the total dissolved cations to total dissolved silica were approximately one at the end of all experiments run at 100°C and greater than one at 45°C, indicating dissolution was sub-stoichiometric with respect to Si at lower temperatures. This is consistent with prior work on individual basaltic mineral dissolution rates that reported preferential release of cations from the bulk silica framework as seen for plagioclase[62] and pyroxene.[63] Because divalent cation concentrations increased to a lesser extent than silica with increasing temperature, higher ratios of silica to cations were observed at 100°C, indicating that while dissolution remained incongruent, release rates became more stoichiometric. Zhang et al.[63] observed similar temperature-induced changes in a series of experiments measuring pyroxene dissolution rates, noting that Mg, Ca, Fe, and Al were released faster than Si from 25 to 100°C, but Si dissolved most rapidly at higher temperatures. An earlier study observed analogous trends in albite dissolution whereby Na and Al

were released faster than Si from 25 to 300°C but dissolution became increasingly congruent with increasing temperature.[64] This was attributed to changes in water properties (i.e., a reduction in density and dielectric constant) and destruction of hydrogen bonds with increasing temperature that facilitate breaking of covalently-bonded compounds (e.g., SiO_2) and hinder dissolution of ionic bonds (e.g., Ca-O, Mg-O).[63] Incongruent dissolution becomes more pronounced at lower pH levels,[65] which was reflected here in the greater cation:silica ratios observed under lower pH conditions in the experiments run at 45°C. While the effect of temperature was less dramatic, the increasing congruency of dissolution with increasing temperature was consistent for both basalts.

In addition to temperature, $NaHCO_3$ and NaCl concentrations characteristic of basaltic reservoirs enhanced dissolution for both the serpentenized and unaltered flood basalt samples. Although the effects of these additives were not isolated, greater dissolution was most likely promoted by NaCl. While Prigiobbe et al.[66] concluded that changes in olivine dissolution rates under varying salt concentrations could be exclusively accounted for by changes in pH, the fact that greater dissolution was observed here in solutions with increased salinity and higher pH levels that would inhibit dissolution indicate NaCl may have a unique impact on dissolution rates under advective transport conditions. Prior work has also shown that enhanced dissolution with salinity becomes more pronounced at higher salt concentrations.[27] However, in contrast to saline aquifers conventionally considered for CO_2 storage, salinity is unlikely to vary significantly across basalt aquifers at typical storage depths and thus may not be a major consideration for site selection.[67]

2.4.3. Model-experiment correlation

As described in Section 2.3, the initial model domain and conditions were aligned with the flow-through experiments introduced in Section 2.2 and discussed in the sections above. Model trends in major dissolved cations were benchmarked to measured effluent concentrations over the experimental time frame. Figure 2.5 demonstrates that the model reasonably captures the dissolution of the key divalent carbonate-forming divalent cations; additional cation comparisons are included in Appendix B (Figure B1). Note that a fraction of the diopside in the calibrated model is assigned a higher specific surface area (SSA) to capture initial Ca and Mg concentration spikes, presumably resulting from rapid initial dissolution of fine-grained surface particles in the flow-through experiment. As noted in Section B1 of Appendix B, only one SSA for diopside is used in subsequent models. Simulations overestimate initial silica concentrations because cations were preferentially released from the bulk silica matrix during the experiment. The model also

underestimates concentrations of monovalent cations, possibly due to incongruent dissolution of feldspars. Despite these limitations, explicit calibration to experimental results was intentionally avoided to provide a representative but not overly-constrained basis for model development.

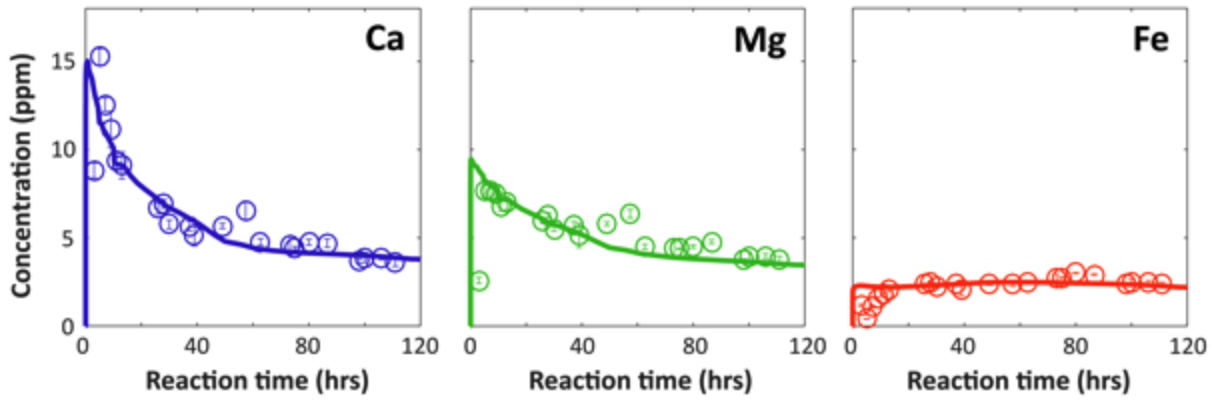

Figure 2.5. Comparison of calibrated model results (solid lines) with experimental effluent chemistry data (open circles) from a core-flooding experiment where CO_2-acidified brine was injected at a constant rate of 5 mL/h through a serpentinized basalt sample under 100°C and 10 MPa P_{CO2}.

2.4.4. Role of transport limitations

To evaluate the effects of transport conditions on carbonation efficiency, simulations were conducted for pure diffusion and pure advection under 8 different hydraulic retention times using the domains illustrated in Figures 2.2b and 2.2c (Section 2.3.4). Discrete outputs of carbonate volume fractions, defined as the volume of carbonates formed per unit volume of porous media in the domain, are plotted as a function of simulation time in Figure 2.6. Carbonation in the pure advection systems is controlled by residence time, and the "optimal" residence time for maximum carbonate precipitation depends on the time frame of interest. For instance, advection promotes more carbonate precipitation than diffusion in the first 1-2 years after commencing CO_2 injection, with lower flow rates becoming more favorable over longer times as carbonates are able to accumulate. Shorter retention times (corresponding to faster flow) lead to greater initial carbonate precipitation driven by rapid dissolution, but these carbonates quickly re-dissolve as continued CO_2 injection increases the acidity of surrounding fluids and reactive primary mineral phases are depleted. Calcite dissolution tracked with diopside depletion at the inlet, leaving behind feldspars that react too slowly to provide sufficient buffering to offset the drop in pH and sustain carbonation. Qiao et al.[68] observed similar behavior in numerical modeling of CO_2 flooding in carbonate reservoirs, whereby instantaneous drops in pH due to CO_2 injection outpaced the rise in pH from mineral dissolution that occurred over longer time frames. Although the models do not

predict re-precipitation in the absence of more rapid pH buffering, these re-dissolved cations would likely re-precipitate further downstream where the CO_2 front has not advanced far enough to reduce the pH below carbonate saturation. These results are partially driven by the size of the model domain but indicate that rapid and continuous CO_2 injection at field scale could erode carbonates formed along main flow paths, particularly if precipitation is highly localized in small clusters. If reactive minerals are abundant near wellbores, high flow rates and high CO_2 partial pressures may favor continued dissolution and inhibit precipitation.

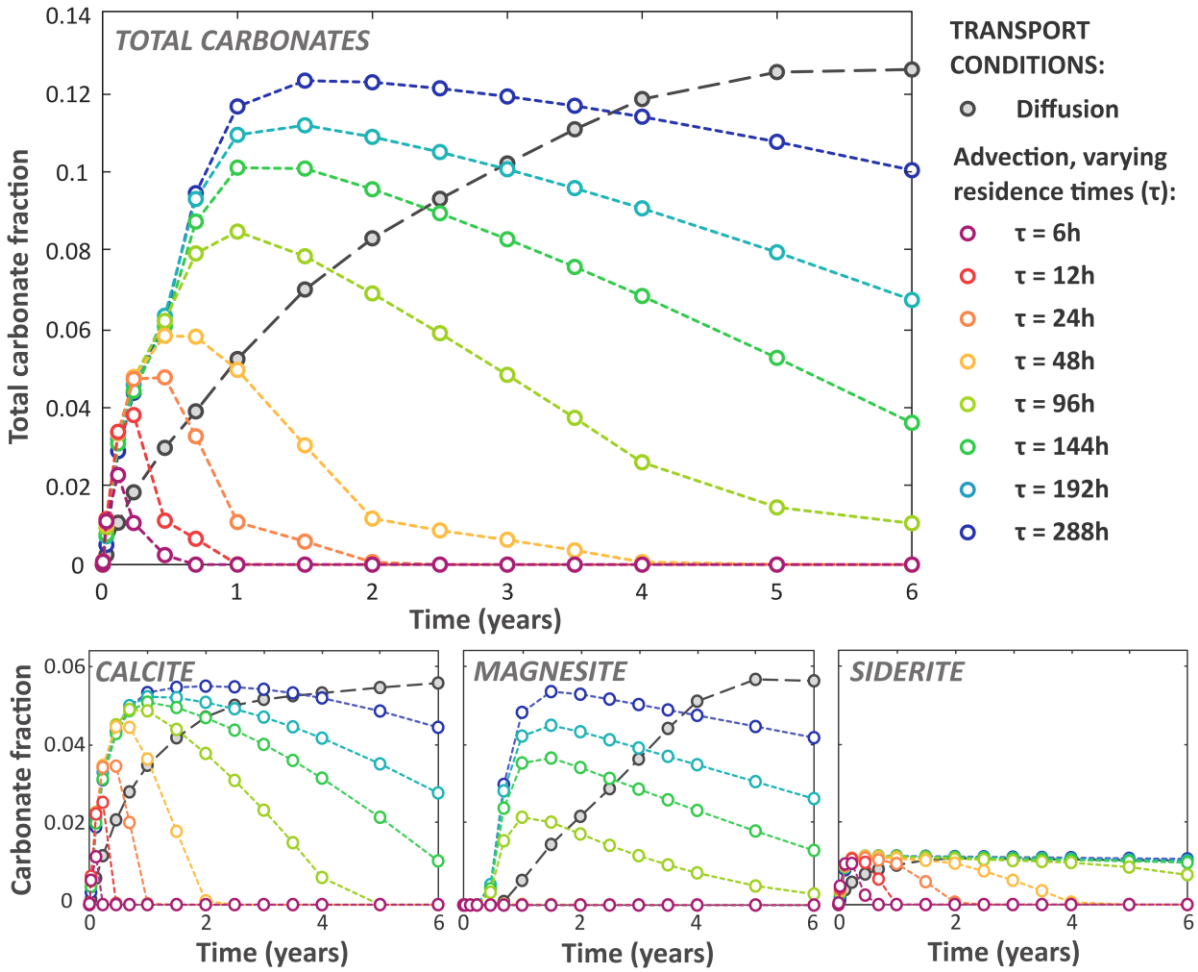

Figure 2.6. Total fraction of carbonates formed (presented as cm^3 of carbonate minerals per cm^3 of the modeled fracture domain) as a function of time for 9 selected transport conditions: pure diffusion and pure advection under 8 different hydraulic retention times. Sub-figures indicate individual contributions from calcite, magnesite, and siderite to total carbonation.

While carbonation efficiency (i.e., the amount of carbonates formed with respect to the amount of divalent cation-bearing minerals dissolved) is highest under diffusive mass transport conditions, greater total volumes of carbonates are formed under advective flow for early time frames (1-2

years) because more divalent cations are available. Carbonates form more slowly in the pure diffusion model but are more stable, reaching quasi steady-state volume fractions over longer time frames and re-dissolving minimally with continued CO_2 penetration. Diffusion also lengthens surface reaction times, maintaining favorable pH levels for carbonate saturation and allowing for greater precipitation over time scales on the order of years. Unless CO_2 injection occurs in areas with high abundances of pre-existing reactive minerals (e.g., calcite), it will likely generate strong advective conditions near the wellbore that result in net dissolution, while most carbonation will occur in low-porosity zones surrounding main flow channels or dead-end fractures further from the wellbore where transport is limited by diffusion.

After two years, most of the dissolved calcium is contained in calcite (87%) under diffusive conditions, while the fraction of carbonated Ca decreases with decreasing residence time for the advection cases. All of the dissolved Ca is released from the domain (i.e., none remains trapped in carbonates) for residence times less than or equal to 24h. Additionally, all diopside in the model domain dissolves after one year but smaller amounts of Ca are still released from anorthite at slower rates. Extended retention times prolong diopside depletion and allow for greater carbonate accumulation, as continued dissolution of reactive minerals releases silicates rapidly enough to provide pH buffering. Although all tested conditions initially yielded net dissolution, the diffusion model achieved net precipitation within 6 weeks. In this case, the contribution of carbonates to the total volume of secondary precipitates declined from 92% at 10 days to 42% after 6 years as amorphous silica and kaolinite accumulated. Similar trends were observed under slow-flow advection, but residence times of 48h or less resulted in net dissolution after 6 years. Note that while the model does not account for effects of passivating layers, secondary precipitation of amorphous silica predicted in all models could reduce carbonation efficiency in actual reservoirs by obstructing CO_2 transport to mineral surfaces and reducing permeability along flow paths.[29] Amorphous silica layers have also been shown to kinetically control olivine dissolution and significantly inhibit carbonation rates at 90 °C.[69]

The subfigures in Figure 2.6 track the contributions of calcite, magnesite, and siderite to the total carbonate fractions at each time step, illustrating how calcite controls carbonation at early time frames while contributions from magnesite and siderite become more significant with continued CO_2 injection. Note that due to uncertainties in actual carbonate precipitation rates, these results are limited by the assumption that carbonate formation is kinetically controlled, i.e.

dissolution and precipitation reactions proceed reversibly according to the same reaction rates (Section 2.3.1). Nucleation kinetics and crystal growth mechanisms (e.g., Ostwald ripening) will also be key considerations in actual systems where critical degrees of supersaturation are required to initiate precipitation.

Because calcite has the fastest kinetic parameters in the model, it forms most rapidly under pure advection with short retention times but also re-dissolves quickly because reactive minerals are depleted and reaction products are transported out of the domain before significant pH buffering can occur. Magnesite consistently had the highest saturation index across the domain (see Appendix B, Figure B6) but only formed at retention times greater than or equal to 96h due to kinetic limitations. Diopside contributed the most to mineral dissolution, providing both Ca and Mg for carbonation, but the fast reaction rate of calcite relative to magnesite leads to preferential calcite precipitation given sufficient Ca availability. The advective models predict magnesite will re-dissolve around the same time as calcite but at a slower rate. Siderite formed to a lesser extent due to kinetic limitations but was more resistant to re-dissolution over longer time frames. The preferential formation of calcite over other carbonates is consistent with prior work that found calcite growth rates exceeded those of magnesite by 6 orders of magnitude[70] and siderite by 8 orders[71] under equivalent conditions and saturation indices. Such studies have attributed the differences in carbonate precipitation kinetics to higher surface charge densities for siderite and magnesite, as the smaller ionic radii of Fe^{2+} and Mg^{2+} relative to Ca^{2+} require higher activation energies to initiate dehydration and subsequent precipitation.[71]

2.4.5. Role of mineral spatial distribution

Modeling results for various spatial realizations of the same bulk mineralogy indicate that mineral heterogeneities may control the location of secondary precipitation but negligibly impact the extent. Figure 2.7 compares the volume fractions of carbonates formed after 2 years for the segmented mineralogy from an actual core sample with a random distribution of comparable bulk composition. While the figures elucidate the effects of heterogeneity on carbonate locations, the variation in total volumes of carbonates formed in the fracture domain over two years attributable to slight differences in primary mineralogy was only 4%. Additional simulations (see Appendix B, Section B5) using random distributions with the same mineral fractions as the random grids in Figure 2.7 produced carbonate volumes within 2-3% of each other at each time step over 10 years, even when reactive minerals were concentrated in large clusters.

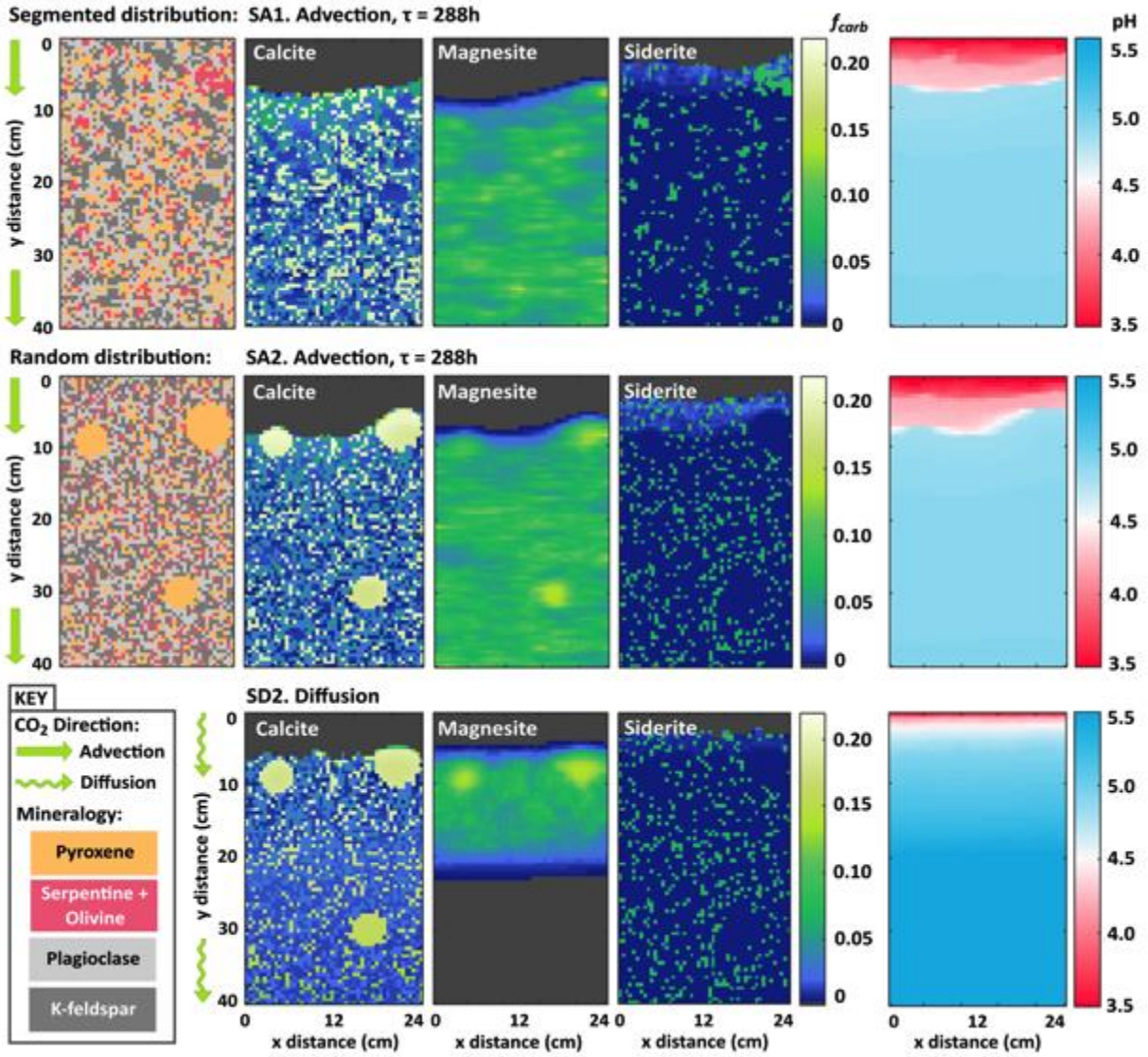

Figure 2.7. Spatial distributions of carbonation (expressed as carbonate fractions, f_{carb}, which represent cm^3 of carbonate per cm^3 of domain volume) across the model domain after 2 years of injection of CO_2-acidified brine for 2 selected heterogeneous distributions with comparable bulk mineral compositions: 1) segmented core sample from flow-through experiments and 2) random distribution with larger pyroxene clusters. Results for 2 flow conditions, low-flow advection and diffusion, are also compared for grid 2.

Despite negligible influence on precipated carbonate volumes, the locations of primary minerals govern the location of carbonate precipitation, which occurs on reactive mineral phases containing the requisite divalent cations. Calcite forms preferentially on pyroxene and to a lesser extent on plagioclase; magnesite is more uniformly distributed but forms in greater volumes on pyroxene and olivine grains; and siderite is localized on olivine, the only Fe-bearing mineral included (Figure 2.7). These observations indicate that for given flow conditions and volume-averaged primary mineral abundances, mineral heterogeneities will not impact the amount of

carbonates formed but will control local solution concentration, which will influence the location of secondary precipitates. In actual systems, heterogeneous nucleation may also contribute to preferential precipitate formation on specific primary minerals.

As expected, pH also governs which carbonates precipitate through its effect on saturation indices. In the simulations, calcite re-dissolved when reactive minerals were depleted and the pH dropped below 4.5, while siderite was still able to form where pH was above 4. This reflects observations in previous experiments with the basalt samples used to calibrate the model, where siderite was the most favorable carbonate precipitate under low pH conditions given comparable amounts of available Ca^{2+}, Mg^{2+}, and Fe^{2+}.[54] Here, the preferential formation of siderite bands behind the dissolving calcite and magnesite fronts likely occurs because sufficient CO_2 and divalent cations are available for precipitation, but the pH has fallen to a point where only siderite reaches saturation. While magnesite generally had the highest saturation index of the three carbonates (see Appendix B, Figure B6), calcite formed more readily due to the kinetic limitations discussed in Section 3.2 and was strongly localized on pyroxene grains that rapidly released Ca^{2+}. Because the difference in reaction rates between the two minerals serving as Ca sources (pyroxene and plagioclase) was far greater than for the minerals contributing Mg (pyroxene and olivine), Mg dissolution and subsequent magnesite precipitation was more uniformly distributed while calcite precipitation was highly localized and coincident with rapid Ca release from pyroxene grains.

Models SA1 and SA2 in Figure 2.7 highlight the influence of transport conditions on the role of heterogeneity. Under advective flow, large calcite precipitates that formed on large contiguous pyroxene clusters dissolved slower than the more uniformly distributed surrounding calcite grains. These larger grains also served as pH buffers to delay model-predicted re-dissolution. This "armoring" effect was less pronounced for pure diffusion because more dissolved silicates were retained with longer reaction times, providing pH buffering for carbonate accumulation and preventing re-dissolution. The segmented mineral grid, which contained few large mineral clusters, also dissolved more uniformly. Thus, mineral spatial distributions impact where minerals dissolve and carbonates precipitate, but the evolution of these reactions will also be influenced by transport regimes. In combination, the results indicate that small-scale heterogeneities may be insignificant, while the combined interactions of transport limitations, geochemical gradients (e.g., in pH), and bulk mineralogy will likely control the extent of mineral carbonation induced by CO_2 injection in basalt reservoirs.

2.4.6. Role of competition with secondary silicates

In models run with additional secondary silicates, the uptake of dissolved cations that had previously diffused out of the domain as clay minerals led to more rapid pore clogging (within 8 years for pure diffusion and 3.5-8 years for slower advection). For faster advection (RT of 24 hrs or less), dissolution predominated over precipitation and pores remained open after 10 years. While smectite forms quickly and is less localized than carbonates with respect to primary minerals, 87% of Mg is contained in magnesite after 2 years. Essentially no zeolite or biotite precipitate for any transport condition. Further details and results are provided in Appendix B (Section B6).

The models indicate competition with clays for divalent cations will not pose a significant direct threat to carbonation under these conditions, as smectite precipitation reduced total predicted carbonate volumes across the model domain by 3-6% after 2 years due primarily to Mg uptake into montmorillonite. In batch experiments on basaltic glass, Hellevang et al.[60] observed smectite growth from 80-150˚C and attributed a lack of Mg- and Fe-carbonates not to competition with clays for divalent cations, but to the potential for smectite coatings to create an energy barrier to nucleation combined with slow carbonate growth kinetics. Even if smectite does not directly impact carbonation by depleting divalent cations or impeding nucleation, our models indicate early clay precipitation could still clog narrow fractures and pore throats, potentially reducing permeability and CO_2 injectivity.[60] Such physical alterations were not considered in this study but will be critical in predicting ultimate CO_2 trapping potentials of basalt reservoirs.

2.5. ENVIRONMENTAL IMPLICATIONS

Two sets of core flooding experiments demonstrated that advection-dominated transport associated with CO_2 injection in primary flow channels will drive net dissolution of natural basalts. Calculated saturation indices indicated precipitation was limited by the low pH resulting from continuous CO_2 injection, and silicate mineral dissolution contributed little pH buffering as dissolved species were quickly transported out of the system due to the short fluid residence time through the cores. Thus, while initial concerns with CO_2 mineralization in natural basalt centered on whether carbonation would quickly clog wellbores and shut down injection operations, it is unlikely that significant mineralization will occur near wellbores or along interconnected fracture networks with strong advective flow of CO_2-acidified fluids. These experiments also confirmed that temperature and salinity enhance silicate mineral dissolution, but further work is needed to establish the sensitivity of dissolution rates to salt concentration and decouple the effect of the

specific aqueous cations contributing to salinity (e.g. Na^+ vs K^+) from overall ionic strength.

Reactive transport models were developed based on these bench-scale experiments and applied to isolate the roles of transport limitations and mineral spatial distributions in controlling mineral carbonation reactions in fractured basalts. Under pure advective flow, carbonates eventually re-dissolved with continued injection as the pH dropped below saturation thresholds and primary reactive silicates needed to buffer injected fluids were depleted. While mineral exhaustion will not be an issue at field scale, depletion of reactive mineral zones along fracture surfaces could leave less reactive altered layers that limit mineral dissolution, allowing the pH to drop low enough that carbonate precipitation is no longer favorable and precipitates are susceptible to re-dissolution. These results indicate that injectivities should be carefully assessed at sites with low abundances of reactive minerals to ensure stable trapping is achieved. Strong advective conditions may prevent carbonation near wellbores and drive a domino effect of carbonate dissolution and re-precipitation along CO_2 flow paths. This chain could promote appreciable carbonation along main conduits in the absence of flow blockage, but in terms of storage security, long-term carbonation will likely occur in diffusive regions within the bulk matrix and in dead-end fractures.

The models presented here assume reactive surface area is proportional to the bulk surface area and evolves with changes in mineral volume fractions. In reality, this may be an oversimplification due to changes in growth site densities at mineral surfaces over time.[40] The SSAs used to compute reactive surface areas are also a source of both uncertainty and model sensitivity. Furthermore, heterogeneous nucleation may accelerate carbonate formation on certain substrate minerals. Incorporating a more robust means of capturing nucleation events and subsequent crystal growth in future modeling efforts will be critical to predicting field-scale rates and extents of mineral carbonation in basalts. Bulk reservoir mineralogy and the chemical composition of resident fluids will also govern the extent of carbonation. For instance, the fact that formation waters surrounding the CarbFix site were near equilibrium with respect to calcite limited re-dissolution of calcite precipitates with continued CO_2 injection.[7] Matter et al.[7] also noted that most carbonates likely precipitated in the porous matrix outside advective flow paths, consistent with model predictions of precipitation in lower porosity zones providing greater rock:water ratios and longer reaction times. Coupling field-scale efforts with efficient reactive transport models can elucidate how subsurface CO_2-water-rock reactions enhance or inhibit carbonation efficiency. Such insight will be crucial in predicting long-term mineral carbonation rates to optimize injection site selection.

REFERENCES

(1) Harvey, O. R.; Qafoku, N. P.; Cantrell, K. J.; Lee, G.; Amonette, J. E.; Brown, C. F. Geochemical Implications of Gas Leakage Associated with Geologic CO_2 Storage— A Qualitative Review. *Environ. Sci. Technol.* **2013**, *47* (1), 23–36. https://doi.org/10.1021/es3029457.

(2) Matter, J. M.; Kelemen, P. B. Permanent Storage of Carbon Dioxide in Geological Reservoirs by Mineral Carbonation. *Nat. Geosci.* **2009**, *2* (12), 837–841. https://doi.org/10.1038/ngeo683.

(3) Gislason, S. R.; Wolff-Boenisch, D.; Stefansson, A.; Oelkers, E. H.; Gunnlaugsson, E.; Sigurdardottir, H.; Sigfusson, B.; Broecker, W. S.; Matter, J. M.; Stute, M. Mineral Sequestration of Carbon Dioxide in Basalt: A Pre-Injection Overview of the CarbFix Project. *Int. J. Greenh. Gas Control* **2010**, *4* (3), 537–545. https://doi.org/10.1016/j.ijggc.2009.11.013.

(4) Schaef, H. T.; McGrail, B. P. Dissolution of Columbia River Basalt under Mildly Acidic Conditions as a Function of Temperature: Experimental Results Relevant to the Geological Sequestration of Carbon Dioxide. *Appl. Geochem.* **2009**, *24* (5), 980–987. https://doi.org/10.1016/j.apgeochem.2009.02.025.

(5) Sissmann, O.; Brunet, F.; Martinez, I.; Guyot, F.; Verlaguet, A.; Pinquier, Y.; Daval, D. Enhanced Olivine Carbonation within a Basalt as Compared to Single-Phase Experiments: Reevaluating the Potential of CO_2 Mineral Sequestration. *Environ. Sci. Technol.* **2014**, *48* (10), 5512–5519. https://doi.org/10.1021/es405508a.

(6) McGrail, B. P.; Schaef, H. T.; Spane, F. A.; Cliff, J. B.; Qafoku, O.; Horner, J. A.; Thompson, C. J.; Owen, A. T.; Sullivan, C. E. Field Validation of Supercritical CO_2 Reactivity with Basalts. *Environ. Sci. Technol. Lett.* **2017**, *4* (1), 6–10. https://doi.org/10.1021/acs.estlett.6b00387.

(7) Matter, J. M.; Stute, M.; Snaebjornsdottir, S. O.; Oelkers, E. H.; Gislason, S. R.; Aradottir, E. S.; Sigfusson, B.; Gunnarsson, I.; Sigurdardottir, H.; Gunnlaugsson, E.; Axelsson, G.; Alfredsson, H. A.; Wolff-Boenisch, D.; Mesfin, K.; Taya, D. F. d. l. R.; Hall, J.; Dideriksen, K.; Broecker, W. S. Rapid Carbon Mineralization for Permanent Disposal of Anthropogenic Carbon Dioxide Emissions. *Science* **2016**, *352* (6291), 1312–1314. https://doi.org/10.1126/science.aad8132.

(8) Peuble, S.; Godard, M.; Luquot, L.; Andreani, M.; Martinez, I.; Gouze, P. CO_2 Geological Storage in Olivine Rich Basaltic Aquifers: New Insights from Reactive-Percolation Experiments. *Appl. Geochem.* **2015**, *52*, 174–190. https://doi.org/10.1016/j.apgeochem.2014.11.024.

(9) Andreani, M.; Luquot, L.; Gouze, P.; Godard, M.; Hoisé, E.; Gibert, B. Experimental Study of Carbon Sequestration Reactions Controlled by the Percolation of CO_2-Rich Brine through Peridotites. *Environ. Sci. Technol.* **2009**, *43* (4), 1226–1231. https://doi.org/10.1021/es8018429.

(10) Xiong, W.; Giammar, D. Forsterite Carbonation in Zones with Transport Limited by Diffusion. *Environ. Sci. Technol. Lett.* **2014**, *1* (8), 333–338. https://doi.org/10.1021/ez500182s.

(11) Giammar, D. E.; Wang, F.; Guo, B.; Surface, J. A.; Peters, C. A.; Conradi, M. S.; Hayes, S. E. Impacts of Diffusive Transport on Carbonate Mineral Formation from Magnesium Silicate-CO_2-Water Reactions. *Environ. Sci. Technol.* **2014**, *48* (24), 14344–14351. https://doi.org/10.1021/es504047t.

(12) Salehikhoo, F.; Li, L.; Brantley, S. L. Magnesite Dissolution Rates at Different Spatial Scales: The Role of Mineral Spatial Distribution and Flow Velocity. *Geochim. Cosmochim. Acta* **2013**, *108*, 91–106. https://doi.org/10.1016/j.gca.2013.01.010.

(13) Li, L.; Salehikhoo, F.; Brantley, S. L.; Heidari, P. Spatial Zonation Limits Magnesite Dissolution in Porous Media. *Geochim. Cosmochim. Acta* **2014**, *126*, 555–573. https://doi.org/10.1016/j.gca.2013.10.051.

(14) Molins, S.; Trebotich, D.; Steefel, C. I.; Shen, C. An Investigation of the Effect of Pore Scale Flow on Average Geochemical Reaction Rates Using Direct Numerical Simulation: Effect of Pore Scale Flow on Geochemical Reaction Rates. *Water Resour. Res.* **2012**, *48* (3), W03527. https://doi.org/10.1029/2011WR011404.

(15) Deng, H.; Ellis, B. R.; Peters, C. A.; Fitts, J. P.; Crandall, D.; Bromhal, G. S. Modifications of Carbonate Fracture Hydrodynamic Properties by CO_2-Acidified Brine Flow. *Energy Fuels* **2013**, *27* (8), 4221–4231. https://doi.org/10.1021/ef302041s.

(16) Wen, H.; Li, L.; Crandall, D.; Hakala, A. Where Lower Calcite Abundance Creates More Alteration: Enhanced Rock Matrix Diffusivity Induced by Preferential Dissolution. *Energy Fuels* **2016**, *30* (5), 4197–4208. https://doi.org/10.1021/acs.energyfuels.5b02932.

(17) Nogues, J. P.; Fitts, J. P.; Celia, M. A.; Peters, C. A. Permeability Evolution Due to Dissolution and Precipitation of Carbonates Using Reactive Transport Modeling in Pore Networks. *Water Resour. Res.* **2013**, *49* (9), 6006–6021. https://doi.org/10.1002/wrcr.20486.

(18) Xu, T.; Kharaka, Y. K.; Doughty, C.; Freifeld, B. M.; Daley, T. M. Reactive Transport Modeling to Study Changes in Water Chemistry Induced by CO_2 Injection at the Frio-I Brine Pilot. *Chem. Geol.* **2010**, *271* (3–4), 153–164. https://doi.org/10.1016/j.chemgeo.2010.01.006.

(19) Ilgen, A. G.; Cygan, R. T. Mineral Dissolution and Precipitation during CO2 Injection at the Frio-I Brine Pilot: Geochemical Modeling and Uncertainty Analysis. *Int. J. Greenh. Gas Control* **2016**, *44*, 166–174. https://doi.org/10.1016/j.ijggc.2015.11.022.

(20) Bacci, G.; Korre, A.; Durucan, S. An Experimental and Numerical Investigation into the Impact of Dissolution/Precipitation Mechanisms on CO_2 Injectivity in the Wellbore and Far Field Regions. *Int. J. Greenh. Gas Control* **2011**, *5* (3), 579–588. https://doi.org/10.1016/j.ijggc.2010.05.007.

(21) Zhang, L.; Soong, Y.; Dilmore, R.; Lopano, C. Numerical Simulation of Porosity and Permeability Evolution of Mount Simon Sandstone under Geological Carbon Sequestration Conditions. *Chem. Geol.* **2015**, *403*, 1–12. https://doi.org/10.1016/j.chemgeo.2015.03.014.

(22) Cao, P.; Karpyn, Z. T.; Li, L. Self-Healing of Cement Fractures under Dynamic Flow of CO_2-Rich Brine. *Water Resour. Res.* **2015**, *51* (6), 4684–4701. https://doi.org/10.1002/2014WR016162.

(23) Steefel, C.; Depaolo, D.; Lichtner, P. Reactive Transport Modeling: An Essential Tool and a New Research Approach for the Earth Sciences. *Earth Planet. Sci. Lett.* **2005**, *240* (3–4), 539–558. https://doi.org/10.1016/j.epsl.2005.09.017.

(24) Marini, L. Geological Sequestration of Carbon Dioxide: Thermodynamics, Kinetics, and Reaction Path Modeling. In *Geological Sequestration of Carbon Dioxide: Thermodynamics, Kinetics, and Reaction Path Modeling*; Elsevier, 2007; Vol. 11, pp 319–409.

(25) Schaef, H. T.; McGrail, B. P.; Owen, A. T. Carbonate Mineralization of Volcanic Province Basalts. *Int. J. Greenh. Gas Control* **2010**, *4* (2), 249–261. https://doi.org/10.1016/j.ijggc.2009.10.009.

(26) Paukert, A. N.; Matter, J. M.; Kelemen, P. B.; Shock, E. L.; Havig, J. R. Reaction Path Modeling of Enhanced in Situ CO_2 Mineralization for Carbon Sequestration in the Peridotite of the Samail Ophiolite, Sultanate of Oman. *Chem. Geol.* **2012**, *330–331*, 86–100. https://doi.org/10.1016/j.chemgeo.2012.08.013.

(27) Wang, F.; Giammar, D. E. Forsterite Dissolution in Saline Water at Elevated Temperature and High CO_2 Pressure. *Environ. Sci. Technol.* **2013**, *47* (1), 168–173. https://doi.org/10.1021/es301231n.

(28) Rosenbauer, R. J.; Thomas, B.; Bischoff, J. L.; Palandri, J. Carbon Sequestration via Reaction with Basaltic Rocks: Geochemical Modeling and Experimental Results. *Geochim. Cosmochim. Acta* **2012**, *89*, 116–133. https://doi.org/10.1016/j.gca.2012.04.042.

(29) King, H. E.; Plumper, O.; Putnis, A. Effect of Secondary Phase Formation on the Carbonation of Olivine. *Environ. Sci. Technol.* **2010**, *44*, 6503–6509.

(30) Aradóttir, E. S. P.; Sonnenthal, E. L.; Björnsson, G.; Jónsson, H. Multidimensional Reactive Transport Modeling of CO_2 Mineral Sequestration in Basalts at the Hellisheidi Geothermal Field, Iceland. *Int. J. Greenh. Gas Control* **2012**, *9*, 24–40. https://doi.org/10.1016/j.ijggc.2012.02.006.

(31) Steefel, C. I.; Appelo, C. A. J.; Arora, B.; Jacques, D.; Kalbacher, T.; Kolditz, O.; Lagneau, V.; Lichtner, P. C.; Mayer, K. U.; Meeussen, J. C. L.; Molins, S.; Moulton, D.; Shao, H.; Šimůnek, J.; Spycher, N.; Yabusaki, S. B.; Yeh, G. T. Reactive Transport Codes for Subsurface Environmental Simulation. *Comput. Geosci.* **2015**, *19* (3), 445–478. https://doi.org/10.1007/s10596-014-9443-x.

(32) Deng, H.; Molins, S.; Steefel, C.; DePaolo, D.; Voltolini, M.; Yang, L.; Ajo-Franklin, J. A 2.5D Reactive Transport Model for Fracture Alteration Simulation. *Environ. Sci. Technol.* **2016**, *50* (14), 7564–7571. https://doi.org/10.1021/acs.est.6b02184.

(33) Soler, J. M. Two-Dimensional Reactive Transport Modeling of the Alteration of a Fractured Limestone by Hyperalkaline Solutions at Maqarin (Jordan). *Appl. Geochem.* **2016**, *66*, 162–173. https://doi.org/10.1016/j.apgeochem.2015.12.012.

(34) Brunet, J.-P. L.; Li, L.; Karpyn, Z. T.; Huerta, N. J. Fracture Opening or Self-Sealing: Critical Residence Time as a Unifying Parameter for Cement–CO_2–Brine Interactions. *Int. J. Greenh. Gas Control* **2016**, *47*, 25–37. https://doi.org/10.1016/j.ijggc.2016.01.024.

(35) Wells, R.; Giammar, D.; Skemer, P. *Sample Library of Natural and Artificial Basalts*; 2016; https://edx.netl.doe.gov/dataset/sample-library-of-natural-and-artificial-basalts/revision_resource/2bcdd2f4-70f0-4b1c-afe7-d1d563680e0c.

(36) McGrail, B. P.; Schaef, H. T.; Ho, A. M.; Chien, Y.-J.; Dooley, J. J.; Davidson, C. L. Potential for Carbon Dioxide Sequestration in Flood Basalts: SEQUESTRATION IN FLOOD BASALTS. *J. Geophys. Res. Solid Earth* **2006**, *111* (B12), n/a-n/a. https://doi.org/10.1029/2005JB004169.

(37) Schindelin, J.; Arganda-Carreras, I.; Frise, E.; Kaynig, V.; Longair, M.; Pietzsch, T.; Preibisch, S.; Rueden, C.; Saalfeld, S.; Schmid, B.; Tinevez, J.-Y.; White, D. J.; Hartenstein, V.; Eliceiri, K.; Tomancak, P.; Cardona, A. Fiji: An Open-Source Platform for Biological-Image Analysis. *Nat. Methods* **2012**, *9* (7), 676–682. https://doi.org/10.1038/nmeth.2019.

(38) Arvidson, R. S. The Dolomite Problem: Control of Precipitation Kinetics by Temperature and Saturation State. *Am. J. Sci.* **1999**, *299* (4), 257–288. https://doi.org/10.2475/ajs.299.4.257.

(39) Roberts, J. A.; Bennett, P. C.; González, L. A.; Macpherson, G. L.; Milliken, K. L. Microbial Precipitation of Dolomite in Methanogenic Groundwater. *Geology* **2004**, *32* (4), 277–280.

(40) Steefel, C. I.; Van Cappellen, P. A New Kinetic Approach to Modeling Water-Rock Interaction: The Role of Nucleation, Precursors, and Ostwald Ripening. *Geochim. Cosmochim. Acta* **1990**, *54* (10), 2657–2677.

(41) Palandri, J. L.; Kharaka, Y. K. *A Compilation of Rate Parameters of Water-Mineral Interaction Kinetics for Application to Geochemical Modeling*; DTIC Document, 2004.

(42) Knauss, K. G.; Johnson, J. W.; Steefel, C. I. Evaluation of the Impact of CO_2, Co-Contaminant Gas, Aqueous Fluid and Reservoir Rock Interactions on the Geologic Sequestration of CO_2. *Chem. Geol.* **2005**, *217* (3–4), 339–350. https://doi.org/10.1016/j.chemgeo.2004.12.017.

(43) Teir, S.; Revitzer, H.; Eloneva, S.; Fogelholm, C.-J.; Zevenhoven, R. Dissolution of Natural Serpentinite in Mineral and Organic Acids. *Int. J. Miner. Process.* **2007**, *83* (1–2), 36–46. https://doi.org/10.1016/j.minpro.2007.04.001.

(44) Orlando, A.; Borrini, D.; Marini, L. Dissolution and Carbonation of a Serpentinite: Inferences from Acid Attack and High P–T Experiments Performed in Aqueous Solutions at Variable Salinity. *Appl. Geochem.* **2011**, *26* (8), 1569–1583. https://doi.org/10.1016/j.apgeochem.2011.06.023.

(45) Pokrovsky, O. S.; Golubev, S. V.; Schott, J. Dissolution Kinetics of Calcite, Dolomite and Magnesite at 25 °C and 0 to 50 Atm PCO_2. *Chem. Geol.* **2005**, *217* (3–4), 239–255. https://doi.org/10.1016/j.chemgeo.2004.12.012.

(46) Golubev, S. V.; Bénézeth, P.; Schott, J.; Dandurand, J. L.; Castillo, A. Siderite Dissolution Kinetics in Acidic Aqueous Solutions from 25 to 100 °C and 0 to 50 Atm PCO_2. *Chem. Geol.* **2009**, *265* (1–2), 13–19. https://doi.org/10.1016/j.chemgeo.2008.12.031.

(47) Pokrovsky, O. S.; Schott, J. Surface Chemistry and Dissolution Kinetics of Divalent Metal Carbonates. *Environ. Sci. Technol.* **2002**, *36* (3), 426–432. https://doi.org/10.1021/es010925u.

(48) Carroll, S. A.; McNab, W. W.; Dai, Z.; Torres, S. C. Reactivity of Mount Simon Sandstone and the Eau Claire Shale under CO_2 Storage Conditions. *Environ. Sci. Technol.* **2013**, *47* (1), 252–261. https://doi.org/10.1021/es301269k.

(49) Tester, J. W.; Worley, W. G.; Robinson, B. A.; Grigsby, C. O.; Feerer, J. L. Correlating Quartz Dissolution Kinetics in Pure Water from 25 to 625C. *Geochem. Cosmochim. Acta* **1994**, *58* (11), 2407–2420.

(50) Huertas, F. J.; Chou, L.; Wollast, R. Mechanism of Kaolinite Dissolution at Room Temperature and Pressure Part II: Kinetic Study. *Geochim. Cosmochim. Acta* **1999**, *63* (19), 3261–3275.

(51) Duan, Z.; Sun, R. An Improved Model Calculating CO_2 Solubility in Pure Water and Aqueous NaCl Solutions from 273 to 533 K and from 0 to 2000 Bar. *Chem. Geol.* **2003**, *193*, 257–271.

(52) Cadogan, S. P.; Maitland, G. C.; Trusler, J. P. M. Diffusion Coefficients of CO_2 and N_2 in Water at Temperatures between 298.15 K and 423.15 K at Pressures up to 45 MPa. *J. Chem. Eng. Data* **2014**, *59* (2), 519–525. https://doi.org/10.1021/je401008s.

(53) Black, J. R.; Carroll, S. A.; Haese, R. R. Rates of Mineral Dissolution under CO_2 Storage Conditions. *Chem. Geol.* **2015**, *399*, 134–144. https://doi.org/10.1016/j.chemgeo.2014.09.020.

(54) Adeoye, J. T.; Menefee, A. H.; Xiong, W.; Wells, R. K.; Skemer, P. A.; Giammar, D. E.; Ellis, B. R. Reaction Products and Evolution of Permeability during Carbon Sequestration in Fractures of Unaltered and Serpentinized Basalt; Goldschmidt Conference, Yokohama, Japan, 2016.

(55) Fritz, B.; Clément, A.; Amal, Y.; Noguera, C. Simulation of the Nucleation and Growth of Simple Clay Minerals in Weathering Processes: The NANOKIN Code. *Geochim. Cosmochim. Acta* **2009**, *73* (5), 1340–1358. https://doi.org/10.1016/j.gca.2008.11.043.

(56) Ellis, B. R.; Peters, C. A. 3D Mapping of Calcite and a Demonstration of Its Relevance to Permeability Evolution in Reactive Fractures. *Adv. Water Resour.* **2016**, *95*, 246–253. https://doi.org/10.1016/j.advwatres.2015.07.023.

(57) Van Pham, T. H. CO_2 Storage–Simulations for Forecasting the Behavior of Injection CO_2 in Geological Formations. **2013**.

(58) Gysi, A. P.; Stefánsson, A. CO_2–Water–Basalt Interaction. Numerical Simulation of Low Temperature CO_2 Sequestration into Basalts. *Geochim. Cosmochim. Acta* **2011**, *75* (17), 4728–4751. https://doi.org/10.1016/j.gca.2011.05.037.

(59) Gysi, A. P.; Stefánsson, A. CO_2-Water–Basalt Interaction. Low Temperature Experiments and Implications for CO_2 Sequestration into Basalts. *Geochim. Cosmochim. Acta* **2012**, *81*, 129–152. https://doi.org/10.1016/j.gca.2011.12.012.

(60) Hellevang, H.; Haile, B. G.; Tetteh, A. Experimental Study to Better Understand Factors Affecting the CO_2 Mineral Trapping Potential of Basalt: Experimental Study to Better Understand Factors

Affecting the CO $_2$ Mineral. *Greenh. Gases Sci. Technol.* **2017**, *7* (1), 143–157. https://doi.org/10.1002/ghg.1619.

(61) Xiong, W.; Wells, R. K.; Giammar, D. E. Carbon Sequestration in Olivine and Basalt Powder Packed Beds. *Environ. Sci. Technol.* **2017**, *51* (4), 2105–2112. https://doi.org/10.1021/acs.est.6b05011.

(62) Casey, W. H.; Westrich, H. R.; Holdren, G. R. Dissolution Rates of Plagioclase at PH = 2 and 3. *Am. Mineral.* **1991**, *76*, 211–217.

(63) Zhang, R.; Zhang, X.; Guy, B.; Hu, S.; De Ligny, D.; Moutte, J. Experimental Study of Dissolution Rates of Hedenbergitic Clinopyroxene at High Temperatures: Dissolution in Water from 25 °C to 374 °C. *Eur. J. Mineral.* **2013**, *25* (3), 353–372. https://doi.org/10.1127/0935-1221/2013/0025-2268.

(64) Zhang, R.; Shumin Hu; Xuetong Zhang. Kinetics of Hydrothermal Reactions of Minerals in Near-Critical and Supercritical Water. *Acta Geol. Sin. Engl. Ed.* **2000**, *74* (2), 400–405.

(65) Brantley, S. L.; Kubicki, J. D.; White, A. F. *Kinetics of Water-Rock Interaction*; Springer: New York, NY, USA, 2008.

(66) Prigiobbe, V.; Costa, G.; Baciocchi, R.; Hänchen, M.; Mazzotti, M. The Effect of CO2 and Salinity on Olivine Dissolution Kinetics at 120C. *Chem. Eng. Sci.* **2009**, *64* (15), 3510–3515. https://doi.org/10.1016/j.ces.2009.04.035.

(67) Reidel, S. P.; Spane, F. A.; Johnson, V. G. *Natural Gas Storage in Basalt Aquifers of the Columbia Basin, Pacific Northwest USA: A Guide to Site Characterization*; Pacific Northwest National Laboratory (PNNL), Richland, WA (US), 2002.

(68) Qiao, C.; Li, L.; Johns, R. T.; Xu, J. Compositional Modeling of Dissolution-Induced Injectivity Alteration during CO_2 Flooding in Carbonate Reservoirs. *SPE J.* **2016**, *21* (03), 0809–0826. https://doi.org/10.2118/170930-PA.

(69) Daval, D.; Sissmann, O.; Menguy, N.; Saldi, G. D.; Guyot, F.; Martinez, I.; Corvisier, J.; Garcia, B.; Machouk, I.; Knauss, K. G.; Hellmann, R. Influence of Amorphous Silica Layer Formation on the Dissolution Rate of Olivine at 90°C and Elevated PCO_2. *Chem. Geol.* **2011**, *284* (1–2), 193–209. https://doi.org/10.1016/j.chemgeo.2011.02.021.

(70) Saldi, G. D.; Jordan, G.; Schott, J.; Oelkers, E. H. Magnesite Growth Rates as a Function of Temperature and Saturation State. *Geochim. Cosmochim. Acta* **2009**, *73* (19), 5646–5657. https://doi.org/10.1016/j.gca.2009.06.035.

(71) Jimenez-Lopez, C.; Romanek, C. S. Precipitation Kinetics and Carbon Isotope Partitioning of Inorganic Siderite at 25°C and 1 Atm. *Geochim. Cosmochim. Acta* **2004**, *68* (3), 557–571. https://doi.org/10.1016/S0016-7037(03)00460-5.

CHAPTER 3

Localized Carbon Mineralization in Fractured Basalts

3.1. BACKGROUND AND MOTIVATION

The need to reduce greenhouse gas emissions quickly and effectively has compelled efforts to leverage the reactivity of basalt or ultramafic reservoirs for secure long-term carbon sequestration. Reactive silicate minerals dissolve rapidly under acidic conditions following CO_2 injection, consuming H^+ and releasing divalent metal cations (e.g. Ca^{2+}, Mg^{2+}, Fe^{2+}) that can ultimately mineralize dissolved CO_2 in the form of stable carbonate minerals. While sedimentary formations such as saline aquifers or depleted oil and gas reservoirs offer storage capacities most relevant to the scale of CO_2 emission reduction targets, these reservoirs rely primarily on short-term solubility and physical trapping mechanisms that present leakage risks if CO_2 is not structurally secured. Given the inherent advantage of mineral trapping for long-term storage security, basalts may be more readily deployable CO_2 repositories in the near term.[1] Recent field tests under the CarbFix project in Iceland[2] and Wallula Basalt Pilot Project in Washington state[3] have demonstrated that considerable CO_2 mineralization occurs within two years of injection, motivating further work on microscale dissolution-precipitation processes driving large-scale sequestration efficiency.

Despite a need to understand how basalt responds to near-wellbore CO_2 injection conditions, few studies have been carried out with advective flow. In percolation experiments on sintered dunite (160°C; 11 MPa P_{CO2}; initial pH 6.7), Andreani et al.[4] only observed significant carbonate-induced porosity alterations in low-flow zones, whereas high-flow zones promoted rapid dissolution followed by the formation of Si-rich passivating layers that created a barrier between fluids and reactive surfaces.[4] Peuble et al.[5] also conducted reactive percolation experiments on sintered olivine cores at a similar pH (6.6) and concluded that higher flow rates improve carbonation efficiency, as permeability reductions blocked transport in low-flow regimes. Luhmann et al.[6,7] observed no carbonate precipitation in flow-through experiments with whole basalt cores (150°C; 15 MPa P_{CO2}), likely due to the low pH (3.3) of the influent, but secondary Si- and Al-rich phases led to slight permeability reductions at lower flow rates. Adeoye et al.[8] also

found no evidence of carbonation in a series of flow-through experiments (45 and 100°C; 10 MPa P_{CO2}) on serpentinized and unaltered basalt cores because low retention times promoted net dissolution. Wolff-Boenisch and Galeczka[9] carried out mixed-flow experiments on glass and crystalline basalt (90°C; 0.6 MPa P_{CO2}) using ammonium bicarbonate as a surrogate for CO_2. Secondary silicates filled pore spaces unless synthetic seawater was injected as a quasi-infinite source of divalent cations, in which case Ca- and Mg-carbonates formed.[9] Related reaction path modeling confirmed continuous fluid injection is necessary to avoid clays and zeolites clogging near-wellbore regions at higher pH.[10]

Collectively, prior static and flow studies demonstrate that the extent of mineral carbonation is a complex function of initial mineralogy, fluid chemistry, and P/T conditions. While studies on whole natural basalts have been limited, early work on powdered olivine carbonation established optimal reaction conditions of 185°C and 14 MPa P_{CO2} in solutions of 640 mM $NaHCO_3$ and 1 M NaCl.[11,12] Theoretically, diffusive mass transfer across the crystal-fluid interface increases with temperature while the driving chemical potential decreases, resulting in maximum carbonation rates around 185°C.[13] In 3-hour stirred batch experiments using 15 wt% solids, Gadikota et al.[14] found the extent of olivine carbonation (with respect to Ca- and Mg-carbonates) increased from 3% at 90°C to 71% at 150°C and 85% at 185°C. The effect of CO_2 partial pressure was less pronounced; an increase from 6.5 to 14.1 MPa under the optimal temperature increased carbonation from 39 to 85%.[14] They also concluded the reaction-enhancing effects of the optimal solution were driven by $NaHCO_3$ serving as both a buffer and source of carbonate ions, as an increase from 0 to 0.64M $NaHCO_3$ improved the 3-hr carbonation yield from 5.8% to 83% at the optimal T and P.[14] The effect of NaCl was deemed negligible, although other work has demonstrated that NaCl enhances dissolution of forsterite[15] and natural basalts.[8] $NaHCO_3$ may also inhibit the formation of reaction-inhibiting silica-rich passivation layers, which slow and could ultimately obstruct carbonation reactions.[16] The effect of high-$NaHCO_3$ solutions has not yet been studied in natural basalts; while $NaHCO_3$ provides pH buffering necessary to initiate and sustain carbonate precipitation, the dissolution rates of the primary silicate minerals contributing divalent cations for carbonation decrease significantly with increasing pH. The roles of 'reaction-enhancing' controls on long-term carbonation efficiency will likely be coupled with transport conditions but have only been closely studied in static systems, motivating the systematic flow-through studies developed here.

The objective of this work is to evaluate how transport limitations in advection- or diffusion-controlled zones influence the extent of carbonation and secondary mineral alteration in natural basalts exposed to flow of CO_2-acidified fluids under relevant geologic storage conditions. Given their demonstrated ability to enhance olivine dissolution and carbonation rates[14,17] but limited investigation in the context of different flow regimes, the roles of temperature and [$NaHCO_3$] were explicitly targeted. A series of three core flooding experiments was carried out using serpentinized basalt cores, where saw-cut surfaces were milled with fractures designed to isolate advective flow channels and diffusion-limited dead-end fractures. Reaction products were characterized through a suite of non-destructive imaging techniques and experimental observations were supplemented with reactive transport models that demonstrated how geochemical gradients drive secondary alteration patterns along fractures. In combination, the results shed new light on conditions favoring permanent CO_2 sequestration through mineral trapping in fractured basalts.

3.2. METHODS

3.2.1. Basalt core preparation

Serpentinized basalt samples from Valmont Butte, Colorado were supplied by Ward's Science. Cores measuring 2.54 cm (1") in diameter and 3.8 cm (1.5") in length were cut in half lengthwise using a precision saw with a diamond blade. One side of each sample was polished with 400-grit sandpaper and the other was milled with a precision CNC milling machine (Roland Model MDX-40a) with a 0.5 mm diamond burr to create the 100-µm deep fractures shown in Figures 3.2 and 3.4. These etched pathways were designed to simulate a main advection-controlled flow channel connected to four dead-end fractures of varying lengths and widths, which represent different diffusion length scales and water:rock ratios. While the aperture size is realistic, these milling patterns are not intended to be representative of natural fractures but rather to address our objectives by studying multiple transport regimes within the same experimental system. Given the low porosity of the bulk matrix (<1%), the advection-controlled pathway essentially serves as an open channel for injected fluid flow. As reported in previous work,[8,18] analysis via wavelength dispersive spectroscopy revealed these samples are heavily serpentinized (14% serpentine and 1% unaltered olivine) and are rich in plagioclase (28% labradorite), pyroxene (21% diopside), and a potassium-rich matrix (32%). Mineral grains are coarse and accessory minerals (e.g. apatite, chromite) occur as inclusions in larger silicate grains.

3.2.2. Core flooding experiments

A series of high-pressure, high-temperature core flooding experiments was designed to investigate the effects of temperature, fluid chemistry, and transport regimes on mineral carbonation. Experimental conditions are summarized in Table 3.1 and explained here; note that further details on the flow-through system are provided in Appendix A. All experiments were conducted with a CO_2 pressure (P_{CO2}) of 10 MPa and confining pressure of 20 MPa under temperatures of 100°C or 150°C. Higher temperatures than would be expected in actual reservoirs were selected to accelerate reactivity over relevant experimental time frames. Influent brines consisting of $NaHCO_3$ in ultrapure water, which was not purged of oxygen prior to the tests, were pre-equilibrated with CO_2 under the experimental temperature and pressure. A representative concentration of 6.3 mM $NaHCO_3$, calculated to match the pH of the injection fluid source at the CarbFix site (8.9 pre-CO_2 injection) at 100°C,[2] was added in the first experiment, resulting in an initial pH of 4.2 after CO_2 equilibration at 100°C and 10 MPa. Influent [$NaHCO_3$] was raised to the solubility limit at ambient conditions (640 mM) in the second (100°C) and third (150°C) tests, yielding starting pH levels of 6.1 and 6.4, respectively. Note that the higher concentration of $NaHCO_3$ is not characteristic of reservoir brines either before injection or after extensive silicate dissolution, but was selected to evaluate pH as a factor in dissolution-precipitation reactions.

Table 3.1. Summary of experimental conditions

Condition	LB-100C	HB-100C	HB-150C
Temperature	100°C	100°C	150°C
P_{CO2}	10 MPa	10 MPa	10 MPa
$P_{Confining}$	20 MPa	20 MPa	20 MPa
Flow rate	1 mL/h	1 mL/h	1 mL/h
[$NaHCO_3$]	6.3 mM	640 mM	640 mM
CO_2 solubility[19]	780 mM	683 mM	608 mM
Initial pH*	4.2	6.1	6.4
Duration	10 days	12 days	12 days

*Initial pH calculated based on charge balance of initial solution (see Appendix A, section A4)

In all experiments, the CO_2-equilibrated brines were injected through the cores at a constant rate of 1 mL/hr; the large associated Péclet number (37) confirms that advection is dominant in the main flow channel. Hereafter, the three experiments are referred to by the labels denoted in Table

3.1, based on the amount of influent $NaHCO_3$ (LB and HB represent low and high bicarbonate, respectively) and temperature (100 or 150°C). In all experiments, differential pressure was continuously logged to infer reaction-induced changes in permeability, but no measurable changes within the sensitivity of the pressure transducers (±10-15 psi, or 0.07-0.1 MPa) were observed.

Effluent samples averaged over 2-hour intervals were collected continuously for the first 8-10 hours of each experiment and then in regular increments (i.e. once every 8-10 hours) for the duration of each test. Samples were acidified with HNO_3 to a pH < 2 and analyzed for major cations (Ca, Mg, Fe, K, Si, Al) via inductively coupled plasma-mass spectrometry (ICP-MS; 7900 Agilent Technologies). These data were used to calculate the pH at each sampling point based on charge balances (see Appendix A, section A4). Activity corrections were applied using the extended Debye-Hückel equation with the B-dot extension, and CO_2 solubility was calculated using the thermodynamic model presented by Duan and Sun.[19] Equilibrium constants and carbonate solubility products were adjusted to temperature and pressure using SUPCRTBL with the DPRONSBL thermodynamic database,[20] a revised and extended version of SUPCRT92.[21] Using the calculated pH, aqueous carbonate speciation, and divalent cation activities at each time step, effluent saturation indices were determined for calcite, aragonite, magnesite, and siderite. Additional details and results for these calculations are provided in Appendix C.

3.2.3. xCT analysis and fracture aperture mapping

Core samples were scanned pre- and post-reaction using x-ray computed tomography (xCT) with a voxel resolution of 23.5 μm (Nikon Metrology XTH225). The data were reconstructed with CT Pro (XT5.1.3, Nikon Metrology, Inc) and exported as .tif stacks, which were processed with ImageJ.[22] For each data set, the fracture was isolated and segmented from the rest of the rock matrix using Ilastik, an interactive software that classifies pixels based on feature sizes and descriptors (e.g., intensity or texture) specified by the user.[23] Here, fracture and matrix pixel classes were manually seeded to train the software, which then segmented the two classes by optimizing the minimal cut between foreground and background seeds based on weighted combinations of intensity and edge filters. The segmented data set was exported as a stack of binary images, which was imported into MATLAB (R2016a) to calculate the volume of fracture space in the sample by multiplying the number of pixels with a value of zero by the voxel resolution. Fracture aperture maps were constructed parallel to the direction of flow by summing the number of "fracture" pixels in each column of each image slice. Volume changes were also calculated as a function of diffusion

distance into dead-end fractures (Section 3.3.5) by averaging the total volume along the fracture width moving from the main flow path toward the ends of the fractures. To reduce noise, the data were binned into 235-μm depth increments by taking the average volume over 10 voxels. Note that no volume change could be calculated for LB-100C because no pre-reaction scan was taken.

3.2.4. Post-reaction sample characterization

After post-experiment xCT scanning, the cores were opened and air-dried to non-destructively characterize reactions on the fracture surfaces. Optical microscopy (Nikon Eclipse LV100ND) was first used to locate and image secondary precipitates with extended depth of focus (EDF), which overlays a series of images focused at successive depths into a single focused image. Depth profiles constructed by incrementally adjusting the focus between the highest and lowest points over an area of interest were converted into surfaces for pseudo-3D imaging. Precipitates were further characterized with scanning electron microscopy coupled with energy-dispersive spectroscopy (SEM/EDS) using an environmental SEM (FEI Quanta 3D e-SEM/FIB), which allowed for relative analyses on the chemical composition of precipitates without cutting or coating the samples. Carbonate crystals were also identified with Raman spectroscopy (532 nm; Renishaw). Raw spectra were processed using the peak analyzer tool in OriginPro 2015 (OriginLab) and compared with mineral standards from the RRUFF database.[24]

3.2.5. Reactive transport modeling

Reactive transport models were developed in CrunchTope[25] based on models calibrated in previous work with the same basalt material.[26] Further details on the code's design and capabilities are provided in the user's manual, while an extended description of the modeling approach in this chapter is supplied in Appendix C (Section C1). The fracture surface was taken as the model domain, which was sized to match the residence time of the primary flow path (22s) and discretized into 4,000 grid cells. Each cell contained a simplified mineralogy consistent with the bulk mineral composition of the starting material. No-flow boundaries were set parallel to the direction of flow. CO_2-acidified fluids matching the composition used in each experiment were injected at a constant flow rate for 10 days. CO_2 diffusion was fixed at 7.5×10^{-9} m^2/s at 100°C.[27] Fractures were assigned a porosity of 0.9 to simulate the upper and lower fracture surfaces reacting with injected fluids, and the matrix porosity was set to 0.05 to allow for precipitation in the unmilled regions between the saw-cut core surfaces where transport is expected to be extremely diffusion-limited. This

approach effectively models a portion of an open fracture (i.e. porosity=1) surrounded by basalt as a bulk volume with fixed amounts of mineral and fracture space. Mineral kinetic data were applied directly from primary literature, while equilibrium constants for aqueous reactions were obtained from the EQ3/EQ6 thermodynamic database. Reactive surface areas were adjusted starting from calculated geometric values to align model outputs with effluent concentrations of carbonate-forming divalent cations from the LB-100C experiment. Key model inputs are summarized in Table C1. Following model calibration (Figure C1), the effect of mineral heterogeneity was incorporated by discretizing and segmenting xCT scans along fracture surfaces into four primary mineral phases (pyroxene, olivine/serpentine, plagioclase, and K-feldspar) using the approach developed by Menefee et al[26] and presented in Chapter 2.

3.3. Results and Discussion

3.3.1. Effluent chemistry

As evidenced by the effluent data in Figure 3.1, both [$NaHCO_3$] and temperature affected patterns in dissolution-driven cation release and uptake by secondary minerals. In all experiments, most major cations exhibited a sharp initial spike followed by a decline to quasi steady-state concentrations. This trend was also observed in previous experiments at higher flow rates,[8] attributed to the rapid dissolution of finer grains at fracture surfaces. Relatively high Ca and Mg concentrations indicate that (Ca,Mg)-rich pyroxene was the most abundant reactive mineral phase. While Mg concentrations were consistent between the two experiments conducted at 100°C, Ca notably differed, which may reflect the dominant reactions occurring under each set of experimental conditions. Similar to our previous low-alkalinity experiments with this basalt,[8] dissolution predominated in LB-100C, leading to high and relatively stable steady-state Ca concentrations. In HB-100C, where calcite hovered near saturation (Figure C3, Appendix C), competing dissolution-precipitation reactions likely resulted in cyclical Ca uptake and release by secondary phases. Precipitation dominated in HB-150C, where faster reaction kinetics at higher temperature may have promoted rapid Ca uptake by secondary minerals while the high pH of the injected fluid limited dissolution of Ca-bearing minerals. HB-150C also produced lower effluent Si concentrations, which reflects greater precipitation of secondary silicates (Section 3.3.4). Low Fe concentrations in all experiments are consistent with the prevalence of Fe-rich coatings on the fracture surfaces, suggesting dissolved Fe rapidly oxidized.

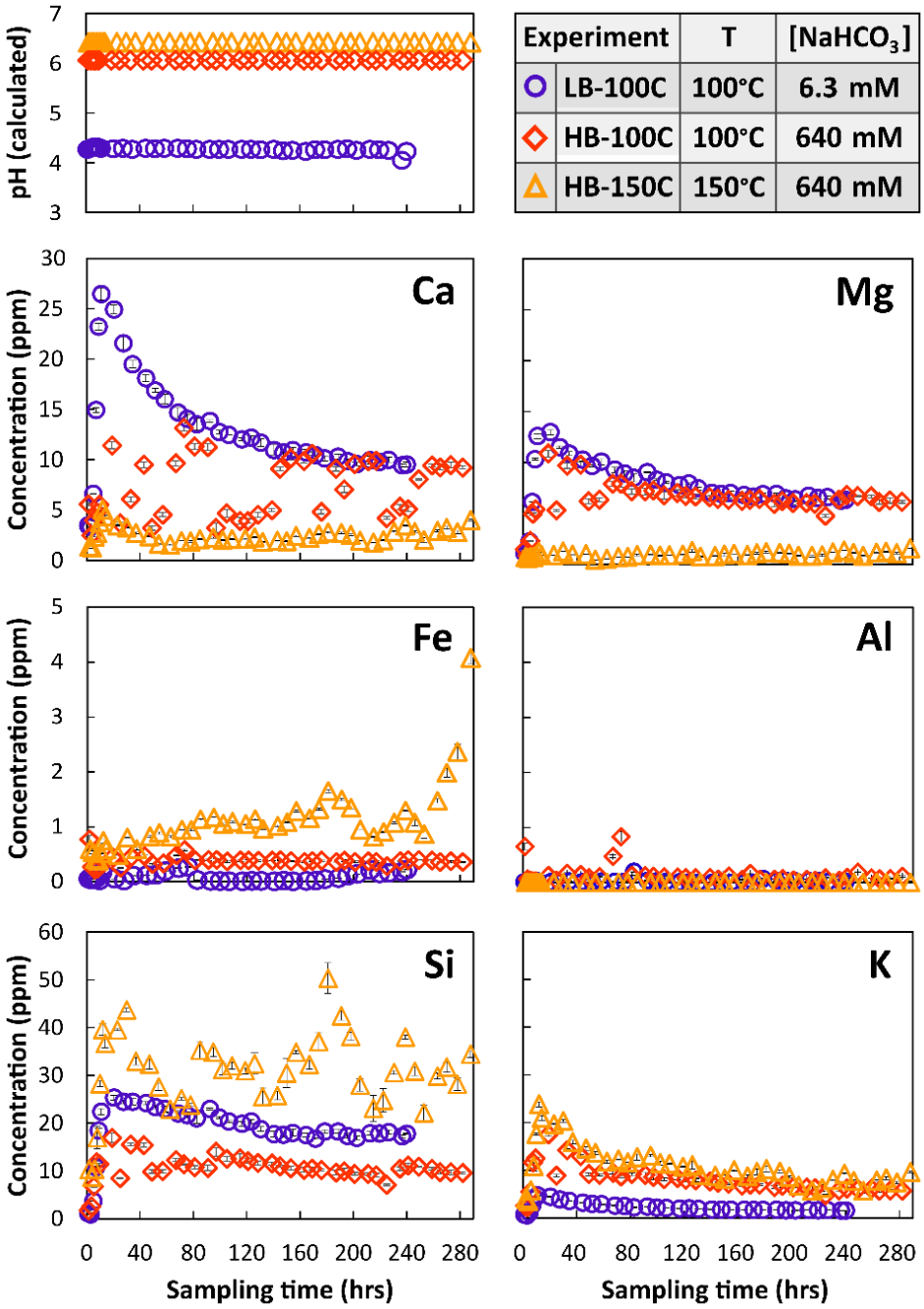

Figure 3.1. Effluent concentrations of major cations analyzed via ICP-MS and calculated pH evolution for each core flooding experiment.

At 150°C, concentrations of the carbonate-forming cations were generally low (<5 ppm), while Si and K were higher than in the lower-temperature experiments. Considering that silicate mineral dissolution rates increase with temperature, the dramatic reduction in effluent Ca and Mg at 150°C likely reflects greater uptake into secondary minerals (Section 3.3.5). Enhanced

dissolution at 150°C is supported by the fact that despite having the highest effluent Fe concentrations, the reacted core in HB-150C was most discolored from Fe oxidation. Saturation indices calculated from the effluent data (Figure C3, Appendix C) indicate siderite was supersaturated while calcite, aragonite, and magnesite were near equilibrium throughout the high-$NaHCO_3$ experiments, suggesting these phases were precipitating within the core. Despite greater release of dissolved cations in LB-100C, all carbonates were undersaturated due to the low effluent pH, which was calculated to range from 4.0 to 4.3 compared to steady-state levels of 6.1 and 6.4 in HB-100C and HB-150C, respectively (Figure 3.1).

3.3.2. Reaction fronts: Effect of geochemical gradients

At lower [$NaHCO_3$], distinct color changes were observed with distance into the dead-end fractures (Figure 3.2). Optical microscopy and SEM-EDS revealed clay-like alteration layers coating the advective flow channel and bases of the dead-end fractures, followed by a band of orange Fe-oxide precipitates and milky amorphous silica coatings deeper into the fractures. Gysi and Stefansson[28] similarly observed Fe-hydroxides, flaky clay mixtures, and white anhedral carbonates of varying morphologies forming in vugs and surfaces of basaltic glass at 40°C. Reactive transport models developed to better understand the precipitation fronts were consistent with experimental observations, predicting sequential bands of kaolinite in the lowest pH zones surrounding the main flow channel; hematite slightly further out; and amorphous silica in the region furthest from milled pathways. This trend is also consistent with early reaction path modeling that predicted kaolinite, goethite, and carbonates would form sequentially in tholeiitic basalt with increasing pH.[29] The models developed to simulate LB-100C indicate the distinct ordering observed here was driven by geochemical gradients, where dissolved CO_2 produced sharp pH gradients as it diffused out of the main flow channel into the dead-end fractures and confined space between the two core surfaces.

In addition to the geochemical gradients moving into the fractures, a highly localized gradient was observed between the milled fracture and confined space between the two saw-cut surfaces where transport was extremely limited. The distinct color gradient in Figure 3.3 likely results from a local pH gradient, where Fe-oxide forms in the more acidic milled pathway and Fe-oxyhydroxide is more favorable at lower water:rock ratios (and thus higher pH) in the confined region. Figure 3.3 also highlights carbonate localization within pores and vugs on the unmilled surface, which is explored further in Section 3.3.3.

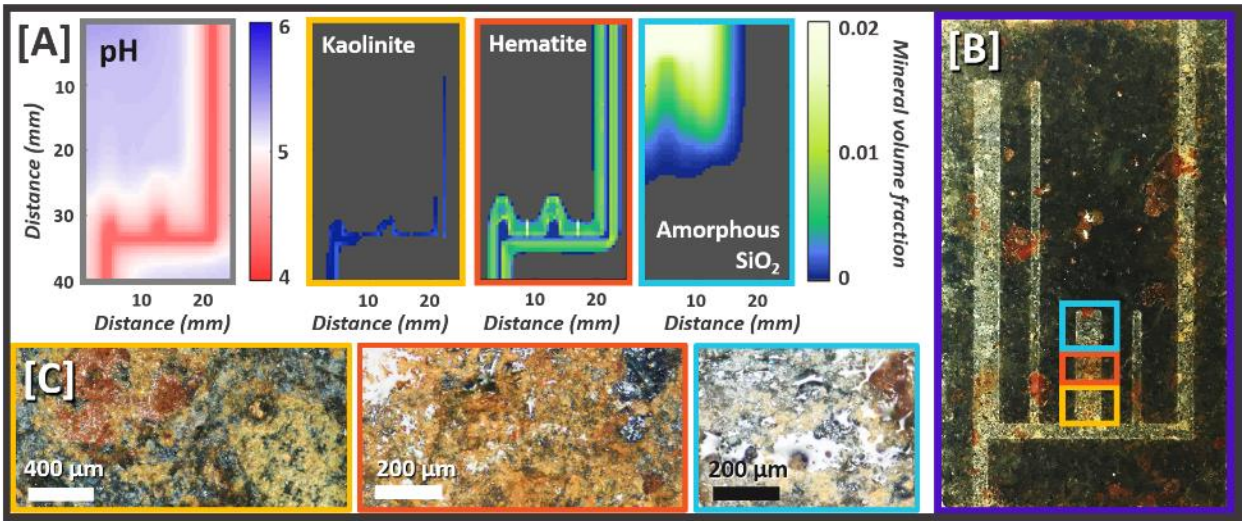

Figure 3.2. Reactive transport models [A] indicate that secondary precipitation fronts observed on the reacted milled surface of the core LB-100C [B] were driven largely by pH gradients that formed as fluid from the acidic injection path diffused into the dead-end fractures. Mineral volume fractions represent mm^3 of mineral per mm^3 of cell volume. The distinct color bands on the reacted core correspond to yellow-brown clays, orange-red Fe-oxides, and white amorphous silica, as illustrated with optical microscopy [C].

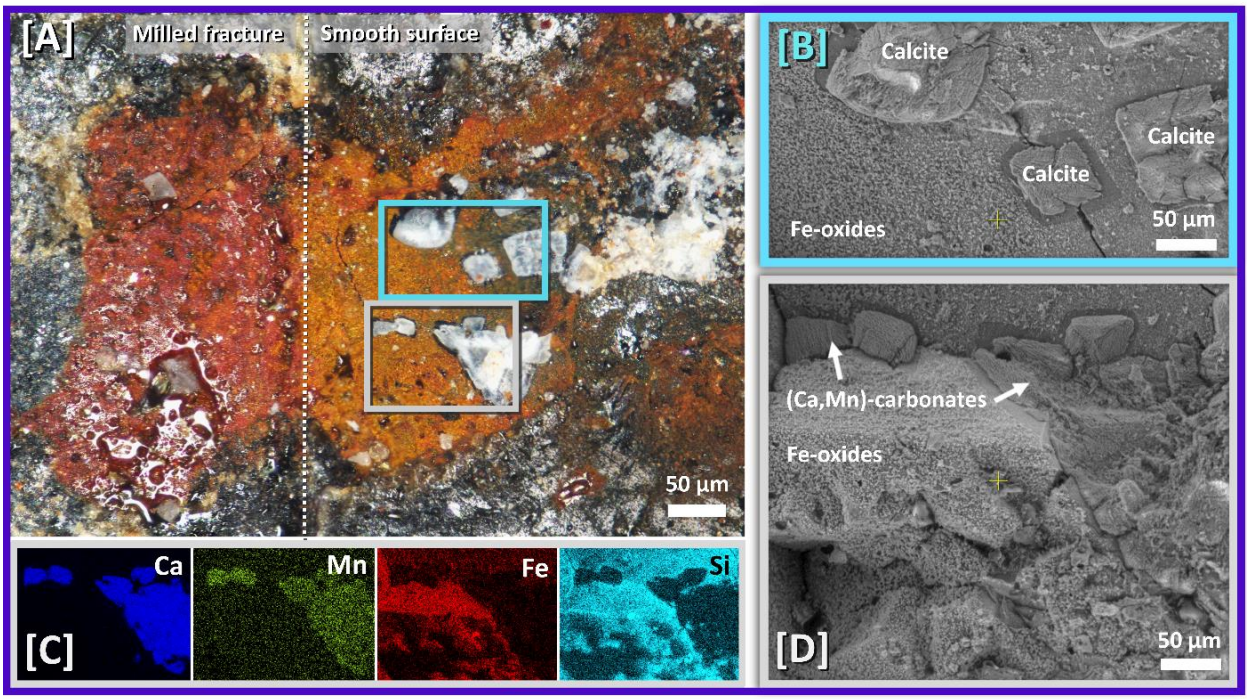

Figure 3.3. Localized formation of Fe-oxides and Ca-carbonates in LB-100C. [A] Optical microscope image showing distinct color gradient in iron oxidation between the milled and confined surfaces; [B] SEM image of Ca-carbonates forming in vugs on the smooth surface, surrounded by a layer of Fe-oxides; [C] EDS maps of [D] Ca-rich, Mn-bearing carbonates surrounded by Fe-oxides.

3.3.3. Localized carbonation: Effect of transport

Post-reaction fracture surfaces revealed strongly localized carbonation in diffusion-limited regions. In LB-100C, carbonates were predominantly Ca-rich and formed in small vugs and vesicles between the saw-cut (i.e., unmilled) fracture surfaces, as demonstrated in Figures C8-C11 of Appendix C. Morphology was also strongly localized, with calcite and aragonite, the two polymorphs of $CaCO_3$, occasionally forming in close proximity (Figure C9). Ca-carbonates typically crystallized on larger grains of pyroxene, which was the most reactive source of Ca in the cores. Smaller Mn-bearing Ca-carbonates (Figure 3.3, Section 3.3.2 and Figure C11, Appendix C) precipitated on olivine, which was the only source of Mn in the basalt cores based on prior characterization.[18] These results are consistent with the reactive transport model that used a heterogeneous mineral distribution from segmented xCT data, which predicts that secondary precipitates will predominantly form on the primary minerals that most readily contribute key divalent cations and that carbonation occurs chiefly in the low-porosity matrix (Figure C10). The simulations indicate this localization results from pH buffering as CO_2 diffuses away from the main flow path combined with a buildup of dissolved Ca around reactive sources, promoting rapid calcite saturation in pore fluids. Preferential nucleation of secondary minerals has been well-demonstrated; for instance, Stockmann et al.[30] found diopside was a much better substrate for calcite nucleation than basaltic glass. Here, the preferential formation of Ca-carbonates on larger reactive mineral grains is more likely driven by local saturation close to the source of Ca, which is achieved more rapidly in transport-limited regions. This hypothesis is consistent with the relative importance of reaction to diffusion time scales in the dead-end fractures; although there is no single meaningful Damköhler number (Da) for the heterogeneous multi-mineral system considered here, a Da value can be calculated for each mineral based on its reaction rate at the experimental temperature and pH conditions. Da values are small (<1) for the slowest-reacting mineral (K-feldspar) but large for the fast-reacting minerals that also serve as the primary cation donors for secondary carbonates (i.e., olivine and pyroxene), indicating that carbonation rates in diffusion-limited zones will be controlled by transport rather than surface reactions.

Ca-rich carbonates also typically coincided with red Fe-rich coatings in LB-100C (Figure 3.3), indicating the Fe content of the dissolving grains rapidly oxidized before it could be incorporated into carbonates. King et al.[31] similarly observed close association between precipitating carbonates and hematite, attributable to the reduction in Fe(III) solubility with Mg-carbonate precipitation.

They note bicarbonate can significantly increase hematite solubility by forming carbonated Fe species in solution under ambient conditions,[31] which may explain the lesser extent of Fe-oxides and precipitation of Fe-bearing carbonates in the high-$NaHCO_3$ experiments (Sections 3.3.4-3.3.5). While carbonation was less localized at higher [$NaHCO_3$] due to much weaker pH gradients between the injection path and basalt matrix, some localized carbonate crystals were found on the unmilled surfaces between the two core halves in both HB-100C and HB-150C (Figures C21 and C28). Across all experiments, strong localization in the most transport-limited regions indicates that carbonation efficiency in natural basalts will be influenced by both the relative abundance and spatial distribution of reactive minerals exposed to CO_2-acidified fluids along fractures.

In all experiments, carbonates predominated in diffusion-controlled regions while the advection-controlled flow path was altered to silica-rich clays. Hellevang et al.[32] observed similar behavior of clays and carbonates in batch experiments on basaltic glass at 100°C, where only smectite overgrowths were observed in lower pH (6.0 and 6.77) experiments but Ca-carbonate crystals also formed when the pH increased to 7.89, 9.14, and 9.68. In our experiments, the distinction in secondary mineralization on and off the injection path likely results from coupled effects of transport and geochemical gradients, where optimal carbonation occurs in diffusion-dominated zones that extend fluid residence times and provide sufficient pH buffering. On the other hand, while no permeability changes were measured in these experiments, the prevalence of clays in the injection paths could eventually obstruct flow in restricted areas and compete with carbonates for divalent cations. Impacts may be more pronounced in natural fractures than in the idealized milled channels created for these experiments, as greater roughness and aperture variability could contribute to precipitation-induced flow blocking at fracture intersections and narrow pore throats. Permeability evolution will also depend on secondary clay mobilization, which in turn depends on mineral spatial distributions along fractures; prior work has demonstrated that preferential dissolution of reactive minerals can lead to mobilization of less soluble particles, occluding key flow paths.[33] Longer-term flow experiments are necessary to determine how such alterations will ultimately impact carbonation efficiency.

3.3.4. Enhanced carbonation: Effect of $NaHCO_3$

Increasing [$NaHCO_3$] from a representative reservoir concentration (6.3 mM) to its solubility limit under ambient conditions (640 mM) substantially enhanced carbonation (Figure 3.4). While the latter fluids are not representative of typical post-injection reservoir brines, the results shed

light on the driving conditions for CO_2 mineralization, as the associated 2-order increase in pH would be expected to increase carbonate precipitation rates but also reduce dissolution rates of the primary basalt minerals. Prior work on natural basalts has not established the implications of this tradeoff for overall carbonation yields, which [$NaHCO_3$] could improve by lowering carbonate saturation thresholds through added [CO_3^{2-}] or inhibit by limiting the availability of carbonate-forming divalent cations. Despite the observed increase in secondary precipitation at high-[$NaHCO_3$], our effluent data reveals dissolution was comparable between the low- and high-bicarbonate experiments at 100°C (Figure 3.1), suggesting that precipitation is the rate-limiting step for carbonation. Previous work has suggested $NaHCO_3$ encourages olivine carbonation by serving as a catalyst[11] or as a buffer and source of carbonate ions.[14] Here, the role of [$NaHCO_3$] is likely attributable to enhanced carbonate mineral saturation at higher pH and [CO_3^{2-}] rather than an independent catalytic effect. Enhanced carbonation at elevated [$NaHCO_3$] was also accompanied by greater clay precipitation within the main flow path (Figure C15), suggesting the benefit of greater divalent cation release for carbonation reactions may be tempered by secondary alteration of dissolving minerals to alumino-silicates that could consume carbonate-forming cations and fill pores near injection zones.

Carbonates only formed in small vugs within the extremely transport-limited unmilled surfaces at low-[$NaHCO_3$], where corresponding model outputs confirm carbonation is most favorable in diffusion-dominated zones that have been buffered to a pH of 5-6 (Figure C10). It follows that injecting fluids within a similar pH range (6.1-6.4) in the high-$NaHCO_3$ experiments allowed carbonates to form in the milled dead-end fractures as well as in the unmilled regions. In contrast to the isolated but well-defined crystals observed on the unmilled surfaces, carbonates in the milled regions generally had more anhedral structures and aggregated in large clusters (see Appendix C, Figures C16-C19). Compared to the unmilled surfaces, higher water:rock ratios in the milled dead-end fractures combined with diffusion-driven transport provided sufficient reactants and residence time for extensive nucleation at elevated [$NaHCO_3$]. At 150°C, smaller carbonate crystals were also observed in the main flow channels (Figure 3.4), likely promoted by the incremental increase in carbonate saturation. Across all experiments, the observed improvements in carbonation with increasing pH indicate that CO_2 mineralization in natural reservoirs may be limited by resident brine alkalinities, which will generally be on par with the low-$NaHCO_3$ experiment. In such systems, initial precipitation may be confined to small pores

and fractures that are accessible to diffusing CO_2 yet distanced enough from injection zones to sufficiently buffer acidified formation fluids.

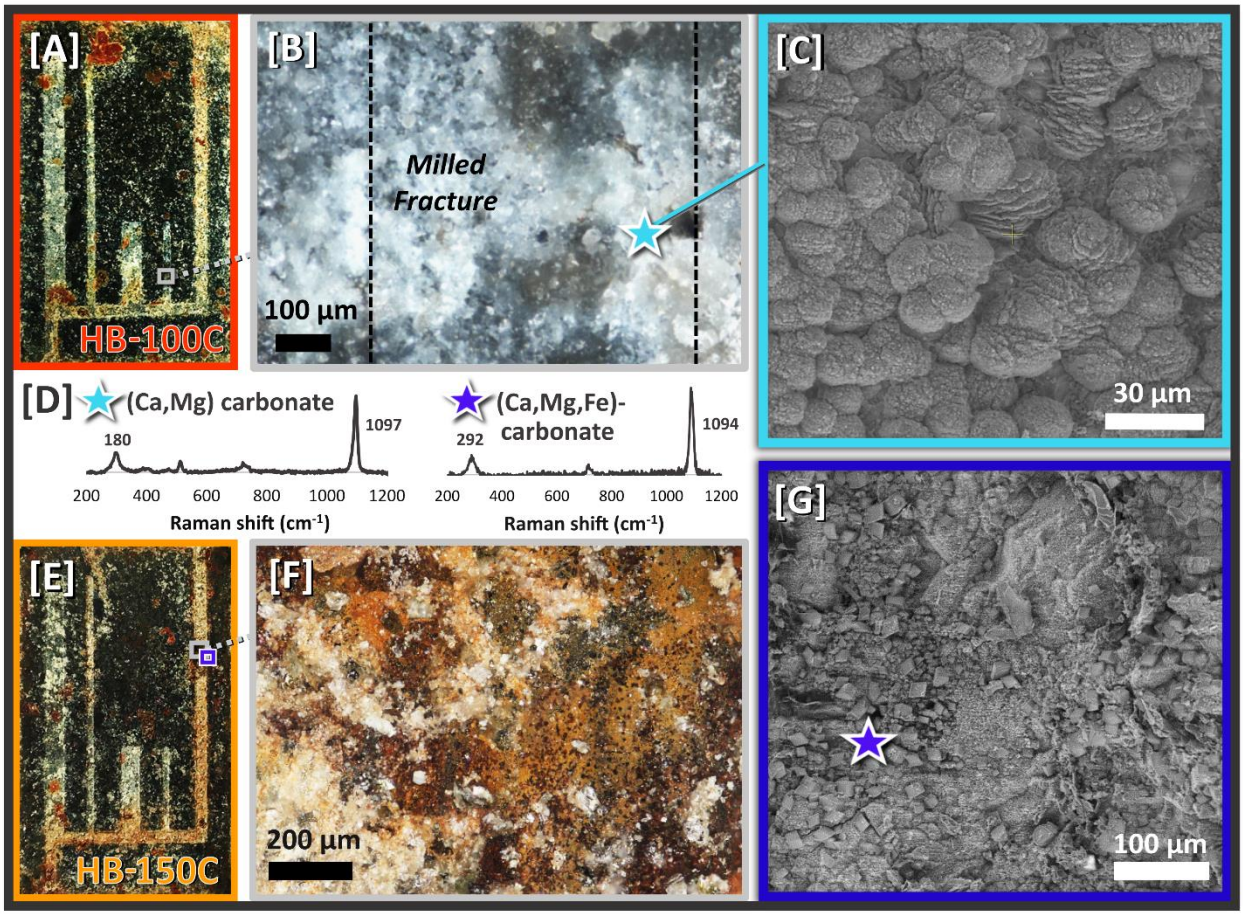

Figure 3.4. Secondary alteration in high-bicarbonate experiments. [A] Reacted milled surface from HB-100C highlighting a region of the short narrow dead-end fracture that [B] optical microscopy and [C] SEM imaging revealed was coated in amorphous carbonates, which were identified as Ca- and Mg-rich via EDS mapping (not shown) and [D] Raman spectroscopy. [E] Reacted milled surface from HB-150C highlighting a region near the inlet where [F] optical microscopy revealed white carbonates forming on clays and Fe-oxides. [G] SEM imaging shows these carbonates are small (<20 µm) with Raman spectra [D] matching standards for Ca-rich ankerite, $Ca(Mg_{0.35}Fe_{0.6}Mn_{0.05})(CO_3)_2$.[24]

In addition to increasing the extent of carbonation, elevated [$NaHCO_3$] promoted a notable shift in the types of carbonates that formed. Whereas only Ca-rich carbonates formed in the first experiment, a 2-order increase of [$NaHCO_3$] in the HB experiments promoted Mg and Fe uptake into carbonates (Figure 3.4). In contrast, Hellevang et al.[32] only observed pure Ca-carbonates on basaltic glass in unpressurized batch experiments at the same temperatures (100 and 150°C). They attributed a lack of Mg- and Fe-bearing carbonates to smectite coatings, which created an activation energy barrier that inhibited nucleation, and slow carbonate growth rates resulting from

large activity ratios of divalent cations to CO_3^{2-}. In similar batch experiments on basaltic glass (under 1-2.5 MPa P_{CO2}), Gysi and Stefansson[34] observed solid solutions of Ca-Mg-Fe carbonates at 75°C, while only calcite formed alongside Ca-Mg-Fe clays, amorphous silica, and zeolites at 150 and 250°C. The apparent contradiction between these results and our experimental trends, where Ca-carbonates predominated at the lowest pH and temperature, may stem from the higher P_{CO2} (10 MPa), use of whole natural basalt cores, or impact of flow in this study. Carbonate supersaturation promoted by elevated [CO_3^{2-}] in the HB-100C and HB-150C experiments likely made it more favorable for Mg and Fe to be incorporated into carbonate crystal structures rather than diffuse out of the system.

The white carbonate clusters that filled the milled fractures in HB-100C (Figures C16-C19) were typically Ca- and Mg-rich and displayed varying morphologies (Figures C17-C18). Considering that more Mg-bearing precipitates formed in HB-100C while effluent Mg concentrations were consistent with LB-100C (Figure 3.1), it appears that higher [$NaHCO_3$] enhanced release of Mg that could be more readily incorporated into carbonates under such high levels of $MgCO_3$ saturation. The presence of Ca- but not Mg-carbonates in the low-$NaHCO_3$ experiment could be explained by carbonate undersaturation combined with the slow precipitation kinetics of Mg-carbonates, which led to mobilization of dissolved Mg. On the other hand, given comparable steady-state release of Mg and Ca from reactive pyroxene grains, small Ca-rich carbonates were able to form in locally saturated vugs and pores due to the rapid rate of calcite precipitation. Schaef et al.[35] also found that Ca-carbonates generally formed first regardless of starting mineralogy, corroborating that kinetic limitations will govern carbonation efficiency in acidic regions that are not limited by dissolution.

Although (Ca,Mg)-carbonates were more common, Fe-bearing carbonates were found on both milled and unmilled surfaces of the reacted high-[$NaHCO_3$] cores, with some exhibiting Raman spectra characteristic of ankerite in HB-150C. While most Fe was still oxidized at the fracture surfaces due to the continual injection of well-oxygenated fluids, Fe-carbonates could prevail under actual injection conditions with progressive depletion of $O_{2(aq)}$ in resident brines. For example, siderite was the only carbonate that formed in prior batch experiments with similar basalt cores (100°C; 10 MPa P_{CO2}) where initial solutions were unbuffered and purged of residual O_2 in the headspace.[36] Reaction path modeling of the CarbFix injection test corroborated that Fe-carbonates predominate at low pH (<5) due to faster olivine dissolution, with carbonates becoming

successively enriched in Mg and then Ca at higher pH.[10] Previous studies have also demonstrated that olivine carbonation improves in later stages of batch experiments with a transition from oxic to anoxic conditions, which disrupts passivating Si-Fe coatings and reactivates olivine dissolution.[37,38] Sissmann et al.[38] concluded olivine carbonation at 120-170°C is optimized in reducing and circum-neutral environments. Although the roles of redox and pH conditions were not decoupled in our experiments, the prevalence of Fe-oxides in all experiments with Fe-bearing carbonates only forming at high [$NaHCO_3$] confirm that low-pe, high-pH reservoirs are necessary to realize the full mineral trapping potential of host rocks.

3.3.5. Fracture bridging: Effect of temperature

While less dramatic than the effects of elevated [$NaHCO_3$], raising the temperature from 100 to 150°C further increased the extent of secondary mineral formation. This impact was quantifiable because precipitation in both high-bicarbonate experiments was visible in post-reaction xCT scans (23.5 µm resolution), often filling the milled fractures and flow path. Segmenting the milled regions in pre- and post-reaction scans (Section 3.2.3) revealed that secondary precipitation reduced the total fracture volume by 35% in HB-100C compared to a 48% reduction in HB-150C. Xiong et al.[36] observed a similar effect in flood basalts reacted with CO_2-acidified DI water under static conditions and the same P_{CO2} (10 MPa), where precipitation filled 5.4% of the exposed fracture volume at 100°C compared to 15% at 150°C over 40 weeks. As hypothesized, the greatest extent of secondary mineralization in our series of core-flooding tests occurred at the highest temperature and influent pH. Gysi and Stefansson[28] also found that secondary precipitates became increasingly supersaturated with a rise in pH, limiting the mobility of dissolved Ca and Mg. This is consistent with the significant reduction in effluent Ca and Mg at 150°C (Figure 3.1) due to greater uptake in carbonates and clays.

Along with increased precipitation, fracture bridging was more common in HB-150C. Spatial distributions of precipitate-filled regions in the milled fractures are illustrated in Figure 3.5(B), which compares segmented binary post-reaction images for HB-100C and HB-150C, as well as the fracture aperture maps provided in Figures C13 and C23 (Appendix C). As previously discussed, surface characterization revealed that closed regions of the main injection path are filled with clays while closures in the dead-end fractures are primarily due to carbonate mineral precipitation. An increased occurrence of fracture bridging at higher temperature is corroborated in Figure 3.5 (C and D), which isolates the change in fracture volume as a function of diffusion

distance into the long narrow dead-end fractures where most complete closures occurred. Both high-bicarbonate experiments displayed a general increase in fracture bridging with diffusion distance, likely attributable to the pH gradient that develops when CO_2-charged fluid in the advective flow path is buffered by basalt dissolution as it diffuses into the dead-end fracture. The extent of fracture filling was more variable with depth in the wider long fractures with greater water:rock ratios (Figures C14 and C24). The fact that carbonates were able to fill the far ends of fractures (Figure 3.5A) despite apparent closures closer to the fluid source aligns with prior packed bed experiments where forsterite carbonation continued beyond a band of maximum precipitation.[39] Here, carbonates likely filled the tips of the dead-end fractures first, which could potentially allow for carbonation reactions to proceed near completion without self-sealing in zones of restricted flow where the majority of CO_2 mineralization is expected to occur.

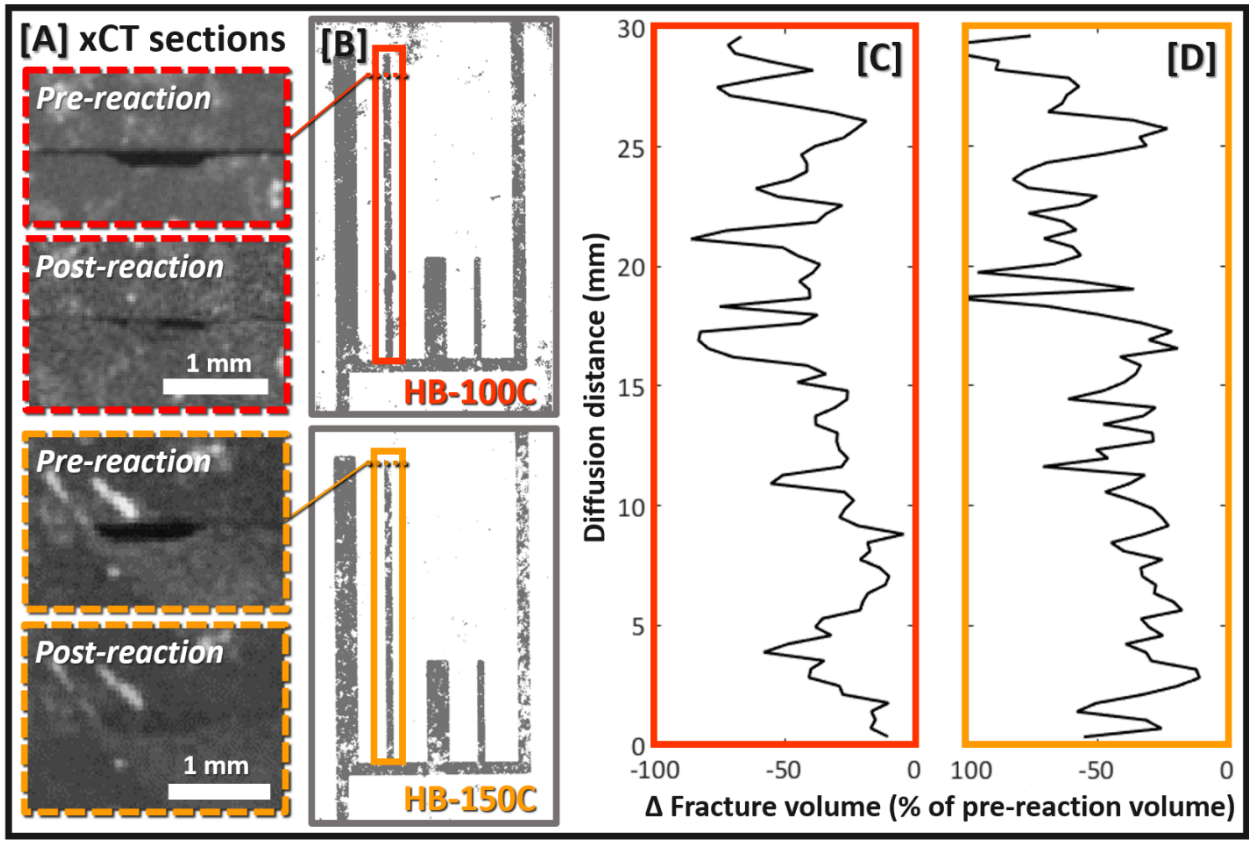

Figure 3.5. Changes in fracture volume between pre- and post-reaction scans as a function of diffusion distance into the long and narrow dead-end fractures for HB-100C [C] and HB-150C [D]. Segmented binary post-reaction xCT images for each experiment [B] depict the spatial distribution of precipitate-filled regions (white) in the milled fractures (grey). Cross sections of the xCT scans exemplifying fracture filling with precipitation (at the locations marked with dashed lines in B) are included in [A].

3.4. ENVIRONMENTAL IMPLICATIONS

This series of core-flooding experiments demonstrates how the coupled effects of geochemistry and transport limitations will control carbon mineralization reactions in basalts targeted for permanent CO_2 storage. The location of secondary precipitation will generally depend on existing brine chemistry and pH gradients induced by flow of CO_2-acidified fluids. Acidic advection-dominated flow paths promote bulk dissolution of the host rock, while most carbonates form in diffusion-dominated zones with sufficient pH buffering. Experimental and modeling results confirm that carbonation will be highly localized on reactive primary mineral grains contributing key divalent cations under conditions of low carbonate saturation, which would be expected to prevail near acidic injection zones and with increasing distance from CO_2 migration pathways where dissolved carbon becomes limiting. While we focused on reactions at microscales, the results are consistent with pilot-scale injections that found carbonates precipitated within vugs and vesicles[3] or in the bulk matrix surrounding primary flow channels.[2]

Consistent with prior batch experiments, elevated temperature and influent [$NaHCO_3$] exceeding anticipated reservoir conditions enhanced the extent of carbonation. While added [$NaHCO_3$] provides a relatively stable source of alkalinity and supplemental dissolved carbon that is not directly applicable to alkaline reservoirs, this study revealed that higher pH levels will be advantageous for mineral carbonation by creating more favorable conditions for precipitation without necessarily compromising adequate silicate dissolution to sustain reactions. Additionally, the more pronounced effect of [$NaHCO_3$] observed here supports previous flow-through experiments with the same basalt samples (see Chapter 2), where net mineral dissolution increased by 14% when the temperature was raised from 45 to 100°C and by 59% when 1.2 mM $NaHCO_3$ and 13.8 mM NaCl were added to the influent at 100°C.[8] Although this increase was primarily attributable to the NaCl, the results in combination with the present study suggest *in situ* fluid chemistry plays a greater role than temperature in basalt dissolution-precipitation reactions. Thus, while selecting formations with strong geothermal gradients will be advantageous, carbonation efficiency may be more strongly limited by the composition of injected fluids and resident brines.

In addition to providing insight regarding the roles of transport, temperature, and fluid chemistry on carbonate yields, this study suggests that the location of secondary precipitates will impact ultimate carbon sequestration capacity. The fact that carbonates formed in narrow confined fracture surfaces between the unmilled surfaces under all tested conditions indicates that basalts

with low porosity and primary fracture permeability may still serve as effective repositories for CO_2 mineralization, provided injectivity is maintained near the wellbore. Furthermore, precipitation first filling the tips of dead-end fractures may allow zones of restricted flow to fully carbonate without self-sealing. Further work is necessary to establish whether fracture-filling carbonation reactions can prove self-sustaining, either by creating effective proppants that maintain fluid access through narrow pore throats or by generating sufficient stress to induce tensile fracturing in the surrounding rock. The latter 'reaction-driven fracturing' mechanism[1] is held as the key to achieving complete carbonation of host reservoirs in the field, thereby maximizing the amount of CO_2 that can be securely stored through mineral trapping. While we did not consider mechanical effects, our work indicates that exceptionally high levels of pH and alkalinity may be necessary to precipitate carbonate volumes capable of driving this continuous renewal of reactive surfaces to support long-term CO_2 injection.

REFERENCES

(1) Matter, J. M.; Kelemen, P. B. Permanent Storage of Carbon Dioxide in Geological Reservoirs by Mineral Carbonation. *Nat. Geosci.* **2009**, *2* (12), 837–841.

(2) Matter, J. M.; Stute, M.; Snaebjornsdottir, S. O.; Oelkers, E. H.; Gislason, S. R.; Aradottir, E. S.; Sigfusson, B.; Gunnarsson, I.; Sigurdardottir, H.; Gunnlaugsson, E.; Axelsson, G.; Alfredsson, H. A.; Wolff-Boenisch, D.; Mesfin, K.; Taya, D. F. d. l. R.; Hall, J.; Dideriksen, K.; Broecker, W. S. Rapid Carbon Mineralization for Permanent Disposal of Anthropogenic Carbon Dioxide Emissions. *Science* **2016**, *352* (6291), 1312–1314.

(3) McGrail, B. P.; Schaef, H. T.; Spane, F. A.; Cliff, J. B.; Qafoku, O.; Horner, J. A.; Thompson, C. J.; Owen, A. T.; Sullivan, C. E. Field Validation of Supercritical CO_2 Reactivity with Basalts. *Environ. Sci. Technol. Lett.* **2016**.

(4) Andreani, M.; Luquot, L.; Gouze, P.; Godard, M.; Hoisé, E.; Gibert, B. Experimental Study of Carbon Sequestration Reactions Controlled by the Percolation of CO_2-Rich Brine through Peridotites. *Environ. Sci. Technol.* **2009**, *43* (4), 1226–1231.

(5) Peuble, S.; Godard, M.; Luquot, L.; Andreani, M.; Martinez, I.; Gouze, P. CO_2 Geological Storage in Olivine Rich Basaltic Aquifers: New Insights from Reactive-Percolation Experiments. *Appl. Geochem.* **2015**, *52*, 174–190.

(6) Luhmann, A. J.; Tutolo, B. M.; Tan, C.; Moskowitz, B. M.; Saar, M. O.; Seyfried, W. E. Whole Rock Basalt Alteration from CO_2-Rich Brine during Flow-through Experiments at 150 °C and 150 Bar. *Chem. Geol.* **2017**, *453*, 92–110.

(7) Luhmann, A. J.; Tutolo, B. M.; Bagley, B. C.; Mildner, D. F. R.; Seyfried, W. E.; Saar, M. O. Permeability, Porosity, and Mineral Surface Area Changes in Basalt Cores Induced by Reactive Transport of CO_2-Rich Brine: Physical Changes from Reaction in Basalt. *Water Resour. Res.* **2017**, *53* (3), 1908–1927.

(8) Adeoye, J. T.; Menefee, A. H.; Xiong, W.; Wells, R. K.; Skemer, P.; Giammar, D. E.; Ellis, B. R. Effect of Transport Limitations and Fluid Properties on Reaction Products in Fractures of Unaltered

and Serpentinized Basalt Exposed to High P_{CO2} Fluids. *Int. J. Greenh. Gas Control* **2017**, *63*, 310–320.

(9) Wolff-Boenisch, D.; Galeczka, I. M. Flow-through Reactor Experiments on Basalt-(Sea)Water-CO_2 Reactions at 90 °C and Neutral pH *Int. J. Greenh. Gas Control* **2018**, *68*, 176–190.

(10) Snæbjörnsdóttir, S. Ó.; Gislason, S. R.; Galeczka, I. M.; Oelkers, E. H. Reaction Path Modelling of In-Situ Mineralisation of CO_2 at the CarbFix Site at Hellisheidi, SW-Iceland. *Geochim. Cosmochim. Acta* **2018**, *220*, 348–366.

(11) O'Connor, W. K.; Dahlin, D. C.; Rush, G. E.; Gerdemann, S. J.; Nilsen, D. N. Aqueous Mineral Carbonation. *Final Rep. DOEARC-TR-04* **2005**, *2*.

(12) Chizmeshya, A. V.; McKelvy, M. J.; Squires, K.; Carpenter, R. W.; Béarat, H. *A Novel Approach to Mineral Carbonation: Enhancing Carbonation While Avoiding Mineral Pretreatment Process Cost*; Arizona State University, 2006.

(13) Kelemen, P. B.; Hirth, G. Reaction-Driven Cracking during Retrograde Metamorphism: Olivine Hydration and Carbonation. *Earth Planet. Sci. Lett.* **2012**, *345–348*, 81–89.

(14) Gadikota, G.; Matter, J.; Kelemen, P.; Park, A. A. Chemical and Morphological Changes during Olivine Carbonation for CO2 Storage in the Presence of NaCl and $NaHCO_3$. *Phys. Chem. Chem. Phys.* **2014**, *16* (10), 4679.

(15) Wang, F.; Giammar, D. E. Forsterite Dissolution in Saline Water at Elevated Temperature and High CO_2 Pressure. *Environ. Sci. Technol.* **2013**, *47* (1), 168–173.

(16) Béarat, H.; McKelvy, M. J.; Chizmeshya, A. V. G.; Gormley, D.; Nunez, R.; Carpenter, R. W.; Squires, K.; Wolf, G. H. Carbon Sequestration via Aqueous Olivine Mineral Carbonation: Role of Passivating Layer Formation. *Environ. Sci. Technol.* **2006**, *40* (15), 4802–4808.

(17) Kelemen, P. B.; Matter, J.; Streit, E. E.; Rudge, J. F.; Curry, W. B.; Blusztajn, J. Rates and Mechanisms of Mineral Carbonation in Peridotite: Natural Processes and Recipes for Enhanced, in Situ CO_2 Capture and Storage. *Annu. Rev. Earth Planet. Sci.* **2011**, *39* (1), 545–576.

(18) Wells, R.; Giammar, D.; Skemer, P. *Sample Library of Natural and Artificial Basalts*; 2016; https://edx.netl.doe.gov/dataset/sample-library-of-natural-and-artificial-basalts/revision_resource/2bcdd2f4-70f0-4b1c-afe7-d1d563680e0c.

(19) Duan, Z.; Sun, R. An Improved Model Calculating CO_2 Solubility in Pure Water and Aqueous NaCl Solutions from 273 to 533 K and from 0 to 2000 Bar. *Chem. Geol.* **2003**, *193*, 257–271.

(20) Zimmer, K.; Zhang, Y.; Lu, P.; Chen, Y.; Zhang, G.; Dalkilic, M.; Zhu, C. SUPCRTBL: A Revised and Extended Thermodynamic Dataset and Software Package of SUPCRT92. *Comput. Geosci.* **2016**, *90*, 97–111.

(21) Johnson, J. W.; Oelkers, E. H.; Helgeson, H. C. SUPCRT92: A Software Package for Calculating the Standard Molal Thermodynamic Properties of Minerals, Gases, Aqueous Species, and Reactions from 1 to 5000 Bar and 0 to 1000 C. *Comput. Geosci.* **1992**, *18* (7), 899–947.

(22) Schindelin, J.; Arganda-Carreras, I.; Frise, E.; Kaynig, V.; Longair, M.; Pietzsch, T.; Preibisch, S.; Rueden, C.; Saalfeld, S.; Schmid, B.; Tinevez, J.-Y.; White, D. J.; Hartenstein, V.; Eliceiri, K.; Tomancak, P.; Cardona, A. Fiji: An Open-Source Platform for Biological-Image Analysis. *Nat. Methods* **2012**, *9* (7), 676–682.

(23) Sommer, C.; Straehle, C.; Koethe, U.; Hamprecht, F. A. Ilastik: Interactive Learning and Segmentation Toolkit. In *Biomedical Imaging: From Nano to Macro, 2011 IEEE International Symposium on*; IEEE, 2011; pp 230–233.

(24) The Power of Databases: The RRUFF Project. In *Highlights in mineralogical crystallography*; Armbruster, T., Danisi, R. M., Eds.; Walter de Gruyter GmbH: Berlin ; Boston, 2016; pp 1–30.

(25) Steefel, C. I.; Appelo, C. A. J.; Arora, B.; Jacques, D.; Kalbacher, T.; Kolditz, O.; Lagneau, V.; Lichtner, P. C.; Mayer, K. U.; Meeussen, J. C. L.; Molins, S.; Moulton, D.; Shao, H.; Šimůnek, J.; Spycher, N.; Yabusaki, S. B.; Yeh, G. T. Reactive Transport Codes for Subsurface Environmental Simulation. *Comput. Geosci.* **2015**, *19* (3), 445–478.

(26) Menefee, A. H.; Li, P.; Giammar, D. E.; Ellis, B. R. Roles of Transport Limitations and Mineral Heterogeneity in Carbonation of Fractured Basalts. *Environ. Sci. Technol.* **2017**, *51*(16), 9352–9362.

(27) Cadogan, S. P.; Maitland, G. C.; Trusler, J. P. M. Diffusion Coefficients of CO_2 and N_2 in Water at Temperatures between 298.15 K and 423.15 K at Pressures up to 45 MPa. *J. Chem. Eng. Data* **2014**, *59* (2), 519–525.

(28) Gysi, A. P.; Stefánsson, A. CO_2-Water–Basalt Interaction: Low Temperature Experiments and Implications for CO_2 Sequestration into Basalts. *Geochim. Cosmochim. Acta* **2012**, *81*, 129–152.

(29) Marini, L. Geological Sequestration of Carbon Dioxide: Thermodynamics, Kinetics, and Reaction Path Modeling. In *Geological Sequestration of Carbon Dioxide: Thermodynamics, Kinetics, and Reaction Path Modeling*; Elsevier, 2007; Vol. 11, pp 319–409.

(30) Stockmann, G. J.; Wolff-Boenisch, D.; Gislason, S. R.; Oelkers, E. H. Do Carbonate Precipitates Affect Dissolution Kinetics? *Chem. Geol.* **2013**, *337–338*, 56–66.

(31) King, H. E.; Plumper, O.; Putnis, A. Effect of Secondary Phase Formation on the Carbonation of Olivine. *Environ. Sci. Technol.* **2010**, *44*, 6503–6509.

(32) Hellevang, H.; Haile, B. G.; Tetteh, A. Experimental Study to Better Understand Factors Affecting the CO_2 Mineral Trapping Potential of Basalt: Experimental Study to Better Understand Factors Affecting the CO_2 Mineral. *Greenh. Gases Sci. Technol.* **2017**, *7* (1), 143–157.

(33) Ellis, B. R.; Fitts, J. P.; Bromhal, G. S.; McIntyre, D. L.; Tappero, R.; Peters, C. A. Dissolution-Driven Permeability Reduction of a Fractured Carbonate Caprock. *Environ. Eng. Sci.* **2013**, *30* (4), 187–193.

(34) Gysi, A. P.; Stefánsson, A. Mineralogical Aspects of CO_2 Sequestration during Hydrothermal Basalt Alteration — An Experimental Study at 75 to 250°C and Elevated P_{CO2}. *Chem. Geol.* **2012**, *306–307*, 146–159.

(35) Schaef, H. T.; McGrail, B. P.; Owen, A. T. Carbonate Mineralization of Volcanic Province Basalts. *Int. J. Greenh. Gas Control* **2010**, *4* (2), 249–261.

(36) Xiong, W.; Wells, R. K.; Menefee, A. H.; Skemer, P.; Ellis, B. R.; Giammar, D. E. CO_2 Mineral Trapping in Fractured Basalt. *Int. J. Greenh. Gas Control* **2017**, *66*, 204–217.

(37) Saldi, G. D.; Daval, D.; Morvan, G.; Knauss, K. G. The Role of Fe and Redox Conditions in Olivine Carbonation Rates: An Experimental Study of the Rate Limiting Reactions at 90 and 150°C in Open and Closed Systems. *Geochim. Cosmochim. Acta* **2013**, *118*, 157–183.

(38) Sissmann, O.; Brunet, F.; Martinez, I.; Guyot, F.; Verlaguet, A.; Pinquier, Y.; Daval, D. Enhanced Olivine Carbonation within a Basalt as Compared to Single-Phase Experiments: Reevaluating the Potential of CO_2 Mineral Sequestration. *Environ. Sci. Technol.* **2014**, *48* (10), 5512–5519.

(39) Giammar, D. E.; Wang, F.; Guo, B.; Surface, J. A.; Peters, C. A.; Conradi, M. S.; Hayes, S. E. Impacts of Diffusive Transport on Carbonate Mineral Formation from Magnesium Silicate-CO_2-Water Reactions. *Environ. Sci. Technol.* **2014**, *48* (24), 14344–14351.

CHAPTER 4

Carbon Mineralization in Reactive Silicate Zones

4.1. BACKGROUND AND MOTIVATION

A mounting need to safely sequester anthropogenic CO_2 emissions has motivated a growing body of research on the viability of permanent CO_2 trapping through mineralization in basalt from bench to pilot scales.[1–5] Unlike sedimentary reservoirs, which store CO_2 as a supercritical fluid that slowly dissolves into formation brines over extended time frames, basalts and other mafic rocks are rich in divalent cation-bearing silicate minerals that react quickly to bind injected CO_2 in the form of stable carbonate minerals.[1] Pilot-scale tests at the CarbFix project in Iceland[5] and Wallula Basalt Pilot Project in Washington state[4] reported that substantial carbonation occurs within 2 years of injection, effectively trapping CO_2 over geologic time scales as natural alkalinity supplied by the reservoir limits re-dissolution of precipitated carbonates. While basalts offer more limited long-term sequestration potential than ubiquitous and extensive sedimentary basins, they may be more readily deployable repositories for commercial-scale geologic carbon storage (GCS) due to this inherent reduction or elimination of leakage risk. The National Academy of Science recently reported that *in situ* carbon mineralization could enable large-scale implementation of negative emissions technologies (NETs) but remains underdeveloped,[6] motivating continued efforts to understand the long-term implications of carbonate precipitation and define reservoir and injection conditions that maximize sequestered CO_2 emissions.

Given the heterogeneous nature of basalts with respect to mineral compositions and distributions, most studies on CO_2 mineralization have focused on single minerals to streamline analysis and interpretation. Of the minerals present in natural basalts, olivine [$(Mg,Fe)_2SiO_4$] holds the most promise for CO_2 fixation because it has the highest stoichiometric ratio of divalent cations to silicates and carbonates quickly under typical GCS reservoir conditions.[7] Pyroxene [$(Ca,Mg,Fe)_2Si_2O_6$] is less efficient than olivine but is generally more abundant and also reacts quickly relative to other basaltic minerals.[8] Moreover, pyroxenes provide a source of dissolved Ca^{2+}, and calcite ($CaCO_3$) precipitation kinetic rates exceed those of magnesite ($MgCO_3$) or

siderite ($FeCO_3$) by several orders of magnitude. Plagioclase feldspars ($NaAlSi_3O_8$-$CaAl_2Si_2O_8$) comprise the majority of the basalt matrix but typically dissolve too slowly to be relevant for CO_2 mineralization. Feldspars also contain Al^{3+}, which tends to form secondary clays that could compete with carbonates for divalent cations.[9] Considering these differences in reactivity and carbonation efficiency, the abundance and distribution of olivine and pyroxene minerals will likely control the inherent CO_2 trapping potential of natural basalt.

The propensity of these minerals to carbonate under representative GCS conditions has been well-demonstrated, particularly for olivine.[9–14] Batch experiments have determined that olivine carbonation rates are maximized at high P_{CO2} (>7 MPa) and temperature. As temperature increases, diffusive mass transfer across the crystal-fluid interface also increases (which benefits carbonation) while driving chemical potential decreases (which acts against carbonation), resulting in maximum carbonation rates around 185°C.[15–17] A set of early experiments on *ex situ* aqueous mineral carbonation determined carbonation rates were further optimized in solutions of 0.64M $NaHCO_3$ and 1M NaCl, which correspond to the maximum solubility of these species at ambient conditions.[15] Gadikota et al.[18] decoupled the roles of $NaHCO_3$ and NaCl, concluding that NaCl provides no significant benefit but $NaHCO_3$ considerably improves carbonation by serving as a pH buffer and carbonate source. Studies on pyroxene have been more limited than olivine but several have investigated carbonation of wollastonite,[19–22] the Ca end member ($Ca_2Si_2O_6$) that reacts faster than Mg- and Fe-pyroxenes but occurs more rarely in nature. Daval et al.[23] found that wollastonite crystals carbonate rapidly (within a couple of days) in CO_2-saturated water at 90°C and 25 MPa P_{CO2}, while forsterite carbonation was inhibited by the development of amorphous silica coatings on grain surfaces. The inhibitory formation of secondary silicates may depend in part on fluid partitioning, as Min et al.[21] found that amorphous silica layers did limit wollastonite carbonation in water-bearing $scCO_2$.

In addition to promising studies on the carbonation potential of individual minerals, batch[24–26] and flow-through[27,28] experiments have demonstrated that whole basalts can effectively trap CO_2 at relevant GCS injection conditions. Carbonates tend to precipitate in diffusion-limited zones and localize on reactive minerals supplying critical divalent cations (i.e. olivine, pyroxene),[28] but the impacts of localized geochemical reactions on long-term injectivity and storage capacity remain unclear. While dissolution may be self-enhancing as removal of mineral surfaces exposes new reactive surfaces, precipitation is generally conceived to be self-limiting as carbonates

progressively clog pores and limit fluid transfer.[29] However, precipitation can also be self-accelerating when secondary phases have larger molar volumes than the primary minerals they replace. Under such conditions, crystallization can generate sufficient stress to induce tensile fracturing in the surrounding rock, a process known as reactive cracking or fracturing.[2,3] In nature, partial to complete carbonation of peridotite (rock with >40% olivine) has been attributed to reaction-induced formation and propagation of new fracture networks driven by the 44% volume increase associated with olivine carbonation.[7,17] More recent batch experiments have evidenced cracking during olivine carbonation at 200°C and 13 MPa P_{CO2}, where precipitation within a wall of sintered olivine caused to interior to expand faster than the surfaces and generated tensile fractures analagous to shrinkage cracking.[30] However, reactive cracking has not been evidenced in basalts under representative geologic storage conditions.

This work explores CO_2 mineralization patterns in diffusion-limited zones of reactive minerals where most carbonation is expected to occur. Prior experiments on packed forsterite beds reported that carbonation resulted in sufficient volume expansion to force the bed upward and create a small gap,[31] but the mechanical impact of expansion on surrounding rock could not be assessed because the system was unconfined and involved a single mineral phase. Here, a series of core flooding experiments was designed to expose packed beds of reactive fine-grained minerals within whole basalts to CO_2-acidified fluids under confining stress at relevant geologic storage conditions. While packed beds are not an accurate representation of mineral availability and accessibility in actual reservoirs, this system allows for exploration of carbonation within zones rich in reactive minerals and potential impacts to the surrounding basalt matrix. Additionally, this chapter explores how diffusion distance along with the composition and grain size of the reactive phase influence carbonation. Results from these experiments and complimentary reactive transport models further resolve geologic conditions that favor mineral carbonation in natural basalts.

4.2. METHODS

4.2.1. Sample preparation

Columbia River flood basalt from Pullman, Washington was obtained from Wards Scientific and sub-cored into 1” (2.5 cm) diameter by 1.5” (4.3 cm) samples. Each core was first cut in half length-wise to create a single uniform fracture for flow. One half of the core was slightly roughened with 120-grit sandpaper to facilitate flow and the other half was drilled to create holes

(2 mm diameter) parallel or perpendicular to the saw-cut fracture, which were then wet-packed with powders of reactive minerals as detailed for each experiment below. Wollastonite (average grain size <30 µm) and olivine (<75 and 212-425 µm) powders were used as received. Although wollastonite carbonation stoichiometrically results in a net volume decrease, precluding reaction-driven mechanical impacts, it was selected due to its rapid carbonation kinetics.

In the first test (hereafter referred to as PB-1 for 'packed bed'), a channel 2 mm in diameter and 2.5 cm long was drilled parallel to the direction of flow on one half of the core and wet-packed with a 1:1 mass ratio of fine-grained wollastonite (<30 µm grain size) to olivine (<75 µm). The end of the packed bed (at the face of the core) was sealed with a thin layer of epoxy to prevent backflow of injected fluids. To prevent dissolution of the reactive material during flow, the packed bed was separated from the injected fluid by another 2-mm diameter hole connecting it to the saw-cut fracture that was packed with non-reactive SiO_2 beads (75 µm diameter, Sigma Aldrich). A schematic illustration of the sample design is presented in Figure 4.1 along with an overview of experimental conditions, which are detailed in Section 4.2.2.

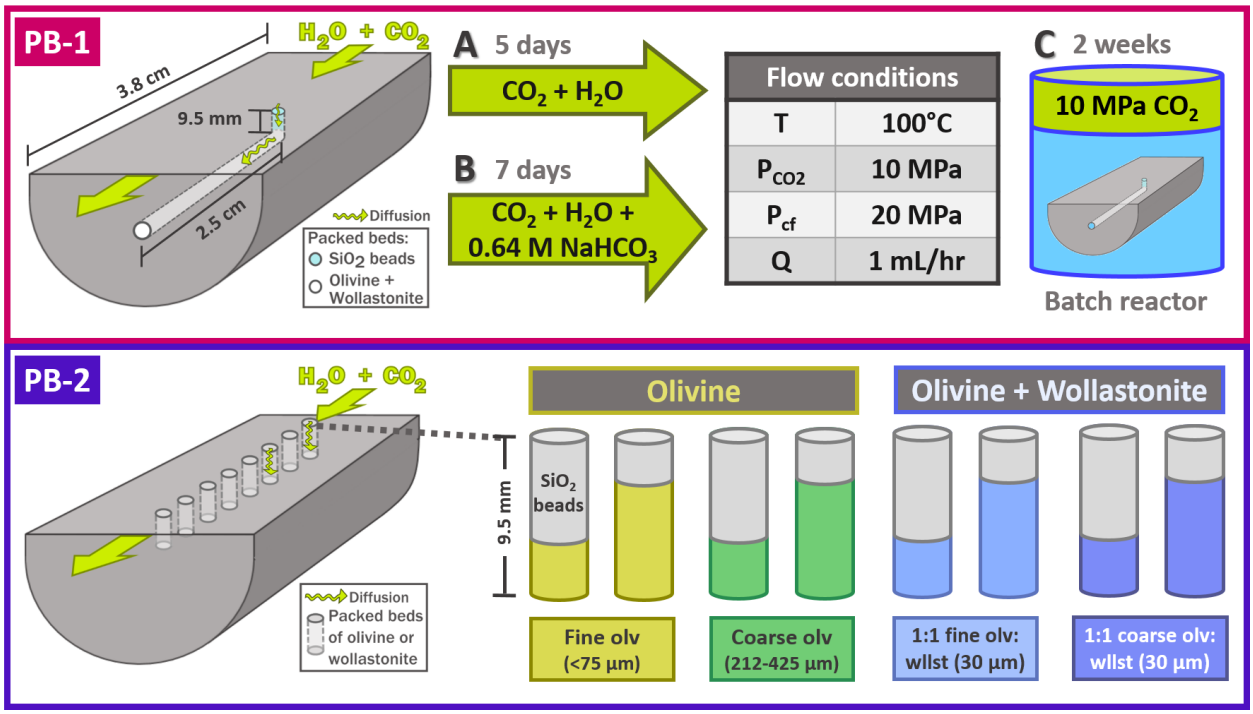

Figure 4.1. Schematic overview of experimental designs. In PB-1, a single packed bed is created parallel to the direction of flow and flow conditions transition from [A] constant flow of CO_2-acidified water to [B] constant flow of CO_2-acidified brine buffered by 0.64 M $NaHCO_3$ to [C] static conditions under the same temperature and CO_2 pressure. In PB-2, 8 vertical packed beds are created perpendicular to the direction of flow with varying depths and reactive mineral compositions as detailed to the right.

In the second experiment (PB-2), eight channels (each 2 mm in diameter and 9.5 mm in depth) were drilled into the saw-cut fracture perpendicular to the direction of flow. As illustrated in Figure 4.1, the content of each hole was varied to test four different reactive mineral compositions at two different diffusion length scales, with a 'shallow' (~3 mm depth) and 'deep' (~6 mm depth) bed created for each composition. The first two sets of packed beds tested the impact of reactive surface area, with fine-grained olivine (<75 µm) in the first set and coarse-grained olivine (212-425 µm) in the second. The second half of the drilled holes also compared grain size with fine-grained olivine in the third set and coarse-grained olivine in the fourth, but fine-grained wollastonite (30 µm) was added in a 1:1 mass ratio with the olivine to evaluate the influence of silicate mineralogy and particularly Ca content on carbonation efficiency. After wet packing the silicate powders, the remaining space in each 9.5-mm hole was packed with SiO_2 beads to create a diffusion barrier between injected fluids and reactive materials.

4.2.2. Core flooding experiments

An overview of the custom-built core flooding system is provided in Appendix A and specific procedures for the experiments conducted in this chapter are summarized here. In each test, the drilled core halves depicted in Figure 4.1 were mated to roughened halves and the cores were secured in chemical-resistant heat-shrink tubing (McMaster Carr) to prevent shifting or loss of material upon removal. Pre-reaction x-ray computed tomography (xCT) scans were collected with a voxel resolution of 23.5 µm (Nikon Metrology XTH225). The assembled core was then placed in a viton sleeve that was positioned between fluid distribution plugs within the biaxial core flooding reactor (Core Laboratories). The reactor was heated to 100°C using a beaker heater connected to a control box (BriskHeat) that maintains temperature within ±1°C. Confining stress was raised to 20 MPa and the initial pore pressure was raised to 10 MPa with DI water before injecting CO_2-acidified brines that had been pre-equilibrated at experimental conditions (i.e. 100°C and 10 MPa P_{CO2}) 24 hours prior to the start. Pore pressure was maintained with a back pressure regulator (Swagelok) and differential pressure was continuously recorded with pressure transducers (WIKA Instrument Corporation) installed upstream and downstream of the core.

PB-1 involved three stages of varying flow conditions as summarized in Figure 4.1. CO_2-equilibrated DI water was first injected for 5 days before removing the core and collecting an xCT scan. The core was then placed back in the reactor and a buffered solution containing 0.64M $NaHCO_3$ was injected for 7 days, after which the core was again removed and scanned. The xCT

data did not evidence precipitation, potentially due to a limited CO_2 supply within the packed bed; to increase the water:rock ratio, the core was unwrapped and the half containing the packed bed was set in a batch reactor filled with DI water for 2 weeks under the same conditions (100°C, 10 MPa P_{CO2}). A final post-reaction xCT scan was taken after this step. In PB-2, CO_2-acidified DI water was continuously injected for 8 days under the same temperature and stress conditions applied in PB-1. A post-reaction xCT scan was also collected. For reference, key conditions for each experiment are summarized in Table 4.1.

Table 4.1. Summary of experimental conditions

Condition	PB-1	PB-2
Temperature	100°C	100°C
P_{CO2}	10 MPa	10 MPa
$P_{Confining}$	20 MPa	20 MPa
Flow rate	1 mL/h	1 mL/h
Duration	5 days with DI → 7 days with 0.64M $NaHCO_3$	8 days
Initial pH*	4.2 → 6.1	4.2

*Initial pH calculated based on charge balance of initial solution

4.2.3. xCT processing and segmentation

Pre-reaction xCT scans were collected following sample assembly in both experiments (Nikon Metrology XTH225). In PB-1, the core was also scanned intermediately after each of the three experimental stages while only one post-reaction scan was taken in PB-2. Scan settings were initially adjusted to optimize resolution and grey value distributions for the flood basalt cores and applied uniformly to each scan to facilitate pre- and post-reaction comparisons. All scans were taken with a beam energy of 185 kV, current of 145 uA, and power of 26.8 W using a 0.25 mm copper filter to remove low-energy x-rays for improved contrast. A total of 3600 projections were collected with 4 frames averaged per projection at a rate of 1.41 frames per second. The data sets were reconstructed with CT Pro (XT5.1.3, Nikon Metrology, Inc).

In PB-1, each scan was cropped to the same region of interest (ROI) in ImageJ[32] to isolate the single packed silicate bed. Void space was segmented using Ilastik, an interactive software that classifies and thresholds pixels based on feature sizes and descriptors specified in manual user seeding.[33] The segmented data were further processed in MATLAB (R2016a), where void

fractions were calculated as the volume of voids divided by the volume of the packed bed. Note that this does not represent the absolute porosity of the packed bed but rather the fraction of void space resolvable in the scans (i.e., voids >26 μm). The pre- and post-reaction scans for PB-2 were not segmented due to limited contrast between the initial and carbonated silicates in the packed beds, as well as the fact that most of the initial porosity was sub-voxel resolution.

4.2.4. Reaction product identification

Following post-reaction xCT scanning, the half of each core containing the packed beds was vacuum-epoxied and saw-cut through the center to create cross sections of the reacted beds (Figure 4.3). The reacted materials were first analyzed non-destructively using an environmental scanning electron microscope (FEI Quanta 3D e-SEM/FIB) with back-scattered electron imaging (BSE) and energy-dispersive x-ray spectroscopy (EDS), which provides chemical data to inform mineral compositions. Carbonate precipitates were identified with Raman spectroscopy (532 nm; Renishaw), where raw spectra were processed in OriginPro 2015 and compared with mineral standards from the RRUFF database.[34]

4.2.5. Thermogravimetric analysis

After qualitatively characterizing reaction products through non-destructive imaging and spectroscopy, the extent of carbonation was roughly quantified with thermal gravimetric analysis (TGA; Netzsch TASC 413 Instrument). By incrementally heating and weighing solid samples, TGA allows for quantification of hydration and carbonation products that decompose at different temperatures. For each run, samples were ground into fine powders and a small aliquot (~10 mg) was placed in a 90 μL aluminum crucible that was first heated to 35°C at a rate of 1°C/min and allowed to stabilize for an hour to remove free water. The sample was then heated to 1000°C at a constant rate of 10°C/min while N_2 gas flowed at 50 mL/min to purge the system. Mass was continuously recorded as different mineral phases decomposed.

The derivatives of the TGA curves (i.e. DTG curves) were used to quantify reaction products. The final mass of the sample upon ignition to 950°C (m_{950}) represents the amount of unreacted material (i.e. silicates that did not become altered during the experiment) and the mass lost on ignition represents hydration and carbonation products that burn off at different temperatures. Thus, the carbonation efficiency (η_c) can be estimated as:

$$\eta_c = \left[\frac{\text{moles Mg and/or Ca trapping } CO_2}{\text{moles Mg and/or Ca available}}\right] = \left[\frac{\text{moles carbonated}}{\text{moles unreacted+hydrated+carbonated}}\right] \quad \textbf{[Eqn 4.1]}$$

The mass of different reaction products can be estimated by taking the area under the DTG curve over the temperature range at which they decompose, which corresponds to 250-450°C for hydration products (m_H) and 450-800°C for carbonates (m_{CO2}).[35,36] The mass of any initial impurities, measured as mass lost in these temperature intervals during ignition of unreacted olivine and wollastonite samples, was also detracted. Note that we did not distinguish between quantities of Ca- and Mg-carbonates because we were only concerned with overall carbonation efficiency and accurate separation is precluded by the fact that the decomposition ranges overlap.

Carbonation efficiencies can then be calculated for each packed bed composition by substituting measured TGA masses and molecular weights into Equation 4.1. For beds with a 1:1 mixture of wollastonite and olivine, the denominator is the total number of moles of Mg and Ca available for reaction, where olivine and wollastonite each represent half of the ignited mass (m_{950}):

$$\text{(moles Mg+Ca)} = 0.5m_{950}\left[\frac{\text{mmol}}{141\text{ mg}}\right]\left[\frac{2\text{ mmol Mg}}{\text{mmol olivine}}\right] + 0.5m_{950}\left[\frac{\text{mmol}}{116\text{ mg}}\right]\left[\frac{\text{mmol Ca}}{\text{mmol wollastonite}}\right] \quad \textbf{[Eqn 4.2]}$$

Thus, the overall carbonation efficiency can be calculated as:

$$\eta_c = \left[\frac{m_{CO2}/44}{m_{950}/88}\right] = 2\left[\frac{m_{CO2}}{m_{950}}\right] \quad \textbf{[Eqn 4.3]}$$

For the pure olivine beds in PB-3, carbonation efficiency is similarly estimated as:

$$\eta_c = \left[\frac{m_{CO2}/44}{m_{950}\left[\frac{\text{mmol}}{141\text{ mg}}\right]\left[\frac{2\text{ mmol Mg}}{\text{mmol olivine}}\right]}\right] = 1.6\left[\frac{m_{CO2}}{m_{950}}\right] \quad \textbf{[Eqn 4.4]}$$

In the core from PB-1, reacted powders were removed in 4-mm increments along the packed bed to evaluate potential changes in carbonation with diffusion distance. Finer distance increments did not provide sufficient mass (at least 10 mg) for TGA and thus were not feasible. In PB-2, shallow (~3 mm) packed beds were analyzed as one sample because they provided just enough material for analysis. The deeper (~6 mm) beds were split into two samples, one in the upper half and one in the lower, to loosely assess whether major reaction products changed with diffusion depth. Note that due to the fact that the saw cut was not perfectly linear, the last deep hole only had enough material for one TGA run and thus only one measurement averaged across the entire depth was obtained. Full DTG results for each analyzed sample are presented in Figure 4.4 for PB-1 and included in Appendix D (Section D1) for PB-2.

4.2.6. Reactive transport modeling

1D reactive transport models were developed in CrunchTope[37] to explore and interpret the impacts of reactive silicate composition and surface area on carbonation within the packed beds. CrunchTope (or its predecessor CrunchFlow) has been applied extensively to environmental problems involving flow through porous media; further details on the code are available in the user's manual. Simulations were conducted with the global implicit approach, which extends time steps as the system approaches steady state to improve computational efficiency.

A schematic overview of the model domain for PB-1 is provided in Figure 4.2. The packed bed was divided into 48 grid cells with dimensions of 0.5 mm on each side. A constant flux boundary was set at the inlet of the bed to allow for CO_2 diffusion with no-flux boundaries imposed on the sides and opposing end. The CO_2 diffusion coefficient was set to $7.5*10^{-9}$ m^2/s, as previously measured at 100°C.[38] CO_2 solubility was calculated directly in the code using the empirical approach established by Duan and Sun.[39] Because the exact initial porosity could not be resolved in the xCT scans, it was nominally set to 40% and updated in the code at each time step based on changes in mineral volume fractions. The model setup for PB-2 was identical except the length was shortened to 30 grid cells with dimensions of 0.2 mm on each side to match the length of the deeper packed beds.

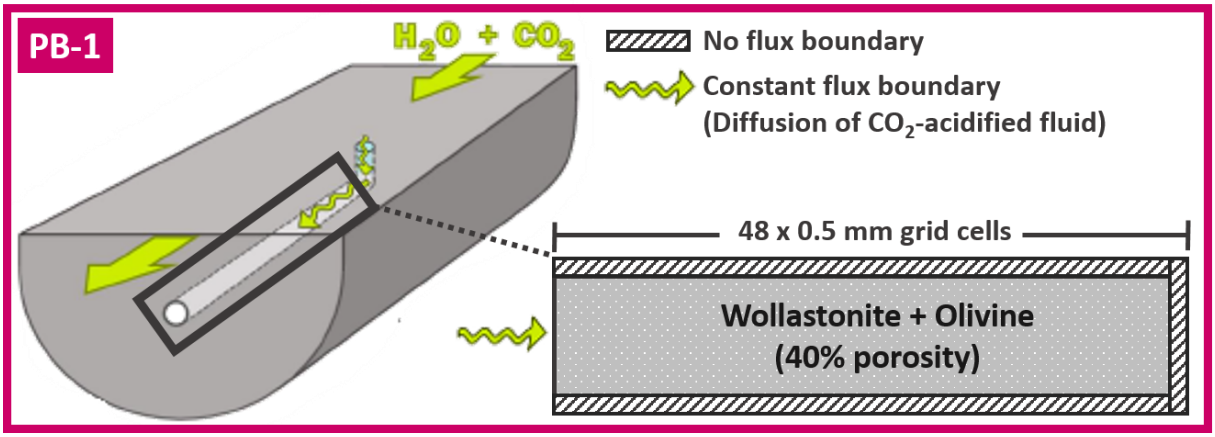

Figure 4.2. Conceptual 1D model domain for PB-1.

To mimic the packed bed compositions, the mineral fraction of each grid cell contained either 100% olivine (i.e., 60% of the total cell volume with 40% pore space) or 50% olivine and 50% wollastonite (i.e., each 30% of the total cell volume). Given the low amount of Fe in the olivine used in the packed beds and fact that no Fe-bearing reaction products were observed, all olivine was modeled as forsterite. Calcite, magnesite, antigorite (an Mg-based serpentine

mineral), and amorphous silica were included as potential secondary phases. All secondary minerals were assigned initial volume fractions of 0 and volume fraction thresholds of 10^{-5} to calculate bulk surface area until the threshold is exceeded, at which point precipitation begins and surface area is updated based on the actual volume fraction and user-defined specific surface area (SSA). BET surface areas reported in literature were used for secondary minerals, while initial geometric surface areas for each primary mineral were calculated based on representative grain sizes of 30 μm for wollastonite, 70 μm for fine-grained olivine, and 320 μm for coarse-grained olivine. Reaction rate parameters were taken from literature and equilibrium constants for aqueous reactions were taken from the EQ3/EQ6 thermodynamic database. Key model inputs are summarized in Table 4.2 below, where reaction rate constants at 100°C were calculated from the Arrhenius relationship using reported values for rates measured at 25°C and activation energy as detailed in prior work.[40]

Table 4.2. Summary of key mineral parameters for reactive transport modeling.

Mineral	SSA (m^2/g)	Acid mechanism		Neutral
		log k, 100°C ($mol/m^2/s$)	n^{H+}	log k, 100°C ($mol/m^2/s$)
Wollastonite	0.069	-3.44[41]	0.4[42]	-6.95[41]
Forsterite				
Fine-grained	0.026	-4.48[41]	0.47[41]	-7.86[41]
Coarse-grained	0.0057	-4.48[41]	0.47[41]	-7.86[41]
Calcite	0.037[43]	0.21[41]	1.0[41]	-4.98[41]
Magnesite	0.0662[43]	-5.87[41]	1.0[41]	-8.51[41]
Antigorite	0.06	-7.54[44]	0.45[44]	-10.1[45]
SiO_2(am)	0.0225[46]	--	--	-6.92[47]

4.3. Results and Discussion

4.3.1. Primary reactive silicates control secondary reaction products

Both experiments evidenced conversion of silicates to carbonates, where the composition of precipitates depended on that of the parent silicates. Despite an equal presence of olivine and wollastonite in PB-1, the resulting carbonates were predominantly $CaCO_3$, which formed as both calcite and aragonite (Figure 4.3). No magnesite was observed but Raman spectra did evidence occasional Mg-bearing $CaCO_3$. In reactive percolation experiments on sintered olivine cores, Peuble et al.[48] observed a similar lack of Mg-carbonates despite the fact that effluent fluids were supersaturated with respect to magnesite. They attributed preferential formation of Ca- and Fe-

carbonates to the fact that Mg^{2+} ions are much more hydrated than Ca^{2+} and Fe^{2+}, hindering their ability to form anhydrous Mg-carbonates.[48] The models developed here also predicted negligible ($<10^{-5}$ by volume fraction) magnesite would form in the mixed beds due to slow reaction kinetics relative to the experimental time frame and confirmed calcite was by far the most favorable secondary mineral in the mixed beds (Figure 4.5, section 4.3.3). Although the models also predict negligible $MgCO_3$ precipitation in the wollastonite-free beds in PB-2, magnesite did form during the experiment but to a lesser extent than $CaCO_3$ in the mixed olivine-wollastonite beds.

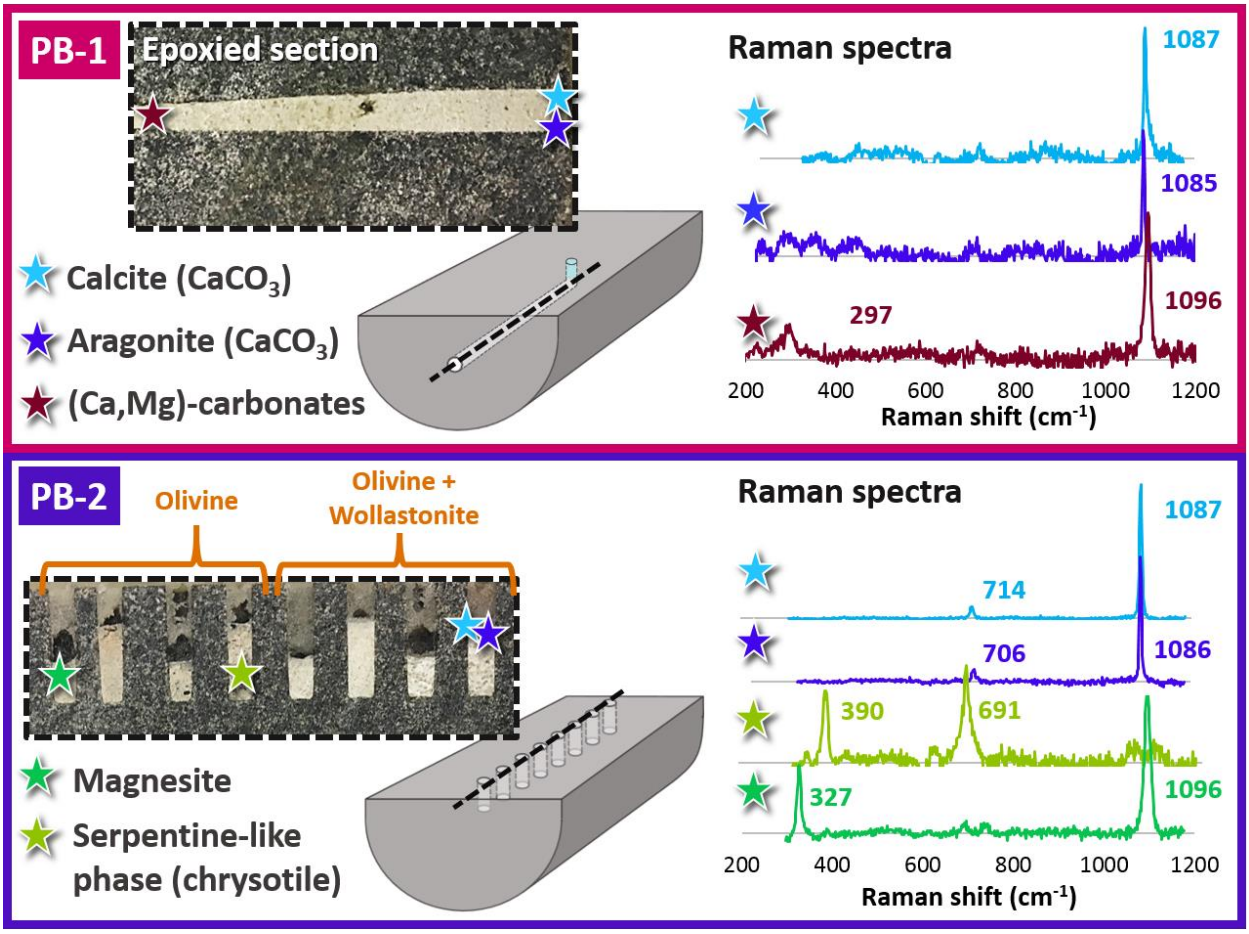

Figure 4.3. Example Raman spectra for reaction products that formed in the packed beds in PB-1 (top) and PB-2 (bottom). Images of the epoxied sections of the cores are included on the left for reference and select Raman spectra highlighting different hydration and carbonation products are presented on the right with annotated peaks.

The favorability of Ca- over Mg-carbonates indicates precipitation was the rate-limiting step in carbonation. The calculated dissolution rates for olivine and wollastonite differ by around an order of magnitude, while calcite precipitation kinetics are several orders of magnitude faster than magnesite. Prior work has also demonstrated that precipitation will be rate-limiting for forsterite

carbonation under relevant GCS conditions due to slow magnesite nucleation and growth kinetics. Giammar et al.[11] found that magnesite only formed in forsterite batch experiments once a critical saturation index (between 0.25 and 1.14 at 95°C) was achieved and precipitation was limited by slow nucleation rates. These combined factors could explain the absence of Mg in our tests; given that $CaCO_3$ typically forms much faster and at lower critical SI values, it would have been more thermodynamically favorable to incorporate Mg into Ca-carbonate structures rather than magnesite. While the reactive transport models only consider carbonate end members (e.g. $CaCO_3$, $MgCO_3$), the results support that Mg will accumulate in the system instead of trapping CO_2 as magnesite, allowing for potential uptake by other secondary phases.

Consistent with this predicted inclination of Mg to form non-carbonate secondary alteration products, olivine hydration products with Raman spectra and morphologies similar to chrysotile (a fibrous serpentine mineral, $Mg_3Si_2O_5(OH)_4$) were also observed in the pure-olivine beds of PB-2, whereas carbonates were the only reaction products in the mixed olivine/wollastonite beds. Example SEM images highlighting the unique fibrous morphologies of these reaction products are included in Section D3 of Appendix D (Figure D14). DTG curves for the pure olivine packed beds also evidenced the presence of hydration products, which decompose at perceptibly lower temperatures than carbonates (see Appendix D, section D1). These hydration products were found in the upper samples taken from the deeper packed beds while carbonates predominated in the lower halves, suggesting that the propensity of dissolved Mg to form hydrated or carbonated reaction products depends strongly on geochemical conditions. Carbonate precipitation typically requires higher pH levels (circum-neutral to basic), which would increase with increasing silicate dissolution as CO_2 diffused deeper into the packed beds, whereas Mg released near the packed bed inlets may have quickly reacted with infiltrating water to form hydrated phases that were more kinetically and thermodynamically favorable than Mg-carbonates. The reactive transport models also predict antigorite, an Mg-serpentine chemically equivalent to chrysotile, would form over magnesite under experimental conditions (Figure 4.5, Section 4.3.3). Peuble et al.[48] similarly found that Mg was preferentially incorporated into hydrous and amorphous phases that may have developed during olivine serpentinization due to destabilization of brucite ($Mg(OH)_2$). Preferential serpentinization of olivine would be detrimental to carbon mineralization efforts, as Mg is consumed in secondary phases that block pore spaces without trapping CO_2 and the resulting serpentine phases are inherently less reactive than unaltered olivine.

Silicate dissolution rates and mechanisms are strongly dependent on crystal structure. While wollastonite dissolves more rapidly than olivine, the complex silicate chains in the pyroxenoid structure result in preferential release of Ca^{2+} and leave thick leached silica layers that can become passivating.[19] In contrast, the isolated silicate tetrahedra in olivine dissolve more stoichiometrically and release silica into the aqueous phase.[49,50] This discrepancy may have contributed to the propensity of released Ca^{2+} to directly trap CO_2 in the form of $CaCO_3$, whereas Mg^{2+} was also incorporated into secondary Mg-silicate products. Although the experiments conducted here did not evidence any passivating or inhibitory effects, secondary amorphous silica phases are known to effectively armor silicate minerals against CO_2-driven dissolution and heterogeneous nucleation of carbonate precipitates.[23,51] Thus, rapid preferential Ca^{2+} leaching from Ca-rich pyroxenes may drive rapid initial carbonate precipitation (as evidenced over these 1-3 week experiments), but the residual leached silica layers may limit the reactivity of underlying minerals and slow carbonation rates over extended multi-year time frames associated with field-scale CO_2 injection.

4.3.2. Localized carbonation fronts

Combined DTG curves from each 4-mm increment along the packed bed in PB-1 are presented in Figure 4.4b. Data for the unreacted materials is also included, where the peak around 650-700°C represents impurities burning off. Sharp peaks in each of the reacted samples between ~600 and 800°C represent the loss of carbonate ions consistent with the temperature range where calcite decomposes.[35] The area under the DTG curve reflects the amount of carbonate loss and, by extension, amount of carbonate initially in the sample. Thus, the compiled curves indicate that the greatest extent of carbonation (58%) occurred in the center of the bed (8-12 mm depth) and decreased slightly near the inlet and end of the bed. Segmentation of the xCT scans taken after each experimental stage in PB-1 revealed that pore space was reduced after flow of CO_2-acidified fluids, which was concomitant with the conversion of wollastonite to calcite evidenced by TGA. This is illustrated in Figure 4.4d, where carbonation efficiency at each depth increment is plotted with changes in porosity between the pre-reaction scan and the post-reaction scans taken after the first (DI water) and second (0.64M $NaHCO_3$) flow-through stages (section 4.2.2). The localized maximum of the carbonation front indicated by these data sets is consistent with prior studies on packed beds of olivine and forsterite powders in static systems, which found carbonation was spatially localized where the opposing diffusion of dissolved CO_2 into and dissolved cations out of the system led to a localized region with a critical magnesite saturation index.[31,52]

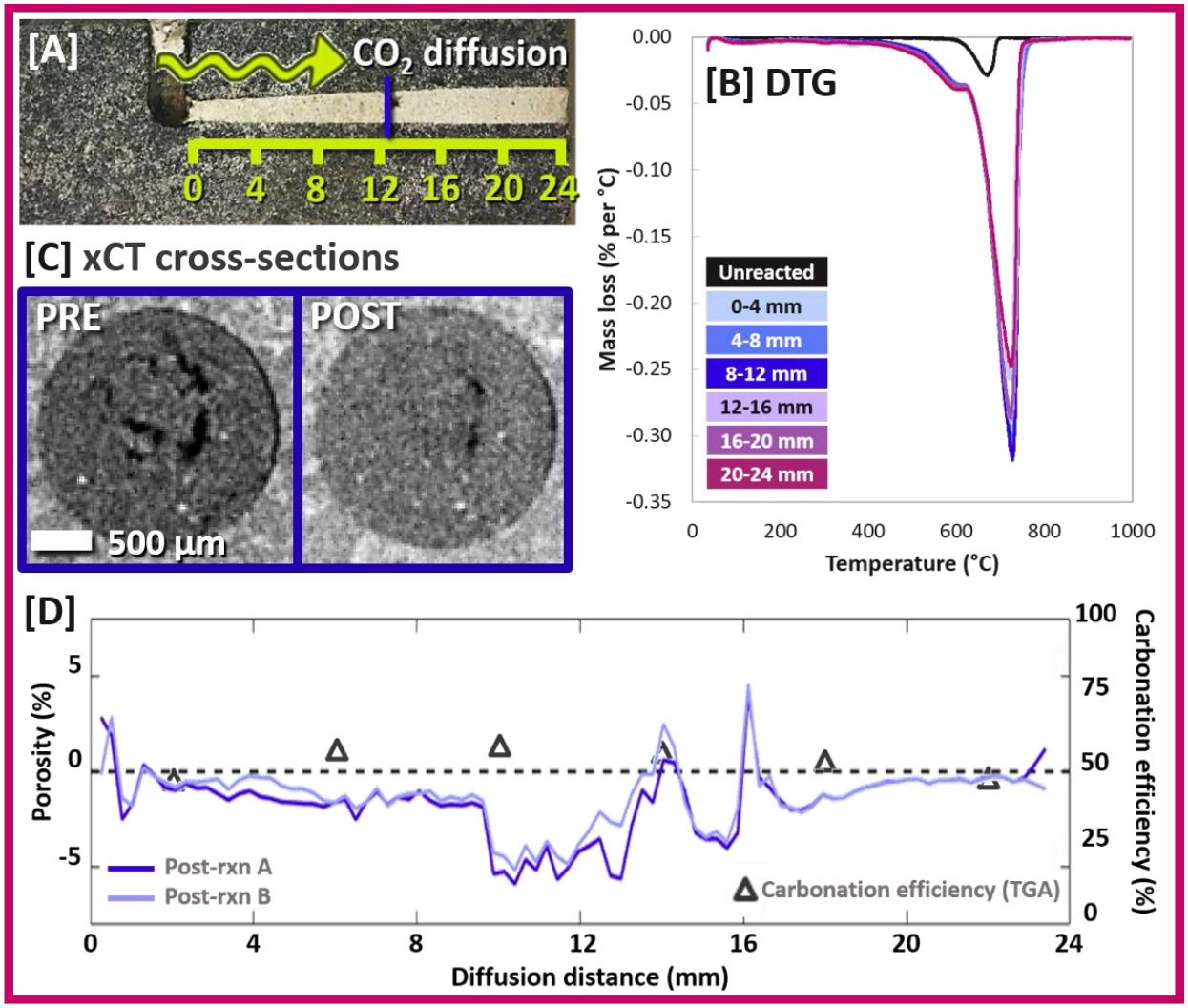

Figure 4.4. Summary of xCT and TGA results from PB-1. [A] The epoxied section cut from the reacted core illustrating where TGA samples were taken in 4-mm increments along the length of the packed bed. [B] Compiled DTG curves for samples taken at each increment in [A], where the difference between the areas under the peaks in the reacted and unreacted samples from ~450-800°C represent the amount of carbonates that formed during reaction. [C] Example pre- and post-reaction xCT cross-sections taken from the center of the packed bed as denoted in [A] revealing closure of pore space due to precipitation. [D] Combined xCT and TGA results. The pre- and post-reaction scans were segmented and the change in porosity was calculated as a function of diffusion distance along the packed bed (solid lines). Carbonation efficiency (estimated based on the DTG curves) is also presented as a function of diffusion distance.

Reactive transport models also predicted localized carbonation fronts would form in the packed beds, consistent with prior batch experiments and 1D modeling of carbonation in natural basalt fractures.[26] In PB-1, calcite volumes are predicted to reach a maximum a short distance into the bed and drop off around halfway (12 mm) in where CO_2 has not fully penetrated and thus wollastonite has not fully dissolved (Figure 4.5a). Forsterite dissolution occurs much more slowly than wollastonite, resulting in lesser amounts of secondary Mg precipitates (primarily antigorite) near the inlet. The results from the short mixed packed beds in PB-2 (Figures 4.5b and 4.5c) are similar with simulations predicting maximum calcite levels in the center of the bed. However, calcite that formed near the inlet at early time frames is predicted to re-dissolve and all wollastonite is dissolved by the end of the simulations because the influent contained no buffering agent (i.e., the experiments were conducted with pure CO_2-acidified water) and the low resulting pH (4-5) promoted dissolution over precipitation. The addition of 0.64 M $NaHCO_3$ in PB-1 creates stable elevated pH levels, allowing for secondary precipitation throughout the bed and preventing re-dissolution. Here, predicted carbonate re-dissolution is partially an artifact of the small model domain; in actual systems, reactive minerals would not be 'depleted' and continued dissolution of surrounding silicates would support favorable pH levels for carbonate precipitation and stability.

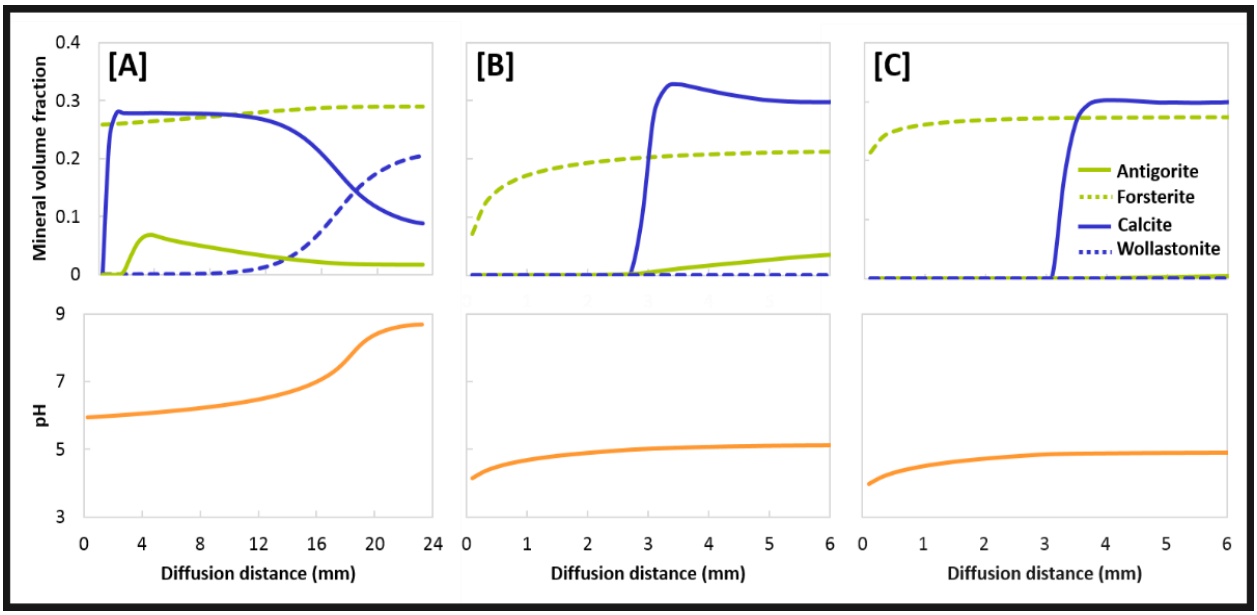

Figure 4.5. Select results from 1D reactive transport simulations for [A] the mixed packed bed in PB-1; [B] the mixed 'deep' beds with fine olivine in PB-2; and [C] the mixed 'deep' beds with coarse olivine in PB-2. The packed beds are exposed to CO_2 on the lefthand side of each plot such that the x-axis represents diffusion distance from the CO_2 source (refer to Figure 4.2 for a visualization of the model domain). The upper panels present model-predicted volume fractions of the key primary and secondary minerals as a function of diffusion distance at the end of the 8-day flow experiments, where dashed lines indicate primary (i.e. dissolving) minerals and solid lines represent secondary (i.e. precipitating) phases. The lower panels show the associated evolution of pH.

4.3.3. Impact of reactive surface area

The increase in reactive surface area associated with the fine-grained olivine used in half of the packed beds for PB-2 did not substantially impact carbonation. TGA results for each sample taken from the packed beds are summarized schematically in Figure 4.6, where the deeper beds were divided into upper and lower samples (except in the last bed, which lacked sufficient material for multiple tests) to evaluate the influence of diffusion distance on carbonation efficiency (Section 4.2.5). Note that full DTG curves for each TGA run along with the unreacted samples are included in Appendix D (Section D1). The calculations revealed no clear trends between olivine grain size and carbonation; while the average carbonation efficiency in the deeper packed beds increased from 8.5% in the pure coarse-grained olivine bed to 12.5% in the pure fine-grained olivine bed, it decreased from 40% in the mixed wollastonite/coarse-grained olivine bed to 30.5% in the mixed wollastonite/fine-grained olivine bed. In the shorter packed beds, there were no significant differences between fine- and coarse-grained olivine beds. This is consistent with the lack of Mg-carbonates observed in post-reaction analyses (Section 4.3.1). Because the extent of olivine reaction was limited while wollastonite carbonated rapidly, the reactive surface area of olivine had minimal bearing on overall carbonation, which was driven by calcite precipitation.

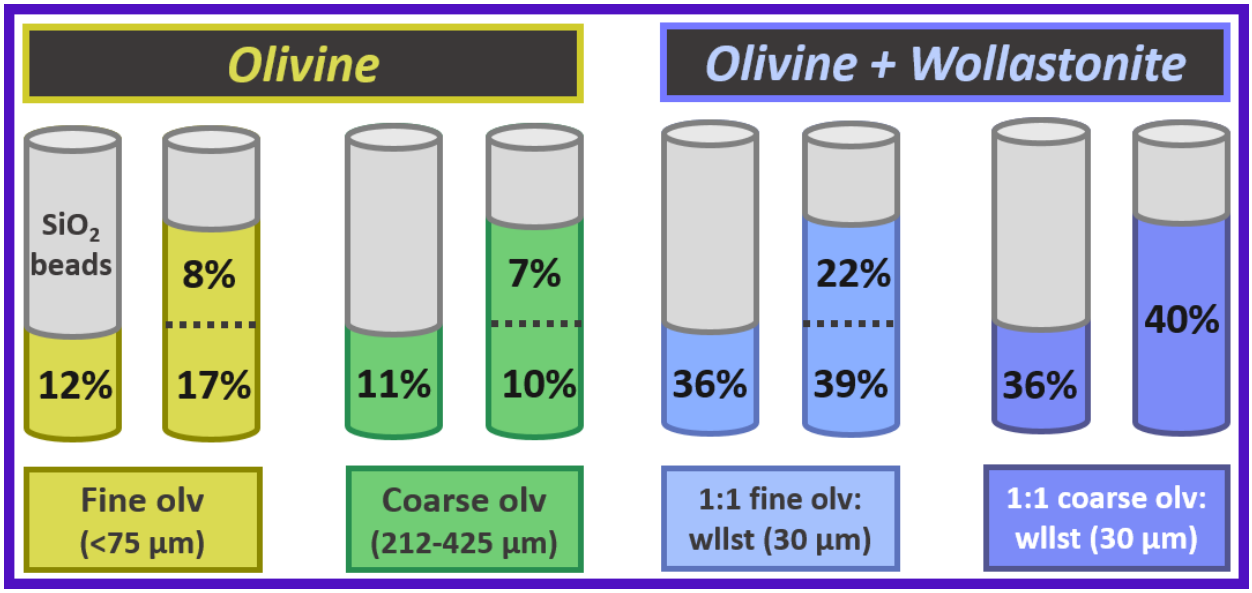

Figure 4.6. Schematic of TGA results from PB-2 summarizing the effects of diffusion depth, grain size, and reactive mineral composition on carbonation efficiency. The percentages reflect the fraction of the initial silicate minerals converted to carbonate minerals during the experiment based on DTG curves (see Appendix D, section D1). Deeper beds where sufficient material was available for analysis were divided into an upper and lower sample to evaluate the influence of diffusion depth, but the last 'deep' bed only contained enough material for one TGA run.

As evidenced by comparison of Figures 4.5b and 4.5c, the reactive transport models confirm that the higher reactive surface area associated with the fine-grained olivine has a limited bearing on the overall carbonation efficiency of the packed beds because negligible Mg-based carbonates formed and wollastonite conversion to calcite was the critical driver. However, the models predicted that olivine surface area would have a greater impact on carbonation efficiency than that suggested by the TGA results, as the predicted calcite volume in the simulated packed bed was 15% higher with fine-grained olivine compared to coarse-grained. Considering that olivine does not directly impact calcite precipitation, this result likely stems from the effect of specific surface area on forsterite reaction kinetics and corresponding impacts to pH levels in the packed beds. While wollastonite dissolved rapidly in PB-2 and was completely depleted by the end of both 8-day simulations, substantial fractions of forsterite remained at the end. Enhanced forsterite dissolution in the fine-grained test thus had a bearing on the overall system pH, which increased slightly from 4.9 (with coarse-grained olivine) to 5.1 (with fine-grained olivine) in the carbonated regions of the packed bed. This slight increase in buffering likely contributed to more favorable precipitation conditions in the fine-grained simulations and highlights the fact that reservoir-scale modeling efforts need to effectively incorporate geochemical reactions involving all basalt minerals, not just those releasing carbonate-forming divalent cations. While silicate minerals that do not directly contribute to carbonation may have ancillary positive benefits, such as buffering pH levels reduced by CO_2 injection, they can also inhibit carbonation if grains are mobilized through dissolution and/or preferential leaching and block pores or fractures downstream. Complex interactions among thermodynamic, aqueous equilibrium, and kinetic conditions will dictate the role of different mineral phases in long-term CO_2 transport and trapping.

As previously discussed, wollastonite drove overall carbonation efficiency because Mg-carbonates were kinetically limited and only Ca-carbonates formed, so the available olivine surface area marginally impacted total carbonation. The models predicted average calcite volume fractions of ~0.25 near the base of the packed beds in PB-2 (Figure 4.5b and 4.5c) compared to average magnesite volume fractions on the order of $10^{-8.5}$ (not shown). However, the models indicated that similarly varying the reactive surface area of wollastonite would not have substantial bearing on the extent of carbonation in the mixed packed beds. Figure D15 compares simulation results for the mixed beds with fine-grained wollastonite and coarse-grained olivine (Figure 4.5c) with an additional simulation where the specific surface area of wollastonite was reduced by an order of

magnitude. Whereas all wollastonite was dissolved by the end of the simulations with fine-grained wollastonite, 7% of the original wollastonite remained at the end of the coarse-grained wollastonite run. This decrease in wollastonite dissolution led to a corresponding 7% reduction in the volume of calcite that formed in the simulated coarse-grained bed. Because wollastonite carbonation proceeds so rapidly, calcite precipitation was transport-limited under these conditions such that increasing the surface reaction rates by increasing the reactive surface area had limited impact on the extent of carbonation reactions.

4.3.4. Impact of diffusion distance

One clear trend from the TGA results for PB-2 was the increase in carbonation efficiency with depth in the deeper packed beds (Figure 4.6). This is consistent with model predictions that carbonation is limited to the deeper regions of the beds where the pH is sufficiently high (~5) to both facilitate carbonate precipitation and prevent re-dissolution (Figure 4.5b and 4.5c). As noted in Section 4.3.1 and demonstrated by the DTG curves in Section D1 of Appendix D, the increase in carbonation with depth coincided with more hydrated Mg-silicate products located near the inlets of the deeper beds. Prior work similarly found that carbonate precipitation increased with diffusion distance into dead-end fractures, while non-carbonate secondary alteration products (e.g. clays and iron oxides) formed in more acidic advection-controlled flow paths.[28] Here, the discrepancy in predominant secondary minerals primarily results from opposing geochemical gradients where local pH levels and concentrations of dissolved cations and CO_2 create distinct zones promoting hydration (i.e. serpentinization) or carbonation. However, the extent to which olivine serpentinization competes with carbonation remains poorly understood. Targeted time-resolved studies are necessary to understand feedback among competing olivine alteration processes in CO_2-brine systems and identify conditions under which olivine hydration is more thermodynamically and/or kinetically favorable than carbonation.[53]

4.4. IMPLICATIONS FOR CO_2 MINERALIZATION

Despite up to 58% conversion of silicates to carbonates, no evidence of reaction-induced fracturing was observed in these tests as precipitates were accommodated by available pore space and simultaneous dissolution of the packed beds. In recent reactive percolation experiments on sintered olivine cores, Peuble et al.[48] similarly found that continuous olivine dissolution offset reductions in porosity due to magnesite and serpentine precipitation. While near-complete

carbonation with volume expansion could outpace dissolution over longer time frames, the rate of carbonate crystallization must also be extremely rapid (near-instantaneous) to induce fracturing before stress can be relieved by viscous deformation of precipitating phases.[7] Reactive cracking may be more favorable in narrow fractures and pores with limited space to accommodate the associated volume expansion, but low-porosity basalts will also have lower overall carbonation and CO_2 trapping potential. Achieving the high rate and extent of carbonation required to propagate new fractures may be extremely rare under relevant GCS conditions. Furthermore, even where reactive cracking is favorable, it may have limited ability to drive self-sustaining carbonation reactions along with a marginal impact on long-term CO_2 mineralization capacity. This study, combined with a lack of consensus in the literature on whether carbonation leads to positive or negative feedback under GCS conditions, emphasizes that both the occurrence and long-term implications of reactive cracking remain poorly understood in the context of engineered CO_2 sequestration systems. While reactive cracking has been well-characterized in more reactive and simplistic analog systems, additional work on natural basalts is necessary to constrain conditions under which fracture propagation is feasible and the extent to which this mechanism could benefit CO_2 mineralization efforts.

REFERENCES

(1) McGrail, B. P.; Schaef, H. T.; Ho, A. M.; Chien, Y.-J.; Dooley, J. J.; Davidson, C. L. Potential for Carbon Dioxide Sequestration in Flood Basalts: SEQUESTRATION IN FLOOD BASALTS. *J. Geophys. Res. Solid Earth* **2006**, *111* (B12), n/a-n/a. https://doi.org/10.1029/2005JB004169.

(2) Kelemen, P. B.; Matter, J. In Situ Carbonation of Peridotite for CO2 Storage. *Proc. Natl. Acad. Sci.* **2008**, *105* (45), 17295–17300.

(3) Matter, J. M.; Kelemen, P. B. Permanent Storage of Carbon Dioxide in Geological Reservoirs by Mineral Carbonation. *Nat. Geosci.* **2009**, *2* (12), 837–841. https://doi.org/10.1038/ngeo683.

(4) McGrail, B. P.; Schaef, H. T.; Spane, F. A.; Cliff, J. B.; Qafoku, O.; Horner, J. A.; Thompson, C. J.; Owen, A. T.; Sullivan, C. E. Field Validation of Supercritical CO_2 Reactivity with Basalts. *Environ. Sci. Technol. Lett.* **2017**, *4* (1), 6–10. https://doi.org/10.1021/acs.estlett.6b00387.

(5) Matter, J. M.; Stute, M.; Snaebjornsdottir, S. O.; Oelkers, E. H.; Gislason, S. R.; Aradottir, E. S.; Sigfusson, B.; Gunnarsson, I.; Sigurdardottir, H.; Gunnlaugsson, E.; Axelsson, G.; Alfredsson, H. A.; Wolff-Boenisch, D.; Mesfin, K.; Taya, D. F. d. l. R.; Hall, J.; Dideriksen, K.; Broecker, W. S. Rapid Carbon Mineralization for Permanent Disposal of Anthropogenic Carbon Dioxide Emissions. *Science* **2016**, *352* (6291), 1312–1314. https://doi.org/10.1126/science.aad8132.

(6) National Academies of Sciences, Engineering, and Medicine. *Negative Emissions Technologies and Reliable Sequestration: A Research Agenda*; National Academies Press: Washington, D.C., 2019. https://doi.org/10.17226/25259.

(7) Kelemen, P. B.; Matter, J.; Streit, E. E.; Rudge, J. F.; Curry, W. B.; Blusztajn, J. Rates and Mechanisms of Mineral Carbonation in Peridotite: Natural Processes and Recipes for Enhanced, in Situ CO_2 Capture and Storage. *Annu. Rev. Earth Planet. Sci.* **2011**, *39* (1), 545–576. https://doi.org/10.1146/annurev-earth-092010-152509.

(8) Wells, R. K.; Xiong, W.; Giammar, D.; Skemer, P. Dissolution and Surface Roughening of Columbia River Flood Basalt at Geologic Carbon Sequestration Conditions. *Chem. Geol.* **2017**, *467*, 100–109. https://doi.org/10.1016/j.chemgeo.2017.07.028.

(9) Olsson, J.; Bovet, N.; Makovicky, E.; Bechgaard, K.; Balogh, Z.; Stipp, S. L. S. Olivine Reactivity with CO2 and H2O on a Microscale: Implications for Carbon Sequestration. *Geochim. Cosmochim. Acta* **2012**, *77*, 86–97. https://doi.org/10.1016/j.gca.2011.11.001.

(10) Béarat, H.; McKelvy, M. J.; Chizmeshya, A. V. G.; Gormley, D.; Nunez, R.; Carpenter, R. W.; Squires, K.; Wolf, G. H. Carbon Sequestration via Aqueous Olivine Mineral Carbonation: Role of Passivating Layer Formation. *Environ. Sci. Technol.* **2006**, *40* (15), 4802–4808. https://doi.org/10.1021/es0523340.

(11) Giammar, D. E.; Bruant, R. G.; Peters, C. A. Forsterite Dissolution and Magnesite Precipitation at Conditions Relevant for Deep Saline Aquifer Storage and Sequestration of Carbon Dioxide. *Chem. Geol.* **2005**, *217* (3–4), 257–276. https://doi.org/10.1016/j.chemgeo.2004.12.013.

(12) Prigiobbe, V.; Costa, G.; Baciocchi, R.; Hänchen, M.; Mazzotti, M. The Effect of CO2 and Salinity on Olivine Dissolution Kinetics at 120C. *Chem. Eng. Sci.* **2009**, *64* (15), 3510–3515. https://doi.org/10.1016/j.ces.2009.04.035.

(13) Qafoku, O.; Kovarik, L.; Kukkadapu, R. K.; Ilton, E. S.; Arey, B. W.; Tucek, J.; Felmy, A. R. Fayalite Dissolution and Siderite Formation in Water-Saturated Supercritical CO2. *Chem. Geol.* **2012**, *332–333*, 124–135. https://doi.org/10.1016/j.chemgeo.2012.09.028.

(14) Wang, F.; Giammar, D. E. Forsterite Dissolution in Saline Water at Elevated Temperature and High CO_2 Pressure. *Environ. Sci. Technol.* **2013**, *47* (1), 168–173. https://doi.org/10.1021/es301231n.

(15) O'Connor, W. K.; Dahlin, D. C.; Rush, G. E.; Gerdemann, S. J.; Nilsen, D. N. Aqueous Mineral Carbonation. *Final Rep. DOEARC-TR-04* **2005**, *2*.

(16) Chizmeshya, A. V.; McKelvy, M. J.; Squires, K.; Carpenter, R. W.; Béarat, H. *A Novel Approach to Mineral Carbonation: Enhancing Carbonation While Avoiding Mineral Pretreatment Process Cost*; Arizona State University, 2006.

(17) Kelemen, P. B.; Hirth, G. Reaction-Driven Cracking during Retrograde Metamorphism: Olivine Hydration and Carbonation. *Earth Planet. Sci. Lett.* **2012**, *345–348*, 81–89. https://doi.org/10.1016/j.epsl.2012.06.018.

(18) Gadikota, G.; Matter, J.; Kelemen, P.; Park, A. A. Chemical and Morphological Changes during Olivine Carbonation for CO2 Storage in the Presence of NaCl and NaHCO3. *Phys. Chem. Chem. Phys.* **2014**, *16* (10), 4679. https://doi.org/10.1039/c3cp54903h.

(19) Daval, D.; Martinez, I.; Corvisier, J.; Findling, N.; Goffé, B.; Guyot, F. Carbonation of Ca-Bearing Silicates, the Case of Wollastonite: Experimental Investigations and Kinetic Modeling. *Chem. Geol.* **2009**, *265* (1–2), 63–78. https://doi.org/10.1016/j.chemgeo.2009.01.022.

(20) Tai, C. Y.; Chen, W.-R.; Shih, S.-M. Factors Affecting Wollastonite Carbonation under CO2 Supercritical Conditions. *AIChE J.* **2006**, *52* (1), 292–299. https://doi.org/10.1002/aic.10572.

(21) Min, Y.; Li, Q.; Voltolini, M.; Kneafsey, T.; Jun, Y.-S. Wollastonite Carbonation in Water-Bearing Supercritical CO $_2$: Effects of Particle Size. *Environ. Sci. Technol.* **2017**, *51* (21), 13044–13053. https://doi.org/10.1021/acs.est.7b04475.

(22) Min, Y.; Jun, Y.-S. Wollastonite Carbonation in Water-Bearing Supercritical CO2: Effects of Water Saturation Conditions, Temperature, and Pressure. *Chem. Geol.* **2018**, *483*, 239–246. https://doi.org/10.1016/j.chemgeo.2018.01.012.

(23) Daval, D.; Sissmann, O.; Menguy, N.; Saldi, G. D.; Guyot, F.; Martinez, I.; Corvisier, J.; Garcia, B.; Machouk, I.; Knauss, K. G.; Hellmann, R. Influence of Amorphous Silica Layer Formation on the Dissolution Rate of Olivine at 90°C and Elevated PCO_2. *Chem. Geol.* **2011**, *284* (1–2), 193–209. https://doi.org/10.1016/j.chemgeo.2011.02.021.

(24) Schaef, H. T.; McGrail, B. P. Dissolution of Columbia River Basalt under Mildly Acidic Conditions as a Function of Temperature: Experimental Results Relevant to the Geological Sequestration of Carbon Dioxide. *Appl. Geochem.* **2009**, *24* (5), 980–987. https://doi.org/10.1016/j.apgeochem.2009.02.025.

(25) Matter, J. M.; Takahashi, T.; Goldberg, D. Experimental Evaluation of in Situ CO $_2$ -Water-Rock Reactions during CO_2 Injection in Basaltic Rocks: Implications for Geological CO_2 Sequestration. *Geochem. Geophys. Geosystems* **2007**, *8* (2), n/a-n/a. https://doi.org/10.1029/2006GC001427.

(26) Xiong, W.; Wells, R. K.; Menefee, A. H.; Skemer, P.; Ellis, B. R.; Giammar, D. E. CO_2 Mineral Trapping in Fractured Basalt. *Int. J. Greenh. Gas Control* **2017**, *66*, 204–217.

(27) Peuble, S.; Godard, M.; Luquot, L.; Andreani, M.; Martinez, I.; Gouze, P. CO_2 Geological Storage in Olivine Rich Basaltic Aquifers: New Insights from Reactive-Percolation Experiments. *Appl. Geochem.* **2015**, *52*, 174–190. https://doi.org/10.1016/j.apgeochem.2014.11.024.

(28) Menefee, A. H.; Giammar, D. E.; Ellis, B. R. Permanent CO_2 Trapping through Localized and Chemical Gradient-Driven Basalt Carbonation. *Environ. Sci. Technol.* **2018**, *52* (15), 8954–8964. https://doi.org/10.1021/acs.est.8b01814.

(29) Emmanuel, S.; Berkowitz, B. Effects of Pore-Size Controlled Solubility on Reactive Transport in Heterogeneous Rock. *Geophys. Res. Lett.* **2007**, *34* (6). https://doi.org/10.1029/2006GL028962.

(30) Zhu, W.; Fusseis, F.; Lisabeth, H.; Xing, T.; Xiao, X.; De Andrade, V.; Karato, S. Experimental Evidence of Reaction-Induced Fracturing during Olivine Carbonation: Fracturing During Olivine Carbonation. *Geophys. Res. Lett.* **2016**, *43* (18), 9535–9543. https://doi.org/10.1002/2016GL070834.

(31) Xiong, W.; Giammar, D. Forsterite Carbonation in Zones with Transport Limited by Diffusion. *Environ. Sci. Technol. Lett.* **2014**, *1* (8), 333–338. https://doi.org/10.1021/ez500182s.

(32) Schindelin, J.; Arganda-Carreras, I.; Frise, E.; Kaynig, V.; Longair, M.; Pietzsch, T.; Preibisch, S.; Rueden, C.; Saalfeld, S.; Schmid, B.; Tinevez, J.-Y.; White, D. J.; Hartenstein, V.; Eliceiri, K.; Tomancak, P.; Cardona, A. Fiji: An Open-Source Platform for Biological-Image Analysis. *Nat. Methods* **2012**, *9* (7), 676–682. https://doi.org/10.1038/nmeth.2019.

(33) Sommer, C.; Straehle, C.; Koethe, U.; Hamprecht, F. A. Ilastik: Interactive Learning and Segmentation Toolkit. In *Biomedical Imaging: From Nano to Macro, 2011 IEEE International Symposium on*; IEEE, 2011; pp 230–233.

(34) The Power of Databases: The RRUFF Project. In *Highlights in mineralogical crystallography*; Armbruster, T., Danisi, R. M., Eds.; Walter de Gruyter GmbH: Berlin ; Boston, 2016; pp 1–30.

(35) Frost, R. L.; Hales, M. C.; Martens, W. N. Thermogravimetric Analysis of Selected Group (II) Carbonateminerals—Implication for the Geosequestration of Greenhouse Gases. *J. Therm. Anal. Calorim.* **2009**, *95* (3), 999.

(36) Zhang, D.; Li, V. C.; Ellis, B. R. Optimal Pre-Hydration Age for CO_2 Sequestration through Portland Cement Carbonation. *ACS Sustain. Chem. Eng.* **2018**, *6* (12), 15976–15981. https://doi.org/10.1021/acssuschemeng.8b03699.

(37) Steefel, C. I.; Appelo, C. A. J.; Arora, B.; Jacques, D.; Kalbacher, T.; Kolditz, O.; Lagneau, V.; Lichtner, P. C.; Mayer, K. U.; Meeussen, J. C. L.; Molins, S.; Moulton, D.; Shao, H.; Šimůnek, J.; Spycher, N.; Yabusaki, S. B.; Yeh, G. T. Reactive Transport Codes for Subsurface Environmental Simulation. *Comput. Geosci.* **2015**, *19* (3), 445–478. https://doi.org/10.1007/s10596-014-9443-x.

(38) Cadogan, S. P.; Maitland, G. C.; Trusler, J. P. M. Diffusion Coefficients of CO_2 and N_2 in Water at Temperatures between 298.15 K and 423.15 K at Pressures up to 45 MPa. *J. Chem. Eng. Data* **2014**, *59* (2), 519–525. https://doi.org/10.1021/je401008s.

(39) Duan, Z.; Sun, R. An Improved Model Calculating CO_2 Solubility in Pure Water and Aqueous NaCl Solutions from 273 to 533 K and from 0 to 2000 Bar. *Chem. Geol.* **2003**, *193*, 257–271.

(40) Menefee, A. H.; Li, P.; Giammar, D. E.; Ellis, B. R. Roles of Transport Limitations and Mineral Heterogeneity in Carbonation of Fractured Basalts. *Environ. Sci. Technol.* **2017**, *51* (16), 9352–9362. https://doi.org/10.1021/acs.est.7b00326.

(41) Palandri, J. L.; Kharaka, Y. K. *A Compilation of Rate Parameters of Water-Mineral Interaction Kinetics for Application to Geochemical Modeling*; DTIC Document, 2004.

(42) Rimstidt, J. D.; Dove, P. M. Mineral/Solution Reaction Rates in a Mixed Flow Reactor: Wollastonite Hydrolysis. *Geochim. Cosmochim. Acta* **1986**, *50* (11), 2509–2516.

(43) Pokrovsky, O. S.; Golubev, S. V.; Schott, J. Dissolution Kinetics of Calcite, Dolomite and Magnesite at 25 °C and 0 to 50 Atm PCO_2. *Chem. Geol.* **2005**, *217* (3–4), 239–255. https://doi.org/10.1016/j.chemgeo.2004.12.012.

(44) Teir, S.; Revitzer, H.; Eloneva, S.; Fogelholm, C.-J.; Zevenhoven, R. Dissolution of Natural Serpentinite in Mineral and Organic Acids. *Int. J. Miner. Process.* **2007**, *83* (1–2), 36–46. https://doi.org/10.1016/j.minpro.2007.04.001.

(45) Orlando, A.; Borrini, D.; Marini, L. Dissolution and Carbonation of a Serpentinite: Inferences from Acid Attack and High P–T Experiments Performed in Aqueous Solutions at Variable Salinity. *Appl. Geochem.* **2011**, *26* (8), 1569–1583. https://doi.org/10.1016/j.apgeochem.2011.06.023.

(46) Tester, J. W.; Worley, W. G.; Robinson, B. A.; Grigsby, C. O.; Feerer, J. L. Correlating Quartz Dissolution Kinetics in Pure Water from 25 to 625C. *Geochem. Cosmochim. Acta* **1994**, *58* (11), 2407–2420.

(47) Carroll, S. A.; McNab, W. W.; Dai, Z.; Torres, S. C. Reactivity of Mount Simon Sandstone and the Eau Claire Shale under CO_2 Storage Conditions. *Environ. Sci. Technol.* **2013**, *47* (1), 252–261. https://doi.org/10.1021/es301269k.

(48) Peuble, S.; Godard, M.; Gouze, P.; Leprovost, R.; Martinez, I.; Shilobreeva, S. Control of CO2 on Flow and Reaction Paths in Olivine-Dominated Basements: An Experimental Study. *Geochim. Cosmochim. Acta* **2019**, *252*, 16–38. https://doi.org/10.1016/j.gca.2019.02.007.

(49) Sanna, A.; Lacinska, A.; Styles, M.; Maroto-Valer, M. M. Silicate Rock Dissolution by Ammonium Bisulphate for PH Swing Mineral CO2 Sequestration. *Fuel Process. Technol.* **2014**, *120*, 128–135. https://doi.org/10.1016/j.fuproc.2013.12.012.

(50) Oelkers, E. H.; Declercq, J.; Saldi, G. D.; Gislason, S. R.; Schott, J. Olivine Dissolution Rates: A Critical Review. *Chem. Geol.* **2018**, *500*, 1–19. https://doi.org/10.1016/j.chemgeo.2018.10.008.

(51) Béarat, H.; McKelvy, M. J.; Chizmeshya, A. V. G.; Gormley, D.; Nunez, R.; Carpenter, R. W.; Squires, K.; Wolf, G. H. Carbon Sequestration via Aqueous Olivine Mineral Carbonation: Role of Passivating Layer Formation. *Environ. Sci. Technol.* **2006**, *40* (15), 4802–4808. https://doi.org/10.1021/es0523340.

(52) Xiong, W.; Wells, R. K.; Giammar, D. E. Carbon Sequestration in Olivine and Basalt Powder Packed Beds. *Environ. Sci. Technol.* **2017**, *51* (4), 2105–2112. https://doi.org/10.1021/acs.est.6b05011.

(53) Miller, Q. R. S.; Schaef, H. T.; Kaszuba, J. P.; Gadikota, G.; McGrail, B. P.; Rosso, K. M. Quantitative Review of Olivine Carbonation Kinetics: Reactivity Trends, Mechanistic Insights, and Research Frontiers. *Environ. Sci. Technol. Lett.* **2019**, *6* (8), 431–442.

CHAPTER 5

Rapid Mineral Precipitation During Shear Fracturing of Carbonate-Rich Shales

5.1. BACKGROUND AND MOTIVATION

The subsurface currently provides roughly 80% of national energy demands and is primed to play a critical role in the development of low-carbon energy systems and the mitigation of climate change.[1] Target reservoirs for emerging technologies, such as enhanced geothermal systems, CO_2-enhanced shale oil recovery, and caprocks for geologic carbon storage, are typically characterized by low permeability and rely heavily on creating or restricting fluid transport through natural and induced fractures. However, our fundamental understanding of how fractures respond to reactive fluid injection under relevant subsurface conditions remains limited, particularly with respect to feedback among geochemical and geomechanical alterations.[2,3] Chemical reactions, namely dissolution of primary minerals and precipitation of secondary minerals from interactions between pore fluids and the host rock, can critically alter fracture permeability and mechanical stability.[2] Intuitively, permeability increases under advection-dominated flow due to free surface mineral dissolution and reaction front instabilities (i.e. wormholing)[4,5] and decreases when secondary precipitates fill pores and fractures, which typically requires longer fluid residence times with diffusion-dominated flow. However, dissolution and compaction of critical asperities (i.e. contact points between fracture surfaces) can lead to permeability reductions despite net dissolution and increased porosity,[3,6,7] which precipitates could counteract by serving as proppants between fracture walls or by generating sufficient crystallization stress to induce tensile fracturing in the surrounding rock.[8,9] The mechanical implications of chemical alterations are further complicated by heterogeneities in composition and structure, as preferential dissolution of more reactive minerals creates porous non-reactive layers that inhibit further reactions along the fracture surface.[10] Improved knowledge of which fracture alteration mechanisms will predominate in a reactive geological system is imperative to predicting permeability evolution at reservoir scales, but to date few experimental studies have explored the dynamics of competing geochemically mediated deformation processes.

While the impacts of mineral dissolution on fracture alteration and fluid transport have been well-documented,[2,5,11,12] precipitation remains relatively enigmatic due in part to inherent difficulties in creating favorable conditions in the lab. Even though the necessary thermodynamic and kinetic conditions are well understood, precipitates often fail to precipitate or otherwise form non-uniformly in relatively uniform environments due to complex interactions among contributing factors that are difficult to resolve or anticipate. For example, Emmanuel and Berkowitz[13] demonstrated through numerical modeling that mixing-induced precipitation can clog some high-porosity regions while others remain unaltered despite conditions appearing equivalent. Precipitation is controlled by a range of chemical and structural factors including mineralogy; pore and grain size distributions; fluid chemistry; and reaction kinetics of the dissolving and precipitating phases. Dissolution-precipitation kinetics are particularly challenging to predict at local scales because rates depend strongly on specific surface area, which evolves nonlinearly with changing porosity[13] and remains poorly constrained in numerical modeling. Furthermore, heterogeneities in all of these parameters can promote strongly localized precipitation that might be overlooked in high-level reservoir simulations but can significantly alter bulk fluid transport if precipitates form along critical flow paths. For instance, during flow through a fractured cement core, Huerta et al.[14] observed that heterogeneous aperture distributions led to fast non-uniform precipitation near the inlet and subsequent flow diversion and channelization. Even spatially uniform precipitates can lead to non-uniform transport alterations as narrow fractures and pore throats may be preferentially sealed.[15]

Precipitates reduce overall porosity but have diverse effects on permeability and pore size distributions. While precipitation generally favors smaller pores with higher reactive surface area, Emmanuel et al.[16] found that precipitation was suppressed in pores less than 10 μm as interfacial energy effects led to increased solubility. In basalt carbonation experiments, Luhmann et al.[17] also observed preferential precipitation in larger pores while the volume of smaller pores and overall specific surface area increased due to dissolution. Even when changes in porosity are constrained, implications for permeability are complex. Noiriel et al.[18] reported that permeability alterations resulting from calcite precipitation in porous columns containing mixtures of glass beads and crushed $CaCO_3$ depended strongly on changes in pore roughness in addition to pore volume; in two columns that experienced comparable decreases in overall porosity, one experienced a greater increase in pore roughness that led to more heterogeneous flow fields and greater reductions in

permeability. The location of precipitates is also significant because pore networks tend to converge and diverge erratically such that even a slight change in overall porosity can substantially impact permeability.[19] For instance, an earlier study by Noiriel et al.[20] reported that dissolution increased the permeability of a limestone core by an order of magnitude while porosity remained nearly constant. Porosity-permeability relationships in a given system cannot be effectively predicted with any single geochemical variable[21] and are highly contingent on the spatial distribution of geochemical reactions, particularly when precipitation is involved.[15] In CO_2 percolation experiments on sintered olivine cores, Peuble et al.[22] reported substantial permeability reductions despite relatively insignificant reductions in overall porosity, which they primarily attributed to localized precipitation that obstructed transport in primary flow paths. Hysteresis effects also complicate modeling efforts, as dissolution-driven permeability increases have been shown to proceed much faster than precipitation-driven permeability reductions.[21] Overall, contradictions among previous results emphasize the challenges associated with accurately predicting how precipitation will affect long-term fracture permeability given the complexity and uncertainty of interactions between geochemical and geomechanical alterations.

In light of the relative dearth of research surrounding the timing, extent, and significance of mineral precipitation in subsurface systems, the objective of this work was to determine how geochemical reactions impact fracture permeability and microstructure with a targeted focus on the role of secondary precipitates. While most precipitation studies have concentrated on the mixing of incompatible fluids to force precipitation from supersaturated fluids,[13,23–25] we explicitly focused on reactions between the injected fluid and host rock. Following preliminary testing to evaluate the reactivity of different rock and fluid compositions, a series of triaxial direct shear experiments was conducted on carbonate-rich shales using $BaCl_2$-rich solutions as the working fluid. Experiments were carried out within an x-ray computed tomography (xCT) scanner, allowing for non-destructive 4D imaging of *in situ* reactions under representative subsurface stress conditions.[26] Computed tomography has been applied extensively in studies of flow through porous media, most frequently under ambient unstressed conditions due to inherent challenges in designing and building experimental systems with x-ray compatibility.[27] Frash et al.[28] were the first to combine *in situ* xCT with direct shear fracturing and permeability measurements under high confining stress, which allows for direct characterization of stress-dependent fractures and avoids damage during stress cycling. Here, the experimental system was designed to create

favorable geochemical conditions for mineral precipitation and to optimize the likelihood of observing precipitate evolution in real time. Disequilibrium in pore fluids following $BaCl_2$ injection drives calcite ($CaCO_3$) dissolution in the host rock, releasing carbonate ions to solution that can then combine with Ba^{2+} to form barium carbonates ($BaCO_3$) when critical saturation levels are achieved and nucleation becomes favorable. The fast dissolution and precipitation rates of $CaCO_3$ and $BaCO_3$, respectively, were expected to promote these reactions over experimentally relevant time scales. Note that barium carbonates are rare in natural systems but were selected here to provide effective x-ray contrast between the host rock and secondary mineral phase, as $BaCO_3$ is roughly 1.6 times denser than $CaCO_3$ and has exhibited strong xCT visibility in prior work.[29] The conversion of $CaCO_3$ to $BaCO_3$ also involves a 27% increase in solid volume, which could compete with dissolution or compaction mechanisms for control on overall permeability.

5.2. Experimental Design and Data Analysis

This section presents precursory results motivating the design of the three experiments presented here as well as general methodology and details on the system setup for all shear tests, which were conducted at Los Alamos National Lab. Section 5.2.1 summarizes key results from preliminary batch experiments that informed our selections of core samples and injected fluid chemistry, which are detailed in Section 5.2.2. Section 5.2.3 provides an overview of the triaxial system setup, including sample assembly, data collection, and x-ray imaging. Further details on x-ray radiography and scan optimization along with techniques for xCT data processing and post-reaction sample characterization are provided in Section 5.2.4.

5.2.1. Preliminary reactivity testing

Initial batch experiments were conducted to determine the relative reactivity of various carbonate-rich materials. Marble and limestone cores (>99% calcite) were obtained from Kocurek Industries and carbonate-rich shales were provided by Chesapeake Energy Corporation and the National Energy Technology Laboratory. Chips saw-cut from cores of each rock were reacted in solutions of 20, 2,000, and 180,000 ppm $BaCl_2$ for 12 hours under ambient conditions. One half of each chip surface was lightly roughened prior to reaction to simultaneously evaluate the potential impact of freshly activated surfaces. The reacted chips were characterized via scanning electron microscopy (SEM) with back-scattered electron imaging (BSE) and energy-dispersive x-ray spectroscopy (EDS). Minimal reaction products were observed at 20 ppm $BaCl_2$ but barium

carbonates formed at 2,000 and 180,000 ppm, with the extent of precipitation greatest at 180,000 ppm. Precipitate morphologies varied from fine needles to more prismatic crystals depending on the substrate material (Figure 5.1) and generally aggregated in larger masses that often coated $CaCO_3$ surfaces in the shale and marble chips, but most limestone samples contained only a few isolated $BaCO_3$ crystals (not shown) or sparse clusters of finer precipitates (Figure 5.1d). Reasons for this discrepancy are unclear considering that the marble and limestone samples were compositionally equivalent and limestone should theoretically dissolve more readily because the porosity and permeability are greater. In general, precipitates also exhibited a preference for freshly roughened over weathered surfaces, suggesting that freshly sheared fractures with abundant reactive surface area would be more conducive to precipitation than saw-cut or pre-fractured samples. This observation motivated the application of triaxial shear tests in this work as opposed to traditional flow-through experiments examining dissolution-precipitation reactions in whole or pre-cut cores. Note that additional documentation of experiments preceding those presented in this chapter is provided in Appendix E.

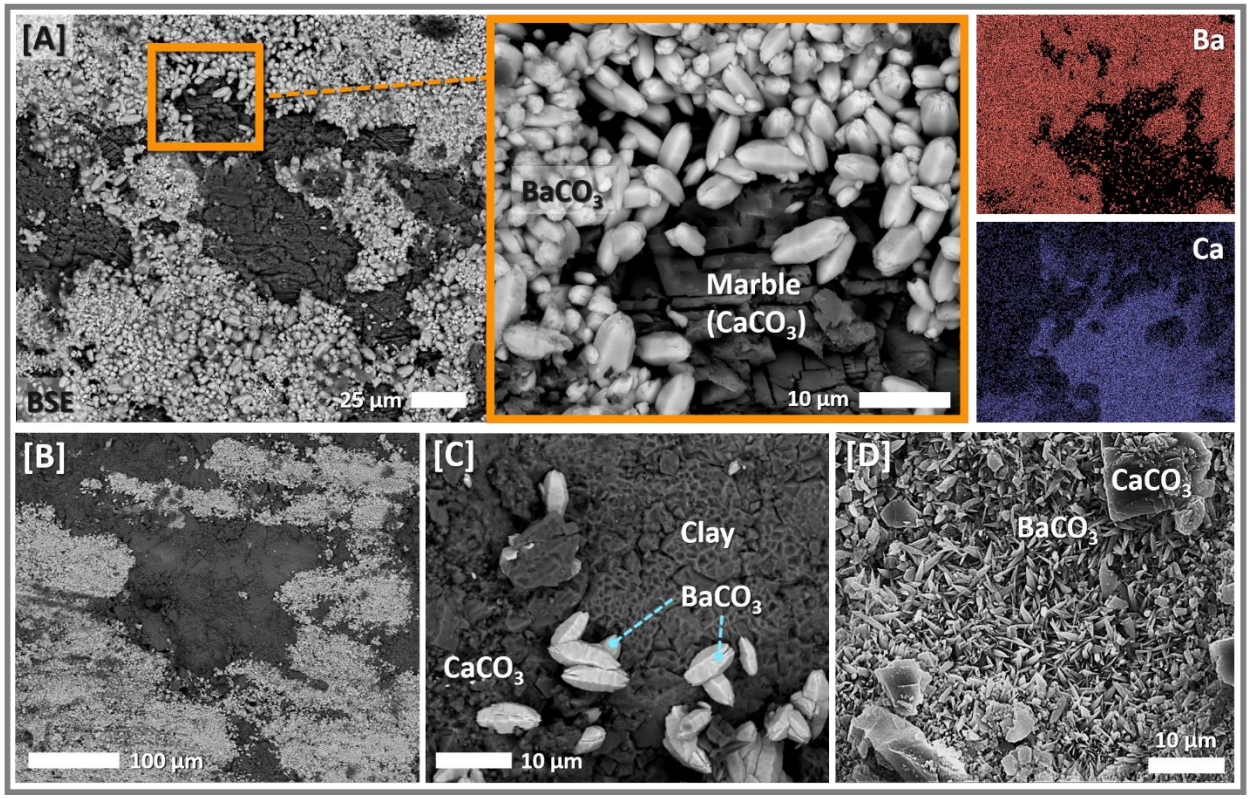

Figure 5.1. Example BSE images and EDS maps revealing small $BaCO_3$ crystals on the surfaces of [A] marble, [B,C] calcite-rich shale, and [D] limestone reacted in solutions of 2,000 ppm $BaCl_2$ at ambient conditions.

5.2.2. Geochemical conditions: Shale cores and fluid chemistry

An initial experiment, reported by Carey et al.[29] and described in Section 5.3.1, resulted in extensive $BaCO_3$ precipitation during shearing of a carbonate-rich Utica shale that was inadvertently exposed to $BaCl_2$-rich fluid. This core, provided by Chesapeake Energy Corporation, was taken from a depth of 1817 m (5960 ft) and consisted of 93% calcite, 2% dolomite, and 5% quartz according to compositional data provided by the company. Juxtaposing the results from this test with the limited extent of precipitation observed in preliminary batch testing with nearly pure calcite rocks (marble, limestone), it was hypothesized that the extensive microfractures formed during shale fracturing uniquely supported the development of secondary minerals. Thus, two shale samples with relatively high calcite content were selected to build on the initial Utica experiment. A similar Utica core plug (also provided by Chesapeake Energy Corporation) was taken from a depth of 1813 m (5948 ft) and contained 82% calcite, 4% quartz, and 10% clay with 1% each of dolomite, organic carbon, pyrite, and apatite. A second core was obtained from a Marcellus shale outcrop and was comprised of 66% carbonate, 19.5% quartz and feldspar, 13% clay, and 1.7% accessory minerals. Core plugs were trimmed to 25.4 mm (1”) in length and measured approximately 25 mm in diameter. While conventional triaxial experiments use a 2:1 length:diameter ratio, a 1:1 ratio was applied here to promote fracturing throughout the entire length of the samples for practical permeability measurements.[28]

As described in Section 5.2.1, initial batch experiments on shale and calcite samples revealed $BaCO_3$ formed in 2,000 and 180,000 ppm $BaCl_2$ solutions but was negligible at 20 ppm. The highest tested concentration (180,000 ppm) was ultimately selected as the primary working fluid for shear fracturing in this study to induce visible precipitation within hours of commencing fluid injection such that precipitate evolution could be captured in xCT scans. Lower concentrations (200 or 2,000 ppm) were also applied as needed to improve x-ray contrast or to test the influence of pore fluid saturation on precipitation rates. Changes in fluid chemistry for each test along with the carbonate content of the cores are summarized in Table 5.1 and detailed in Section 5.3.

5.2.3. Triaxial direct shear with x-ray imaging

Figure 5.2 illustrates the sample assembly for direct shear testing. Cores were first positioned between two asymmetric semi-circular stainless-steel thrust collars that focus shear stress along a central plane, with porous screens placed between each collar and core end. Channels built into

the collars allow for fluid flow into and out of the core. All samples were aligned with the shear platens oriented 45° to bedding planes because previous work has indicated that the resulting fracture permeability peaks when shearing occurs near this angle.[26] As noted previously, these experiments were designed to maximize the potential for observing reaction-induced fracture alterations in real time, so this fracture alignment was selected to maximize the probability of generating fracture apertures that were large enough to be observed in x-ray radiography under elevated stress conditions. This setup is also relevant to field applications as bedding planes are ubiquitous in natural systems and are often subjected to shear stresses at varying orientations in oil and gas shales.[30]

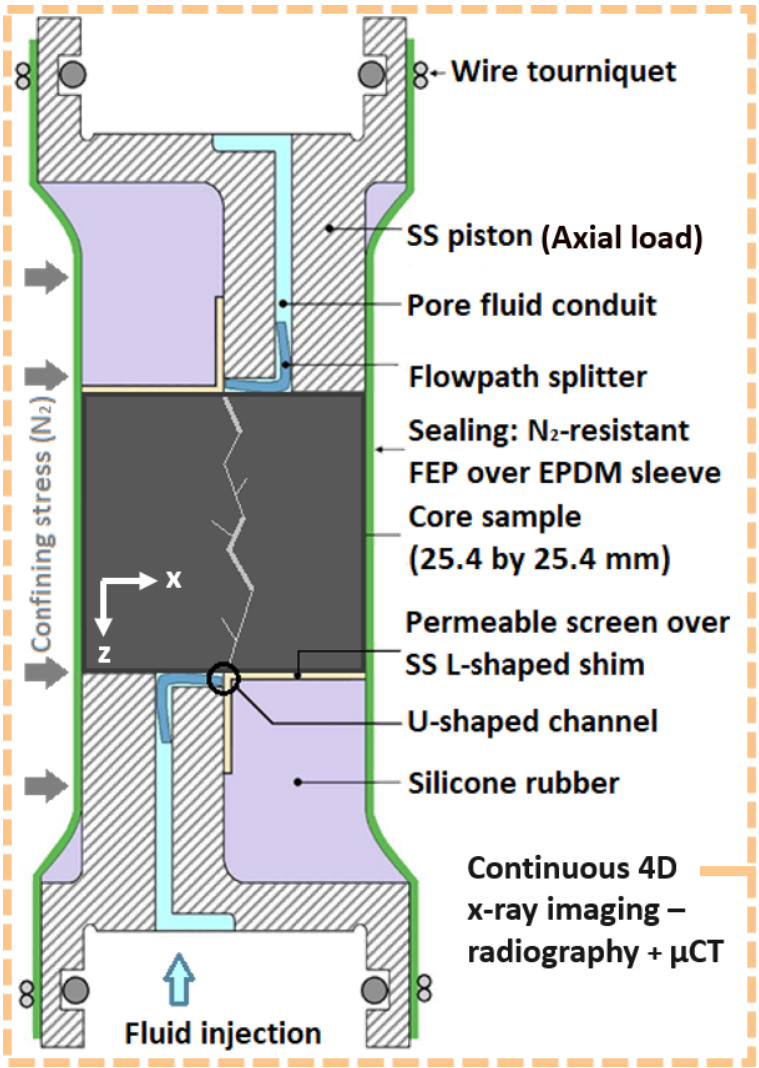

Figure 5.2. Schematic of triaxial direct shear system sample assembly, adapted from Frash et al.[31] The sample assembly is loaded into an aluminum triaxial core holder within a µCT scanner. The reference axes used in xCT analyses are shown relative to the core orientation, with the y-axis perpendicular to the x-z plane in the figure.

Because nitrogen gas was used as the confining fluid to optimize x-ray transparency, a rubber sleeve (EPDM) was placed around the core and collars to prevent N_2 intrusion. The assembly was jacketed with chemical-resistant heat-shrink tubing (FEP), secured with wire tourniquets on the upper and lower collars for reinforced sealing, before being loaded into a triaxial core holder comprised of aluminum for x-ray transparency. The core holder and all upstream and downstream flow lines are built into a Hytec cabinet equipped with a 150 kV Hamamatsu micro-focus x-ray tube and Varian panel with 127-µm pixels for live x-ray imaging and micro-computed tomography (µCT). Additional details on the system's design and capabilities are provided by Carey et al.[26] and Frash et al.[28,31]

Three triaxial direct shear experiments were conducted to promote mineral precipitation during shear fracturing, as summarized in Table 5.1 and described in detail in Section 5.3. Each experiment involved one or more shear events with varying concentrations of $BaCl_2$ in the pore fluid to test the influence of fracture geometry and fluid chemistry, respectively, on secondary precipitation and resulting impacts to fracture permeability and structure. We also selected cores with varying calcite fractions to test the hypothesis that the extent of precipitation would increase with increasing reactive mineral content. All experiments were conducted at room temperature (~20°C) under varying stress conditions that are detailed for each experiment below. Fluids were injected with high-pressure syringe pumps (Teledyne ISCO) controlled by DIsco software,[32] which also records flow, pressure, and displacement data. The upstream and downstream pore pressures were held at 1.5 and 0.5 MPa, respectively, and confining stress was held at 3.5 MPa for initial shear events. Cores were directly sheared by increasing the axial stress with a constant flow rate of 0.5 mL/min through the axial pump until failure occurred, after which the system was allowed to stabilize at isotropic stress conditions. Permeability was measured continuously based on flow rate and pressure readings recorded by the pumps and high-precision Quartzdyne pressure transducers installed upstream and downstream of the core. Displacement was monitored with a linear variable differential transformer (LVDT) mounted on the upper (downstream) end of the triaxial cell. X-ray radiographs were also taken continuously at a rate of 3.75 frames per second while xCT scans were taken at points of critical changes in experimental conditions.

Table 5.1. Summary of key experimental conditions

Condition	US-01	US-02	MS-01
Shale formation	Utica	Utica	Marcellus
Carbonate content	93%	82%	66%
Confining stress*	3.5 MPa	3.5 MPa	3.5 MPa
Upstream pore P	1.5 MPa	1.5 MPa	1.5 MPa
Downstream pore P	0.5 MPa	0.5 MPa	0.5 MPa
Shear orientation	45° to bedding	45° to bedding	45° to bedding
Injected [$BaCl_2$]	Not measured**	180,000 ppm	200 → 2,000 → 180,000 ppm
Injectate pH+	--	6.9	7.1 → 7.1 → 6.9
xCT scan timings	End of experiment	After each confining step	After adjusting [$BaCl_2$]

*Confining stress during initial shearing; note that confining stresses were subsequently changed to evaluate stress-permeability relationships as detailed in the text.

**In this experiment, DI water was used as the injected fluid and the [Ba^{2+}] was not directly measured because it was residual from a previous test using 18 wt% (180,000 ppm) $BaCl_2$ as a contrast agent.[29]

+Initial pH of injected $BaCl_2$ solution calculated in CrunchTope[33] with equilibrium constants from the EQ3/EQ6 thermodynamic database. Note that pH values are approximate as they are based on activity coefficients calculated using the extended Debye-Huckel equation with the B-dot extension that are not accurate for high ionic strength solutions.

5.2.4. Post-reaction xCT analysis and sample characterization

In the initial experiment (US-01), x-ray radiography was collected continuously at a rate of 0.7 frames per second but only one *in situ* xCT scan was acquired at the end of the test. All x-ray data were collected in the industrial µCT scanner described in Section 5.2.3 at a beam energy of 150 kV with a 25-µm spot size. For the next two experiments, xCT scan parameters were optimized for speed and quality in order to capture rapid changes in mineralogy and fracture structure. Preliminary testing revealed high-power scans (150 kV, 500 µA) lasting approximately 17 minutes provided sufficient quality for processing and segmentation within a reasonable time frame. Scans were taken at a rate of 3.75 fps with 800 projections and 5-frame averaging. Voxel resolutions were approximately 27 µm in US-01 and 46.5 µm in US-02 and MS-01.

Raw radiographs were calibrated with light corrections taken in the empty chamber and dark corrections collected with the x-rays off. All xCT scans were reconstructed using RECON software at LANL. Ring removal was applied to reduce noise in the images, which were output as TIF stacks for further processing. Fractures were first segmented in MATLAB (version 2016b) using

a simple thresholding process to create a binary 3D dataset where the z axis is parallel to the direction of shear along the length of the core; x is perpendicular to the shear direction; and y is perpendicular to the shear (xz) plane (Figure 5.2). Aperture maps were then generated by summing the fracture voxels in each column (y axis on 2D cross sections) along the x axis over the length of the core (z axis). Note that black (zero-aperture) regions are not necessarily completely closed but are below the voxel resolutions of the xCT scans (27 μm in US-01; 46.5 μm in US-02 and MS-01). Excluding scan artifacts due to rings and beam hardening, the uncertainty in segmentation calculations is within ±1.5 voxels (i.e., 40.5 μm for US-01 and 70 μm for US-02 and MS-01). Because both samples contained Fe-bearing accessory minerals (mainly pyrite) exhibiting a similar x-ray intensity as $BaCO_3$, the precipitates were segmented in sections along the direction of shearing that excluded high-intensity primary minerals from the analysis. Precipitation maps were created with the same workflow as the aperture maps to facilitate comparison between the spatial distributions of precipitates and fractures. Areas with no resolvable precipitate volumes may still contain small crystals or surface coatings of secondary minerals, but due to the complex factors controlling CT intensity in voxels with multiple potential components (e.g. shale, voids, precipitates, pyrite, etc.), we did not estimate the volume of precipitate that that could be missed by our segmentation method. In US-02, segmented fracture and precipitate volumes were also summed across the core for each scan to quantify changes with increasing confining stress (section 5.4.4). Note that scans taken during injection of 180,000 ppm $BaCl_2$ were not segmented due to limited contrast between the injected fluid within fractures and surrounding shale.

After non-destructive analyses were complete, fractured samples were secured in heat shrink tubing and vacuum-impregnated with epoxy for sectioning. Thin sections oriented 45° to the primary shear fractures were characterized via SEM with BSE imaging, using EDS mapping and point analyses to obtain compositional data on reaction products. Note that while EDS provides chemical data on mineral phases from which compositions can be inferred, it is not a tool for explicit mineral identification. More refined techniques to determine exact crystal structures and zoning were not pursued because the focus of this work was on factors driving precipitation, where the extent of precipitates was more important than their composition, and precipitate volumes were too small for destructive analyses such as x-ray diffraction.

5.3. TRIAXIAL DIRECT SHEAR FRACTURING

The following sections present methodology and results for each experiment. Section 5.3.1 details experimental procedures for each test with corresponding lab data (i.e. shear stress, confining stress, permeability, and injectate [$BaCl_2$]) and provides context for changes in stress and fluid conditions within and among experiments. Sections 5.3.2. 5.3.3, and 5.3.4 then provide results from xCT analyses and post-reaction sample characterization for US-01, US-02, and MS-01, respectively. Stress-permeability data are also included in these sections to highlight where changes in stress-permeability data correspond to precipitation and fracture alterations observed in x-ray imaging. Refer to Table 5.1 for details on experimental conditions.

5.3.1. Series overview: Experiment procedures and stress-permeability data

Figure 5.3 (pg. 94) compares stress-permeability data for each experiment. Changes in confining and direct shear stress are plotted on the left axes; resulting changes in permeability based on recorded pressure differentials and flow rates are plotted on the right axes; and changes in injected (pore) fluid chemistry during US-02 and MS-01 are denoted by the shaded regions with labeled [$BaCl_2$]. Note that these data are also included in the individual results sections for each experiment to mark points where xCT scans and select radiographs were taken.

The first experiment (US-01) involved direct shearing of a nearly pure-carbonate Utica shale core that was used as received (i.e., partially dehydrated). The intended pore (i.e. injection) fluid was DI water but the core was initially subjected to a $BaCl_2$-rich solution that had not been completely purged from the pore lines following a prior test. Carey et al.[29] estimated this solution was dilute, containing ~19.5 ppm Ba^{2+}, but results from the subsequent experiments conducted here indicate the actual concentration was at or near the 180,000 ppm that had been used in the prior test. The core was initially sheared under 3.5 MPa confining stress, where shear failure was marked by a sharp drop in direct shear stress around 80 MPa and concomitant increase in permeability from <1 μD to ~0.25 mD (Figure 5.3a). Axial stress was held above 60 MPa for the next 15 minutes, during which time permeability gradually decreased to ~0.2 mD, and then the stress was returned to isotropic conditions (3.5 MPa) while permeability rose sharply again to a peak of 0.43 mD. Confining stress was incrementally raised to 7, 10.5, and 14 MPa for stress-permeability measurements that are not discussed in this study and then decreased in the same steps to return to 3.5 MPa. Each change in confining stress produced a sharp drop in permeability

followed by a continuing steady decrease until the next stress step. Continuous x-ray radiography provided live imaging of the primary fracture and a post-reaction xCT scan was taken *ex situ* (i.e., without confining stress) to obtain 3D imaging. Radiographs evidenced opaque precipitates forming within 10 minutes of shearing that motivated the subsequent experiments, as detailed in Section 5.3.2.

In the second test (US-02), a less calcite-rich Utica core was used as received (i.e., partially dehydrated) with an initial condition of 180,000 ppm $BaCl_2$ injection fluid at the upstream face of the core. As noted in the methods, this concentration was selected because (a) it was the maximum value the core in US-01 would have been exposed to and (b) preliminary testing revealed barium carbonates formed quickly on calcite-rich samples reacted in 180,000 ppm $BaCl_2$ solutions (Section 5.2.1). The upstream pore pressure was held constant at 1.5 MPa and back pressure at 0.5 MPa using syringe pumps with a maximum flow limit set at 0.25 mL/min. A pre-reaction xCT scan was taken under 3.5 MPa isotropic stress before the core was sheared to 1 mm displacement at 3.5 MPa confining pressure. The axial stress was then increased until the sample failed around 25 MPa (Figure 5.3b). Upon shear failure, the permeability rose sharply to ~100 mD and then continued to increase to a maximum of ~235 mD before falling to ~50 mD while the flow lines were purged with DI water to improve x-ray contrast. Back-to-back xCT scans were taken immediately after shearing to capture mineral dissolution-precipitation reactions resulting from continuous flow of the high-[$BaCl_2$] fluid through fresh fracture networks. Because the high [Ba] impeded x-ray contrast between the fracture and surrounding rock, the injection fluid was replaced with DI water after the second scan. Following fluid breakthrough, evidenced by lightening of the fracture as DI replaced the dense $BaCl_2$ solution, another xCT scan was taken before raising the confining pressure in successive steps (6, 10, 15, 20, 25, and 30 MPa) to obtain fracture aperture and permeability data under varying effective stress states. An xCT scan was taken at each step to characterize fracture evolution with increasing stress and to capture potential dissolution-precipitation reactions in real time. Radiography was recorded continuously between all xCT scans with the x-ray beam aligned parallel to the opposing direct shear platens and resulting fractures.

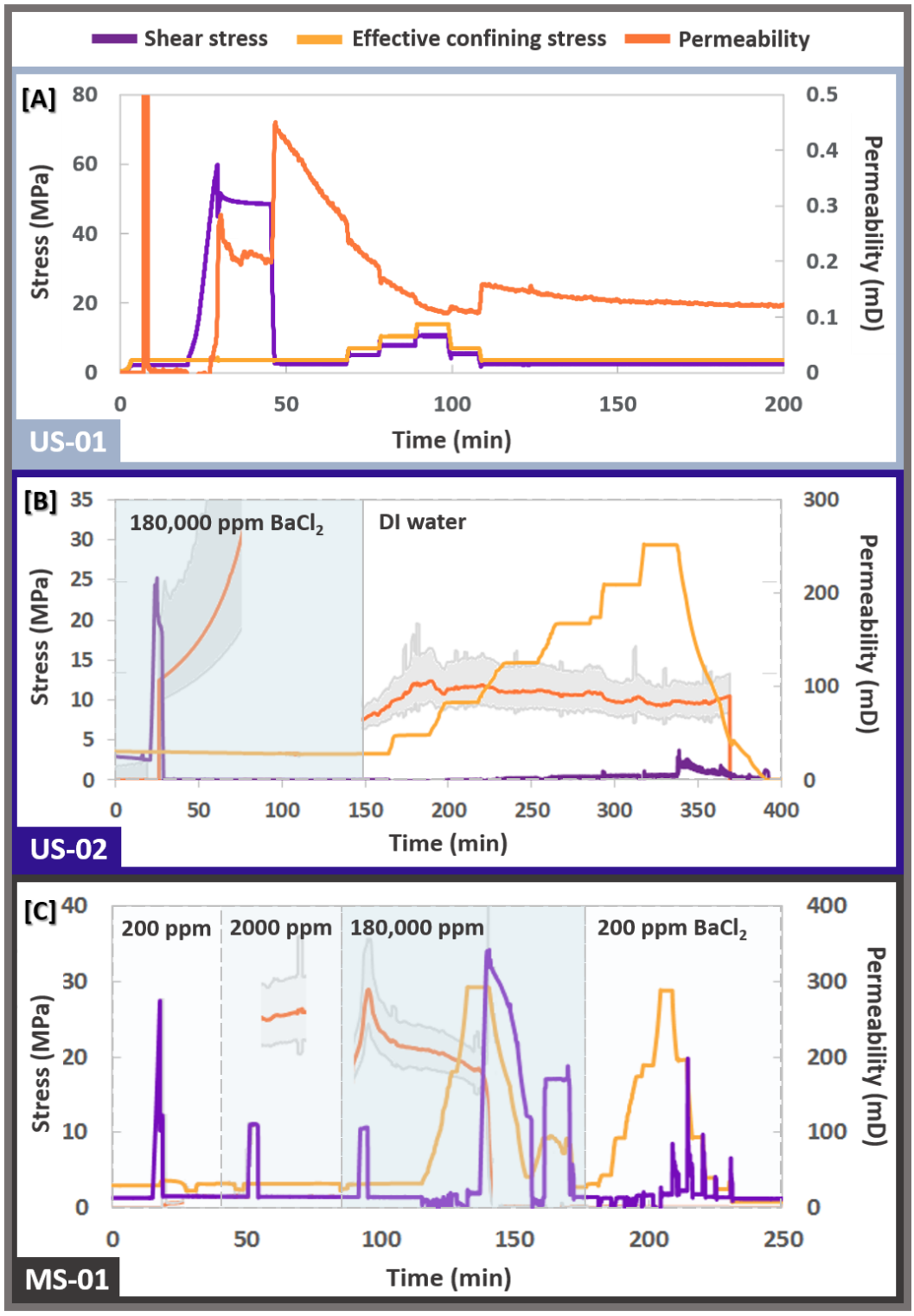

Figure 5.3. Stress-permeability data for the series of three triaxial direct shear tests, highlighting experimental procedures with respect to changes in stress and fluid conditions in [A] US-01, [B] US-02, and [C] MS-01. Shear and confining stress are displayed on the left axis, permeability is presented on the right, and changes in injected fluid chemistry are denoted by the labeled shaded regions for US-02 and MS-01. Note that for US-01, DI water was injected throughout the test but the core was exposed to up to 180,000 ppm of residual $BaCl_2$ in the pore lines. Experimental conditions are summarized in Table 5.1.

The final experiment (MS-01) involved more shear steps and fluid changes. After a pre-reaction xCT scan, the Marcellus core was sheared to 0.5 mm of displacement under 3.5 MPa confining stress with a lower concentration of 200 ppm $BaCl_2$ in the pore fluid to evaluate precipitation potential at low $BaCO_3$ supersaturation. Upstream and downstream pressure limits were maintained at 1.5 and 0.5 MPa, respectively, with a flow limit of 1 mL/min. Another xCT scan was taken immediately after shearing and the pore fluid was then replaced with a 2,000 ppm $BaCl_2$ solution to enhance the likelihood of precipitation, as no precipitates were observed in the live radiographs during the initial shear event and subsequent stabilization. The more concentrated 2,000 ppm solution was injected at a higher flow rate (10 mL/min) until it reached the core, at which point the original flow limits were restored and the sample was re-sheared to 1 mm displacement while maintaining 3.5 MPa confining stress. After collecting a post-shear xCT scan, the pore fluid was replaced with 180,000 ppm $BaCl_2$ to improve the likelihood of precipitation and the process of re-shearing (to 1.5 mm displacement) and xCT scanning was repeated. Similar to US-02, fluid breakthrough was determined by a change in contrast in x-ray radiographs, where increasing [$BaCl_2$] increased the opacity in the shear fracture. Note that the first peak in the shear stress curve (Figure 5.3c) represents the stress required to induce shear fracturing in the original specimen, while subsequent peaks correspond to the residual stress required to re-activate this fracture. Following the third shear step and xCT scan, the confining stress was raised to 30 MPa and the core was re-sheared. Axial stress was then held constant and the core was dynamically sheared by steadily releasing confining stress to 5 MPa, which induces additional shear displacement as falling confining pressure causes the pistons to slide. The aim of this process was to promote further fracturing in the core and test the hypothesis that because this core had the lowest calcite content, more freshly activated fracture surfaces needed to be created to expose sufficient calcite-rich regions for observable dissolution and precipitation to occur.

The remaining shear displacement steps in this experiment were imposed to study stress-permeability relations that are not the primary focus of this work, but are included in this study because they affected the final state of the core with respect to fracture geometry and secondary precipitation. Once the system had stabilized after dynamic shearing, the core was hydrosheared by raising the pore pressure to 2 MPa under a constant 10 MPa confining stress. Hydroshear refers to shear induced by fluid flow through a fracture as opposed to shear induced by the external shear stress created by increasing the axial piston displacement in previous steps. This step was

conducted here to demonstrate whether effective stress conditions leading to hydroshear were equivalent to those for external shear for the Marcellus core, which was not a primary objective of this study. Following this step, the pore fluid was replaced with 200 ppm $BaCl_2$ to improve x-ray contrast, and confining stress was incrementally raised to 3.5, 5, 10, 20, and 30 MPa to obtain stress-aperture data. The confining stress was then lowered in the same increments with additional measurements taken at each step. Each step down in confining pressure induced a shear event, evidenced by the sharp peaks in direct shear stress toward the end of the test (Figure 5.8a). A final xCT scan was taken before depressurizing the system and removing the core, which was secured in heat shrink tubing to prevent loss of precipitates and fragments generated in shearing.

5.3.2. US-01: High-carbonate Utica shale

Results from the first shear experiment are summarized in Figure 5.4. After peaking at 0.43 mD, the permeability fell steadily over the remainder of the experiment, which included a series of step increases in confining stress to obtain stress-permeability data that is not the focus of this study. During this time, continuous x-ray radiographs evidenced opaque white material accumulating in the fracture (Figure 5.4b). The permeability increased slightly as confining stress was returned to 3.5 MPa in the final stage of the experiment and then decreased gradually over the next 5 hours as the system was held under isotropic stress conditions, reaching a final value of 0.084 mD that reflects an irreversible loss of permeability compared with the permeability measured directly following fracturing.

A post-reaction xCT scan revealed the opaque materials observed in radiographs corresponded to dense precipitates that ultimately filled much of the fracture network. Cross sections taken parallel (Figure 5.4d) and perpendicular (Figure 5.4e) to the direction of shear indicated precipitates were concentrated at the inlet and outlet of the core, which is demonstrated in the map of segmented precipitates (Figure 5.4c) that shows their spatial distribution in a 2D projection perpendicular to the shear plane. Fracture apertures were also segmented but note that because most of the original fractures were filled with precipitate, this map does not represent the original post-shear fracture network.

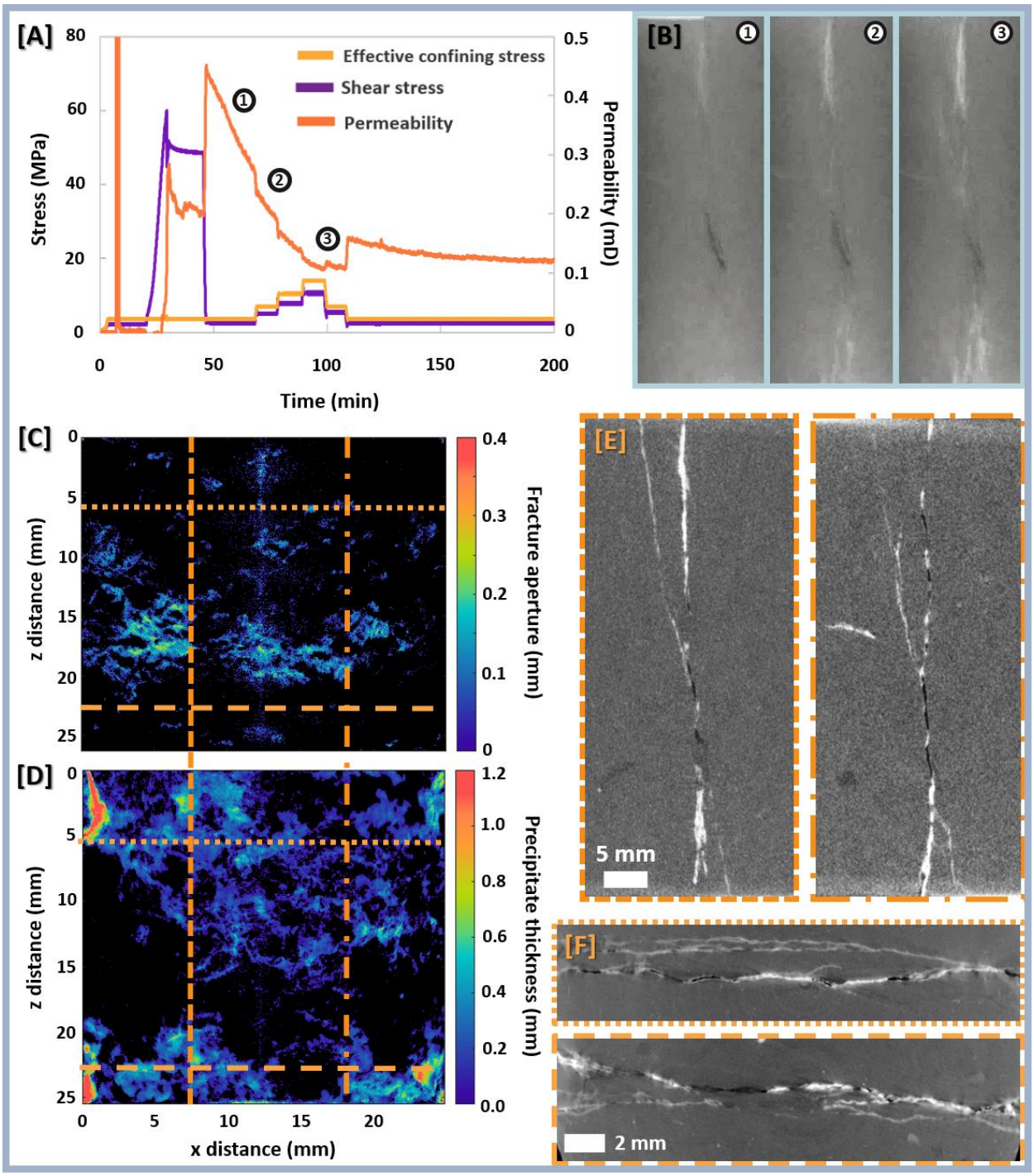

Figure 5.4. Summary of stress-permeability, x-ray radiography, and processed xCT data for US-01. [A] Changes in axial and confining stress, permeability, and pore pressure during the experiment. [B] Radiographs at the time points marked in [A] showing opaque white precipitates accumulating at the inlet and outlet of the main fracture, concomitant with declining permeability. A post-reaction xCT scan was segmented to illustrate spatial distributions of [C] fracture apertures and [D] precipitates, both shown in 2D projections perpendicular to the shear plane. Dashed, dash-dot, and dotted lines delineate positions of cross-sections highlighted in E and F that reveal white precipitate infill. The sections in [E] were taken perpendicular to the primary shear fracture along the length of the core (y-z plane) and those in [F] were taken in the x-y plane along the direction of shear.

Precipitates were identified as barium carbonates in SEM analysis of a thin section cut 45° to the primary shear fracture. Select BSE images and EDS maps indicating the presence of $BaCO_3$ within the $CaCO_3$-rich shale matrix are presented in Figure 5.5. Some fracture networks were essentially cemented with precipitates, which generally formed as needle-like crystals perpendicular to fracture walls. The SEM observations (Figure 5.5) revealed greater concentrations of precipitates in regions with smaller apertures and with significant fragmentation or fault gouge.

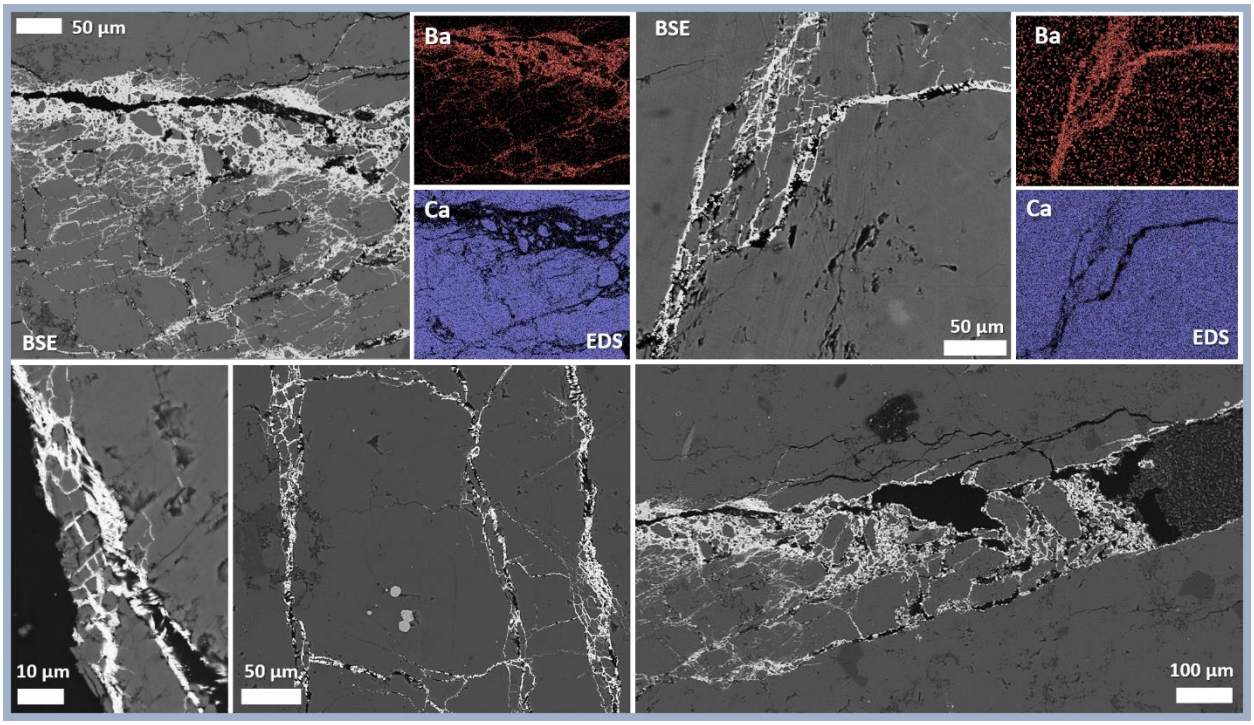

Figure 5.5. Example BSE images and select corresponding EDS maps from a thin section cut 45° to the primary shear fracture in US-01. EDS revealed $BaCO_3$ precipitates within fractures in a $CaCO_3$-rich matrix.

5.3.3. US-02: Carbonate-rich Utica shale

Stress-permeability and xCT data for the second Utica shale experiment are presented in Figure 5.6. Whereas only a post-reaction xCT scan was collected in US-01, a total of 10 rapid scans were taken over the course of this experiment to improve the temporal resolution of precipitation reactions. Successive xCT scans taken directly following shearing (locations 2 and 3 in Figure 5.6a) revealed that opaque white material, similar to precipitates observed in US-01, formed within 20 minutes of shearing. These precipitates were more clearly visible in a fourth scan collected after breakthrough of DI water. Following this scan, the confining pressure was increased incrementally to 30 MPa with an xCT scan taken upon stabilization at each step (5-10 in Figure 5.6a). Permeability increased to 112 mD as confining pressure was raised to 6 MPa and then decreased

gradually to ~80 mD over subsequent step increases in confining stress (up to 30 MPa) due to fracture closures, as evidenced by aperture reductions across the 2D projections of fractures segmented from xCT scans in Figure 6d. Precipitates were also segmented (Figure 5.6c) but did not change significantly over the course of the experiment; their stability despite fracture closure is also apparent in the xCT cross sections (Figure 5.6b).

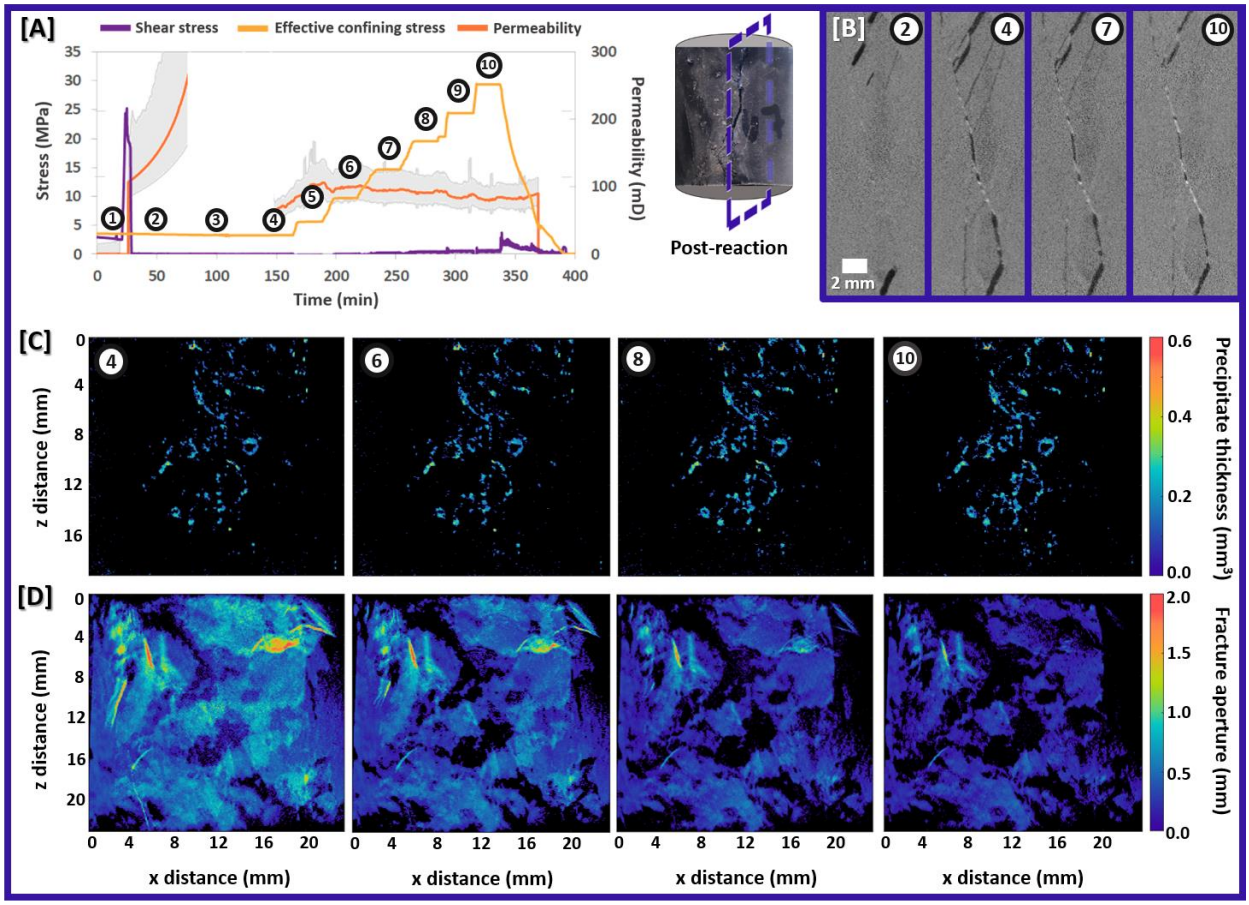

Figure 5.6. Summary of stress-permeability and xCT processing results for US-02. [A] Permeability evolution with changes in direct shear and confining stress, where grey shading corresponds to uncertainty in permeability measurements and blank regions indicate data were invalid. Circled numbers indicate where xCT scans were taken. The image of the core shows the location of the cross-sections in B-D. [B] Sections of selected reconstructed xCT scans along the primary shear fracture evidence precipitates forming within the first post-shear xCT scan and filling portions of the fracture. The xCT data were then segmented to map spatial distributions of [C] precipitates and [D] fracture apertures in 2D projections.

The reacted core was thin-sectioned 45° to the primary shear fracture for SEM analysis. Select BSE images and a representative combined EDS map identifying barium- and calcium-carbonates are presented in Figure 5.7. Precipitates did not cement fracture networks to the extent observed in US-01 but coated or filled fractures in many locations, particularly where apertures were narrow or fragmentation was abundant.

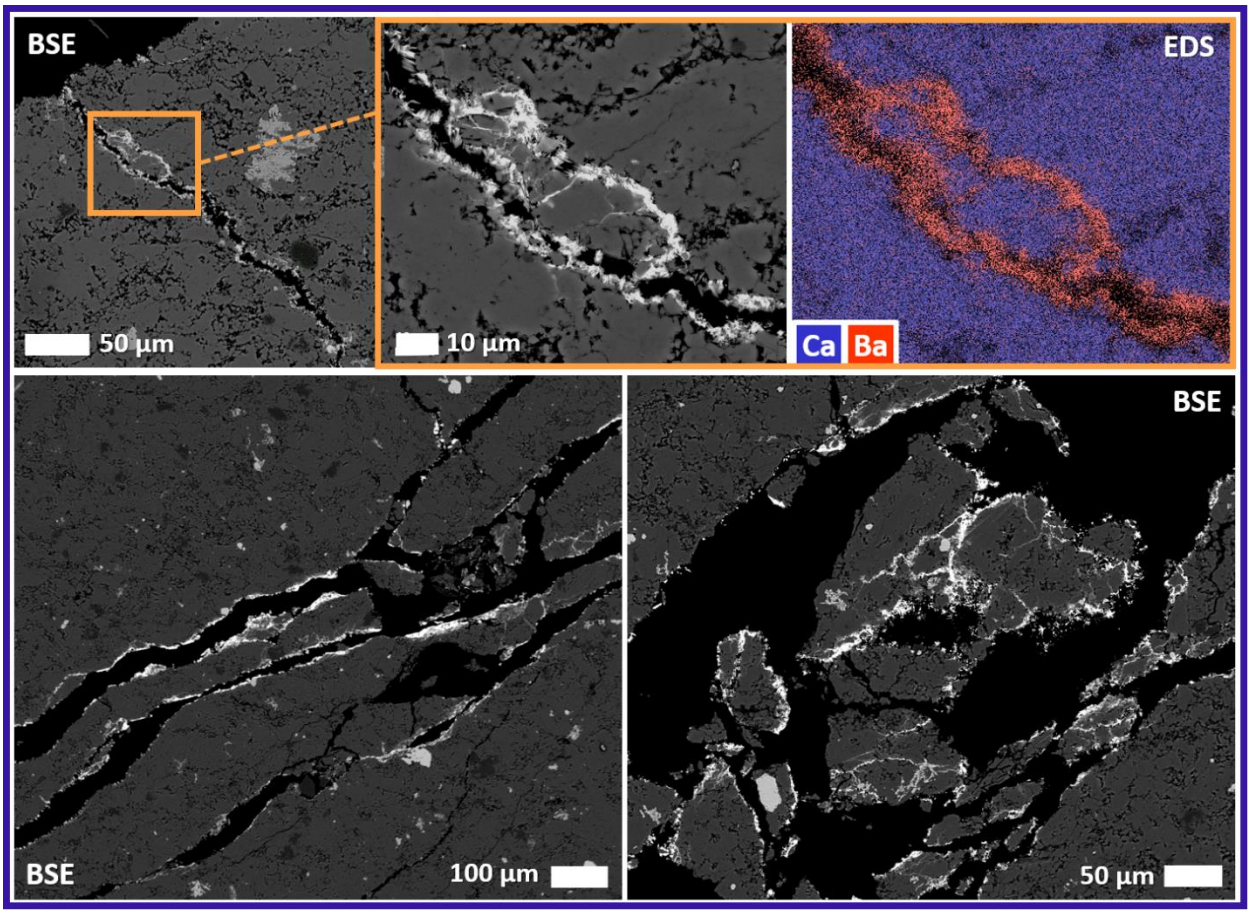

Figure 5.7. Example BSE and EDS images from a thin section cut 45° to the main shear fracture in US-02 highlighting $BaCO_3$ precipitation in microfractures.

5.3.4. MS-01: Carbonate-rich Marcellus shale

As detailed in Section 5.3.1, the final experiment on a carbonate-rich (66% calcite) Marcellus core was the most complicated with a series of three direct shear steps followed by dynamic shearing and hydroshearing. In Figure 5.8a, sample displacement aligning with each shear event is included below the stress-permeability data that was presented in Figure 5.3c. The core was displaced to 0.5 mm during the first shear event, 1.0 mm during the second, 1.5 mm during the third, and 3.2 mm during dynamic shearing. The series of ascending and descending confining pressure changes following hydroshear indirectly caused shear stress that resulted in slight further displacement to 3.4 mm. By contrast, the Utica cores were only displaced to a total of 0.9 and 1 mm in US-01 and US-02, respectively. Permeability rose to ~240 mD following the second shear event and ~280 mD following the third, after which it steadily decreased to 138 mD before suddenly plunging below 1 µD during dynamic shearing. Reasons for this permeability drop are discussed in Section 5.4.3.

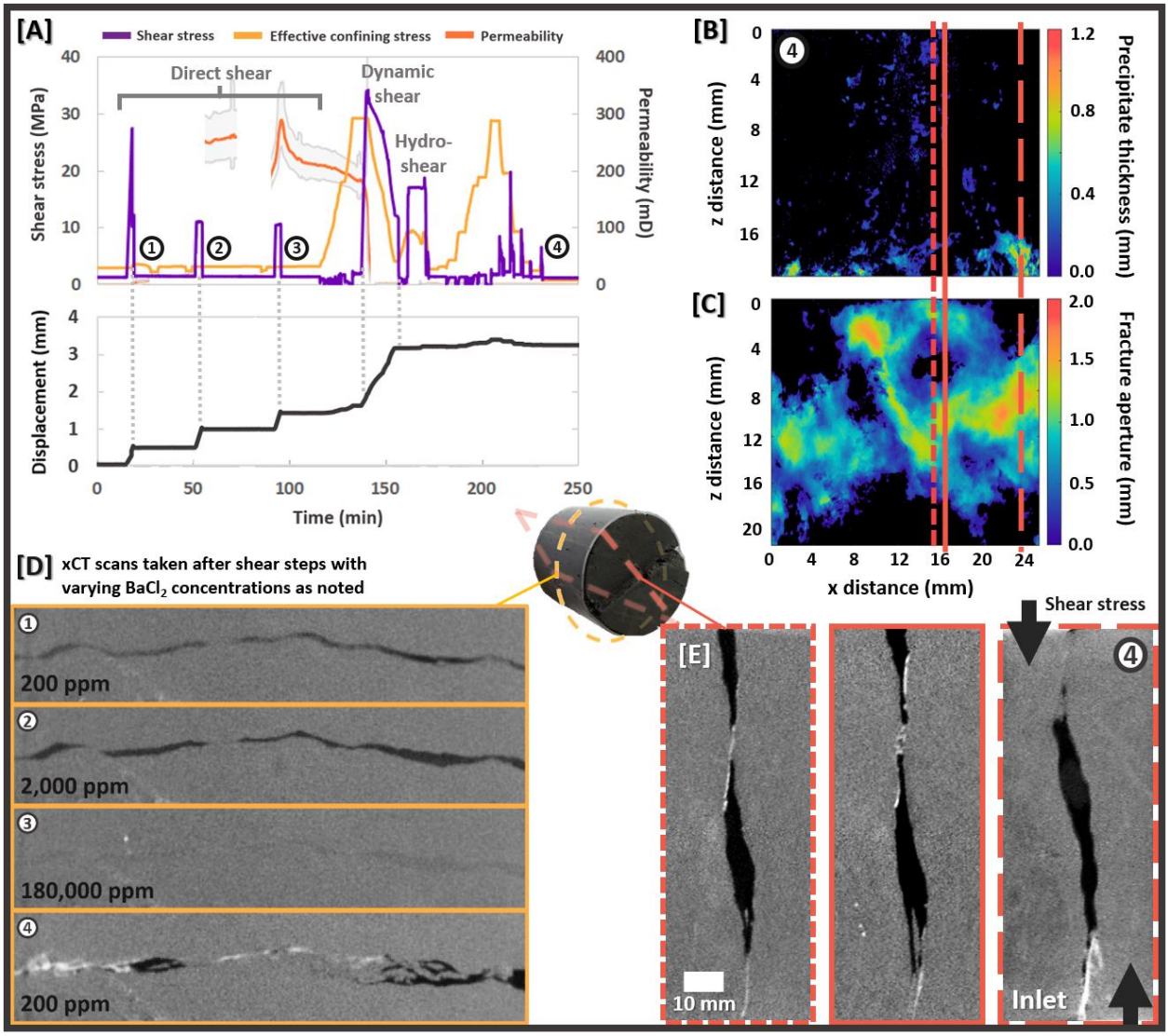

Figure 5.8. Summary of stress-permeability and xCT results for MS-01. [A] Permeability evolution with changes in direct shear and confining stress, where grey shading corresponds to uncertainty in permeability measurements and blank regions indicate data were invalid. Circled numbers indicate when xCT scans were taken. [B] Precipitate and [C] fracture aperture maps derived from segmentation of the final xCT scan (#4). Solid, dashed, and dotted lines show position of cross-sections in E. [D] Cross sections from post-shear xCT scans taken at the four locations noted in (A) that exemplify fracture and precipitate evolution with changes in stress and injected fluid chemistry. The location of cross-sections is shown in the central 3D image. [E] Sections from the final xCT scan taken perpendicular to the direction of shear, which represent y-z planes from the sections delineated in the x-z maps in [C] and [D]. White precipitates are evident in narrow regions between fracture walls.

An xCT scan was collected after each direct shear step (locations 1-3 in Figure 5.8a) and at the end of the experiment (4). Cross-sections from each scan are compared in Figure 5.8d, revealing that significant shearing occurred and white precipitates formed between the third direct shear step and the final scan taken ~2.5 hours later. The exact timing of precipitation is discussed in Section

5.4.1. Segmentation of the final xCT scan demonstrated that precipitation was concentrated at the inlet (Figure 5.8b) and in regions with small fracture apertures (Figure 5.8c). These observations are better visualized in xCT sections perpendicular to the direction of shear that depict precipitation favoring narrow gaps between fracture walls (Figure 5.8e). Comparing segmented 2D maps with xCT cross sections provides a more complete picture of *in situ* processes; for example, the region of greatest precipitation in the lower righthand corner of Figure 5.8b occurs in a region of small sub-resolution apertures (Figure 5.8c) that appear in the corresponding perpendicular xCT section (far right panel of Figure 5.8e) illustrating precipitation filling a narrow fracture at the core inlet.

Select BSE images from thin section analysis are provided in Figure 5.9 along with a representative EDS spectrum indicating that precipitates were barium carbonates. Consistent with observations in the xCT scans, precipitation was less abundant relative to the Utica shale experiments but more fault gouge formed due to the greater number of shear fracturing events and sample displacement (Figure 5.3).

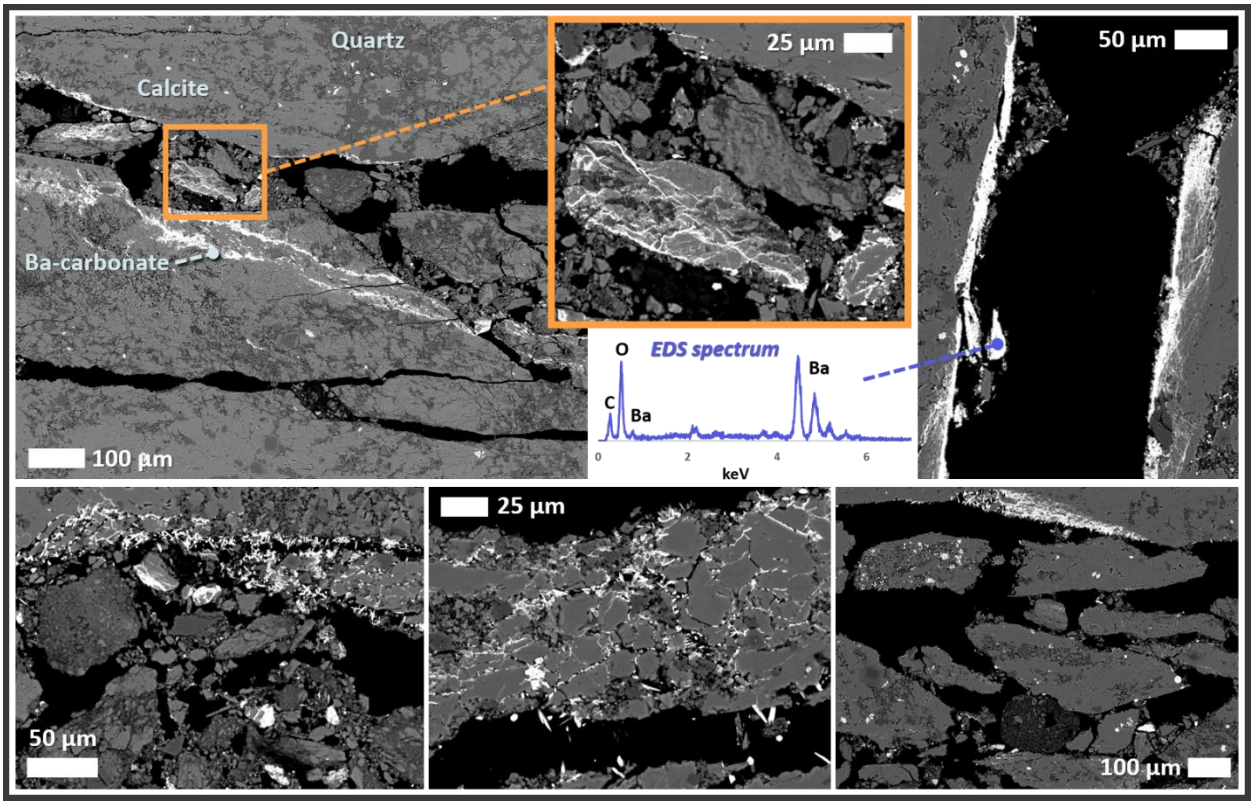

Figure 5.9. Select BSE images from a thin section cut 45° to the main shear fracture in MS-01. An example EDS spectrum for barium carbonate precipitate is included in the center.

5.4. DISCUSSION

5.4.1. Rapid mineral precipitation

Within 10 minutes of shearing the original Utica shale (US-01), opaque secondary minerals appeared in x-ray radiographs centered on the main fracture. Over the next hour precipitates continued to accumulate in fractures as permeability fell by a factor of 2 (Figure 5.4a).[29] Dense precipitates similarly formed within 20 minutes of shearing the second Utica shale (US-02), but permeability changed minimally over the remaining 4 hours of the test. In both cases, BSE/EDS analyses of thin sections cut 45° to the primary shear fractures (see sections 5.3.1 and 5.3.2) indicated the precipitates were barium carbonate ($BaCO_3$). Because crystalline witherite occurs rarely in natural environments, the precipitates could have formed as solid solutions between Ba- and Ca-carbonates during the short experimental time frames;[34] however, impurities were likely minor because witherite crystal structures can only uptake small amounts of Ca^{2+} due to significant differences in the ionic radii and physicochemical properties of the divalent cations.[35] Additionally, EDS spectra evidenced minor to no calcium in carbonate precipitates.

Precipitation was less abundant in the second Utica shale experiment (US-02) but occurred at a similar rate. As evidenced by Figure 5.6b, opaque white precipitates began to appear in the middle of the fracture during the first post-shear xCT scan, which was completed within 20 minutes of fracture generation. Precipitates remained stable with increasing confining pressure (steps 5-10 in Figure 5.6a) and the amount did not change significantly over time, likely because the transition from 180,000 ppm $BaCl_2$ to DI water at about 150 minutes removed the source of Ba^{2+} and pore fluids quickly became undersaturated. The speed of precipitation following initial shearing in both Utica experiments is likely driven by the freshly activated fracture surfaces generated in direct shearing combined with injection of high [Ba^{2+}], which allowed $BaCO_3$ saturation to be achieved with nominal calcite dissolution. Fragments and fault gouge generated in shearing increased the available reactive surface area, which would have directly influenced effective mineral dissolution and precipitation rates,[36] while dissolution of fine grains along the new fractures quickly released CO_3^{2-} that buffered local pH levels and combined with excess [Ba^{2+}] in pore fluids to form $BaCO_3$. The initial batch experiments (Section 5.2.1) support the need for freshly activated fracture surfaces, as tests revealed precipitates only formed on surfaces that had been roughened right before submerging a shale chip in 2,000 ppm $BaCl_2$ solution (Figure 5.1b). In this particular system, precipitation may also be accelerated by the fact that the dissolving and precipitating

phases were both carbonates, which could lower the degree of supersaturation required to overcome energy barriers for nucleation.[18]

MS-01 confirmed that near-immediate $BaCO_3$ precipitation upon shearing is driven by high levels of [Ba^{2+}], as precipitates only formed with 180,000 ppm $BaCl_2$ in the pore fluid but not after shearing with 200 or 2,000 ppm $BaCl_2$ (at displacements of 0.5 mm and 1 mm, respectively). The lack of precipitation at lower [$BaCl_2$], despite the generation of significant fault gouge and associated reactive surface area in shearing, is consistent with batch testing (see Section 5.2.1) and stems from low levels of supersaturation. In forsterite carbonation experiments, Giammar et al.[37] similarly found that magnesite nucleation was inhibited below a critical SI. However, the delay in precipitation after raising the injectate [$BaCl_2$] to 180,000 ppm indicates that the process is not solely controlled by fluid saturation but also fracture geometry. No precipitates were observed in the xCT scan collected after the third shear step, which was completed following breakthrough of the 180,000 ppm $BaCl_2$ solution and resulted in further displacement to 1.5 mm (Figure 5.8b). Roughly an hour later radiographs evidenced brightening at the fracture inlet directly following dynamic shearing, which displaced the sample to 3.2 mm as confining pressure was released from 30 to 5 MPa. Precipitation at the inlet was confirmed in the final xCT scan, collected after hydroshearing and additional stress-permeability measurements with step changes in confining pressure. Precipitates also formed in other regions of the fracture, but only at narrow choke points where the fracture walls converged. While the fracture is difficult to resolve in the third xCT scan due to limited contrast between the dense $BaCl_2$-rich injectate and shale matrix, the fracture geometry was still relatively clean (i.e. with limited observable fragmentation), which may have limited nucleation. The shear steps that followed resulted in significantly more damage and fault gouge that may have stimulated precipitation by increasing available reactive surface area. In combination, results from the shear tests are consistent with the fact that reaction kinetics depend on both geochemical (i.e. pH, saturation state) and physical (i.e. specific surface area and accessibility of reactive surfaces) conditions.

The discrepancy in the amount of precipitate formed in similar shales that were subjected to the same shearing process may be partially attributable to the difference in carbonate content. Whereas US-01 contained 95% total carbonate (93% calcite and 2% dolomite) with the remainder comprised of quartz, US-02 had 82% calcite and a much higher clay content (10%). The exceptionally high carbonate content in US-01 allowed for rapid dissolution and pH buffering that

created favorable conditions for near-immediate precipitation in the freshly formed fractures. As expected, the shale with the lowest initial carbonate content (MS-01) produced the least amount of $BaCO_3$. In this test, precipitation only occurred after intensive shearing that resulted in significant damage in the fracture (Figure 5.9) and displacement to over 3 mm, whereas the Utica cores were only displaced to ~1 mm before precipitation began. Essentially, because there was less calcite in the Marcellus core, more rock needed to be 'crushed' to expose sufficient reactive surfaces for observable dissolution and precipitation to occur. An additional shear test with 180,000 ppm $BaCl_2$ on a calcite-poor dolomite core, which was excluded from this manuscript for clarity, produced no resolvable precipitates in x-ray radiography and minimal precipitation on fracture surfaces, likely due to the fact that dolomite dissolution kinetics are several orders of magnitude slower than calcite. A lack of precipitation in calcite-limited cores exposed to the same highly concentrated fluids and fractured under the same conditions corroborates that adequate reactive mineral content is necessary for precipitation induced by water-rock interactions. However, the fact that initial batch tests evidenced greater precipitation on marble cores than limestone with the same nearly pure calcite composition indicates that dissolution-precipitation reactions are influenced by other material properties beyond mineralogy that could not be defined in this study. Despite lesser extents of precipitation, both US-02 and MS-01 exhibited non-uniformity in the spatial distribution of $BaCO_3$ analogous to the uneven patterns observed in US-01. Factors driving this trend of strongly localized precipitation along fracture networks are further explored in Section 5.4.2.

5.4.2. Localized mineral precipitation

Figures 5.4(c, d), 5.6(c, d) and 5.8(b, c) compare 2D distributions of segmented fracture apertures and precipitates at select stress stages throughout US-01, US-02, and MS-01, respectively. The x axis represents distance along the direction of shearing and the z axis represents distance along the length of the core, with the values at each point reflecting the total fracture or precipitate width in the y-direction. Note that the aperture map in US-01 is of limited value because most fractures were filled with precipitates such that dimensions of actual apertures created in shearing are largely unknown.

Given the low permeability and connected porosity of shales that limit fluid accessibility in the bulk matrix, precipitation was limited to the fractures created in direct shearing. This is most clear in 3D renderings of the segmented precipitate and fracture space, where $BaCO_3$ aligns with the

single through-fracture generated in MS-01 and the two oblique through-fractures formed in US-02. Note that precipitation also occurred along the primary shear fracture in US-01 but a 3D segmentation of the fracture network is omitted because, as noted in Section 5.3.2, most of the original fracture space was filled with precipitates and thus was not captured by the post-reaction scan. The 3D segmentations also highlight differences in reactivity, as precipitation was weakest in the test with the largest fractures and lowest calcite content (MS-01). Precipitates generally formed in small apertures where rock:water ratios and reactive surface area were greatest. In US-02, precipitate segmentation indicated the maximum width of a fracture filled with precipitate was 0.6 mm (Figure 5.6c). An inverse relationship between saturation index and fracture aperture could be attributable to associated water:rock ratios, where injected Ba^{2+} and dissolved CO_3^{2-} are "diluted" within larger volumes (wide apertures) and concentrated within narrow apertures. Additionally, smaller fluid volumes in narrow fractures are more quickly buffered by $CaCO_3$ dissolution; $BaCO_3$ saturation is more readily achieved at higher pH levels because a greater extent of dissolved inorganic carbon is in the form of carbonate ions (CO_3^{2-}).

While precipitates appeared to fill larger apertures near the inlet in MS-01, the 2D maps are not a perfect representation as multiple narrower fractures stacked orthogonally to the main shear plane are summed and displayed as a single larger aperture. Cross-sections of the final xCT scan reveal that precipitation was strongest at narrow 'choke points' where opposing fracture surfaces came together and weaker along wider fractures, where precipitates occasionally coated the surfaces but did not bridge apertures (Figure 5.8e). This occurs in part because precipitation favors (and potentially requires) fresh reactive surfaces, which the xCT and SEM data indicated were generally more abundant in narrow choke points created in shear displacement than in wider open fractures characterized by tensile parting. Thin sections confirmed that smaller apertures are generally more favorable for precipitation but are not a complete indicator of where precipitates will form, even when mineralogy and fluid chemistry are relatively homogeneous. As evidenced by the BSE images in Figures 5.5, 5.7, and 5.9, precipitates often completely filled narrow microfractures (<10 μm) but were non-existent or limited to isolated coatings along walls of wider fractures. As noted in Section 5.4.1 these precipitates likely were not pure witherite but Ca-bearing $BaCO_3$, which has the same orthorhombic crystal structure as aragonite [35]. Precipitates were typically needle-like in structure, similar to observations in batch testing (Section 5.2.1), and grew orthogonal to fracture walls.

The uneven distributions of precipitates observed in xCT scans and microscale imaging are consistent with previous work linking initial small-scale heterogeneities to localized mineral reactions and associated structural alterations.[21,24,38] Here, precipitates formed non-uniformly in all experiments but followed different patterns of localization along primary flow paths. Precipitation was concentrated near the inlet and outlet of US-01; the fracture interior of US-02; and near the inlet of MS-01. Spatial patterns of precipitation are affected by the rates of local surface reactions relative to fluid transport, which can be quantified by the dimensionless Damköhler number (*Da*), as well as the relationship between advective and diffusive transport (Péclet number, *Pe*). While dimensionless numbers are not quantified here because relevant inputs (e.g. flow velocities and reaction rates) are highly variable and uncertain throughout the complex geometry of the shear-induced microfractures where *Pe* and *Da* would be of interest, some of the general trends observed in this work are consistent with prior studies that evaluated dimensionless numbers in more well-constrained systems. Detwiler[2] observed that low *Da* (i.e., reaction kinetics are slow relative to advective transport) led to uniform mineral dissolution but high *Da* promoted channelization, leaving outlying regions of the fracture unexposed to injected fluids. A recent study also found that the extent of preferential dissolution increased with increasing heterogeneities in velocity and mineral distributions in carbonate-rich cores.[39] In lattice-Boltzmann simulations on simplified porous media, Kang et al.[40] showed that under higher Péclet and Damköhler numbers (i.e., advective conditions), precipitates first clog smaller fractures and decrease with distance from the fluid inlet. Noiriel et al.[18] also found that column-scale precipitation rates depend strongly on saturation index, which is greatest near column inlets. These findings are consistent with the general trends observed along primary shear fractures in US-01 and MS-01, where preferential precipitation near the inlet indicates dissolution proceeded quickly upon contact with high-[$BaCl_2$] fluids and precipitates nucleated once a critical supersaturation threshold was achieved. Non-uniform precipitation was also likely influenced by non-uniform flow, where inaccessible regions were devoid of precipitates because the injected fluid was the only source of barium in the system.

In this study, strong precipitate localization observed in all tests resulted from heterogeneities in mineral composition and distribution; local pore fluid saturation; reactive surface areas of exposed grains; and fracture roughness and microstructure. BSE analyses indicated $BaCO_3$ formed almost exclusively on $CaCO_3$, which was the primary carbonate source in the host rocks and exhibits dissolution kinetics orders of magnitude faster than other minerals (e.g. clay, quartz) in

the shale matrices. Previous work has shown similar preferential nucleation of secondary phases occurs on the primary reactive minerals that contribute key constituent cations and is most pronounced in low-flow zones where transport is primarily controlled by diffusion.[38,41] Jones and Detwiler[24] also demonstrated that mineral heterogeneities can promote localized precipitation-induced aperture reductions, channeling flow into regions with lower reactivity. Here, rapid precipitation in the most reactive regions may have similarly diverted flow and slowed reaction progress, preventing further growth and accumulation of precipitates. In addition to preferential precipitation on reactive minerals, thin section analyses confirmed that precipitation was generally more favorable in more heavily sheared regions with extensive microfractures and fragmentation, but in many of these regions precipitates effectively cemented some fragments or fractures while not forming on adjacent ones (e.g. Figure 5.9).

Mineralogical and structural variations combined with transport limitations likely created or enhanced small-scale chemical heterogeneities with respect to saturation indices. Localized $CaCO_3$ dissolution promotes rapid pH buffering given the fast reaction kinetics of $CaCO_3$, but similarly rapid $BaCO_3$ precipitation could quickly consume released carbonate ions and neutralize surrounding fluids, precluding further $BaCO_3$ nucleation in adjacent regions with lower reactivity despite abundant Ba^{2+} in the pore fluid. In combination, mineralogical heterogeneities inherent to the core and structural heterogeneities generated during shearing create spatial inconsistencies in properties such as reactive surface area and saturation states, which in turn strongly impact precipitation kinetics. Even in homogeneous mineral systems, actual precipitation rates along fracture walls may vary in response to changes in conditions such as pressure, pore fluid composition, and the morphology of underlying mineral surfaces.[18] It is unclear how precipitate localization observed here would translate to similar mineralogies at reservoir scales, as previous work has suggested the significance of mineral spatial distributions diminishes when reactive minerals are abundant in bulk.[42] However, the idiosyncratic trend of precipitates forming haphazardly throughout fracture networks despite a relatively uniform thermodynamic drive highlights the challenges associated with predicting precipitation reactions even when reservoir conditions are well constrained.

5.4.3. Precipitation-induced permeability alterations

The initial permeability of the intact samples was immeasurable (<1 μD). After sample failure in the first Utica experiment (US-01), permeability increased near-instantaneously to 0.25 mD; fell slightly over the next 15 minutes as axial stress was held over 60 MPa; and peaked at 0.43 mD upon return to isotropic stress conditions at 3.5 MPa (Section 5.3.2). Over the remainder of the experiment, permeability decreased by 80% relative to its peak. Most of this reduction occurred within the first hour after initial shearing, concomitant with progressive infilling of precipitates within the fracture that was evidenced by the growth and intensification of bright regions in radiographs aligned with the shear plane. While the direct effects of precipitates on fracture permeability could not be delineated due to simultaneous changes in isotropic pressure, analysis of the post-reaction xCT scan indicates that precipitation filled substantial portions of the fracture network and likely obstructed fluid transport (Figures 5.4d and 5.4e). Extrapolation of the tail of the permeability curve indicated it would take roughly 45 hours for permeability to fall below 1 μD, which would essentially seal the fracture network.

In contrast to the notable permeability reductions observed in US-01, precipitation in the second Utica experiment (US-02) was less extensive and failed to definitively impact fluid transport. The rapid precipitation evidenced in xCT scans acquired directly after shearing may have contributed to the permeability reduction between 75 and 150 minutes (Figure 5.6a). Additionally, the select fracture filling observed in xCT scans could drive local permeability reductions that were not captured in bulk measurements across the entire specimen. Precipitate volumes and fracture permeability remained relatively stable for the remainder of the test, which involved a series of stepwise increases in effective stress as DI water continued to flow through the core. Menefee et al.[43] provide 3D videos of the segmentations (see Supporting Information) that highlight how precipitation led to conflicting permeability trends between the two Utica experiments; whereas smaller and more isolated pockets of $BaCO_3$ formed in US-02, leaving pathways open to continued injection, the abundance of precipitation along the entirety of the main fracture in US-01 would be expected to restrict flow.

In the final test, permeability increased following the initial direct shear steps (peaking around 280 mD) but dropped below 1 μD during the fourth shear (dynamic shearing). The third and fourth shear steps were both conducted with 18 weight percent $BaCl_2$ in the pore fluid but it is unclear whether the permeability reductions were attributable to precipitation, particularly near the fluid

inlet; clay mobilization and clogging; or changes in fracture geometry, such as compaction of asperities. While the final xCT scan revealed precipitates filling the fracture inlet, the exact timing of precipitation relative to permeability changes in MS-01 is unclear given that over 2 hours elapsed between the penultimate and final scans with multiple changes in direct shear and confining stress along with a switch to more dilute pore fluid (200 ppm $BaCl_2$) following hydroshearing (~180 minutes). However, the fact that these precipitates appeared in radiographs around the time of the permeability decline observed during dynamic shearing indicates they may have contributed to restricted flow, similar to the permeability reductions associated with precipitate accumulation at the fracture inlet and outlet in US-01. Although the overall extent of $BaCO_3$ was lowest in this experiment, preferential precipitation near the inlet could have resulted in a greater impact on permeability than the more dispersed precipitation in US-02.

While this study focused on how precipitation affects permeability, the rate and extent of precipitation may be correlated with initial fracture permeability. Following shear failure, permeability peaked around 0.43 mD in US-01 compared with 235 mD in US-02 and 280 mD in MS-01. The less apparent changes to permeability in US-02 and MS-01 may partly be a consequence of the high fracture permeability, which might require more precipitation to cause a significant change in permeability. The permeability values are consistent with observed differences in fracture apertures, which were smallest in US-01 (generally <0.3 mm in segmented fractures not filled with precipitates). In addition to larger average apertures, the mm-scale fracture network in US-02 was more extensive with two oblique fractures that spanned the entire length of the core. MS-01 only produced one main shear fracture but apertures were much larger, averaging ~1 mm parallel to the flow direction. Considering that precipitates formed preferentially where fracture walls converged in US-02 and MS-01, the narrow initial shear fractures created in US-01 likely established favorable conditions for precipitation along the entire fracture rather than at intermittent fracture constrictions.

5.4.4. 4D fracture and precipitate evolution

While the focus of this study was on geochemical reactions, US-02 concomitantly tested fracture evolution under increasing effective stress states. Total fracture and precipitate volumes across the core, calculated from the segmented xCT datasets (section 5.2.4), are plotted as a function of confining stress in Figure 5.10. Quantitatively, the total fracture volume across the core decreased by a factor of 4 from initial shearing at 3.5 MPa to the final step at 30 MPa while

precipitate volumes changed minimally; the slight apparent rise in precipitation in Figure 5.10 is consistent with variations in scan quality rather than a reflection of active precipitate growth. Visually, the near-immediate precipitation observed upon shearing with high-$BaCl_2$ fluid was followed by minimal growth for the duration of the experiment (Figure 5.6c), while fracture apertures notably closed with increasing confining stress (Figure 5.6d). Most changes occurred in narrower fractures, which visibly decreased in aperture with increasing stress and in some areas were essentially closed (i.e., apertures fell below the voxel resolution) by 30 MPa. As discussed in Section 5.4.2, narrow fractures were also where the majority of precipitation occurred. In actual systems where precipitates progressively accumulate due to continued exposure to reactive fluids, increasing stress could accelerate fracture sealing by mechanically reducing apertures as they are simultaneously filled with precipitates.

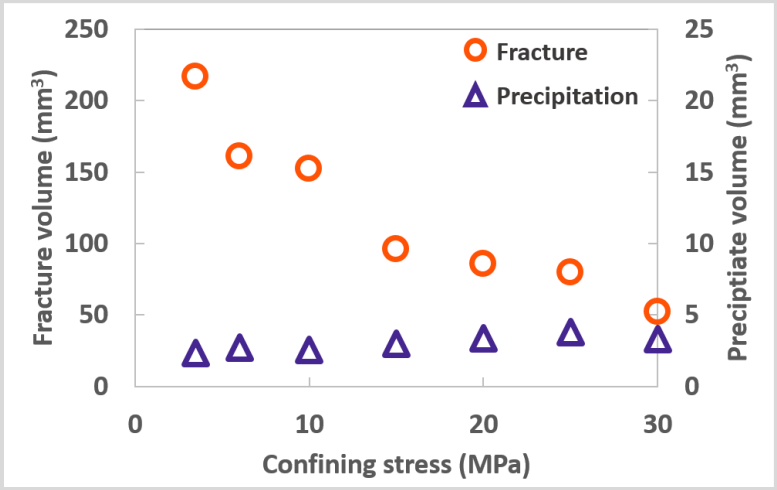

Figure 5.10. Changes in total fracture and precipitate volumes as a function of confining stress in US-02. Volumes were summed across the entire core based on segmented xCT datasets for each confining step.

Despite narrowing apertures and active precipitation, permeability did not decrease significantly in this test (Figure 5.5a). The dense precipitates may have served as proppants in some regions, creating effective asperities that resisted complete fracture closure. Prior work has demonstrated that secondary minerals can form in porous layers along fracture walls that prop open fractures without completely blocking fluid access.[8] In percolation experiments subjecting pre-fractured quartz-monzonite samples to calcite-saturated fluid, Aben et al.[44] similarly found that calcite precipitation reduced fracture volume but negligibly affected permeability. This was primarily due to the fact that most precipitation occurred in sheltered regions downstream of flow barriers such as fracture steps, kinks, and asperities, leaving main channels unobstructed, while calcite crystals replaced or supported asperities once they grew large enough to span fracture

walls.[44] In addition to location, the ability of secondary precipitates to maintain fracture permeability or structural integrity will depend on their ability to resist re-dissolution and relative rates of primary mineral dissolution. After injecting synthetic hydraulic fracturing fluid through a Marcellus shale core without acid, Vankeuren et al.[45] reported that the absence of acid-induced calcite dissolution resulted in net fracture volume reductions due to mixing-induced barite precipitation, which could either constrict flow or complement proppants to maintain fracture apertures over longer time frames. Conversely, dissolution in excess of precipitation can lead to asperity removal and fracture compaction[6,46] or channelization and fracture opening.[47,48] In addition to competing reactions, precipitates could be impacted by changes in environmental conditions such as temperature and pressure swings that were not explicitly evaluated in this study. While all experiments were conducted ~20°C, calcite exhibits retrograde solubility and thus may be more resistant to dissolution at the higher temperatures anticipated in most target reservoirs (50-70°C), while increasing $BaCO_3$ solubility with temperature could temper the speed and extent of precipitation observed in our low-temperature experiments. On the other hand, carbonate reaction kinetics increase with temperature, which could accelerate the rate and extent of both $CaCO_3$ dissolution and $BaCO_3$ precipitation in the system considered here. More generally, temperature-dependent mineral properties (e.g. solubility, reaction kinetics) will influence both the propensity of a secondary phase to form and its resistance to deformation over time. Further work is necessary to define conditions under which new precipitates are sufficiently recalcitrant to improve fracture stability (e.g. by counteracting asperity dissolution or mechanical compaction) and understand the mechanical implications of competing chemical processes under a range of reservoir conditions.

5.4.5. Implications for multi-scale modeling

Results from this work underscore several challenges associated with modeling reactive subsurface systems. As discussed in Section 5.4.2, key determinants of dissolution-precipitation reactions (e.g. specific surface area, surface reactivity, saturation index) are subject to strongly localized variations that are nearly impossible to resolve in complex microfracture networks. Prior work has also shown that detailed knowledge of fracture geometry is necessary to accurately calculate permeability and flow,[49] but sufficient resolution of apertures and mineral composition, particularly at fracture intersections, is difficult to achieve with realistic computational efficiency. Even if aperture distributions and geochemical conditions are well-constrained, our experiments demonstrate precipitation can occur inconsistently despite relatively uniform thermodynamic

drive, which further complicates application of simulation results. This was evidenced in 1D reactive transport models that were developed here to complement experimental results but ultimately omitted from this study because they added complexity with marginal utility. The 1D models failed to capture observed heterogeneities in precipitation patterns, predicting secondary minerals would automatically form where they were thermodynamically and kinetically favorable. This limitation stems partly from oversimplifications necessary to achieve computational efficiency in the simulations, such as distilling rough and complex fracture surfaces into single apertures and relying on published data for individual minerals that may not directly translate to heterogeneous systems. Integrating reactive transport and geomechanics into models from pore to continuum scales remains an open challenge in precipitation-dominated systems.

As discussed in the introduction, low-permeability formations rely on fracture flow rather than matrix flow and thus the location of precipitates (e.g., in dead-end zones vs. critical pore throats) along with the extent to which they coat or bridge fracture surfaces will drive long-term permeability changes that may inhibit fluid injection or production. In addition, precipitation on fracture walls may modify matrix-fracture communication, perhaps limiting transport of chemical or thermal constituents into the fracture network. To date, dissolution-precipitation reactions have been incorporated into pore network models to evaluate porosity-permeability evolution[21] but the resulting redistribution of mineral mass throughout fracture networks has not been fully captured in modeling efforts.[46] Yasuhara et al.[50] developed mechanistic models describing compaction of loose quartz aggregates that account for mass redistribution via dissolution between grains, diffusion from grain interfaces to pores, and precipitation on free faces and found that the dominant processes evolve with interconnected changes in stress, pore space, and grain contact area. Subsequent models of these processes in idealized fractures were validated with observational data from flow-through experiments on novaculite and limestone, but multiple fitting parameters were adjusted to achieve reasonable fits to experimental changes in apertures and effluent chemistry.[46] In our study, simulations would fail to predict the location of all precipitation reactions because two adjacent microfractures with equivalent apertures and geochemical conditions could exhibit conflicting behavior with respect to actual formation of precipitates. Effectively capturing spatial distributions of precipitates is extremely challenging without forcing or overly constraining input parameters, which diminishes the utility of the model by limiting applications to other systems or extensions to greater spatial and temporal scales. The latter may be the most significant issue, as

challenges associated with anticipating or even retroactively evaluating non-uniform precipitation at core scales will be exacerbated when extending modeling efforts to larger systems. Even if precipitation patterns can be effectively predicted at scale, the implications may be unclear, as different precipitates may have different effects on permeability depending on their unique crystal habit, but mineral-specific data necessary to improve precipitation-permeability relationships are limited.[51] While upscaling our core-scale results was beyond the scope of this study, prior work has indicated that pore-scale spatial heterogeneities in chemical and physical properties will impact continuum-scale reaction kinetics and need to be considered in reservoir models to more accurately predict precipitate localization.[52]

5.5. CONCLUSIONS

This study highlights the challenges associated with predicting geochemical reactions and consequent alterations in subsurface reservoirs exposed to reactive fluids. Optimizing experimental conditions for secondary mineralization resulted in rapid precipitation due to a combination of fast reaction kinetics, which were accelerated by high reactive surface areas generated in direct shearing, and artificially high levels of supersaturation that reduced nucleation energy barriers. In the most reactive system, precipitates quickly filled narrow apertures and blocked fluid transport sufficiently to reduce permeability by ~80% within hours of shear fracturing. The extent of precipitation in three different experiments presented here decreased with decreasing carbonate ($CaCO_3$) content in the shale matrix, but all experiments exhibited strong precipitate localization due to feedback among mineralogical, geochemical, and structural heterogeneities either inherent to the host rock or created during shear. Spatial distributions of precipitates are critical in low-permeability shales that rely on fractures for fluid flow, as even small volumes of precipitates can have pronounced impacts on long-term transport and injectivity if they coat fracture walls, form in narrow pore throats, or occur along critical flow paths.

Whereas most related experimental studies have focused on mixing-induced precipitation resulting from introduction of incompatible fluids, such as when barite scale forms following injection of sulfate-rich fluids into barium-rich reservoir fluids, we demonstrate that interactions between fluids and the surrounding rock are also significant factors in precipitation reactions but are objectively more difficult to predict and prevent. As such, subsurface fluid-rock interactions that have not been rigorously characterized at the pore- and core-scale are often oversimplified or overlooked in reservoir-scale modeling efforts. At the core scale, discrepancies in the timing,

extent, and distribution of precipitates formed in similar shales during these experiments reflect lingering idiosyncrasies associated with precipitation processes. Even when a secondary mineral is thermodynamically and kinetically favored to form throughout a given system, its nucleation and growth may be highly localized and depends on complex and dynamic feedback among geophysical and geochemical conditions that cannot be predicted *a priori*. Furthermore, where precipitates do form, resulting impacts to fluid transport and accessibility are driven by interconnected alterations to porosity, permeability, and grain size distributions. While this work focused on the role of geochemical reactions, geomechanical factors will also control the impact of precipitation on fluid transport through fracture systems. For example, Frash et al.[53] discuss several factors governing changes in fracture permeability including changing stress conditions and fracture reactivation but also emphasized that the behavior of fractures depended on the stress at which fractures were originally generated.

In a broader context, these results contribute to our understanding of how fractures respond to geochemical alterations under subsurface stress conditions. Precipitation reactions are still poorly understood but play key roles, both positive and negative, in efficient reservoir exploitation for existing and emerging energy applications. Most intuitively, sufficient quantities of precipitates can limit reservoir injectivity or productivity by clogging fractures and blocking critical fluid flow paths. However, precipitates can be desirable in applications such as geologic carbon storage, where CO_2 trapping through mineralization represents the most secure and permanent form of carbon sequestration.[54] Precipitation can also be leveraged for targeted permeability reduction in operations where fluid migration needs to be actively controlled, such as geologic carbon storage and enhanced geothermal energy production.[55] While our experiments indicated highly reactive reservoirs can promote sudden and extensive precipitation in the presence of reactive fluids that may lead to fracture sealing, observations also suggested that localized precipitates in less reactive systems can serve as effectual proppants that prevent compaction-driven fracture closure with increasing stress without completely sealing fractures from further flow. The rapid precipitation reactions observed here could also serve as analogs to natural systems where the ability of precipitates to counteract fracture sealing requires near-immediate rates of crystallization because closure stresses act instantaneously. Further work is needed to more thoroughly define conditions under which precipitates serve to maintain permeability, by propping or even propagating fractures, or reduce permeability through pore clogging and fracture sealing.

REFERENCES

(1) Pyrak-Nolte, L. J.; DePaolo, D. J.; Pietra, T. *Controlling Subsurface Fractures and Fluid Flow: A Basic Research Agenda*; USDOE Office of Science (SC)(United States), 2015.

(2) Detwiler, R. L. Experimental Observations of Deformation Caused by Mineral Dissolution in Variable-Aperture Fractures: Dissolution and Deformation in Fractures. *J. Geophys. Res. Solid Earth* **2008**, *113* (B8). https://doi.org/10.1029/2008JB005697.

(3) Yasuhara, H.; Elsworth, D. Compaction of a Rock Fracture Moderated by Competing Roles of Stress Corrosion and Pressure Solution. *Pure Appl. Geophys.* **2008**, *165* (7), 1289–1306. https://doi.org/10.1007/s00024-008-0356-2.

(4) McGuire, T. P.; Elsworth, D.; Karcz, Z. Experimental Measurements of Stress and Chemical Controls on the Evolution of Fracture Permeability. *Transp. Porous Media* **2013**, *98* (1), 15–34. https://doi.org/10.1007/s11242-013-0123-4.

(5) Polak, A.; Elsworth, D.; Liu, J.; Grader, A. S. Spontaneous Switching of Permeability Changes in a Limestone Fracture with Net Dissolution: Spontaneous Switching of Permeability Changes. *Water Resour. Res.* **2004**, *40* (3). https://doi.org/10.1029/2003WR002717.

(6) Ellis, B. R.; Fitts, J. P.; Bromhal, G. S.; McIntyre, D. L.; Tappero, R.; Peters, C. A. Dissolution-Driven Permeability Reduction of a Fractured Carbonate Caprock. *Environ. Eng. Sci.* **2013**, *30* (4), 187–193. https://doi.org/10.1089/ees.2012.0337.

(7) Walsh, S. D. C.; Du Frane, W. L.; Mason, H. E.; Carroll, S. A. Permeability of Wellbore-Cement Fractures Following Degradation by Carbonated Brine. *Rock Mech. Rock Eng.* **2013**, *46* (3), 455–464. https://doi.org/10.1007/s00603-012-0336-9.

(8) Lisabeth, H. P.; Zhu, W.; Kelemen, P. B.; Ilgen, A. Experimental Evidence for Chemo-Mechanical Coupling during Carbon Mineralization in Ultramafic Rocks. *Earth Planet. Sci. Lett.* **2017**, *474*, 355–367. https://doi.org/10.1016/j.epsl.2017.06.045.

(9) Noiriel, C.; Renard, F.; Doan, M.-L.; Gratier, J.-P. Intense Fracturing and Fracture Sealing Induced by Mineral Growth in Porous Rocks. *Chem. Geol.* **2010**, *269* (3–4), 197–209. https://doi.org/10.1016/j.chemgeo.2009.09.018.

(10) Deng, H.; Steefel, C.; Molins, S.; DePaolo, D. Fracture Evolution in Multimineral Systems: The Role of Mineral Composition, Flow Rate, and Fracture Aperture Heterogeneity. *ACS Earth Space Chem.* **2018**, *2* (2), 112–124. https://doi.org/10.1021/acsearthspacechem.7b00130.

(11) Garing, C.; Gouze, P.; Kassab, M.; Riva, M.; Guadagnini, A. Anti-Correlated Porosity–Permeability Changes During the Dissolution of Carbonate Rocks: Experimental Evidences and Modeling. *Transp. Porous Media* **2015**, *107* (2), 595–621. https://doi.org/10.1007/s11242-015-0456-2.

(12) Noiriel, C.; Gouze, P.; Madé, B. 3D Analysis of Geometry and Flow Changes in a Limestone Fracture during Dissolution. *J. Hydrol.* **2013**, *486*, 211–223. https://doi.org/10.1016/j.jhydrol.2013.01.035.

(13) Emmanuel, S.; Berkowitz, B. Mixing-Induced Precipitation and Porosity Evolution in Porous Media. *Adv. Water Resour.* **2005**, *28* (4), 337–344. https://doi.org/10.1016/j.advwatres.2004.11.010.

(14) Huerta, N. J.; Hesse, M. A.; Bryant, S. L.; Strazisar, B. R.; Lopano, C. L. Experimental Evidence for Self-Limiting Reactive Flow through a Fractured Cement Core: Implications for Time-Dependent Wellbore Leakage. *Environ. Sci. Technol.* **2013**, *47* (1), 269–275. https://doi.org/10.1021/es3013003.

(15) Beckingham, L. E. Evaluation of Macroscopic Porosity-Permeability Relationships in Heterogeneous Mineral Dissolution and Precipitation Scenarios: Evaluation of Permeability

Relationships. *Water Resour. Res.* **2017**, *53* (12), 10217–10230. https://doi.org/10.1002/2017WR021306.

(16) Emmanuel, S.; Ague, J. J.; Walderhaug, O. Interfacial Energy Effects and the Evolution of Pore Size Distributions during Quartz Precipitation in Sandstone. *Geochim. Cosmochim. Acta* **2010**, *74* (12), 3539–3552. https://doi.org/10.1016/j.gca.2010.03.019.

(17) Luhmann, A. J.; Tutolo, B. M.; Bagley, B. C.; Mildner, D. F. R.; Seyfried, W. E.; Saar, M. O. Permeability, Porosity, and Mineral Surface Area Changes in Basalt Cores Induced by Reactive Transport of CO_2-Rich Brine: Physical Changes from Reaction in Basalt. *Water Resour. Res.* **2017**, *53* (3), 1908–1927. https://doi.org/10.1002/2016WR019216.

(18) Noiriel, C.; Steefel, C. I.; Yang, L.; Bernard, D. Effects of Pore-Scale Precipitation on Permeability and Flow. *Adv. Water Resour.* **2016**, *95*, 125–137. https://doi.org/10.1016/j.advwatres.2015.11.013.

(19) Pruess, K.; Müller, N. Formation Dry-out from CO_2 Injection into Saline Aquifers: 1. Effects of Solids Precipitation and Their Mitigation. *Water Resour. Res.* **2009**, *45* (3). https://doi.org/10.1029/2008WR007101.

(20) Noiriel, C. Investigation of Porosity and Permeability Effects from Microstructure Changes during Limestone Dissolution. *Geophys. Res. Lett.* **2004**, *31* (24). https://doi.org/10.1029/2004GL021572.

(21) Nogues, J. P.; Fitts, J. P.; Celia, M. A.; Peters, C. A. Permeability Evolution Due to Dissolution and Precipitation of Carbonates Using Reactive Transport Modeling in Pore Networks. *Water Resour. Res.* **2013**, *49* (9), 6006–6021. https://doi.org/10.1002/wrcr.20486.

(22) Peuble, S.; Godard, M.; Luquot, L.; Andreani, M.; Martinez, I.; Gouze, P. CO_2 Geological Storage in Olivine Rich Basaltic Aquifers: New Insights from Reactive-Percolation Experiments. *Appl. Geochem.* **2015**, *52*, 174–190. https://doi.org/10.1016/j.apgeochem.2014.11.024.

(23) Zhang, C.; Dehoff, K.; Hess, N.; Oostrom, M.; Wietsma, T. W.; Valocchi, A. J.; Fouke, B. W.; Werth, C. J. Pore-Scale Study of Transverse Mixing Induced $CaCO_3$ Precipitation and Permeability Reduction in a Model Subsurface Sedimentary System. *Environ. Sci. Technol.* **2010**, *44* (20), 7833–7838. https://doi.org/10.1021/es1019788.

(24) Jones, T. A.; Detwiler, R. L. Fracture Sealing by Mineral Precipitation: The Role of Small-Scale Mineral Heterogeneity: Mineral Precipitation in Fractures. *Geophys. Res. Lett.* **2016**, *43* (14), 7564–7571. https://doi.org/10.1002/2016GL069598.

(25) Tartakovsky, A. M.; Redden, G.; Lichtner, P. C.; Scheibe, T. D.; Meakin, P. Mixing-Induced Precipitation: Experimental Study and Multiscale Numerical Analysis: Mixing-Induced Precipitation. *Water Resour. Res.* **2008**, *44* (6). https://doi.org/10.1029/2006WR005725.

(26) Carey, J. W.; Lei, Z.; Rougier, E.; Mori, H.; Viswanathan, H. Fracture-Permeability Behavior of Shale. *J. Unconv. Oil Gas Resour.* **2015**, *11*, 27–43. https://doi.org/10.1016/j.juogr.2015.04.003.

(27) Wildenschild, D.; Sheppard, A. P. X-Ray Imaging and Analysis Techniques for Quantifying Pore-Scale Structure and Processes in Subsurface Porous Medium Systems. *Adv. Water Resour.* **2013**, *51*, 217–246. https://doi.org/10.1016/j.advwatres.2012.07.018.

(28) Frash, L. P.; Carey, J. W.; Lei, Z.; Rougier, E.; Ickes, T.; Viswanathan, H. S. High-Stress Triaxial Direct-Shear Fracturing of Utica Shale and in Situ X-Ray Microtomography with Permeability Measurement: SHALE FRACTURE, MCT, AND PERMEABILITY. *J. Geophys. Res. Solid Earth* **2016**, *121* (7), 5493–5508. https://doi.org/10.1002/2016JB012850.

(29) Carey, J. W.; Frash, L. P.; Viswanathan, H. S.; others. Dynamic Triaxial Study of Direct Shear Fracturing and Precipitation-Induced Transient Permeability Observed by in Situ x-Ray Radiography. In *50th US Rock Mechanics/Geomechanics Symposium*; American Rock Mechanics Association, 2016.

(30) Weng, X.; Chuprakov, D.; Kresse, O.; Prioul, R.; Wang, H. Hydraulic Fracture-Height Containment by Permeable Weak Bedding Interfaces. *GEOPHYSICS* **2018**, *83* (3), MR137–MR152. https://doi.org/10.1190/geo2017-0048.1.

(31) Frash, L. P.; Carey, J. W.; Welch, N. J. Scalable En Echelon Shear-Fracture Aperture-Roughness Mechanism: Theory, Validation, and Implications. *J. Geophys. Res. Solid Earth* **2019**, *124* (1), 957–977. https://doi.org/10.1029/2018JB016525.

(32) Frash, L. P. *DIsco*; Los Alamos National Laboratory: Richard P. Feynman Center for Innovation: Los Alamos National Laboratory: Richard P. Feynman Center for Innovation, 2016.

(33) Steefel, C. I.; Appelo, C. A. J.; Arora, B.; Jacques, D.; Kalbacher, T.; Kolditz, O.; Lagneau, V.; Lichtner, P. C.; Mayer, K. U.; Meeussen, J. C. L.; Molins, S.; Moulton, D.; Shao, H.; Šimůnek, J.; Spycher, N.; Yabusaki, S. B.; Yeh, G. T. Reactive Transport Codes for Subsurface Environmental Simulation. *Comput. Geosci.* **2015**, *19* (3), 445–478. https://doi.org/10.1007/s10596-014-9443-x.

(34) Mavromatis, V.; van Zuilen, K.; Purgstaller, B.; Baldermann, A.; Nägler, T. F.; Dietzel, M. Barium Isotope Fractionation during Witherite (BaCO3) Dissolution, Precipitation and at Equilibrium. *Geochim. Cosmochim. Acta* **2016**, *190*, 72–84. https://doi.org/10.1016/j.gca.2016.06.024.

(35) Astilleros, J. M.; Pina, C. M.; Fernández-Dıaz, L.; Putnis, A. The Effect of Barium on Calcite 1014 Surfaces during Growth. *Geochim. Cosmochim. Acta* **2000**, *64* (17), 2965–2972.

(36) Gouze, P.; Luquot, L. X-Ray Microtomography Characterization of Porosity, Permeability and Reactive Surface Changes during Dissolution. *J. Contam. Hydrol.* **2011**, *120–121*, 45–55. https://doi.org/10.1016/j.jconhyd.2010.07.004.

(37) Giammar, D. E.; Bruant, R. G.; Peters, C. A. Forsterite Dissolution and Magnesite Precipitation at Conditions Relevant for Deep Saline Aquifer Storage and Sequestration of Carbon Dioxide. *Chem. Geol.* **2005**, *217* (3–4), 257–276. https://doi.org/10.1016/j.chemgeo.2004.12.013.

(38) Menefee, A. H.; Giammar, D. E.; Ellis, B. R. Permanent CO_2 Trapping through Localized and Chemical Gradient-Driven Basalt Carbonation. *Environ. Sci. Technol.* **2018**, *52* (15), 8954–8964. https://doi.org/10.1021/acs.est.8b01814.

(39) Al-Khulaifi, Y.; Lin, Q.; Blunt, M. J.; Bijeljic, B. Pore-Scale Dissolution by CO_2-Saturated Brine in a Multimineral Carbonate at Reservoir Conditions: Impact of Physical and Chemical Heterogeneity. *Water Resour. Res.* **2019**, *55* (4), 3171–3193. https://doi.org/10.1029/2018WR024137.

(40) Kang, Q.; Zhang, D.; Chen, S. Simulation of Dissolution and Precipitation in Porous Media: Dissolution and Precipitation in Porous Media. *J. Geophys. Res. Solid Earth* **2003**, *108* (B10). https://doi.org/10.1029/2003JB002504.

(41) Menefee, A. H.; Li, P.; Giammar, D. E.; Ellis, B. R. Roles of Transport Limitations and Mineral Heterogeneity in Carbonation of Fractured Basalts. *Environ. Sci. Technol.* **2017**, *51* (16), 9352–9362. https://doi.org/10.1021/acs.est.7b00326.

(42) Li, L.; Peters, C. A.; Celia, M. A. Effects of Mineral Spatial Distribution on Reaction Rates in Porous Media. *Water Resour. Res.* **2007**, *43* (1), n/a-n/a. https://doi.org/10.1029/2005WR004848.

(43) Menefee, A. H.; Welch, N. J.; Frash, L. P.; Hicks, W.; Carey, J. W.; Ellis, B. R. Rapid Mineral Precipitation During Shear Fracturing of Carbonate-Rich Shales. *J. Geophys. Res. Solid Earth* **2020**, *125* (6). https://doi.org/10.1029/2019JB018864.

(44) Aben, F. M.; Doan, M.-L.; Gratier, J.-P.; Renard, F. Experimental Postseismic Recovery of Fractured Rocks Assisted by Calcite Sealing: Experimental Recovery of Fractured Rocks. *Geophys. Res. Lett.* **2017**, *44* (14), 7228–7238. https://doi.org/10.1002/2017GL073965.

(45) Vankeuren, A. N. (P).; Hakala, J. A.; Jarvis, K.; Moore, J. E. Mineral Reactions in Shale Gas Reservoirs: Barite Scale Formation from Reusing Produced Water As Hydraulic Fracturing Fluid. *Environ. Sci. Technol.* **2017**, *51* (16), 9391–9402. https://doi.org/10.1021/acs.est.7b01979.

(46) Elsworth, D.; Yasuhara, H. Mechanical and Transport Constitutive Models for Fractures Subject to Dissolution and Precipitation. *Int. J. Numer. Anal. Methods Geomech.* **2010**, *34* (5), 533–549. https://doi.org/10.1002/nag.831.

(47) Luquot, L.; Gouze, P. Experimental Determination of Porosity and Permeability Changes Induced by Injection of CO2 into Carbonate Rocks. *Chem. Geol.* **2009**, *265* (1–2), 148–159. https://doi.org/10.1016/j.chemgeo.2009.03.028.

(48) Deng, H.; Peters, C. A. Reactive Transport Simulation of Fracture Channelization and Transmissivity Evolution. *Environ. Eng. Sci.* **2019**, *36* (1), 90–101. https://doi.org/10.1089/ees.2018.0244.

(49) Olson, J. E.; Laubach, S. E.; Lander, R. H. Combining Diagenesis and Mechanics to Quantify Fracture Aperture Distributions and Fracture Pattern Permeability. *Geol. Soc. Lond. Spec. Publ.* **2007**, *270* (1), 101–116.

(50) Yasuhara, H. A Mechanistic Model for Compaction of Granular Aggregates Moderated by Pressure Solution. *J. Geophys. Res.* **2003**, *108* (B11). https://doi.org/10.1029/2003JB002536.

(51) Xie, M.; Mayer, K. U.; Claret, F.; Alt-Epping, P.; Jacques, D.; Steefel, C.; Chiaberge, C.; Simunek, J. Implementation and Evaluation of Permeability-Porosity and Tortuosity-Porosity Relationships Linked to Mineral Dissolution-Precipitation. *Comput. Geosci.* **2015**, *19* (3), 655–671. https://doi.org/10.1007/s10596-014-9458-3.

(52) Li, L.; Peters, C. A.; Celia, M. A. Upscaling Geochemical Reaction Rates Using Pore-Scale Network Modeling. *Adv. Water Resour.* **2006**, *29* (9), 1351–1370. https://doi.org/10.1016/j.advwatres.2005.10.011.

(53) Frash, L. P.; Carey, J. W.; Ickes, T.; Porter, M. L.; Viswanathan, H. S. Permeability of Fractures Created by Triaxial Direct-Shear and Simultaneous x-Ray Imaging. In *American Rock Mechanics Association*; 2018.

(54) Matter, J. M.; Kelemen, P. B. Permanent Storage of Carbon Dioxide in Geological Reservoirs by Mineral Carbonation. *Nat. Geosci.* **2009**, *2* (12), 837–841. https://doi.org/10.1038/ngeo683.

(55) Plattenberger, D. A.; Ling, F. T.; Peters, C. A.; Clarens, A. F. Targeted Permeability Control in the Subsurface via Calcium Silicate Carbonation. *Environ. Sci. Technol.* **2019**, *53* (12), 7136–7144. https://doi.org/10.1021/acs.est.9b00707.

CHAPTER 6
Conclusions and Future Work

6.1. CONCLUSIONS AND IMPLICATIONS

This dissertation demonstrates that basalts can effectively trap CO_2 in the form of stable carbonate minerals under relevant geologic carbon storage conditions. The risk of CO_2 leakage has been one of the main impediments to the development of large-scale carbon capture and storage systems and this inherent capacity to permanently mineralize CO_2 could make basalts the most readily deployable GCS repositories. However, this work also indicates that CO_2-driven precipitation reactions may ultimately self-limit reservoir storage capacities as secondary minerals may preferentially form in narrow fractures or pore throats and restrict flow. In combination, the results advance our ability to predict the timing and extent of mineral precipitation reactions, which are notoriously difficult to reproduce in the lab under relevant subsurface conditions but remain critical to the development of energy production and carbon storage systems. Key findings from this dissertation are summarized here and directions for future work are mapped in Section 6.2.

Coupled experimental and modeling efforts identified key controls on the extent and spatial distribution of CO_2 mineralization reactions in natural basalt fracture systems. Transport limitations are particularly important, as advection-dominated flow drives net basalt dissolution while most long-term CO_2 trapping will occur in diffusion-limited regions of the basalt matrix and dead-end fractures. This result, in combination with recent pilot tests,[1,2] indicates that rapid carbonation at the wellbore is unlikely to prematurely shut down injection operations as most precipitation will occur long after injection has ended or in regions further away from injection zones. Mineral heterogeneity strongly influences the spatial distribution of precipitation reactions, leading to highly localized carbonation on primary minerals contributing key divalent cations, but has minimal bearing on the extent of carbonation, which will more strongly depend on bulk reactive mineral content. Low levels of salinity in injected fluids increased the extent of basalt dissolution, while greater alkalinity enhanced the extent of carbonation. Elevated temperatures increased both dissolution and carbonation rates, indicating reservoirs with strong geothermal

gradients will be advantageous for maximizing carbonation potential. However, elevated temperature and alkalinity also increased the extent of secondary clay precipitation in primary flow paths, which could compete with carbonate minerals for divalent cations and reduce injectivity over longer time frames. Experiments with packed beds of reactive silicate minerals also indicated that olivine carbonation may be limited by preferential hydration or serpentinization of dissolved Mg, as precipitation of Mg-carbonates is kinetically limited. Further work is necessary to define the impact of competing silicate alteration processes that form non-carbonate secondary minerals (e.g. clay weathering, serpentinization) on long-term carbonation efficiency.

Collectively, this work reveals how complex interactions between reservoir geochemistry and transport conditions drive the extent and spatial distribution of carbon mineralization reactions in basalt fractures, which will inform selection of storage sites and injection schemes that maximize CO_2 trapping potential. Complementary experiments and modeling efforts on both basalt and shale revealed that geochemical reactions induced by reactive fluid injection were strongly localized due to complex feedback among mineral, geochemical, and structural heterogeneities. Precipitates formed most extensively in regions with higher rock:water ratios (e.g. narrow apertures and pores) and where fluid transport was limited to diffusion. While experiments focused on natural basalt (Chapters 2-4) did not evidence any permeability alterations resulting from these reactions, triaxial shear experiments on carbonate-rich shales revealed that secondary mineral precipitation can dramatically impact fracture permeability, which ultimately controls fluid transport in tight reservoirs targeted for new forms low-carbon energy production and CO_2 sequestration. The shear experiments (Chapter 5) indicated that the spatial distribution of carbonate precipitates may be more important than the extent, as small quantities of precipitates at critical fracture contact points or intersections can completely obstruct flow. Predicting the timing and location of precipitation reactions is thus critical to safe injection and monitoring operations, but is nearly impossible to achieve *a priori* as the localized variations in chemical and structural conditions that drive localized precipitation cannot be resolved across reservoir scales. Additionally, the rapid precipitation leading to obstructive permeability reduction primarily occurred in complex freshly activated fractures rather than existing fracture systems that could be more readily characterized. Understanding the fundamental mechanisms that control the extent and location of geochemical reactions in the subsurface is critical to predicting the long-term implications of precipitates for reservoir permeability, fluid injectivity, and ultimate CO_2 sequestration capacity.

In a broader context, this dissertation highlights how precipitation reactions play critical roles, both positive and negative, in our ability to effectively utilize subsurface resources for emerging energy technologies. While precipitates are most commonly held as a nuisance to subsurface injection operations, as mineral scale deposits can damage or clog wellbores and are challenging to remove, precipitation can be desirable in applications such as CO_2 sequestration or in systems where fluid migration can be actively controlled through targeted permeability reduction. The results of this work compel further efforts to leverage precipitation reactions in novel ways that can reduce the environmental risks and impacts of subsurface energy systems.

6.2. DIRECTIONS FOR FUTURE WORK

The findings of this dissertation motivate several directions for future research, including:

Impacts of weathering on basalt carbonation

The shear tests in Chapter 5 revealed that precipitation occurs more rapidly in freshly activated fractures, especially compared to the relatively smooth and clean-cut fractures that were milled into the basalt samples prior to reactive fluid injection (Chapters 2-3). While reservoir stimulation (e.g. hydraulic fracturing) could be applied in the field to similarly generate fresh reactive fracture surfaces, more likely scenarios will involve direct subsurface injection due to the costs and risks associated with induced fracturing. Thus, most CO_2 flow and carbonation reactions will occur within existing subsurface fractures that have undergone physical and chemical weathering processes resulting from exposure to varying fluids and environmental conditions over long time frames. In particular, changes in temperature and reservoir chemistry can significantly alter both the mineralogy and accessibility of fracture surfaces; for example, dissolution and preferential leaching of cations can leave secondary silicate layers that obstruct fluid access to underlying reactive minerals. Clays that are already present in natural basalt may reduce surface reactivity by creating a barrier between CO_2-acidified fluid and underlying silicates, while the conversion of basalt minerals to clays during CO_2 injection compete with carbonates for divalent cations. As observed in Chapters 2 and 3, clays will also restrict flow by filling and blocking pores and fractures. Future experiments should compare carbonation in ‘fresh’ samples with samples that have been previously exposed to CO_2 and other fluids (e.g. high-salinity brines) commonly found in target reservoirs to evaluate the impacts of weathering-induced chemical and structural alterations on basalt dissolution and carbonation rates.

Offshore CO_2 mineralization

Continental basalts are more accessible to CO_2 emission sources, but in reality most of the world's mafic reservoirs and thus CO_2 mineralization potential are located offshore. While the logistics of CO_2 transport and sub-ocean storage are more challenging, offshore storage could be more widely accepted and readily deployable as the risks and consequences of leakage are even lower. Offshore storage may also provide opportunities to optimize CO_2 injection strategies, as seawater provides an effectively unlimited supply of water that could be used to pre-dissolve CO_2 and thereby accelerate the subsurface carbonation process. Preliminary reservoir modeling on sub-ocean basalts in the Cascadia basin has suggested that water-alternating-gas injection may accelerate CO_2 mineralization by increasing the dispersion of dissolved CO_2, thus increasing the total contact area between CO_2 and reactive mineral surfaces throughout the reservoir.[3] However, the specific impacts of seawater on CO_2-basalt-water interactions remain unclear. Salinity may enhance basalt dissolution kinetics (Chapter 2), while dissolved anions (e.g. SO_4^{2-}) may interact with dissolved cations that were present in reservoir brines or released during basalt dissolution to form mineral scales (e.g. $CaSO_4$) that can ultimately shut down injection operations. Differences in physicochemical processes should also be evaluated; for instance, sub-ocean reservoirs will be fully saturated, which may accelerate CO_2 solubility trapping and further reduce leakage risks.

These knowledge gaps could be addressed through integrated batch experiments and basin-scale modeling. Basalt carbonation experiments under salinity, temperature, and pressure conditions characteristic of sub-ocean reservoirs are needed to obtain and/or refine critical model inputs, such as the specific surface area and kinetic reaction rates of typical basalt silicates. Models should incorporate multiphase flow of CO_2 and brines along with geochemical reactions. Pending data availability, models can be calibrated and/or validated with field data from an emerging pilot project involving offshore CO_2 injection in the Cascadia basin. Reservoir simulations can then be conducted to systematically evaluate the most efficient and effective CO_2 injection schemes (e.g. pure CO_2 injection, aqueous CO_2 pre-dissolved in water, WAG with various numbers and durations of CO_2 and seawater injection cycles). Improving the accuracy of reservoir modeling in CO_2-brine systems will benefit both onshore and offshore CO_2 injection projects, particularly by discerning injection techniques that maximize CO_2 mineralization in a particular reservoir and limit inhibitory processes such as mineral scaling.

Life cycle impacts

As best practices for *in situ* CO_2 mineralization become more clear through integrated reservoir-scale modeling efforts and pilot injection tests, life cycle assessment and techo-economic analysis will be critical tools in charting the most environmentally favorable and logistically feasible CCS pathways. The cost of carbon capture is commonly held as rate-limiting, but storage costs can also vary widely depending on factors such as reservoir depth, site permitting and remediation requirements, transport distances, and long-term monitoring requirements. Results from the CarbFix project indicate pre-dissolving CO_2 in water can enhance carbonation rates and reduce leakage risks, but may cost over double direct CO_2 injection in conventional sedimentary basins and increase the energy penalty on CO_2 sources.[4] There may be tradeoffs between optimizing CO_2 mineralization efficiency (e.g. through reservoir stimulation or co-injecting buffering agents to accelerate carbonation rates) and the associated energy requirements, which will partially offset sequestered emissions. Additionally, full CCS with carbon mineralization may be limited by spatial disconnects between major CO_2 sources and basalt sinks, whereas sedimentary basins such as saline aquifers are ubiquitous. As noted above, offshore sites may offer greater storage capacities than any onshore option but pose added costs and environmental burdens in transporting CO_2 further and injecting it deeper. Systems-level environmental and economic analyses that incorporate risk can be applied to parse out tradeoffs between the enhanced storage security associated with carbonation in basalts and the relative simplicity and accessibility of storage in onshore sedimentary formations, namely saline aquifers and depleted oil and gas fields.

Reaction-driven cracking

While self-accelerating reaction-driven fracturing (or reactive cracking) is commonly held as the key to optimizing CO_2 trapping potential in basalt, no evidence of fracture propagation induced by carbonate precipitation was observed in the work presented here. A previous study reported experimental evidence of cracking during carbonation of sintered olivine at 200°C, but the fracture patterns were reminiscent of natural weathering and resulted from non-uniform volume expansion as precipitation caused the interior of a sintered wall to expand faster than the surfaces.[5] Other studies have demonstrated that volume-increasing mineral alteration and replacement reactions, such as hydration of CaO[6] or MgO,[7] can generate sufficient stress to induce fracturing, but these reactions are not direct analogues for natural basalt systems. Despite the lack of experimental evidence for reactive cracking under relevant GCS conditions in this dissertation and in any

previous studies to date, natural analogues indicate reactive cracking can drive near-complete carbonation in ultramafic rocks. For example, peridotites are often found to be completely hydrated (i.e. serpentinite) and less commonly completely carbonated (i.e. listvenite), attesting that olivine alteration reactions can proceed to completion in natural systems despite the tendency of secondary alteration products to self-limit continued reaction.[8] Listvenite outcrops in Oman likely formed at temperatures of 80-130°C and under low P_{CO2} (1-5 bar), suggesting the elevated P_{CO2} associated with CO_2 injection may further enhance carbonation rates. Full carbonation of peridotite reservoirs holds the potential to mineralize up to 10^8 $GtCO_2$,[9] but whether this process can occur under conditions and time frames relevant to anthropogenic CO_2 sequestration efforts remains unclear. Even if reactive cracking occurs, the low permeability of peridotites relative to basalt may ultimately limit CO_2 injectivity, and overall carbonation efficiency may be controlled by competition between the positive feedback induced by fracturing and negative feedback loops such as surface passivation or fracture blocking.[9] Peridotite carbonation experiments under a range of flow, chemical, and environmental conditions could help to isolate the conditions and time scales over which reactive cracking can occur and whether this phenomenon is unique to peridotites, as no evidence of self-sustaining carbonation has been observed in basalt or other mafic rocks.

Carbonation of olivine results in up to a 44% increase in solids volume and the associated conversion of chemical potential energy into work could generate enough stress to stimulate reactive fracturing.[10] Fundamentally, for the differential stress created by the precipitating mineral to initiate reactive cracking, the crystallization pressure (P_{crys}) must exceed the tensile strength of the surrounding rock. P_{crys} is proportional to the molar volume (V_m) and saturation state (ratio of ion activity product, Q, to equilibrium constant, K) of the precipitate according to the relationship first introduced by Correns:[11,12]

$$P_{crys} = \frac{RT}{V_m} ln\left(\frac{Q}{K}\right) \qquad \textbf{(Eqn. 6.1)}$$

The maximum crystallization pressures associated with olivine carbonation are on the order of 100 MPa depending on temperatures and pressures,[13] exceeding the tensile strength of natural basalt which typically ranges from 10-20 MPa.[14] Reactive cracking may also be supported by the exothermic nature of carbonation, which could sustain reaction rates after initial heating to create a positive feedback loop.[15] The theoretical potential for carbonation-induced fracturing motivates continued research to identify conditions necessary to induce and sustain reactive cracking.

Additional experiments in the direction of reactive cracking can focus on improving our understanding of analogue systems involving volume-increasing mineral replacement or alteration reactions that have been well-demonstrated to generate sufficient stress to fracture surrounding rock. For instance, during the hydration of periclase (MgO) to form brucite ($Mg(OH)_2$), Kuleci et al.[7] observed fracturing in a synthetic calcite matrix induced by swelling of the periclase grains. Jamveit et al.[16] found microfractures resulting from volume expansion during olivine serpentinization, which Plumper et al.[17] attribute to localized stresses in surface pertubations from anisotropic olivine dissolution. Jamtveit et al.[18] demonstrated that complex fragmentation processes drive leucite ($KAlSi_2O_6$) replacement by analcime ($NaAlSi_2O_6*H_2O$), whereby volume changes divide initial leucite crystals into progressively smaller volumes. This hierarchical fracturing process can continually generate fresh reactive surface area, leading to much faster bulk replacement rates than if the process were exclusively controlled by reactive transport.[18] High-temperature, high-pressure experiments involving MgO or CaO hydration within a natural rock matrix could further constrain physical and chemical conditions under reactive cracking occurs as well as necessary conditions for this feedback loop to be sustained. Fluids containing high levels of divalent carbonate-forming cations would further increase the likelihood of reactive cracking by increasing the initial carbonate saturation state, which would theoretically increase the achievable carbonate crystallization pressure (Eqn. 6.1). Reactive cracking also likely requires unique transport conditions with sufficient renewal of fluid access for dissolution to progress but sufficient residence time for precipitates to nucleate and grow. Experimental results should be incorporated into and interpreted with coupled geochemical-geomechanical models to better understand the onset and implications of reactive cracking in field-scale CO_2 injection operations.

Further work in this direction can complement ongoing efforts to understand reaction-driven cracking mechanisms, but these experiments may be difficult to interpret in the context of actual subsurface injection operations, especially with respect to CO_2 storage in natural basalts. While the above discussion demonstrates that reactive cracking is thermodynamically favorable in olivine-bearing basalt, the energy available for fracture-inducing work will be tempered by entropy changes and thermal diffusion during exothermic crystallization reactions.[8] Additionally, volume-expanding reactions must be rapid to induce fracturing before stress can be relieved by viscous deformation of precipitating phases.[19] Thus, while additional work could elucidate conditions and time scales under which reactive cracking occurs in natural basalts, fracture propagation requires

a combination of near-instantaneous rates of carbonate precipitation (with significant volume expansion) and extremely high crystallization pressures (exceeding the tensile strength of basalt) that may be irrelevant to engineered CO_2 mineralization systems.

Geochemical-geomechanical feedback

Chapter 5 highlighted how new fracture formation can significantly enhance the rate and extent of geochemical reactions through increased fluid access and generation of rock fragments with high reactive surface area. However, it remains unclear how stress conditions and fracture mechanics influence mineral reactivity or how geochemical reactions impact mechanical properties that control fracture initiation, stability, and propagation. Complex feedback among flow, mechanics, and geochemical reactions can result in significant changes to fracture connectivity and flow behavior, such as short-circuiting or blocking flow. Further work is needed to understand feedback among these processes and define conditions under which coupled geochemical-geomechanical interactions may limit or enhance fluid transport. The long-term implications of precipitation reactions also remain poorly understood as stress-induced changes in fracture stability (e.g. through mechanical compaction or shear failure) can result in redissolution and distribution of secondary mineral phases. Additional work is needed to more thoroughly define scenarios under which precipitates can serve to maintain fracture permeability, such as by propping open or propagating fractures, or reduce permeability through fracture sealing. Predicting how fracture flow behavior evolves in response to interplay among fluid chemistry and external stressors is notoriously difficult but will be critical to advancing subsurface technologies for low-carbon energy production and large-scale CO_2 sequestration.

REFERENCES

(1) Matter, J. M.; Stute, M.; Snaebjornsdottir, S. O.; Oelkers, E. H.; Gislason, S. R.; Aradottir, E. S.; Sigfusson, B.; Gunnarsson, I.; Sigurdardottir, H.; Gunnlaugsson, E.; Axelsson, G.; Alfredsson, H. A.; Wolff-Boenisch, D.; Mesfin, K.; Taya, D. F. d. l. R.; Hall, J.; Dideriksen, K.; Broecker, W. S. Rapid Carbon Mineralization for Permanent Disposal of Anthropogenic Carbon Dioxide Emissions. *Science* **2016**, *352* (6291), 1312–1314. https://doi.org/10.1126/science.aad8132.

(2) McGrail, B. P.; Schaef, H. T.; Spane, F. A.; Cliff, J. B.; Qafoku, O.; Horner, J. A.; Thompson, C. J.; Owen, A. T.; Sullivan, C. E. Field Validation of Supercritical CO_2 Reactivity with Basalts. *Environ. Sci. Technol. Lett.* **2017**, *4* (1), 6–10. https://doi.org/10.1021/acs.estlett.6b00387.

(3) Goldberg, D.; Aston, L.; Bonneville, A.; Demirkanli, I.; Evans, C.; Fisher, A.; Garcia, H.; Gerrard, M.; Heesemann, M.; Hnottavange-Telleen, K.; Hsu, E.; Malinverno, C.; Moran, K.; Park, A.-H. A.; Scherwath, M.; Slagle, A.; Stute, M.; Weathers, T.; Webb, R.; White, M.; White, S. Geological Storage of CO2 in Sub-Seafloor Basalt: The CarbonSAFE Pre-Feasibility Study Offshore Washington State and British Columbia. *Energy Procedia* **2018**, *146*, 158–165. https://doi.org/10.1016/j.egypro.2018.07.020.

(4) Gislason, S. R.; Broecker, W. S.; Gunnlaugsson, E.; Snæbjörnsdóttir, S.; Mesfin, K. G.; Alfredsson, H. A.; Aradottir, E. S.; Sigfusson, B.; Gunnarsson, I.; Stute, M.; Matter, J. M.; Arnarson, M. Th.; Galeczka, I. M.; Gudbrandsson, S.; Stockman, G.; Boenisch, D. W.-; Stefansson, A.; Ragnheidardottir, E.; Flaathen, T.; Gysi, A. P.; Olssen, J.; Didriksen, K.; Stipp, S.; Menez, B.; Oelkers, E. H. Rapid Solubility and Mineral Storage of CO2 in Basalt. *Energy Procedia* **2014**, *63*, 4561–4574. https://doi.org/10.1016/j.egypro.2014.11.489.

(5) Zhu, W.; Fusseis, F.; Lisabeth, H.; Xing, T.; Xiao, X.; De Andrade, V.; Karato, S. Experimental Evidence of Reaction-Induced Fracturing during Olivine Carbonation: Fracturing During Olivine Carbonation. *Geophys. Res. Lett.* **2016**, *43* (18), 9535–9543. https://doi.org/10.1002/2016GL070834.

(6) Lambart, S.; Savage, H. M.; Robinson, B. G.; Kelemen, P. B. Experimental Investigation of the Pressure of Crystallization of $Ca(OH)_2$: Implications for the Reactive Cracking Process. *Geochem. Geophys. Geosystems* **2018**, *19* (9), 3448–3458. https://doi.org/10.1029/2018GC007609.

(7) Kuleci, H.; Ulven, O. I.; Rybacki, E.; Wunder, B.; Abart, R. Reaction-Induced Fracturing in a Hot Pressed Calcite-Periclase Aggregate. *J. Struct. Geol.* **2017**, *94*, 116–135. https://doi.org/10.1016/j.jsg.2016.11.009.

(8) Kelemen, P. B.; Hirth, G. Reaction-Driven Cracking during Retrograde Metamorphism: Olivine Hydration and Carbonation. *Earth Planet. Sci. Lett.* **2012**, *345–348*, 81–89. https://doi.org/10.1016/j.epsl.2012.06.018.

(9) Kelemen, P.; Benson, S. M.; Pilorgé, H.; Psarras, P.; Wilcox, J. An Overview of the Status and Challenges of CO2 Storage in Minerals and Geological Formations. *Front. Clim.* **2019**, *1*, 9. https://doi.org/10.3389/fclim.2019.00009.

(10) Power, I. M.; Harrison, A. L.; Dipple, G. M.; Wilson, S. A.; Kelemen, P. B.; Hitch, M.; Southam, G. Carbon Mineralization: From Natural Analogues to Engineered Systems. *Rev. Mineral. Geochem.* **2013**, *77* (1), 305–360. https://doi.org/10.2138/rmg.2013.77.9.

(11) Correns, C. W. Growth and Dissolution of Crystals under Linear Pressure. *Discuss. Faraday Soc.* **1949**, *5*, 267–271.

(12) Beinlich, A.; Austrheim, H. In Situ Sequestration of Atmospheric CO2 at Low Temperature and Surface Cracking of Serpentinized Peridotite in Mine Shafts. *Chem. Geol.* **2012**, *332–333*, 32–44. https://doi.org/10.1016/j.chemgeo.2012.09.015.

(13) Kelemen, P. B.; Savage, H.; Hirth, G. Reaction-Driven Cracking During Mineral Hydration, Carbonation and Oxidation. In *Poromechanics V*; American Society of Civil Engineers: Vienna, Austria, 2013; pp 823–826. https://doi.org/10.1061/9780784412992.099.

(14) Schultz, R. A. Limits on Strength and Deformation Properties of Jointed Basaltic Rock Masses. *Rock Mech. Rock Eng.* **1995**, *28* (1), 1–15. https://doi.org/10.1007/BF01024770.

(15) Kelemen, P. B.; Matter, J. In Situ Carbonation of Peridotite for CO2 Storage. *Proc. Natl. Acad. Sci.* **2008**, *105* (45), 17295–17300.

(16) Jamtveit, B.; Malthesorenssen, A.; Kostenko, O. Reaction Enhanced Permeability during Retrogressive Metamorphism. *Earth Planet. Sci. Lett.* **2008**, *267* (3–4), 620–627. https://doi.org/10.1016/j.epsl.2007.12.016.

(17) Plümper, O.; Røyne, A.; Magrasó, A.; Jamtveit, B. The Interface-Scale Mechanism of Reaction-Induced Fracturing during Serpentinization. *Geology* **2012**, *40* (12), 1103–1106. https://doi.org/10.1130/G33390.1.

(18) Jamtveit, B.; Putnis, C. V.; Malthe-Sørenssen, A. Reaction Induced Fracturing during Replacement Processes. *Contrib. Mineral. Petrol.* **2009**, *157* (1), 127–133. https://doi.org/10.1007/s00410-008-0324-y.

(19) Kelemen, P. B.; Matter, J.; Streit, E. E.; Rudge, J. F.; Curry, W. B.; Blusztajn, J. Rates and Mechanisms of Mineral Carbonation in Peridotite: Natural Processes and Recipes for Enhanced, in Situ CO_2 Capture and Storage. *Annu. Rev. Earth Planet. Sci.* **2011**, *39* (1), 545–576. https://doi.org/10.1146/annurev-earth-092010-152509.

APPENDIX A

Core Flooding Experiments

A1. CORE FLOODING SYSTEM OVERVIEW

To perform the experiments in Chapters 2-4 of this dissertation, two high-temperature, high-pressure core flooding systems were constructed at the University of Michigan. The first features a stainless steel biaxial core holder (or reactor) and the second a composite carbon fiber triaxial reactor with working pressures up to 6,000 psi (Core Laboratories). Both reactors are designed to inject fluids through geologic core samples (0.5 to 1" diameter) under relevant subsurface stress conditions. In the biaxial reactor, a floating distribution plug provides constant contact with the core during compression, whereas stainless steel spacers must be added in the triaxial reactor to accommodate varying sample lengths. This section will focus on the design and operation of the biaxial flow system, which was used for all published experiments; however, the triaxial system essentially functions in the same way with the exception that the reactor enables independent control of axial and radial confining stresses. A schematic overview of the biaxial system is provided in Figure A1 and its operation is detailed below.

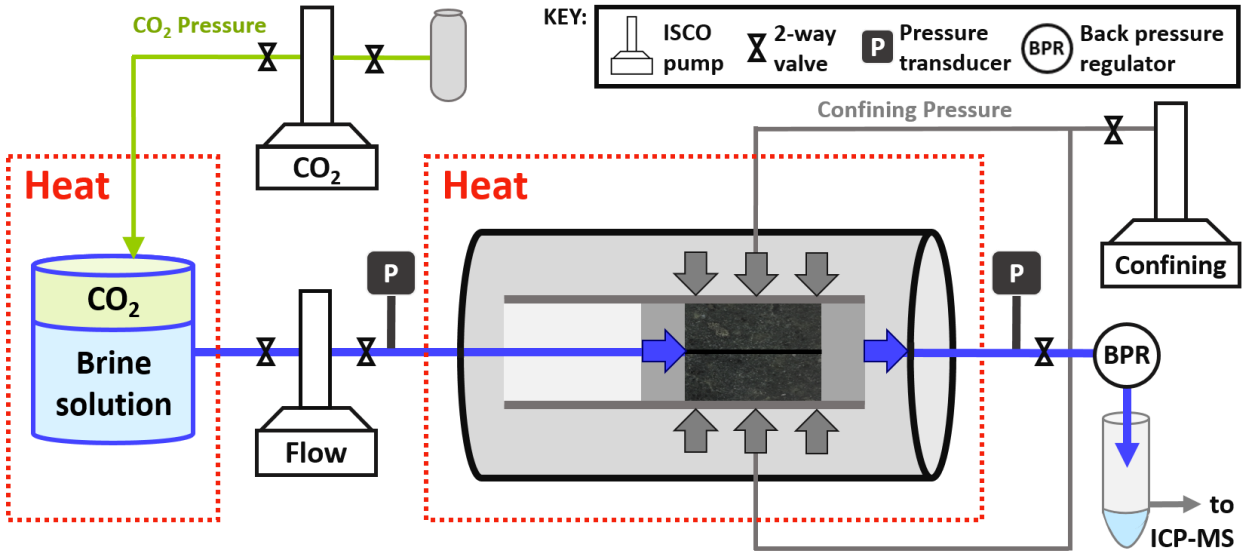

Figure A1. Schematic overview of high-temperature, high-pressure biaxial core flooding system

A2. BIAXIAL CORE FLOODING SYSTEM COMPONENTS

As depicted in Figure A1, the setup includes a stainless steel 600-mL batch reactor with working pressure up to 5,000 psi (Parr Instrument) to equilibrate fluids prior to injection. Flow lines consist of 1/8" or 1/16" 316 stainless steel tubing pressure-rated to 8,500 and 12,000 psi, respectively (Swagelok Company). All fittings and valves are also comprised of Swagelok 316 stainless steel and are rated from 8,000 psig (for 1/4" fittings) to 11,000 psig (1/16"). Pressure relief valves are set up to 6,000 psi. Pressure transducers (WIKA Instrument Corporation) and gages (Swagelok Company) are installed upstream and downstream of the reactor to monitor differential pressure changes. The transducers are connected to a data acquisition (DAQ) board (National Instruments) and pressures are logged in LabVIEW, which was calibrated to convert voltage signals from the transducers into corresponding pressure readings. System pressure is controlled with a back-pressure regulator (Swagelok Company, $C_v = 0.06$), which also allows for continuous effluent sample collection (Section A4) without disrupting the fluid injection rate. The batch and biaxial reactors are wrapped with a beaker heater connected to a temperature control box (BriskHeat), which maintains internal temperatures within ±1°C of the set point based on feedback from an internal thermocouple (Type K, Omega Engineering). Note that during experiments, the insulation tape is also wrapped around the reactors and beaker heaters to minimize heat loss. Fluid pressure and flow are controlled by high-pressure syringe pumps (Teledyne Isco).

A3. BIAXIAL CORE FLOODING SYSTEM OPERATION

In all experiments, injected fluids are first equilibrated with CO_2 in the batch reactor for ~24 hours under experimental temperature and pressure conditions using a 500-mL syringe pump (500hp, Teledyne Isco) to maintain constant CO_2 pressure in the headspace. Saw-cut core samples are secured in chemical-resistant heat shrink tubing to prevent shifting of the two halves during reaction. The assembled cores are then placed in a viton sleeve, which is positioned in the biaxial core holder between the floating distribution plug and end cap. The confining pressure is raised to 20 MPa (3,000 psi) using a 266-mL syringe pump (260D,Teledyne Isco) and the core holder is heated to the experimental temperature. Prior to starting each experiment, the injected fluid (without CO_2) is used to pressurize the system and set the back pressure slightly above the target PCO_2 to prevent in-line CO_2 degassing. Initial fracture permeability is then measured by injecting at a high flow rate (10 mL/hr) for several minutes, recording differential pressure (as measured by

the upstream and downstream transducers) when readings stabilize, and repeating this process at progressively lower flow rates. After permeability testing, any remaining fluid is injected through the core and the flow-through pump is refilled with CO_2-acidified fluid from the batch reactor. This fluid is then injected at a higher flow rate (5-10 mL/hr) until CO_2 breakthrough is achieved, at which point the pump is set to the desired flow rate and the experiment begins. Effluent samples are collected continuously over 1- or 2-hr intervals for the first 8-12 hours and then in regular increments (e.g., one every 8-10 hrs) for the duration of the experiment. Differential pressure is continuously logged throughout each experiment (National Instruments, LabVIEW 2013).

A4. Effluent Sampling and Calculations

Effluent chemistry is monitored throughout all core flooding experiments to provide insight on primary mineral dissolution and secondary mineral saturation. Aliquots of each sample are acidified with HNO3 to a pH < 1 and analyzed via inductively coupled plasma-mass spectroscopy (ICP-MA; 7900 Agilent Technologies) to measure concentrations of major cations, including Ca^{2+}, Mg^{2+}, Fe^{2+}, Si^{4+}, Na^{+}, K^{+}, and Al^{3+}. In the experiments conducted in Chapter 2, the flow rate was high enough that sufficient sample volumes were obtained to take a second aliquot for analysis of major anions (SO_4^{2-}, Cl^{-}) via ion chromatography (DX-100 IC, Dionex). Based on the effluent chemistry data, solution pH was calculated at each sampling point from charge balances under the constraint of electroneutrality. CO_2 solubility under experimental conditions was calculated based on the thermodynamic model presented by Duan and Sun.[1] Aqueous carbonate speciation is governed by the following reactions, where aqueous CO_2 phases are denoted as $H_2CO_3^*$:

$$H_2CO_3^* = H^+ + HCO_3^- \qquad K_{a1}$$

$$HCO_3^- = H^+ + CO_3^{2-} \qquad K_{a2}$$

Equilibrium constants for water (K_w) and carbonates (K_{a1}, K_{a2}) were adjusted to experimental temperatures and pressures using SUPCRT92BL with the DPRONS92BL thermodynamic database.[2,3] The difference between measured cation and anion concentrations was attributed to bicarbonate, which can be calculated in terms of the total amount of carbon (C_T) in the system:

$$HCO_3^- = C_T * \{[H^+](K_{a1})^{-1} + 1 + K_{a2}[H^+]^{-1}\}^{-1}$$

pH was then calculated from electroneutrality (i.e., charges in solution sum to 0). Activity corrections for experiments with higher ionic strength were estimated with the Davies equation.

A5. Fracture Permeability Calculations

Fracture permeability is estimated using the cubic law, where the fracture walls are modeled as parallel plates separated by a uniform aperture.[4] This equivalent hydraulic aperture (b_h) can be calculated from the measured pressure differential along the core sample (ΔP); length (L) and width (w) of the core; viscosity of the fluid (μ); and volumetric flow rate (Q):[5]

$$b_h = \left[\frac{12\mu LQ}{\Delta P w}\right]^{1/3}$$

Permeability can be derived by applying Darcy's law for flow through porous media to the conceptual fracture bounded by parallel plates:[4]

$$Q = \frac{-kLb_h\Delta P}{\mu}$$

Combining equations 4 and 5, fracture permeability can then be calculated as:

$$k = \frac{{b_h}^2}{12}$$

Note that in the core flooding experiments presented in Chapters 2-4, permeability data are not reported because no measurable pressure changes (i.e. outside the sensitivity of the transducers, ±10-15 psi or ±0.07-0.1 MPa) were observed.

References

(1) Duan, Z.; Sun, R. An Improved Model Calculating CO2 Solubility in Pure Water and Aqueous NaCl Solutions from 273 to 533 K and from 0 to 2000 Bar. *Chem. Geol.* **2003**, *193* (3–4), 257–271. https://doi.org/10.1016/S0009-2541(02)00263-2.

(2) Johnson, J. W.; Oelkers, E. H.; Helgeson, H. C. SUPCRT92: A Software Package for Calculating the Standard Molal Thermodynamic Properties of Minerals, Gases, Aqueous Species, and Reactions from 1 to 5000 Bar and 0 to 1000 C. *Comput. Geosci.* **1992**, *18* (7), 899–947.

(3) Zimmer, K.; Zhang, Y.; Lu, P.; Chen, Y.; Zhang, G.; Dalkilic, M.; Zhu, C. SUPCRTBL: A Revised and Extended Thermodynamic Dataset and Software Package of SUPCRT92. *Comput. Geosci.* **2016**, *90*, 97–111. https://doi.org/10.1016/j.cageo.2016.02.013.

(4) Zimmerman, R. W.; Bodvarsson, G. S. Hydraulic Conductivity of Rock Fractures. *Transp. Porous Media* **1996**, *23* (1), 1–30.

(5) Ellis, B. R.; Fitts, J. P.; Bromhal, G. S.; McIntyre, D. L.; Tappero, R.; Peters, C. A. Dissolution-Driven Permeability Reduction of a Fractured Carbonate Caprock. *Environ. Eng. Sci.* **2013**, *30* (4), 187–193. https://doi.org/10.1089/ees.2012.0337.

APPENDIX B

Supporting Information for Chapter 2

B1. SPECIFIC SURFACE AREA CALCULATIONS

Initial estimates for specific surface areas were calculated taking mineral grains as smooth spheres with average diameters of 122 μm, 123 μm, 99 μm, and 143 μm for olivine, pyroxene, plagioclase, and serpentine, respectively. Although the K-rich matrix had no discernible grains, the average phenocryst size of the samples (122μm) was used to calculate a specific surface area for modeling K-feldspar. Effective surface areas for each mineral were first calculated from the diameters (d) as $6d^{-1}$, a modification accounting for surface site reactivity,[1,2,3] and divided by mineral densities to obtain specific surface areas in m^2/g. These values were then fine-tuned where appropriate to improve the fit of the model to experimental results with a focus on aligning the divalent metal cations necessary for mineral carbonation (Ca^{2+}, Mg^{2+}, Fe^{2+}). For instance, the calculated SSA for diopside significantly underestimated Ca and Mg dissolution and failed to match the sharp initial spike observed experimentally. Assigning a larger specific surface area to a fraction (18%) of the diopside content while maintaining a lower value for the remainder effectively captured this early peak corresponding to rapid dissolution of finer surface particles. While a fraction of high-SSA diopside was included in the initial 'calibrated' model to simulate experimental data, it was excluded from subsequent models extending beyond experiments (i.e. only the smaller SSA value accounting for the majority of diopside in the calibrated model was applied to the models discussed in the results of the manuscript). Reducing the SSA of fayalite by an order of magnitude from the calculated geometric value and adjusting the reaction rate, as described in Section B2, effectively reproduced the Fe data (Figure 2.5, Section 2.4.3 of the dissertation). Raising the SSA for antigorite by an order of magnitude from that of forsterite also improved the model fit and is consistent with higher reported SSA's for serpentines[4] relative to unserpentinized olivine.[5,6,7] The calculated SSA values were applied for all other minerals.

As noted in the manuscript and further detailed in the CrunchTope user's manual, secondary mineral precipitation begins when a threshold mineral volume fraction is exceeded. At this point, the bulk surface area of the mineral can be calculated based on its volume fraction and a user-specified SSA. In the models presented here, secondary minerals were assigned BET surface areas reported in literature[8] with the exception of amorphous silica. Previous studies have incorporated large surface areas for amorphous silica due to its small size in solution. Carroll et al.[9] reported BET surface areas ranging from 50-280 m^2/g, several orders of magnitude greater than BET estimates for the other secondary minerals. However, the favorability of relatively rapid amorphous silica precipitation in the model introduced instability when specific surface areas of greater order than 10^{-2} m^2/g were applied. A value of 0.0225 m^2/g was selected, which corresponds to BET surface area for quartz determined by Tester et al.[10] The actual volume of SiO_2(am) precipitate formed was not a key result in this study and did not impact precipitation of other secondary minerals because the models do not consider potential passivating effects.

B2. MODEL CALIBRATION

Input parameters selected in model calibration are documented in Section 2.3.2 of the dissertation (see Table 2.2), but further details on their derivation are provided here. Direct application of the bulk mineral composition determined from initial sample characterization[11] failed to adequately reproduce effluent chemistry trends from the flow-through experiment used in calibration. This result is likely two-fold: the mineral compositions along the surface and main flow path could deviate from bulk mineralogy, and the incongruency of dissolution differed among primary minerals. To this end, primary mineral volume fractions were fine-tuned to within 2-3% of the bulk sample composition determined in prior work[12] to match the magnitudes of effluent concentrations. Calibration was achieved by primarily adjusting the bulk composition, as described in this section, and individual SSA's, as discussed in Section B1.

While unserpentinized olivine accounted for only 1% of initial sample composition, a higher percentage was included in the model as a combination of its two end members, forsterite and fayalite. The olivine in the serpentinized core was characterized as Mg-rich (Fo_{70}), but olivine was modeled as 75% fayalite (Fe_2SiO_4) and 25% forsterite (Mg_2SiO_4) to match effluent Fe and Mg concentrations. In the core-flooding experiment, Fe likely dissolved from both pyroxenes and olivines, but Fe-bearing pyroxene failed to replicate observed Fe trends that contrast the sharp

initial peaks and declines to a quasi steady-state observed for Ca and Mg.[11] To simplify the model, only fayalite was included as an Fe source, but its rapid dissolution kinetics still failed to capture the absence of an initial spike observed experimentally. While fayalite is known to dissolve faster than forsterite at far from equilibrium conditions, the reaction rate of fayalite in the models was calculated by setting its rate at 25°C (k_{25}) to that of forsterite. For all other minerals, reaction rates selected from literature were used directly (Table 2.2). The SSA of fayalite was also adjusted to optimally match the Fe data, as noted in Section B1.

The plagioclase in the serpentinized basalt sample was characterized as labradorite, which was modeled as 60% anorthite ($CaAl_2Si_2O_8$) and 40% albite ($NaAlSi_3O_8$) in accordance with the stoichiometric ratios of Ca^{2+} and Na^+ determined via previous wavelength-dispersive spectroscopy.[12] To better emulate the sample reactivity, kinetic data for labradorite was applied for both plagioclase end-members. Ca-rich pyroxene was modeled as diopside ($CaMgSi_2O_6$), while the K-rich matrix was taken as K-feldspar ($KAlSi_3O_8$) due to the need for a discrete mineral input in the code. Serpentine was modeled as antigorite containing only Mg in the octahedral sites ($Mg_3SiO_5(OH)_4$) because including Fe substitutions failed to influence effluent Fe concentrations due to slow reaction kinetics.

Effluent Si, Na, Al, and K concentrations could only be matched in the models by increasing cation:silica ratios for plagioclase and K-feldspar, likely due to incongruent dissolution during the flow-through experiment. However, altering mineral stoichiometry in the database was purposefully omitted from the models to avoid over-constraining inputs to the set of experimental conditions used in calibration. Significant adjustments to reaction rates for the feldspars also produced better fits for the cations, but explicit fitting to effluent data was again avoided to maintain a more representative model based on established empirical kinetic data. The resulting comparisons of simulated and experimental effluent concentrations of Si, Na, Al, and K from the calibrated model are provided in Figure B1. The overestimation of silica dissolution influenced the amount of predicted amorphous silica and kaolinite precipitation, but because the model does not include mechanisms to account for inhibitory effects of these minerals on carbonation, carbonate volume fractions did not exhibit sensitivity to volumes of secondary silicate precipitates. Thus, to avoid over-constraining the models in matching all effluent data, calibration was focused on matching experimental trends for the divalent cations contributing to the mineral carbonation reactions of interest.

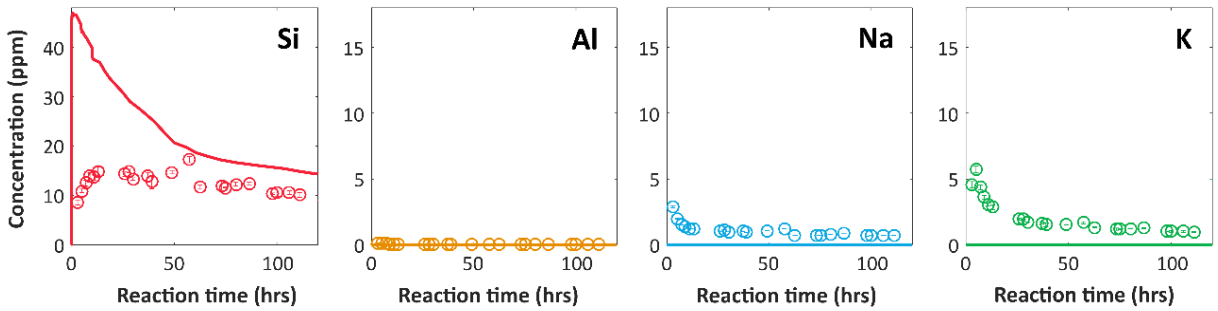

Figure B1. Comparison of Si, Al, Na, and K concentrations from experimental effluent data and the calibrated model. Circles represent measured concentrations and solid lines are model results.

B3. Model Validation

As noted in Section 2.3.2 of Chapter 2, model mineralogy was adjusted to reproduce results from a core flooding experiment conducted with the same conditions and etched fracture pathway as the test used in calibration but with an unserpentinized basalt sample (experiment FB-2). This core had a similar bulk mineralogy with the exception of a higher abundance of unserpentinized olivine (9%) and lower fraction of serpentine (1%). Again, mineral volume fractions were adjusted to within 2-3% of those derived from WDS analyses of bulk mineralogy for this sample. The SSA values for "large-grain" diopside and forsterite were reduced to half of those used in the calibrated models to match reduced Ca and Mg effluent concentrations, respectively, for the unserpentinized basalt experiment. A portion of the diopside (2%) was again set to a smaller grain size, using the higher specific surface area (0.11 m^2/g) obtained in the calibrated model, to account for rapid initial cation mobilization. Adjusted primary mineral volume fractions and SSA values are reported in Table B1; all inputs for secondary minerals remained the same.

Table B1. Adjusted mineral volume fractions and SSA's for matching effluent data from the FB-2 core flooding experiment on an unserpentinized flood basalt (100°C; 10 MPa P_{CO2}; flow rate 5 mL/h)

Primary Minerals	Initial Volume Fraction (%)	SSA (m^2/g)	
		Calculated (geometric)*	Selected
Diopside	20	0.0148	0.0017*
Albite	13	0.0225	0.0225
Anorthite	19	0.0225	0.0225
Antigorite	2	0.0165	0.18
Forsterite	4	0.0148	0.009
Fayalite	5	0.0148	0.0018
K-feldspar	35	0.019	0.019

*Diopside is further sub-divided such that 18% of the core has the selected SSA of 0.0017 m^2/g and 2% has a larger SSA of 0.11 m^2/g corresponding to smaller grain sizes.

The resulting simulation (Figure B2) produced a similar match to the divalent cation effluent data as the results for the calibration. Similar to model calibration for the other major cation species (Figure B1), silica dissolution was overestimated while Na^+ and K^+ were underestimated, likely due to incongruent dissolution in the experiments that the models do not account for.

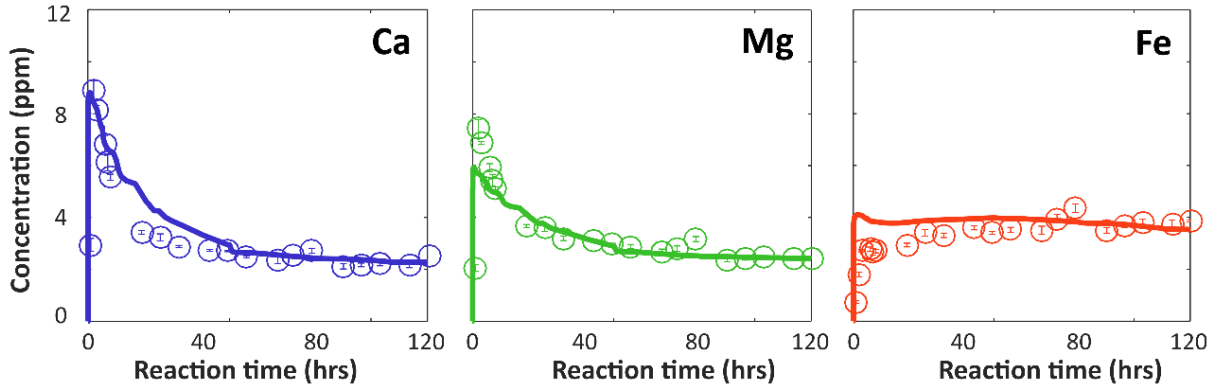

Figure B2. Model validation. Comparison of model output and experimental effluent data for an unserpentinized flood basalt experiment (100 °C; 10 MPa P_{CO2}; 5 mL/h) which was simulated through slight adjustments to mineral inputs from the calibrated model.

B4. Mapping Mineral Spatial Distributions

Discretized mineral maps were developed as inputs to heterogeneous CrunchFlow models using an approach similar to that demonstrated by Ellis and Peters[13] for 3D mapping of calcite spatial distribution in carbonate rocks. A reacted serpentinized basalt core sample from the experiments used in calibration (section B1) was first sectioned and imaged with a JEOL scanning electron microscope (Hitachi) using an incident beam energy of 15 keV and working distance of 10 mm. Specific mineral phases were identified based on elemental compositions from energy dispersive x-ray spectroscopy (EDS) images in representative sections analyzed at a scale of 100 μm and a working knowledge of the sample composition from initial characterization via WDS.[12] An example is provided in Figure B3, where iron-rich minerals with no silica were identified as chromite (or ilmenite if Ti was also present); areas with Ca, Mg and Si represent as pyroxene (diopside); regions with Mg and Si but no Ca as serpentine or olivine; the presence of Na and/or Ca with Al signifies plagioclase (labradorite); and potassium-rich regions as the K-rich matrix.

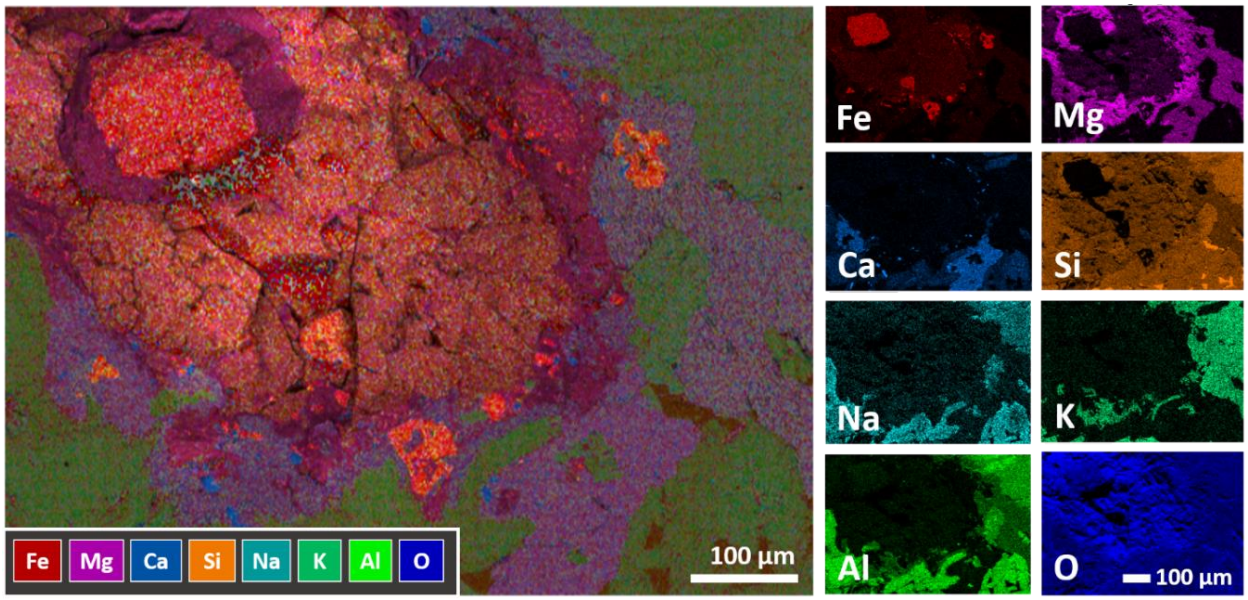

Figure B3. Example BSE images taken from a section of reacted core sample to identify minerals.

Corresponding back-scattered electron (BSE) images were generated for each analyzed site so that identified minerals could be mapped to distinct features in cross-sectional X-ray computed tomography (xCT) scans of the reacted core sample. SEM sites were spatially aligned with these scans based on the measured distance along the core where the section was cut and the resolution of the xCT slices (12 µm). The xCT slices were processed in ImageJ to reconstruct the surface parallel to the direction of flow. To align the mineral map with the CrunchFlow model domain, this image was discretized into 0.05 x 0.05 mm blocks, where individual voxels were replaced with a single value corresponding to the average voxel intensity across the grid cell. Ranges in voxel intensities corresponding to each identified mineral phase were then used to assign one of four mineral phases to each block: pyroxene, olivine/serpentine, plagioclase, or the K-rich matrix. Note that we excluded several of the less reactive trace mineral phases (e.g. chromite, ilmenite, apatite), which were interspersed as inclusions in larger olivine, pyroxene, and feldspar grains, from the model to reduce unnecessary complexity and improve computational efficiency. The relative mineral abundances of the four included minerals noted in Figure B4 align well with the composition previously determined by WDS analyses (21% diopside, 28% plagioclase, 14% serpentine, and 32% potassium matrix),[12] corroborating the ability of this approach to coarsely capture mineral spatial distributions along the flow path.

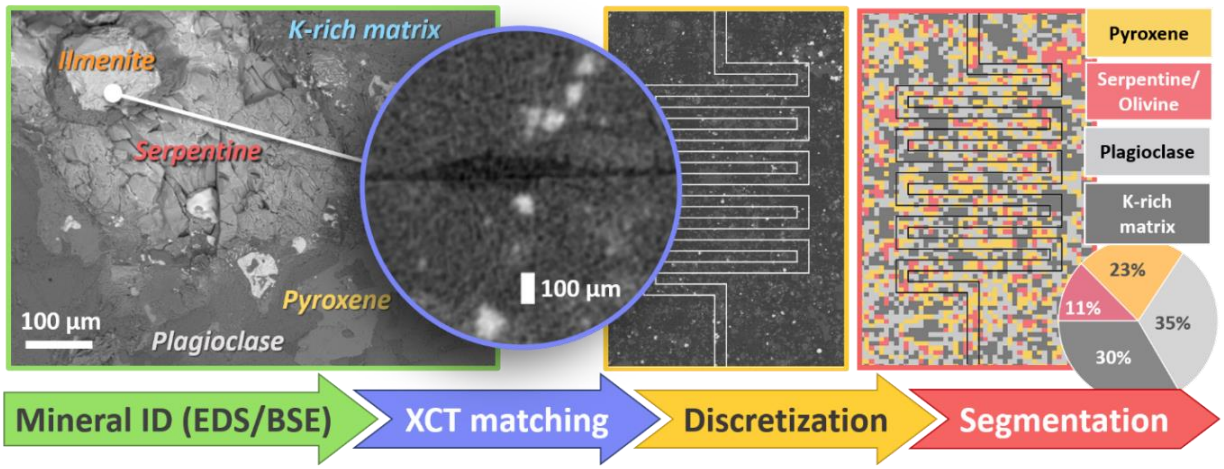

Figure B4. Workflow schematic for producing a discretized mineral map aligned with the CrunchFlow model domain.

As detailed in previous sections, the pyroxene is classified as diopside; plagioclase as labradorite; Mg-rich serpentine as antigorite; and K-rich matrix as K-feldspar. The low abundance of olivine and the fact that its composition is similar to serpentine inhibited its distinct identification in the lower-resolution xCT images. Thus, olivine and serpentine are combined as one mineral phase for segmentation. In the models, olivine/serpentine cells were assigned volume fractions of forsterite, fayalite, and antigorite corresponding to the relative abundances of each mineral used in the homogeneous calibrated model. For example, since forsterite comprises 1% of the mineral volume in the model domain and forsterite, fayalite, and antigorite have a combined abundance of 15%, forsterite is assigned a volume fraction of 1/15 (or 6.67% of the total mineral volume) in the "olivine/serpentine" cells used in the heterogeneous models. The remainder of these cells is comprised of 3/15 (20%) fayalite, which was 3% of the bulk composition in the calibrated model, and 11/15 (73.3%) serpentine, which accounted for 11% of the bulk sample composition. Note that these percentages are applied to the mineral volume in the cell (not total volume) to obtain the mineral volume fractions within that cell. For instance, the fayalite fraction of the total cell volume would be (0.2)*(0.4) = 0.08 in models with a porosity of 60% such that all primary mineral volume fractions sum to the total mineral volume fraction of 40%. Labradorite cells were modeled similarly, consisting of 40% albite and 60% anorthite according to the actual sample stoichiometry. Pyroxene cells consisted solely of diopside and cells for the K-rich matrix only contained K-feldspar.

B5. Additional Results

Volume fraction maps for secondary precipitates not shown in Figure 2.7 of Section 2.4.5 (i.e. kaolinite and amorphous silica) are provided in Figure B5 below. SA1 corresponds to pure advection with a residence time of 288h for the segmented mineral distribution; SA2 uses the same flow conditions as SA1 but with the "random" mineral grid presented in the manuscript; and SD2 uses the same "random" grid as SA2 but the flow is set to pure diffusion. Amorphous silica is most concentrated on larger clusters of the most reactive silicates (i.e. olivine and pyroxene) where kaolinite is not present. The highest volume fractions of kaolinite form in the feldspar cells (i.e. plagioclase and K-feldspar).

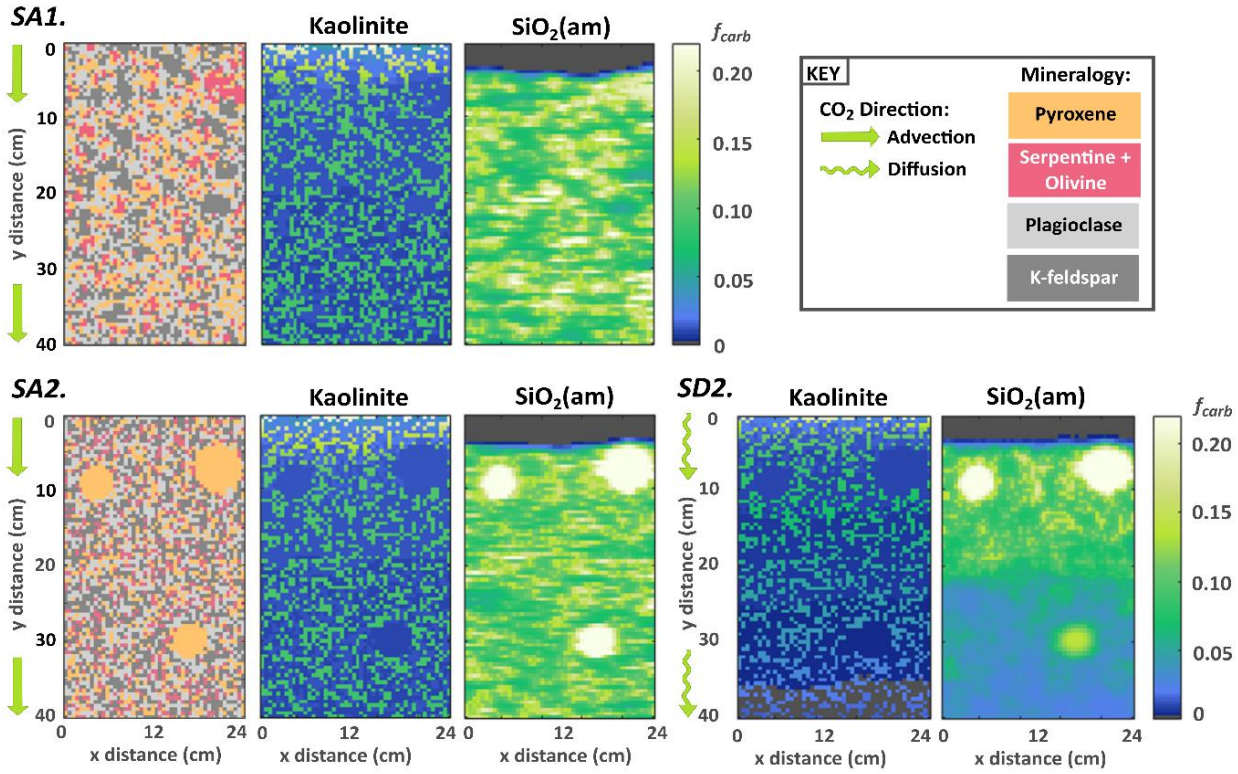

Figure B5. Mineral volume maps for kaolinite and amorphous silica (SiO_2(am)) precipitation predicted by the models presented in Figure 2.7 (Chapter 2 of the dissertation).

Secondary mineral saturation indices for the models presented in Figure 2.7 are also provided below. As noted in the discussion, magnesite had the highest saturation index of the three carbonates but calcite formed in the greatest volume fractions due to faster kinetics. Saturation indices were higher for pure diffusion (SD2) than for pure advection (SA2 and SA1).

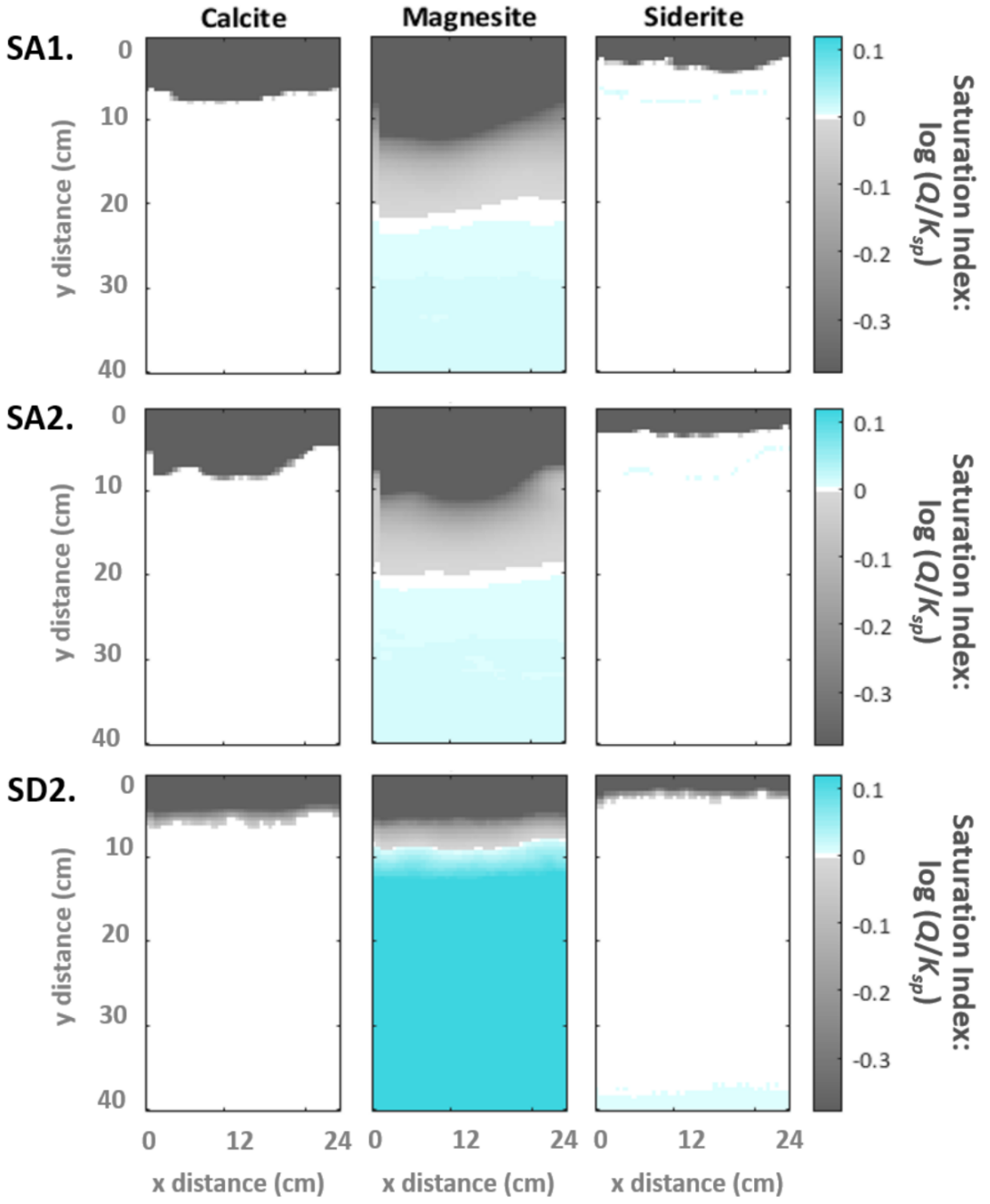

Figure B6. Carbonate saturation indices for the models presented in Figure 2.7 (Chapter 2).

As noted in the manuscript, only one of many randomly generated mineral distributions was included as a point of comparison to the segmented mineral grid developed for the actual fracture surface of the basalt core used in calibration. Results for additional mineral grids under pure diffusion (i.e. the same flow conditions as Model SD2) are presented below to highlight how primary mineral species and larger mineral "clusters" promote preferential secondary precipitate

formation. As illustrated in the figures, each of these grids has the same domain-averaged primary mineral abundance, even when large clusters of certain minerals are included. Results for secondary mineral volume fractions and pH after 2 years of simulation are presented for each grid.

Figure B7 below shows secondary mineral volumes for a grid where every cell is randomly generated with no specified "clusters." Calcite still forms preferentially on pyroxene, but note that the maximum volume fraction in a given cell is lower than that in the domain presented in Models SA2 and SD2 (Figure 2.7, Section 2.4.5) where greater volume fractions formed on the larger contiguous pyroxene clusters than on smaller or isolated pyroxene cells. The pie chart indicates the initial volume fractions of each primary mineral, which are consistent with those of the two mineral grids presented in Figure 2.7.

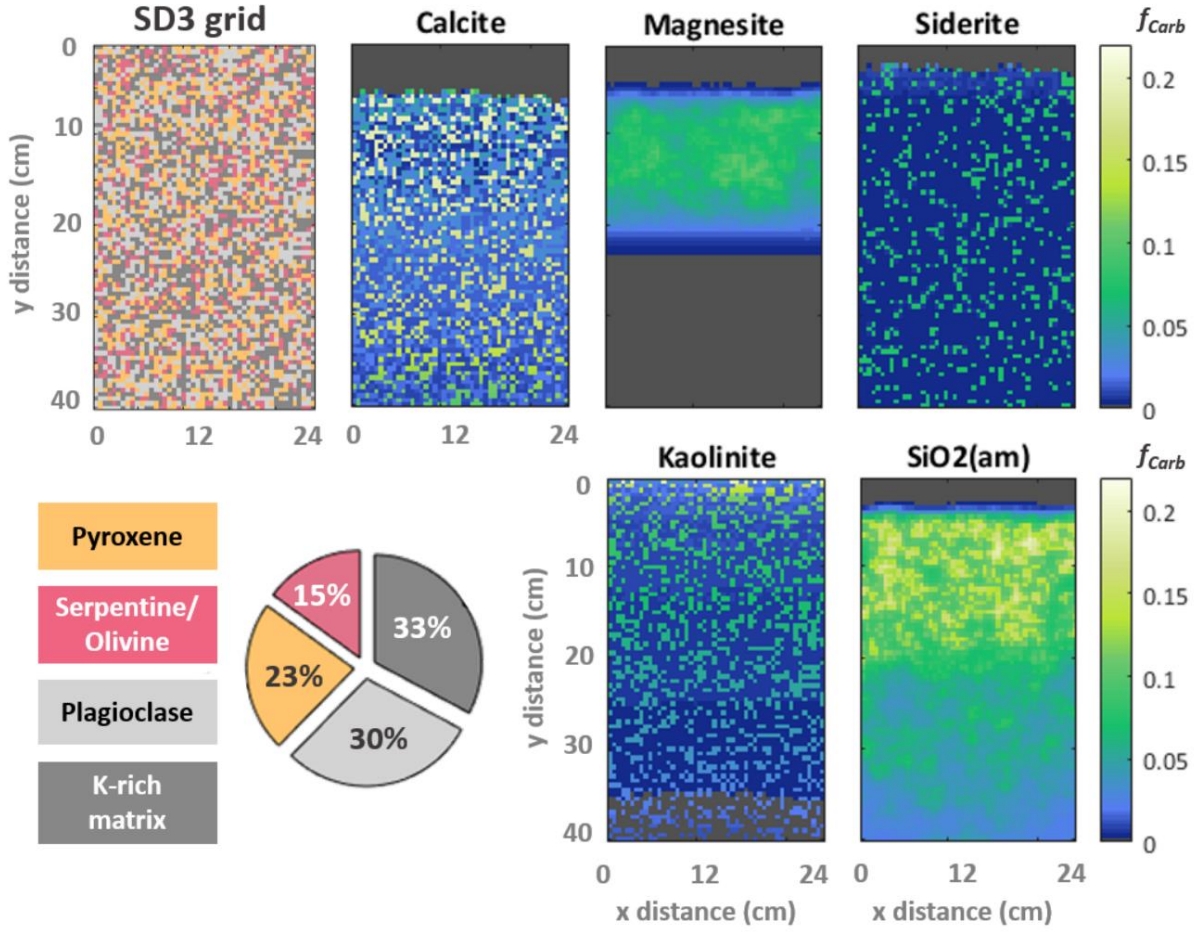

Figure B7. Secondary mineral volume fractions resulting from pure diffusion of CO_2-acidified water after 2 years for a random mineral distribution (SD3) with no included mineral "clusters."

Figure B8 includes one specified cluster for each of the four minerals. Each cluster has the same set radius but the location of each is randomly generated. The same mineral volume fractions used in the random distributions presented in Figure 2.7 of the manuscript and in Figure B7 above were maintained, which are also equivalent to the bulk composition of the segmented core sample. The larger clusters highlight preferential formation of secondary precipitates on the primary minerals that serve as cation "seeds": calcite on pyroxene; siderite on Fe-bearing olivine; and kaolinite on plagioclase. Little secondary precipitation occurs on K-feldspar, as its dissolution is inhibited by slow reaction kinetics. Magnesite and amorphous silica precipitate more uniformly because more than one primary mineral contributes the necessary cations for these precipitates.

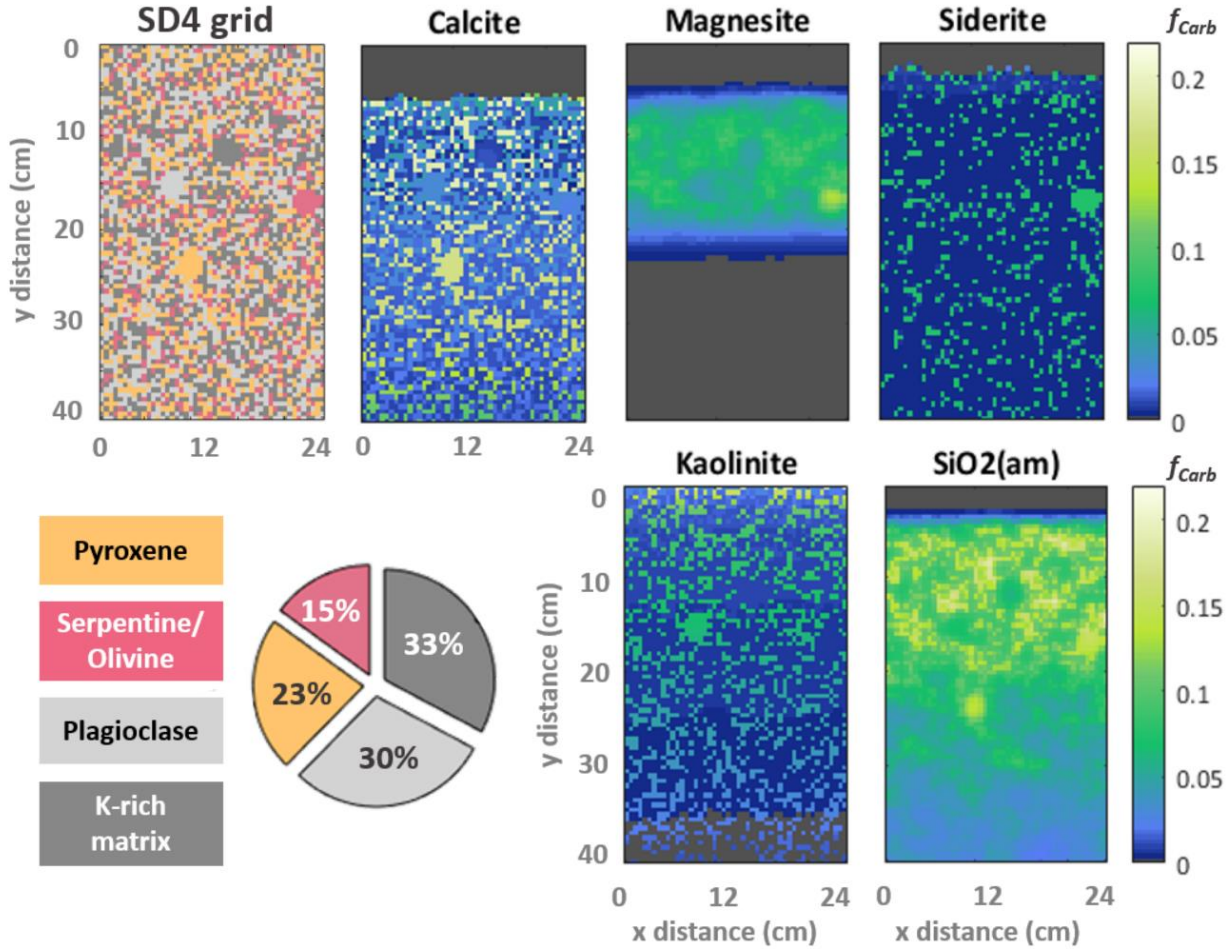

Figure B8. Secondary mineral volume fractions resulting from pure diffusion of CO_2-acidified water after 2 years for a random mineral distribution (SD4) that includes a larger "cluster" of each of the four primary mineral phases.

Figure B9 compares total carbonate volumes as a function of time for the mineral grids in Figures B7 and B8 to both the segmented grid from the actual core sample (SD1) and the random grid presented in Figure 2.7 (SD2) under the same flow condition, pure diffusion. As evidenced by the figure, net carbonation does not vary significantly with the distribution of minerals provided that the bulk compositions (i.e. initial volume fractions of primary minerals) are the same in each domain. Slight deviations are largely due to rounding errors in achieving set volume fractions using a fixed number of grid cells in the MATLAB code used to generate the random grids.

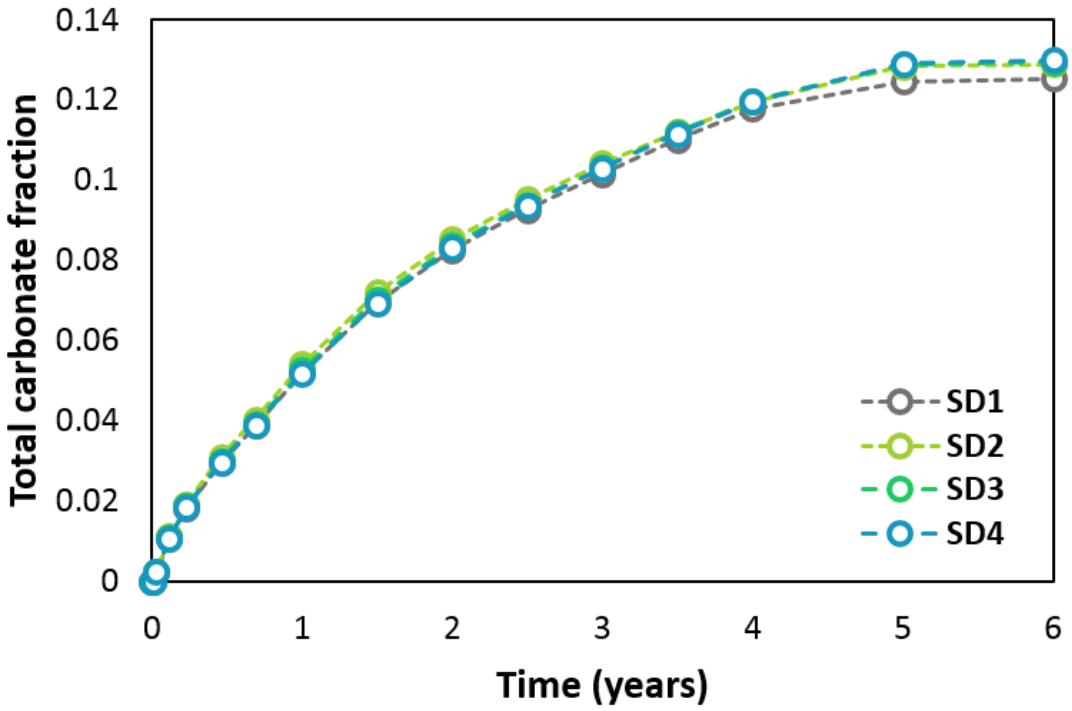

Figure B9. Total carbonate fraction (cm^3 carbonates formed per cm^3 of model domain) as a function of time for pure diffusion over 4 different mineral distributions with the same domain-averaged mineral composition.

B6. Simulations with Additional Secondary Silicates

As discussed in Sections 2.3.5 and 2.4.5 of the dissertation, additional simulations were run adding smectite (modeled as 4 end-members of montmorillonite), biotite (annite and phlogopite), and zeolite (laumontite) as potential secondary minerals. Kinetic data and BET surface areas used in these models are summarized in Table B2 below. Note that a BET surface area reported for heulandite was used for laumontite.

Table B2. Model inputs for additional secondary mineral phases

Mineral	BET SSA (m^2/g)	Acid mechanism		Neutral	Basic mechanism	
		log *k*, 100°C ($mol/m^2/s$)	n^{H+}	log *k*, 100°C ($mol/m^2/s$)	log *k*, 100°C ($mol/m^2/s$)	n^{OH-}
Annite	2.13[14]	-9.07[15]	0.525[15]	-11.78[15]	--	--
Phlogopite	2.13[14]	-9.07[15]	0.525[15]	-11.78[15]	--	--
Laumontite	1.715[16]	--	--	-10.56[17]	--	--
Ca-Montmorillonite	65.2[18]	-11.02[15]	0.22[15]	-12.72[15]	-12.72[15]	-0.13[15]
K-Montmorillonite	65.2[18]	-11.02[15]	0.22[15]	-12.72[15]	-12.72[15]	-0.13[15]
Mg-Montmorillonite	65.2[18]	-11.02[15]	0.22[15]	-12.72[15]	-12.72[15]	-0.13[15]
Na-Montmorillonite	65.2[18]	-11.02[15]	0.22[15]	-12.72[15]	-12.72[15]	-0.13[15]

A comparison of these modeling results with those shown in Figure 2.6 is presented in Figure B10 below. Models are only compared over 3 years as pore spaces became clogged in some of the slower advection cases at this time. As noted in the manuscript, carbonate volumes are reduced by the precipitation of divalent cation-bearing clays. The impact of clays on carbonation is most pronounced under diffusive conditions and slow-flow advection. This reduction in carbonation stems primarily from Mg uptake into montmorillonite, which is more pronounced for slower flow over longer time frames. Under pure diffusion, the fraction of dissolved Mg retained in magnesite after 6 years is reduced from 81% in the original models to 68% when considering smectites, while the Ca and Fe balances are not significantly altered. After 2 years, 87% of Ca is still retained in calcite, while the 99% of dissolved Fe that had precipitated as siderite after 2 years is reduced to 95% (with the remainder as dissolved Fe) in the clay models. The additional secondary precipitation also did not affect the amount of Ca, Mg, or Fe dissolved in the domain.

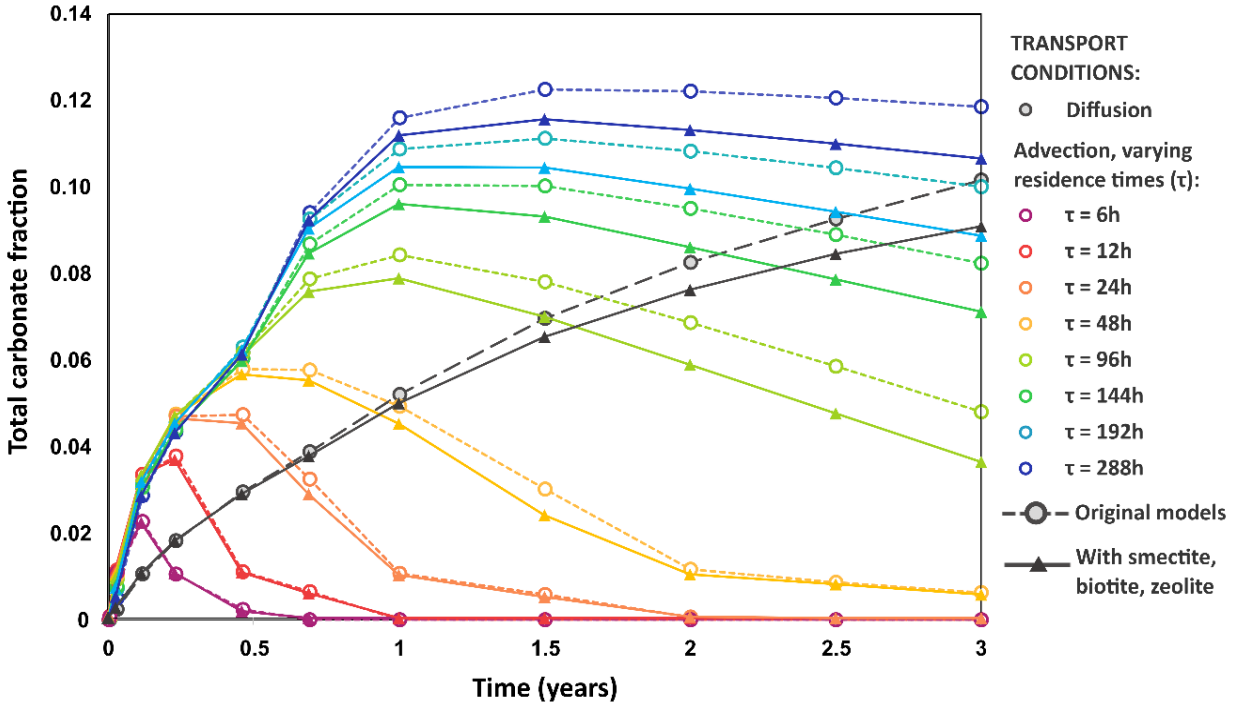

Figure B10. Comparison of total carbonate volume fractions (cm^3 carbonates per cm^3 of model domain) for the transport models run with and without smectites, zeolite, and biotite as potential secondary minerals.

REFERENCES

(1) Beckingham, L. E.; Mitnick, E. H.; Steefel, C. I.; Zhang, S.; Voltolini, M.; Swift, A. M.; Yang, L.; Cole, D. R.; Sheets, J. M.; Ajo-Franklin, J. B.; DePaolo, D. J.; Mito, S.; Xue, Z. Evaluation of Mineral Reactive Surface Area Estimates for Prediction of Reactivity of a Multi-Mineral Sediment. *Geochim. Cosmochim. Acta* **2016**, *188*, 310–329. https://doi.org/10.1016/j.gca.2016.05.040.

(2) Mito, S.; Xue, Z.; Sato, T. Effect of Formation Water Composition on Predicting CO2 Behavior: A Case Study at the Nagaoka Post-Injection Monitoring Site. *Appl. Geochem.* **2013**, *30*, 33–40. https://doi.org/10.1016/j.apgeochem.2012.08.020.

(3) Brantley, S. L.; White, A. F.; Hodson, M. E. Surface Area of Primary Silicate Minerals. In *Growth, dissolution and pattern formation in geosystems*; Springer, 1999; pp 291–326.

(4) Park, A.-H. A.; Fan, L.-S. Mineral Sequestration: Physically Activated Dissolution of Serpentine and PH Swing Process. *Chem. Eng. Sci.* **2004**, *59* (22–23), 5241–5247. https://doi.org/10.1016/j.ces.2004.09.008.

(5) Brantley, S. L.; Mellott, N. P. Surface Area and Porosity of Primary Silicate Minerals. *Am. Mineral.* **2000**, *85* (11–12), 1767–1783.

(6) Wang, F.; Giammar, D. E. Forsterite Dissolution in Saline Water at Elevated Temperature and High CO_2 Pressure. *Environ. Sci. Technol.* **2013**, *47* (1), 168–173. https://doi.org/10.1021/es301231n.

(7) Giammar, D. E.; Bruant, R. G.; Peters, C. A. Forsterite Dissolution and Magnesite Precipitation at Conditions Relevant for Deep Saline Aquifer Storage and Sequestration of Carbon Dioxide. *Chem. Geol.* **2005**, *217* (3–4), 257–276. https://doi.org/10.1016/j.chemgeo.2004.12.013.

(8) Navarre-Sitchler, A.; Steefel, C. I.; Sak, P. B.; Brantley, S. L. A Reactive-Transport Model for Weathering Rind Formation on Basalt. *Geochim. Cosmochim. Acta* **2011**, *75* (23), 7644–7667. https://doi.org/10.1016/j.gca.2011.09.033.

(9) Carroll, S.; Mroczek, E.; Alai, M.; Ebert, M. Amorphous Silica Precipitation (60 to 120 C): Comparison of Laboratory and Field Rates. *Geochim. Cosmochim. Acta* **1998**, *62* (8), 1379–1396.

(10) Tester, J. W.; Worley, W. G.; Robinson, B. A.; Grigsby, C. O.; Feerer, J. L. Correlating Quartz Dissolution Kinetics in Pure Water from 25 to 625C. *Geochem. Cosmochim. Acta* **1994**, *58* (11), 2407–2420.

(11) Adeoye, J. T.; Menefee, A. H.; Xiong, W.; Wells, R. K.; Skemer, P.; Giammar, D. E.; Ellis, B. R. (Submitted). Effect of Transport Limitations and Fluid Properties on Reaction Products in Fractures of Unaltered and Serpentinized Basalt Exposed to High PCO_2 Fluids. *Int. J. Greenh. Gas Control*.

(12) Wells, R.; Giammar, D.; Skemer, P. *Sample Library of Natural and Artificial Basalts*; 2016; https://edx.netl.doe.gov/dataset/sample-library-of-natural-and-artificial-basalts/revision_resource/2bcdd2f4-70f0-4b1c-afe7-d1d563680e0c.

(13) Ellis, B. R.; Peters, C. A. 3D Mapping of Calcite and a Demonstration of Its Relevance to Permeability Evolution in Reactive Fractures. *Adv. Water Resour.* **2016**, *95*, 246–253. https://doi.org/10.1016/j.advwatres.2015.07.023.

(14) Chon, C.-M.; Kim, J. G.; Moon, H.-S. Kinetics of Chromate Reduction by Pyrite and Biotite under Acidic Conditions. *Appl. Geochem.* **2006**, *21* (9), 1469–1481. https://doi.org/10.1016/j.apgeochem.2006.06.012.

(15) Palandri, J. L.; Kharaka, Y. K. *A Compilation of Rate Parameters of Water-Mineral Interaction Kinetics for Application to Geochemical Modeling*; DTIC Document, 2004.

(16) Ragnardsdottir, K. V. Dissolution Kinetics of Heulandite at PH 2-12 and 25C. *Geochem. Cosmochim. Acta* **1993**, *57*, 2439–2449.

(17) Kiryukhin, A.; Xu, T.; Pruess, K.; Apps, J.; Slovtsov, I. Thermal–Hydrodynamic–Chemical (THC) Modeling Based on Geothermal Field Data. *Geothermics* **2004**, *33* (3), 349–381. https://doi.org/10.1016/j.geothermics.2003.09.005.

(18) Dogan, A. U.; Dogan, M.; Onal, M.; Sarikaya, Y.; Aburub, A.; Wurster, D. E. Baseline Studies of the Clay Minerals Society Source Clays: Specific Surface Area by the Brunauer Emmett Teller (BET) Method. *Clays Clay Miner.* **2006**, *54* (1), 62–66.

APPENDIX C

Supporting Information for Chapter 3

C1. REACTIVE TRANSPORT MODELING

As noted in the manuscript, 2D reactive transport models for the experiments in Chapter 3 were based on Crunchtope[1] models developed by Menefee et al.[2] (and presented in Chapter 2) for flow-through experiments that used the same serpentinized basalt samples but with an advection-dominated flow path and higher flow rate.[3] In this study, effluent data from the first experiment (LB-100C) served as the 'benchmark' for model calibration. The fracture surface was taken as the model domain, which consisted of 4,000 grid cells with dimensions of 0.5x0.5x0.11 mm. The domain "height" was calculated to match the experimental residence time based on the total domain volume and experimental flow rate (1 mL/hr). The milled fracture patterns were modeled with a higher porosity (90%) and permeability (10^{-3} m^2) than in the bulk rock matrix (5%; 10^{-20} m^2). Similar to the models presented in Chapter 2, fractures were assigned a small fraction of minerals (as opposed to 100% porosity) in order to simulate reactions along the fracture walls. The matrix porosity is higher than the bulk sample porosity (<1%) in order to prevent rapid pore clogging, which causes instability in the code. Including a small fraction of minerals in the fracture is necessary to simulate reactive surfaces along the upper and lower walls of the milled zones in two-dimensional models. Longitudinal and transverse dispersivity values were set to 0.1 and 0.01 mm, respectively. The diffusion coefficient was fixed at 7.5×10^{-9} m^2/s, corresponding to the mean value for CO_2 in water at 100°C reported in prior work.[4] CO_2 solubility was calculated directly in the code using the empirical relationship developed by Duan and Sun,[5] and activity coefficients were also calculated in the code using the extended Debye-Huckel approach. Equilibrium constants for aqueous reactions were obtained from the EQ3/EQ6 thermodynamic database.

In addition to the major carbonate phases (calcite, siderite, and magnesite), amorphous silica, kaolinite, Mg-montmorillonite, and hematite were included as potential secondary minerals. These phases were selected from a larger initial secondary mineral set that included various smectites, micas, and zeolites because the models become less stable with excessive secondary precipitates.

Mg-montmorillonite was selected to represent smectite clays, as it was the only phase to form in appreciable quantities in test simulations. Kaolinite and amorphous silica were also favorable under experimental conditions and thus included in the models, and hematite was selected to represent Fe-oxides. Iron oxidation was assumed to occur rapidly and treated as an equilibrium reaction, where O_2 and Fe(II) are included as primary aqueous species and Fe(III) as a secondary species (note that this process was excluded from the previous models in Chapter 2). The bulk surface area of secondary minerals is calculated from initial volume fractions of 0 and volume fraction thresholds of 10^{-5}; once this threshold is exceeded, precipitation begins and surface area is calculated from the mineral volume fraction and user-defined specific surface area (SSA). All secondary minerals were assigned BET surface areas from literature (Table C1).

Table C1. Mineral kinetic data used in reactive transport models.

Mineral	Initial Volume Fraction (%)	Acid mechanism		Neutral	Basic mechanism		SSA (m^2/g)	
		log *k*, 100°C ($mol/m^2/s$)	n^{H+}	log *k*, 100°C ($mol/m^2/s$)	log *k*, 100°C ($mol/m^2/s$)	n^{OH-}	Calculated (geometric)*	Selected
Primary Minerals								
Diopside	18	-2.97[6]	0.71[6]	-9.68[6]	--	--	0.0148	0.0036
Diopside, fine-grain	4	-2.97[6]	0.71[6]	-9.68[6]	--	--	--	0.062
Albite	12	-6.47[7]	0.50[7]	-9.66[7]	--	--	0.0225	0.0225
Anorthite	18	-6.47[7]	0.50[7]	-9.66[7]	--	--	0.0225	0.0225
Antigorite	11	-7.54[8]	0.45[8]	-10.1[9]	--	--	0.0165	0.18
Forsterite	2	-4.48[6]	0.47[6]	-7.85[6]	--	--	0.0148	0.012
Forsterite, fine-grain	1	-4.48[6]	0.47[6]	-7.85[6]	--	--	--	0.3
Fayalite	1	-3.53^{++}	0.47[6]	-9.48[6]	--	--	0.0148	0.018
K-feldspar	33	-7.63[6,7]	0.50[6]	-11.29[6]	-17.9[6]	-0.823[6]	0.019	0.019
Secondary Minerals								
Calcite	0	0.21[6]	1.0[6]	-4.98[6]	--	--	--	0.003
Magnesite	0	-5.87[6]	1.0[6]	-8.51[6]	--	--	--	0.0662[10]
Siderite	0	-1.76[11]	0.90[11]	-6.69[7]	--	--	--	0.105[12]
SiO_2(am)	0	--	--	-6.92[13]	--	--	--	0.0225[14]
Kaolinite	0	-8.99[6]	0.777[6]	-12.4[6]	-16.4[6]	-0.472[6]	--	8.16[15]
Mg-Montmorillonite	0	-11.02[6]	0.22[6]	-12.72[6]	-12.72[6]	-0.13[6]	--	65.2[16]
Hematite	0	-7.06[6]	1.0[6]	-12.27[6]	--	--	--	38[17]

*Geometric surface areas calculated as smooth spheres based on average phenocryst grain sizes, which were then adjusted when necessary to the 'selected values' in model calibration to experimental data.[2]

As with the initial models, assigning a higher SSA to 18% of the diopside was necessary to replicate the sharp initial spikes in effluent Ca and Mg concentrations, reflecting the rapid initial dissolution of finer grains along the fracture surface that may have been present as a result of milling. Note the model results in Figure C1 were taken at the outlet of the advection-driven flow path to simulate sampling downstream of the core in the experimental system. Although the Ca:Mg

ratio of diopside in the actual samples (measured by WDS) was nearly 1:1, initial simulations with this stoichiometry greatly overestimated effluent Mg concentrations even when the amounts and reaction rates of other Mg-bearing minerals were reduced, indicating Ca was preferentially released from pyroxene in these experiments. To match the greater effluent Ca concentrations in LB-100C (despite increased calcite precipitation relative to the experiments used in the original models), the Ca:Mg ratio of diopside was adjusted to 3:1 in the database, and the specific surface area of calcite was reduced by an order of magnitude. Additionally, more forsterite was added to match higher effluent Mg and a fraction was assigned a higher specific surface area to match the sharp initial Mg spike. The inclusion of "finer-grained" diopside and forsterite effectively simulated the sharp initial spikes in Ca and Mg concentrations. This setup combined with the same inputs for feldspar minerals used in the original models produced results consistent with the effluent evolution of carbonate-forming divalent cations in LB-100C (Figure C1), so no further adjustments were made to "calibrate" the models to this set of experiments. Further details on specific surface area calculations and adjustments are provided in Menefee et al.[2]

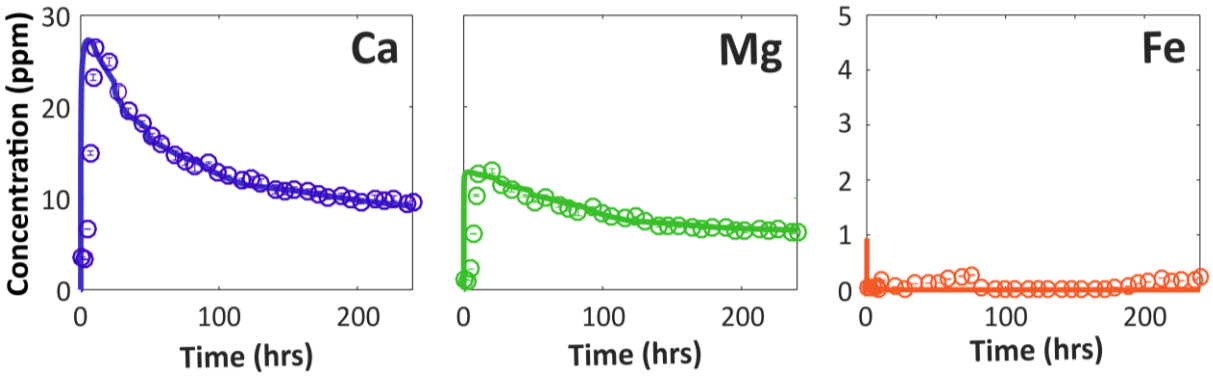

Figure C1. Model outputs of major carbonate-forming divalent cation concentrations (smooth lines) compared with experimental effluent chemistry data (circles) for LB-100C experiment (100°C, 10 MPa P_{CO2}, 6.3 mM $NaHCO_3$).

After benchmarking the model inputs to experimental effluent data, mineral heterogeneity was incorporated using the approach developed by Menefee et al[2] and presented in Chapter 2. Minerals were first identified in the starting material using scanning electron microscopy (SEM) with back-scattered electron imaging (BSE) and energy-dispersive x-ray spectroscopy (EDS). Identified minerals were then mapped to corresponding regions of xCT slices to determine associated voxel intensities. To generate a heterogeneous domain for modeling, the xCT scan for LB-100C was processed in ImageJ to construct a 2D image of the saw-cut surface parallel to the direction of

flow. This image was then discretized from its voxel resolution of 23.5 µm to larger 0.5 x 0.5 mm blocks, where the original voxels were replaced with a single value corresponding to the average voxel intensity within each block. Mineral spatial distributions were mapped by assigning one of four primary mineral phases (pyroxene, olivine/serpentine, plagioclase, or K-feldspar) to each block using intensity ranges and thresholds determined during mineral identification. As in previous modeling work, accessory minerals were excluded from the models for computational efficiency. A schematic overview of the mineral identification and segmentation workflow is included in Figure C2. The map used in modeling LB-100C contained 12% olivine/serpentine; 23% pyroxene; 29% plagioclase; and 36% K-feldspar, consistent with the bulk composition of the starting material and that used in the homogeneous models. The same inputs from the uniform benchmark model were applied in the heterogeneous model, but the fine-grained diopside and forsterite were excluded from the matrix cells due to numerical instability.

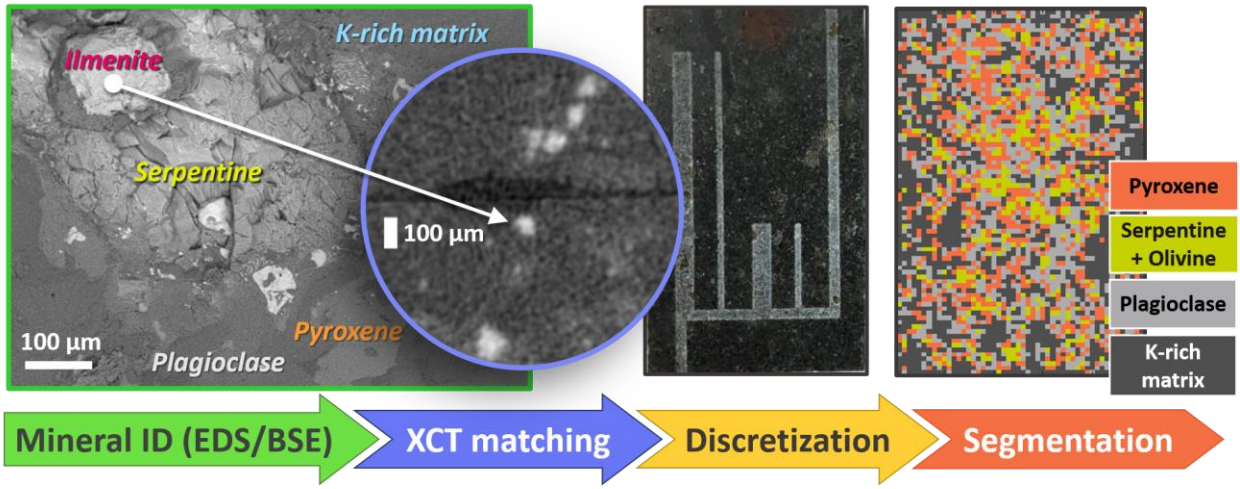

Figure C2. Mineral mapping process for creating representative heterogeneous model domains

C2. Carbonate Saturation Indices

Saturation indices for calcite, aragonite, magnesite, and siderite were calculated based on the effluent chemistry data. The solubility products for each mineral under experimental pressure and temperature conditions, along with equilibrium constants for the carbonate species, were determined using SUPCRTBL with the DPRONSBL thermodynamic database,[18] a revised and extended version of SUPCRT92 with the DPRONS92 database.[19] As noted in the manuscript, pH values at each time step were calculated from charge balances on the effluent chemistry data, where major dissolved cations were measured via ICP-MS and the predominant anions balancing the

electroneutrality of the system are assumed to be bicarbonate and carbonate. Activity corrections were applied using the extended Debye-Huckel equation (B-dot method), adjusting the constants for each experimental temperature (100 or 150°C). The carbonate ion activity, which was computed using carbonate equilibrium reactions and the calculated pH values at each time step, was multiplied by Ca, Mg, and Fe activities to determine ion activity products for $CaCO_3$, $MgCO_3$, and $FeCO_3$, respectively. For each carbonate mineral, saturation indices were then calculated as the log of the ratio of the ion activity product to its solubility product under the experimental P and T. The results are summarized in Figure C3. Saturation indices were also calculated for amorphous silica, but were undersaturated for all experiments and are not included here in the interest of space.

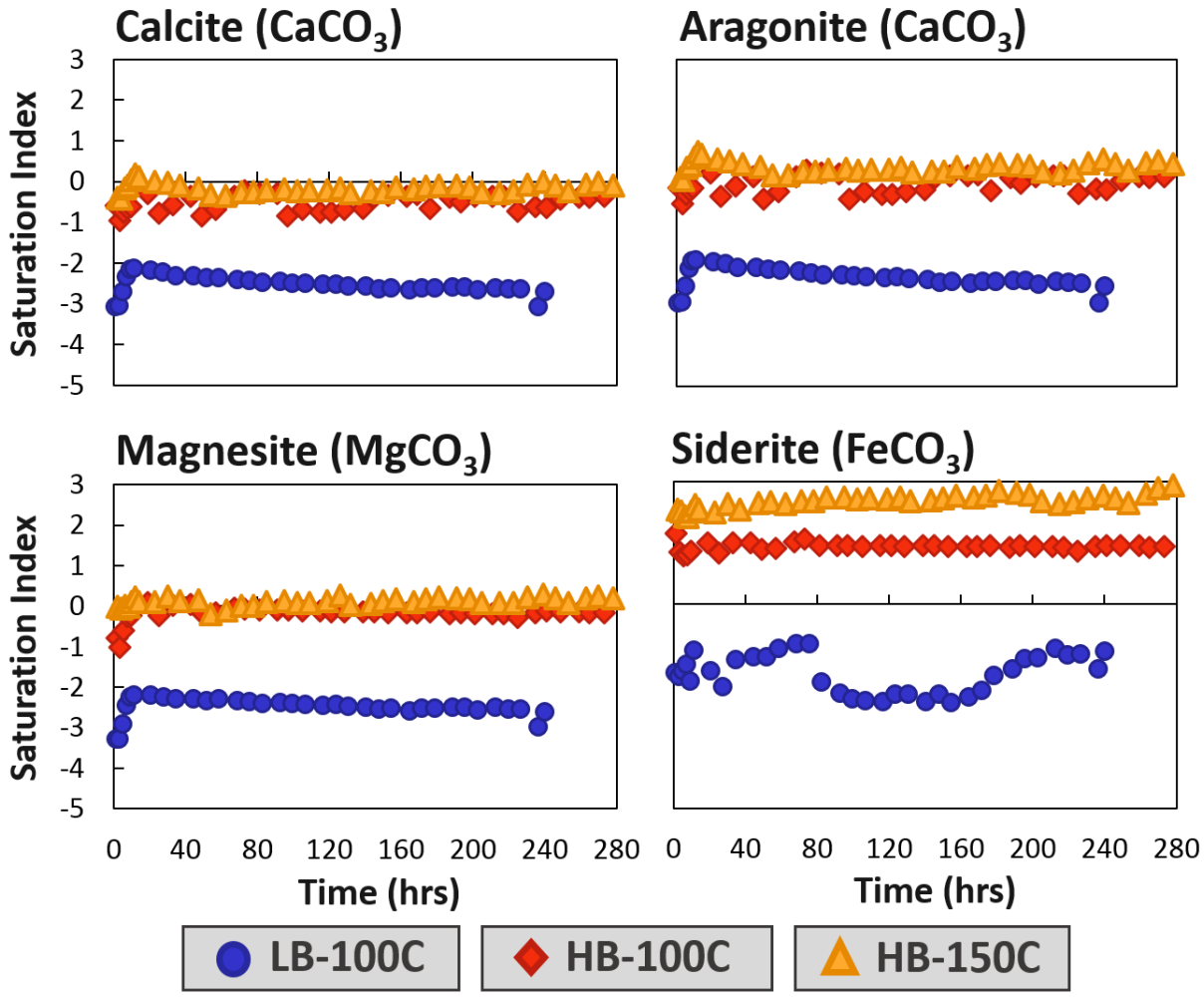

Figure C3. Calculated carbonate saturation indices in effluent samples.

C3. Additional Results: LB-100C

Following the first experiment at lower T and [$NaHCO_3$], small white carbonate crystals were visible in the unmilled regions of the saw-cut core surfaces (Figure C4b). Most of the larger crystals were found on both surfaces, indicating they bridged the small vugs or pore spaces in which they formed. Larger pyroxene grains turned orange-red due to oxidation of the Fe content.

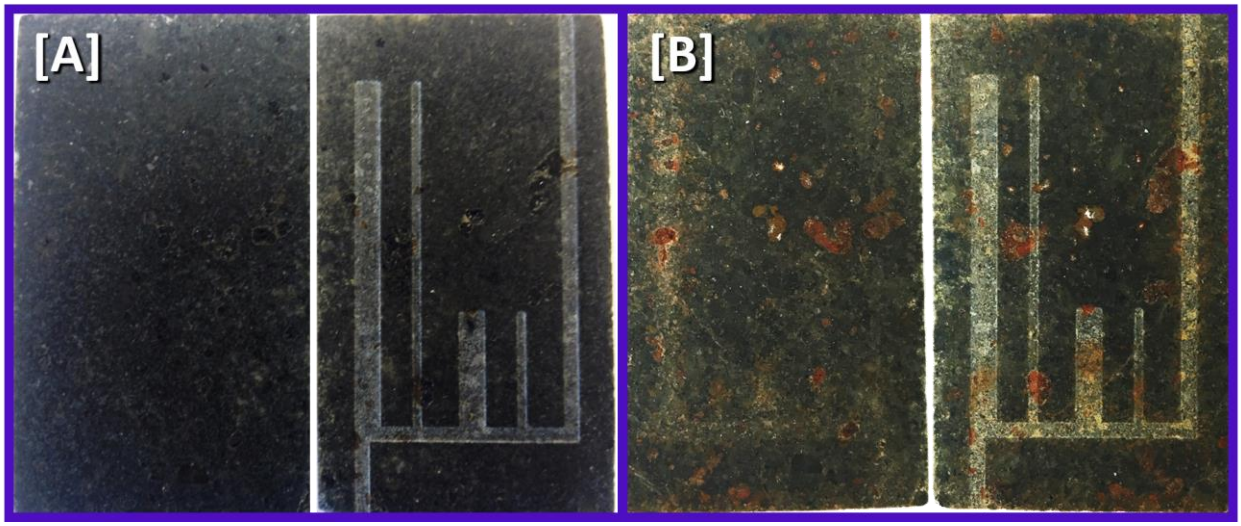

Figure C4. Comparison of [A] pre- and [B] post-reaction saw-cut basalt surfaces for LB-100C. In each image, the polished side of the core is on the left and the milled side on the right.

As discussed in Chapter 3, distinct color gradients were also evident moving from the main flow path into the dead-end fractures (Figure C5).

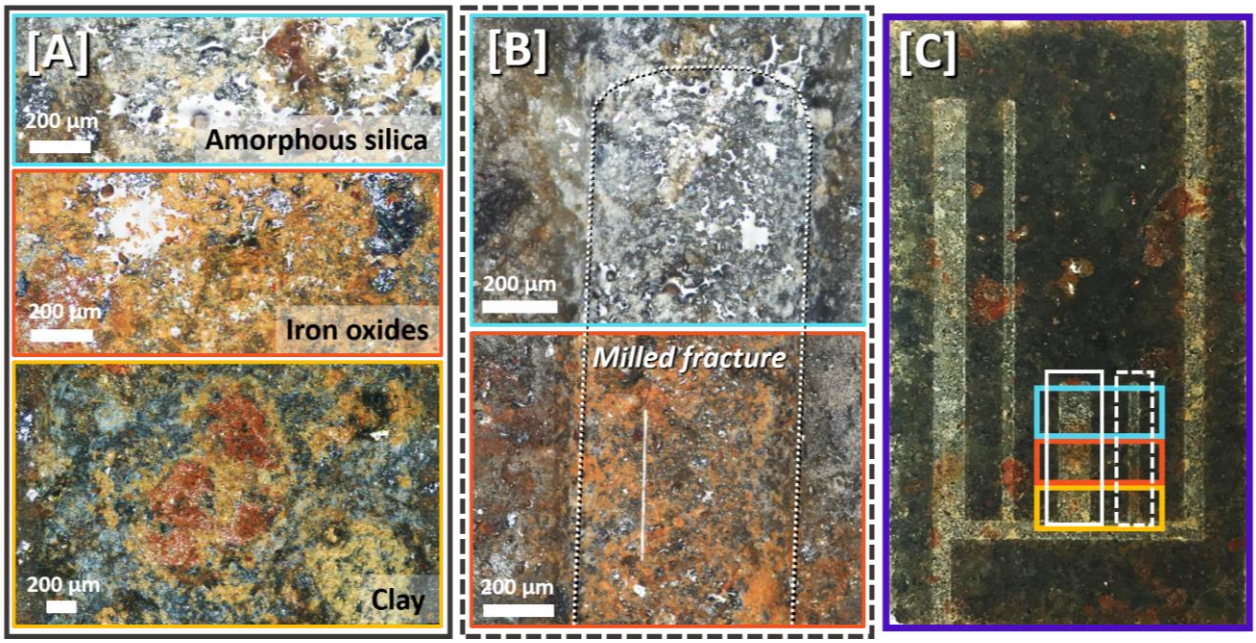

Figure C5. Fracture surfaces [C] evidenced geochemical gradients, where optical microscopy [A, B] shows clay minerals closest to the injection zone followed by bands of iron oxides and amorphous silica.

In the main flow channel, secondary precipitation mainly occurred as thin coatings and alteration layers. Larger Ca- and Mg-rich pyroxene grains were often weathered (yellow regions in the figures below) and coated with thin orange and red layers of Fe-oxides (Figure C6). Fe-oxides also occasionally formed as small (20-50 µm) red crystals within the flow path (Figure C7).

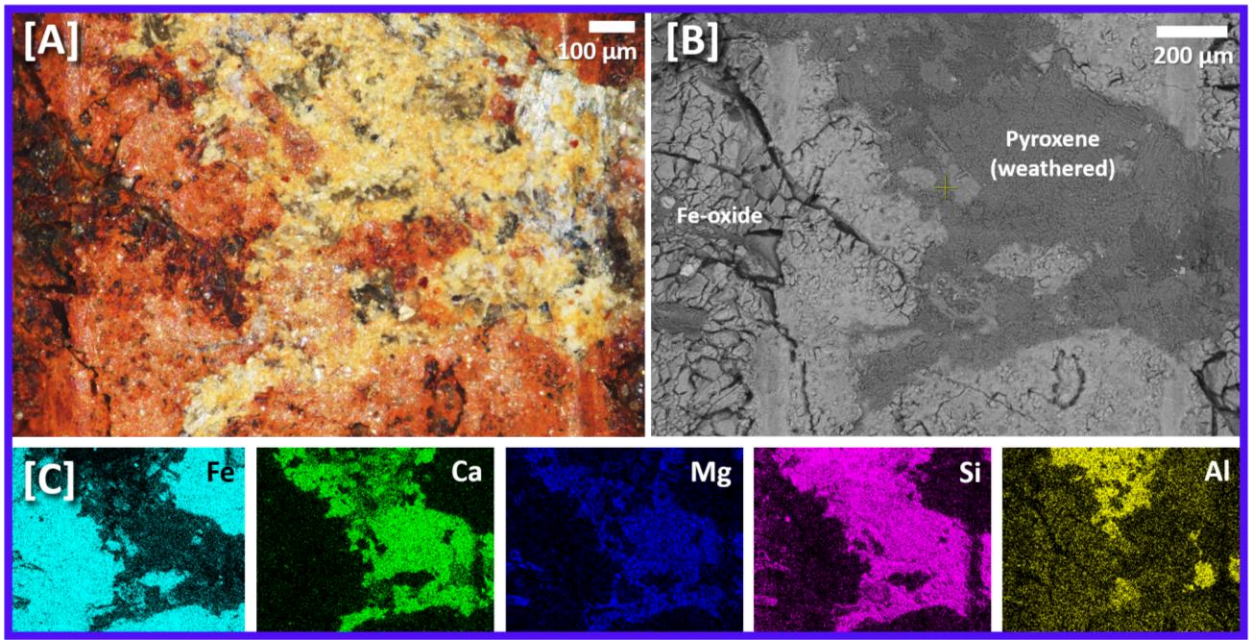

Figure C6. Fe-oxidation of a larger pyroxene grain along the inlet flow path, shown in [A] optical microscope image; [B] BSE image; and [C] EDS maps corresponding to the BSE image in [B].

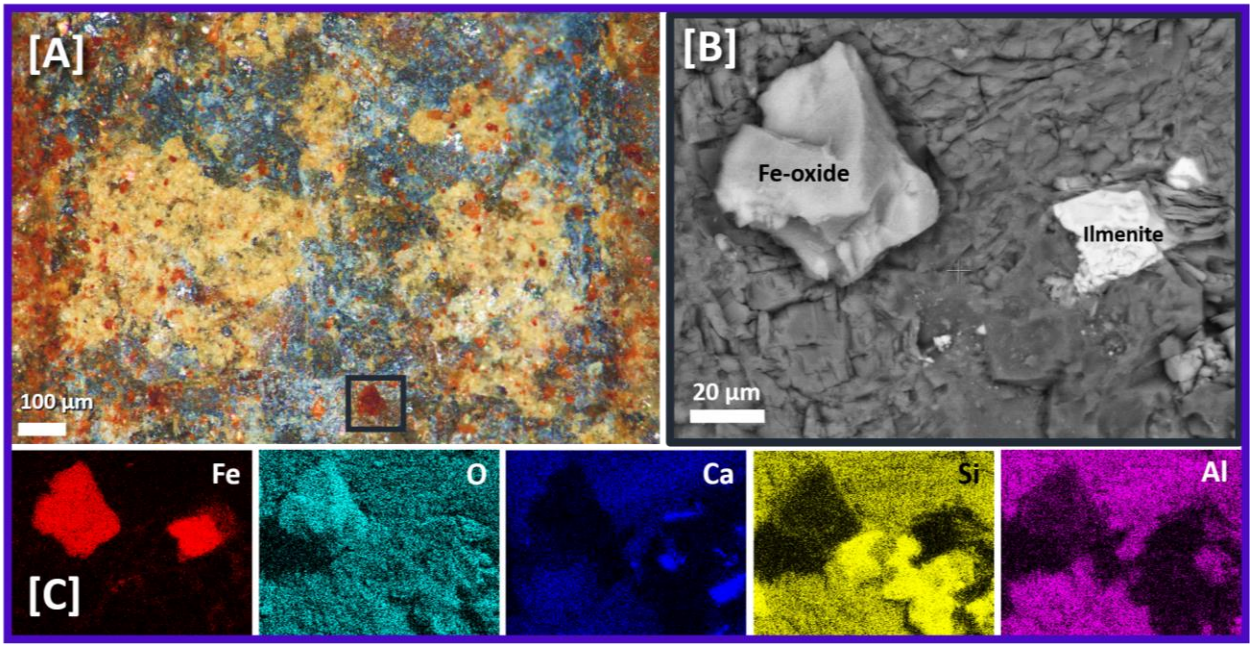

Figure C7. [A] Optical microscope image showing small red Fe-oxide crystals forming within the inlet flow path, and [B] close-up BSE image of a larger red crystal with [C] corresponding EDS maps.

As discussed in Chapter 3, carbonates were limited to the confined unmilled surfaces between the two core halves in LB-100C. Figure C8 illustrates how the largest Ca-carbonate crystal, identified as aragonite via Raman spectroscopy, formed in a vug while an Fe-rich layer coats the surrounding surface.

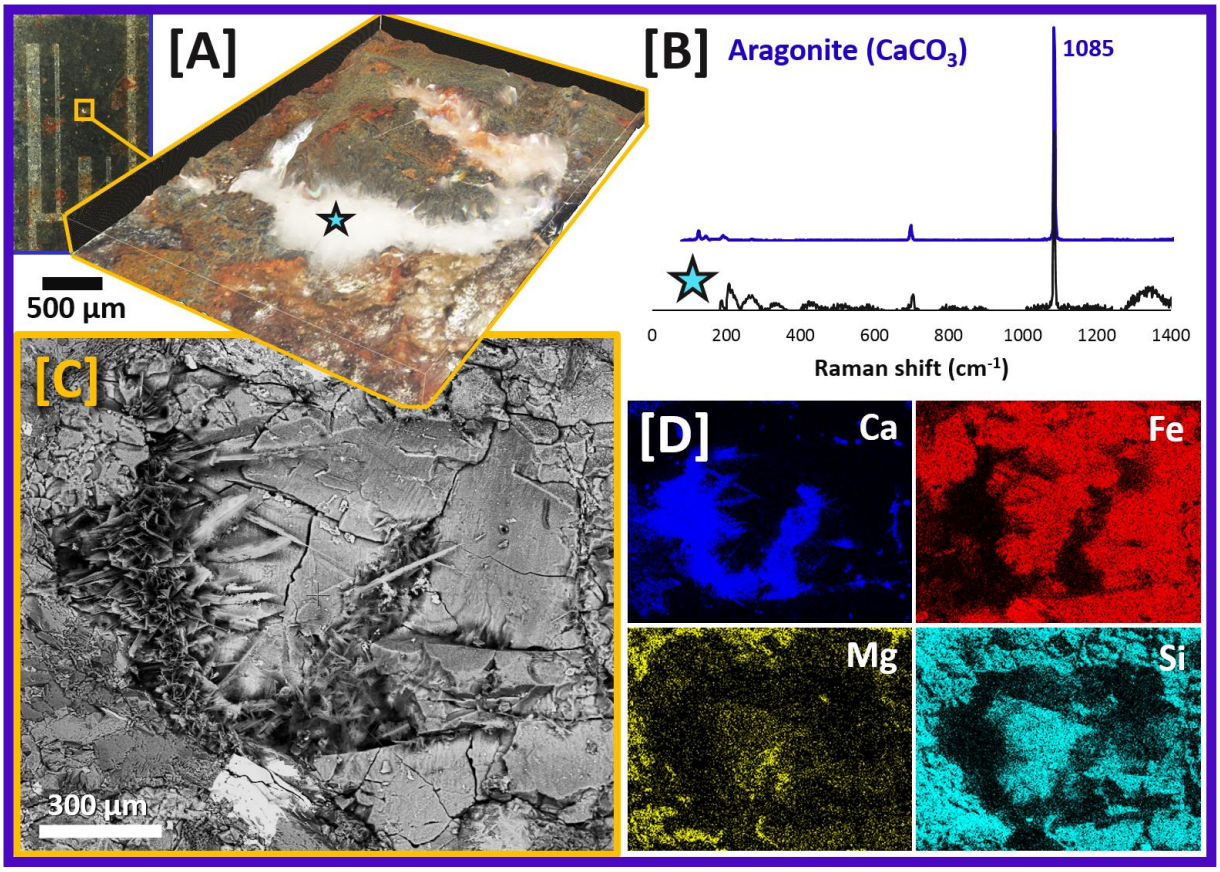

Figure C8. Large aragonite ($CaCO_3$) crystal pooling in a vug between the two saw-cut basalt surfaces, demonstrated with [A] 3D optical microscope imaging; [B] identification via Raman spectroscopy, where the spectra (in grey) aligns with the standard for aragonite; [C] BSE imaging; and [D] selected EDS maps corresponding to the region in [C]. The location of the crystal on the core surface (milled side) is denoted by the yellow box on the image in the upper lefthand corner.

Carbonates were also localized with respect to morphology, as evidenced by the close proximity of the aragonite and calcite crystals that formed on a larger pyroxene grain in Figure C9. The red coating reflects the rapid oxidation of the Fe content in the pyroxene. The juxtaposition of the Ca-polymorphs likely results from variations in the morphology of the underlying grains. Prior work attempting to differentiate the conditions promoting aragonite over calcite precipitation has indicated aragonite is favored at higher temperatures and pH and in the presence of certain divalent cations, including Mg.[20] Stockmann et al.[21,22] also attributed the formation of aragonite in the dissolution of basaltic glass but not diopside to the presence of metals released in basaltic glass dissolution. In transport-limited regions of the confined surfaces, localization of cation release may have influenced the morphology of crystallizing Ca-carbonates.

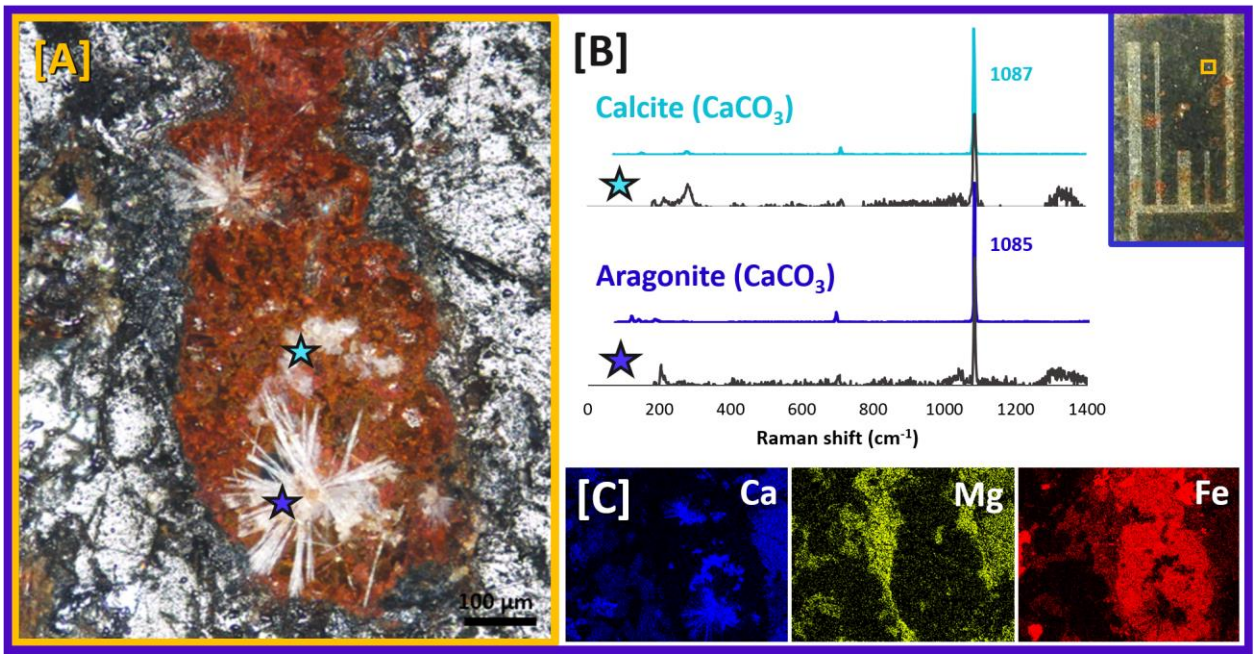

Figure C9. Aragonite and calcite crystals forming in close proximity on a large pyroxene grain. [A] optical microscope image; [B] identification via Raman spectroscopy; and [C] selected EDS maps of the region in [A]. The location of this region on the milled core surface is denoted by the yellow box on the image in the upper righthand corner.

The heterogeneous reactive transport model also predicted calcite precipitation would be highly localized on larger pyroxene grains in the bulk matrix (Figure C10). In the simulations, this is driven by pH buffering (as CO_2 diffuses away from the main flow path) and buildup of dissolved Ca in the diffusion-limited regions that promote relatively rapid supersaturation of calcite, which is able to precipitate due to its rapid precipitation rate under these conditions. Note that not all predicted locations of calcite precipitation were observed experimentally because the model assumes a uniform porosity and does not account for microscale variations in pore structure or accessibility to CO_2-rich fluids, both of which influence the favorability of calcite nucleation and growth in the experimental system.

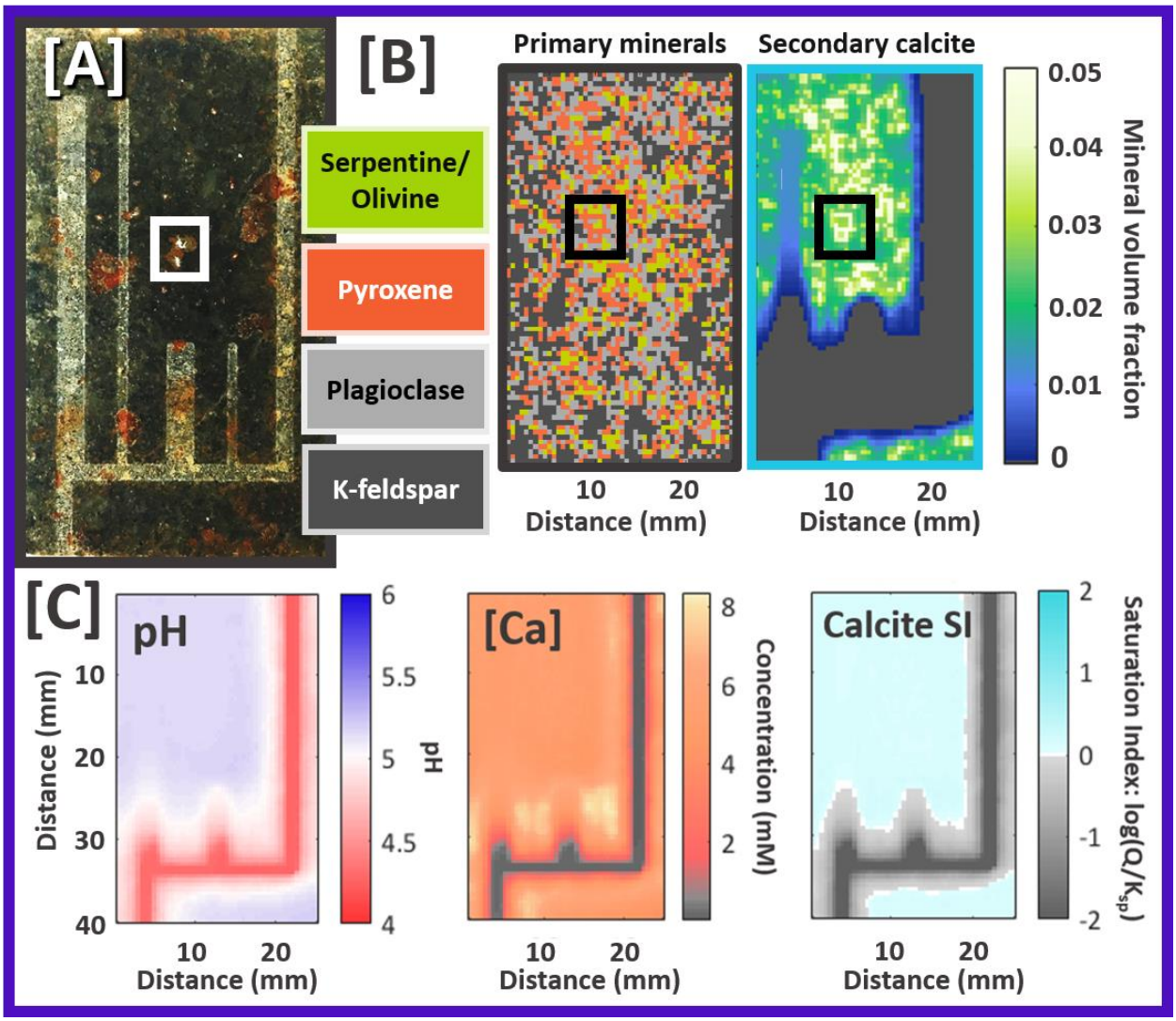

Figure C10. Localized calcite precipitation on larger pyroxene grains observed post-reaction [A] was predicted by a heterogeneous reactive transport model [B] simulating LB-100C. Additional results for pH, dissolved Ca, and calcite saturation index across the domain are provided in [C].

In several areas on the confined (unmilled) saw-cut surfaces, small (~20 µm) Mn-rich carbonates formed over Fe-rich layers, as exemplified in Figure C11. Here, the carbonates formed ring-like structures, and one crystal had a Raman spectra characteristic of pure $MnCO_3$.

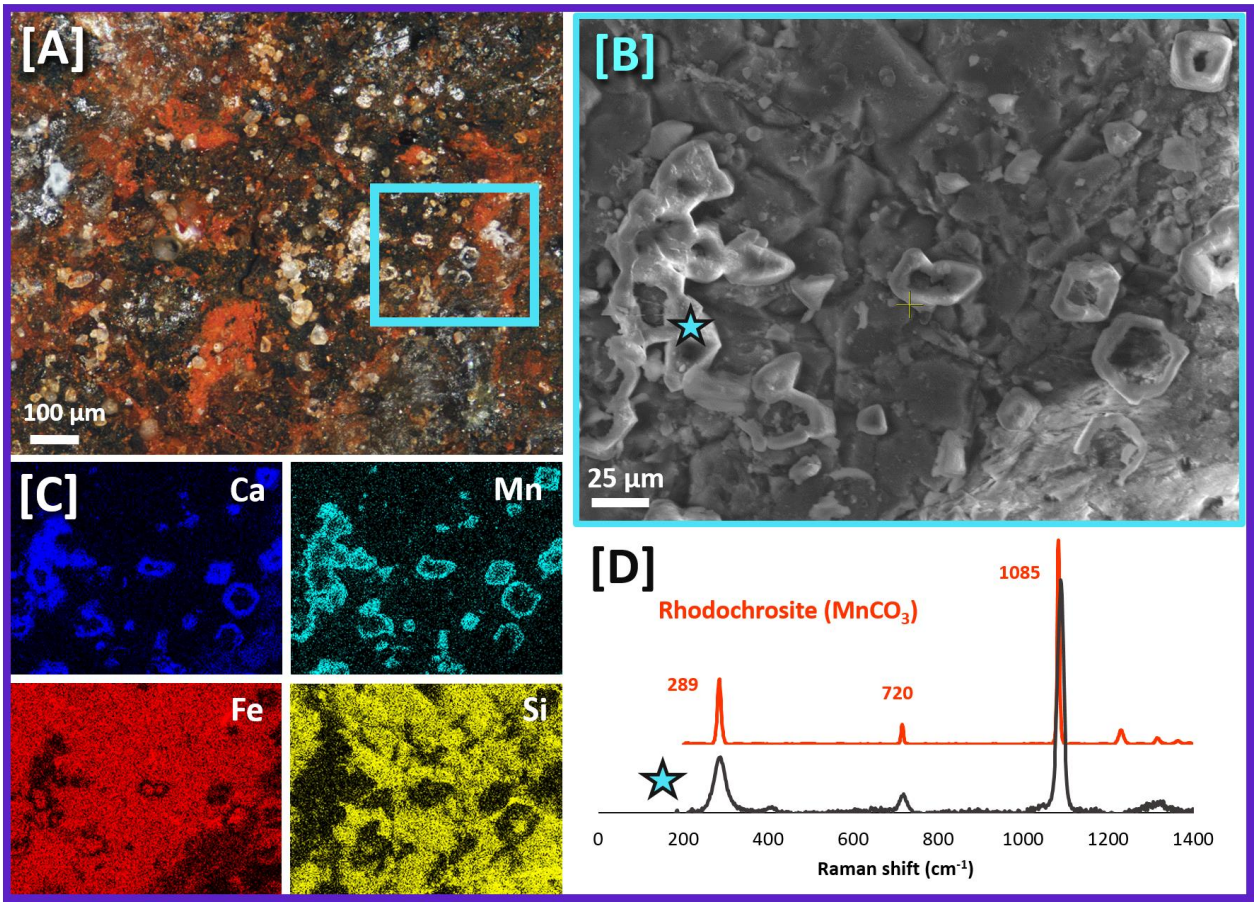

Figure C11. Mn-rich carbonates forming on the unmilled surface (of the milled side of the core) in LB-100C, illustrated with [A] an optical microscopy image; [B] SEM image; [C] EDS maps, where the carbonate 'rings' are Ca- and Mn-rich but silica-poor; and [D] a Raman spectra of the crystal marked with a star in the SEM image [B], which aligns well with a standard spectra (in red) for $MnCO_3$ from the RRUFF database.

C4. Additional Results: HB-100C

Holding temperature at 100°C while raising [$NaHCO_3$] by ~2 orders of magnitude produced a visible increase in precipitation on both saw-cut core surfaces (Figure C12). Changes in fracture aperture following CO_2 injection were quantified via xCT segmentation (Figure C13).

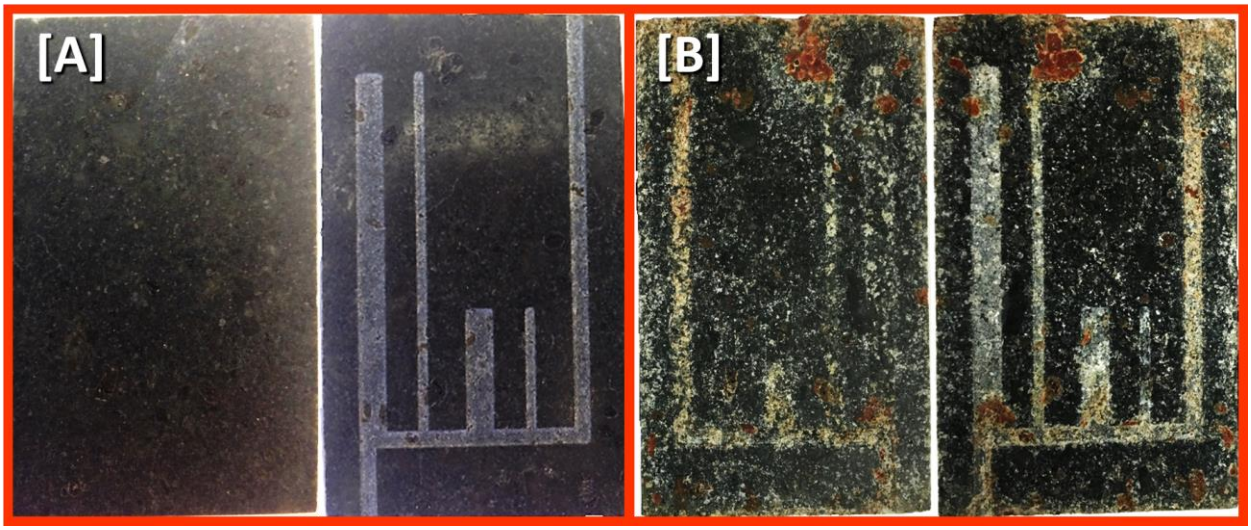

Figure C12. Comparison of [A] pre- and [B] post-reaction saw-cut basalt surfaces for HB-100C. In each image, the polished side of the core is on the left and the milled side on the right.

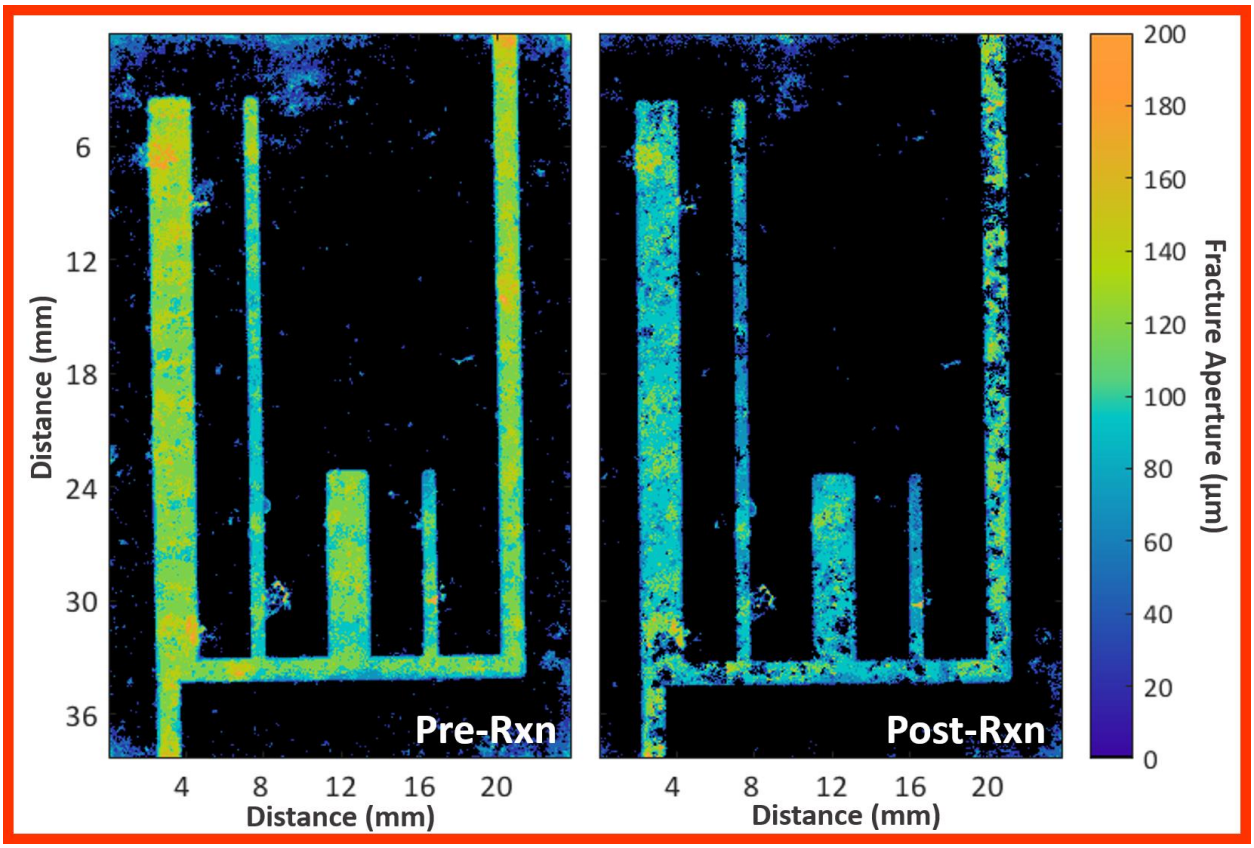

Figure C13. Fracture aperture maps for HB-100C based on segmentation of pre- and post-reaction xCT scans. Dark regions in post-reaction fractures indicate aperture reduction from secondary precipitation.

Fracture volumes calculated from the segmentation revealed the total amount of milled fracture space was reduced from 23.7 pre-reaction to 15.5 mm^3 post-reaction. To evaluate spatial trends in local aperture reduction, changes in fracture volume were also calculated as a function of distance into the longer dead-end fractures (Figure C14). While the long and narrow dead-end fractures, which exhibited the greatest extent of filling in both HB-100C and HB-150C, displayed a general increase in fracture closure with diffusion distance, no clear trends were evident in the wider fractures containing higher water:rock ratios.

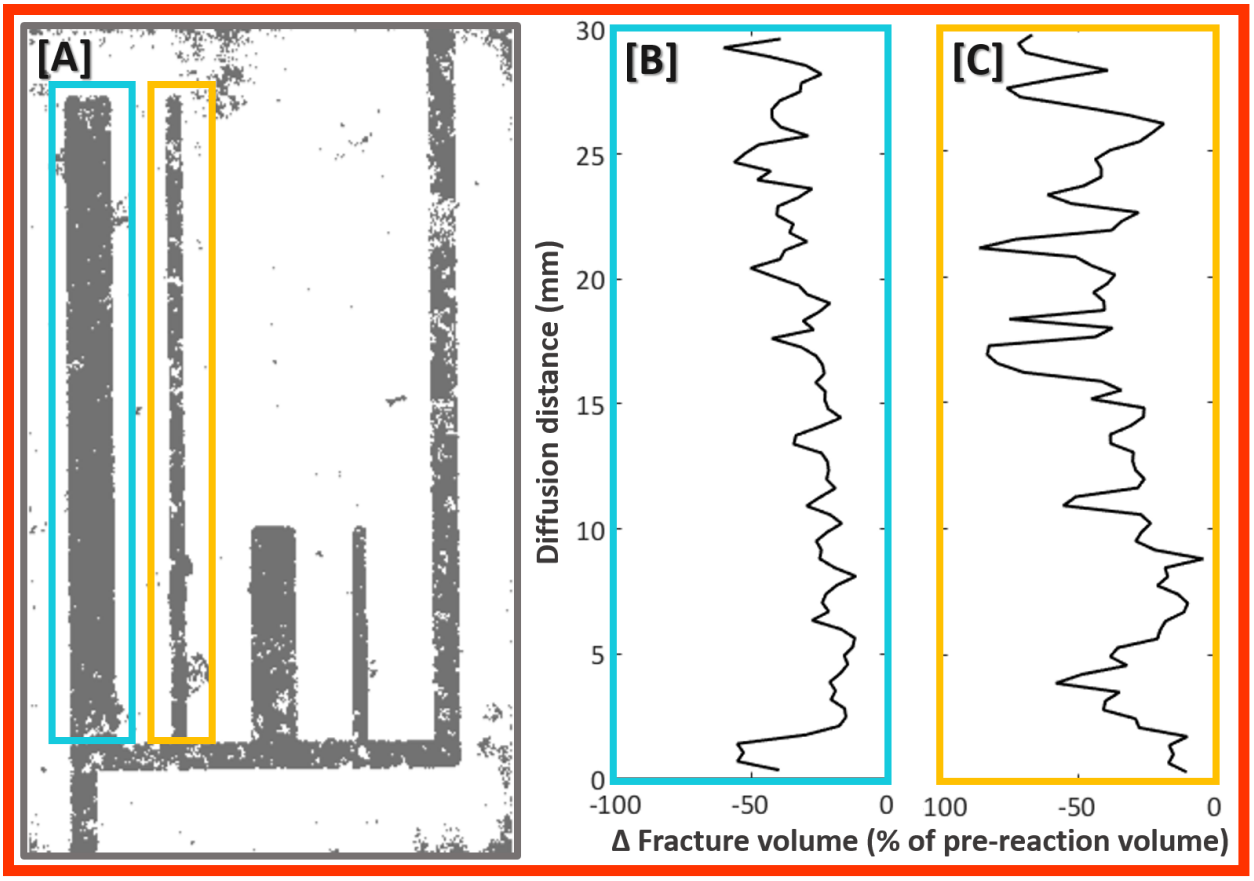

Figure C14. Fracture volume changes as a function of diffusion distance for HB-100C. [A] Binary post-reaction aperture map, where white regions within the fractures correspond to complete fracture closure (i.e., bridging) due to precipitation. In each scan, fracture volumes were also calculated along the width of the fractures in 235-µm depth increments moving from the main flow path into the fracture. The changes in volume between pre- and post-reaction scans were then calculated as a function of distance into the long [B] wide and [C] narrow dead-end fractures.

Similar to LB-100C, the main flow channel was weathered to clay-like silicates, as evidenced in Figure C15. Whereas thin coatings were observed in LB-100C, xCT scans revealed that clays partially or nearly completely filled the flow paths in HB-100C. Some had structures resembling kaolinite (Figure C15[C]).

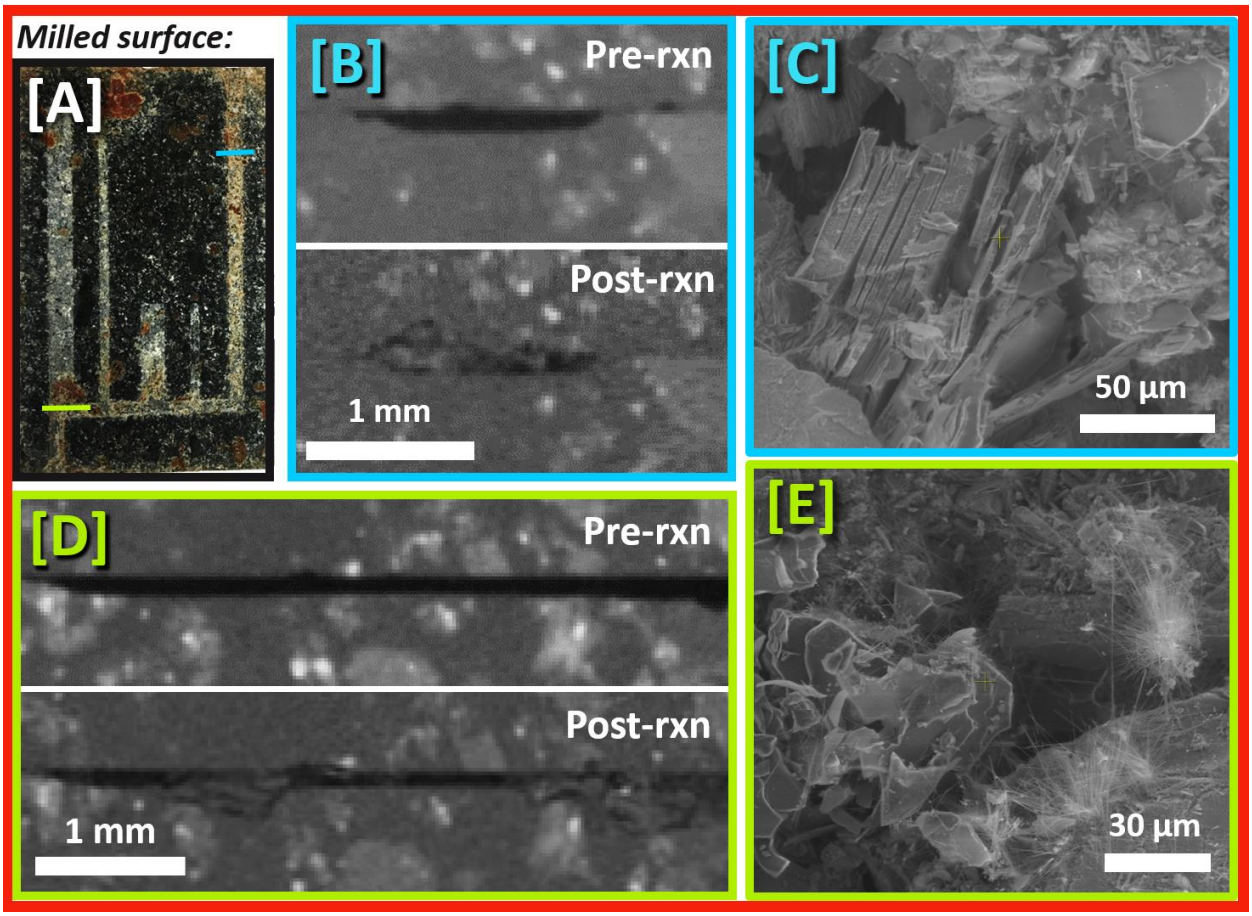

Figure C15. Clay weathering in the main flow path. [A] The two colored lines indicate two locations on the flow paths where [B and D] slices from the xCT data, taken perpendicular to the direction of flow, revealed partial to nearly complete fracture filling with precipitates. In the same locations, SEM images [C and E] show silica-rich clay-like structures on the surface of the milled flow path.

Whereas carbonates predominantly formed in unmilled regions of the core in LB-100C, carbonation also occurred in the milled dead-end fractures in HB-100C. Figure C16 demonstrates partial fracture filling with large clusters of amorphous Ca- and Mg-rich carbonates that coated both the milled and polished core surfaces. Optical microscope and SEM imaging revealed these carbonates formed more amorphously and ubiquitously than the isolated but well-defined crystals in LB-100C. The morphology of the carbonate crystals varied with diffusion distance into this

fracture, evidenced on both the milled (Figure C17) and polished (Figure C18) sides of the core. Amorphous carbonates were found in the long wide fracture (Figure C19) and clusters of carbonates were also observed on the unmilled surface, as illustrated in Figure C20. The black carbonate crystals and Fe-oxide layers in the center of the carbonate "ring" are likely due to the presence of Mn. Figure C21 provides another example of carbonation in an unmilled region, but here Ca-carbonates formed distinct individual star-shaped crystals more similar to those in the first experiment. As in LB-100C, carbonates were often associated with orange or red coatings of Fe-oxides on larger pyroxene grains.

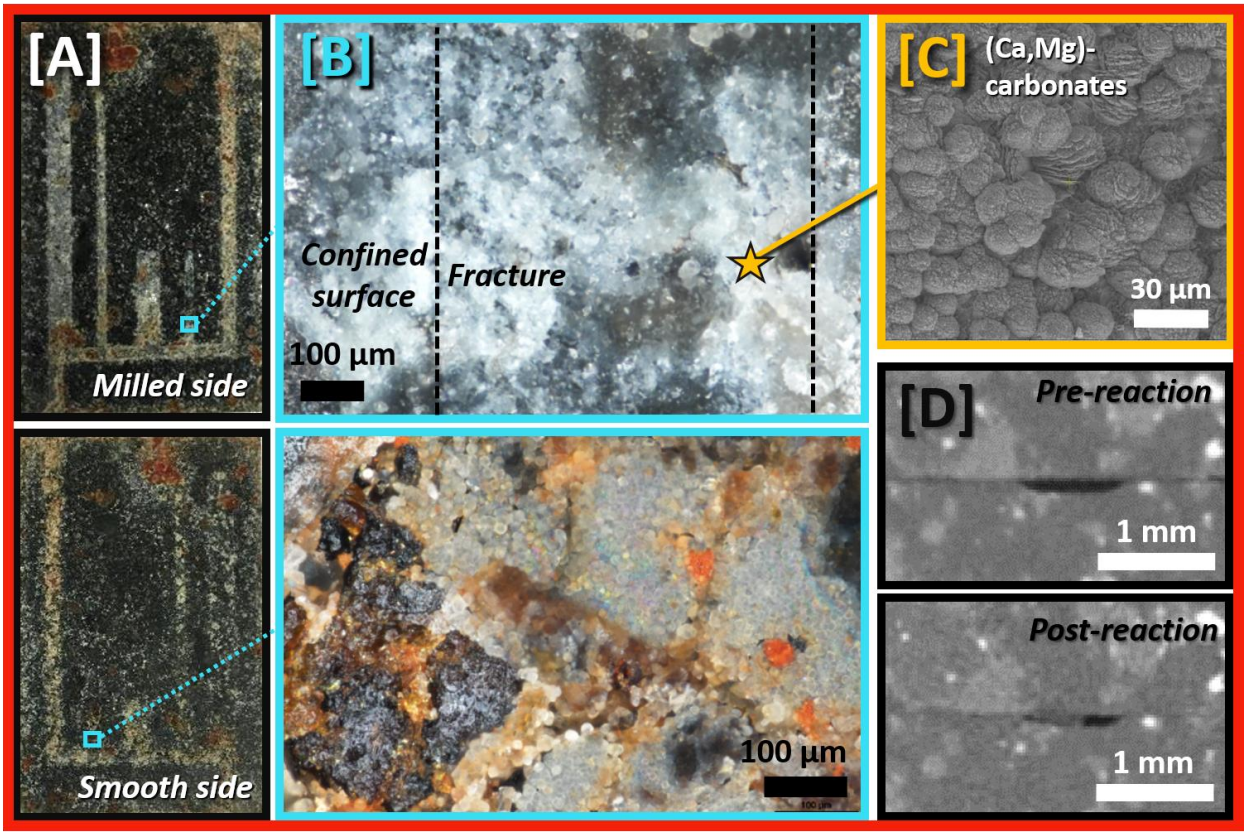

Figure C16. Carbonates partially filling a region of the short and narrow dead-end fracture in HB-100C, [A] highlighted on the milled (top) and polished (bottom) sides of the saw-cut basalt. Both surfaces were coated with white sphere-like crystals, shown in [B] optical microscope and [C] SEM images, where they were identified as Ca- and Mg-rich carbonates via EDS mapping and point analysis (not shown). [D] Cross sections of the xCT data in this region revealed the precipitates partially filled the fracture.

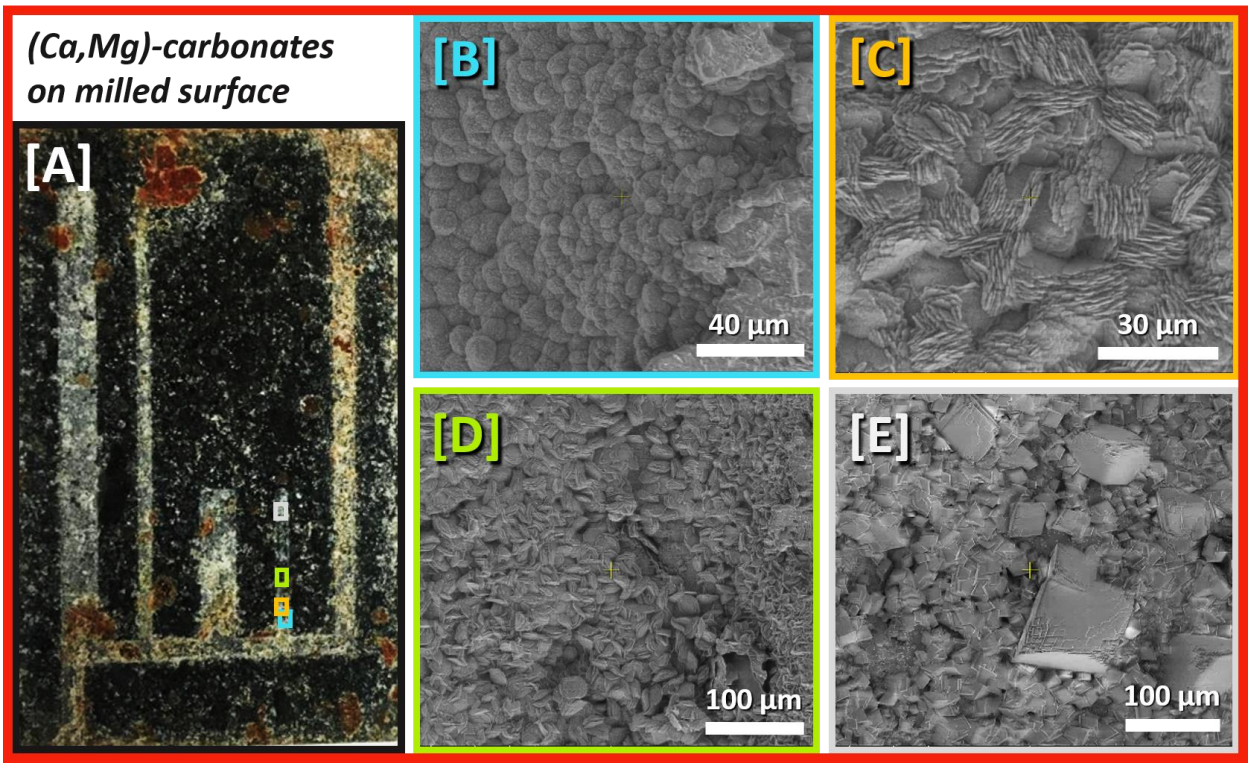

Figure C17. SEM images revealing different carbonate morphologies [B-E] at different locations [A] along the milled surface of the short and narrow dead-end fracture.

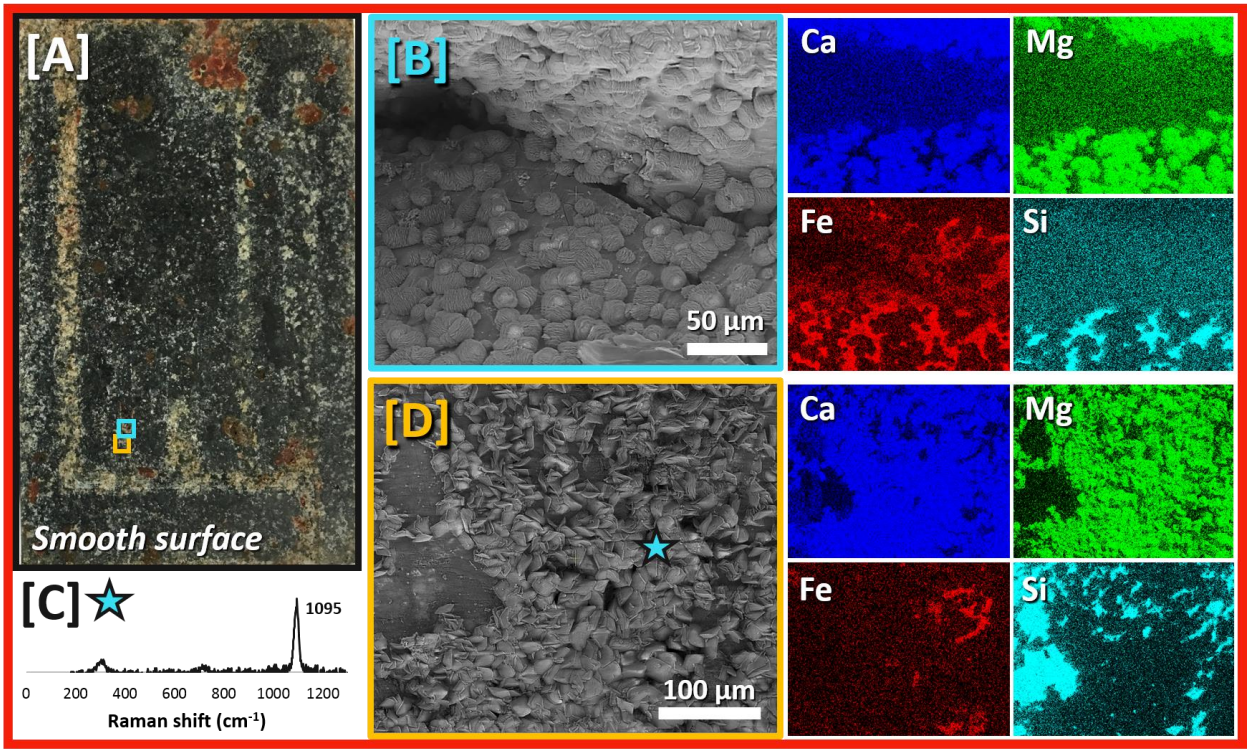

Figure C18. Ca-Mg carbonate morphologies in different locations [A] on the smooth polished surface of the short and narrow dead-end fracture. [B and D] SEM images and EDS maps of amorphous Ca- and Mg-rich carbonates, some of which had Raman spectra characteristic of magnesite [C].

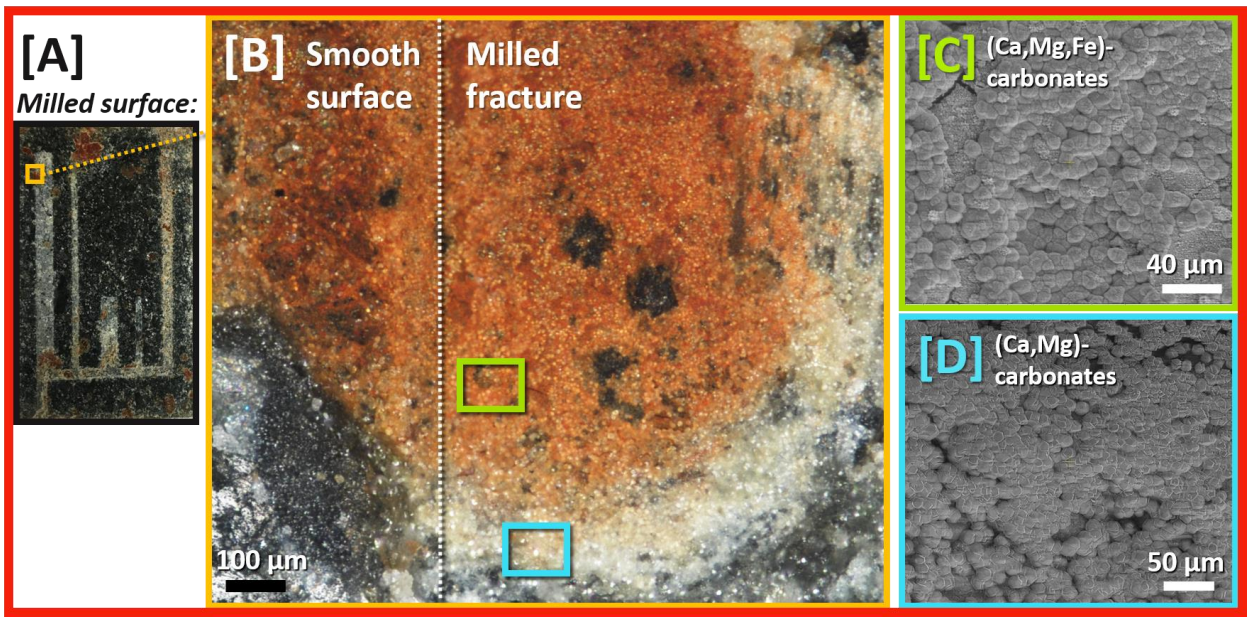

Figure C19. Carbonates forming at the end of the long and wide dead-end fracture [A]. Large masses of orange crystals visible in the optical microscope [B] were identified as Fe-rich carbonates via SEM [C] and EDS point analysis (not shown), and white crystal masses correspond to Ca- and Mg-rich carbonates [D].

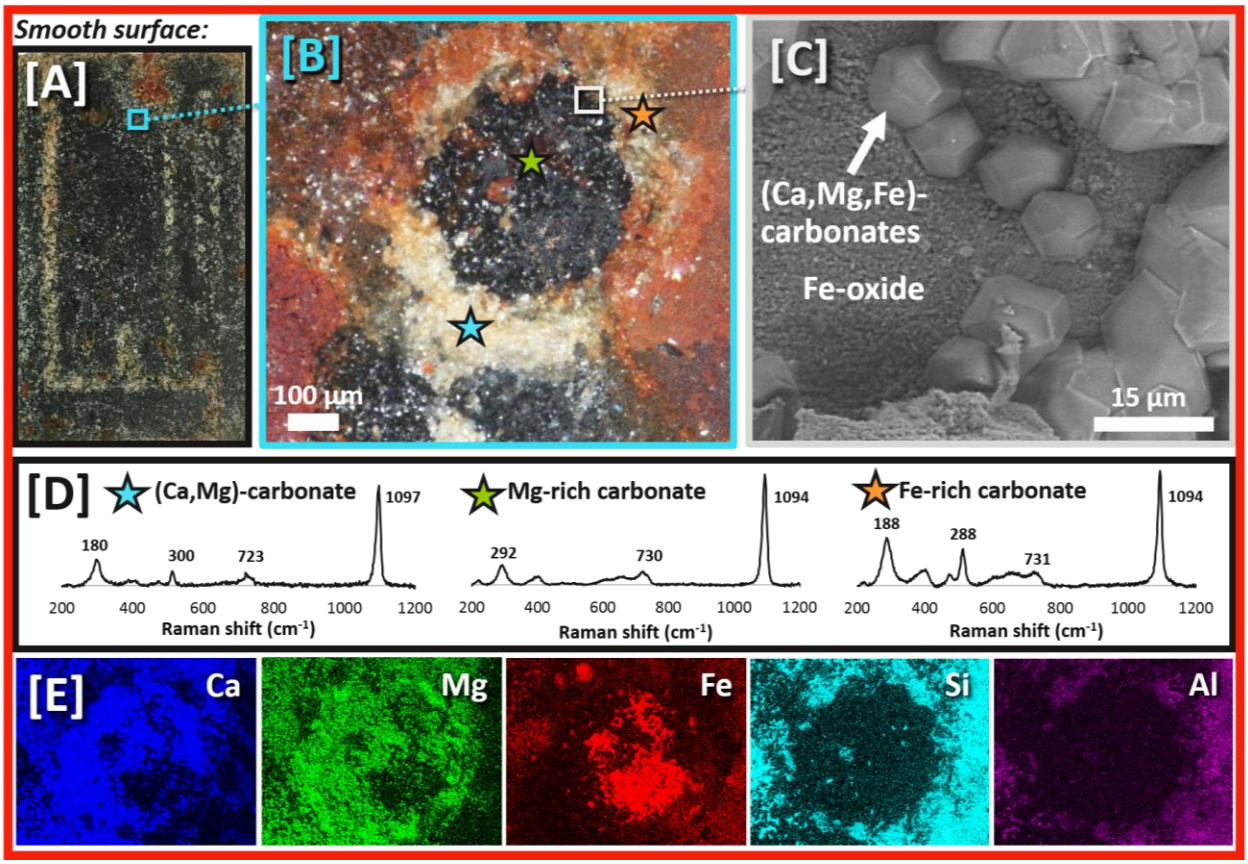

Figure C20. Ring of mixed carbonates in HB-100C. The location boxed in [A] on the polished saw-cut surface is magnified in [B] an optical microscope image, where mixed Ca-, Mg-, and Fe-bearing carbonates were identified via [C] SEM with [E] EDS mapping and point analysis along with [D] Raman spectroscopy.

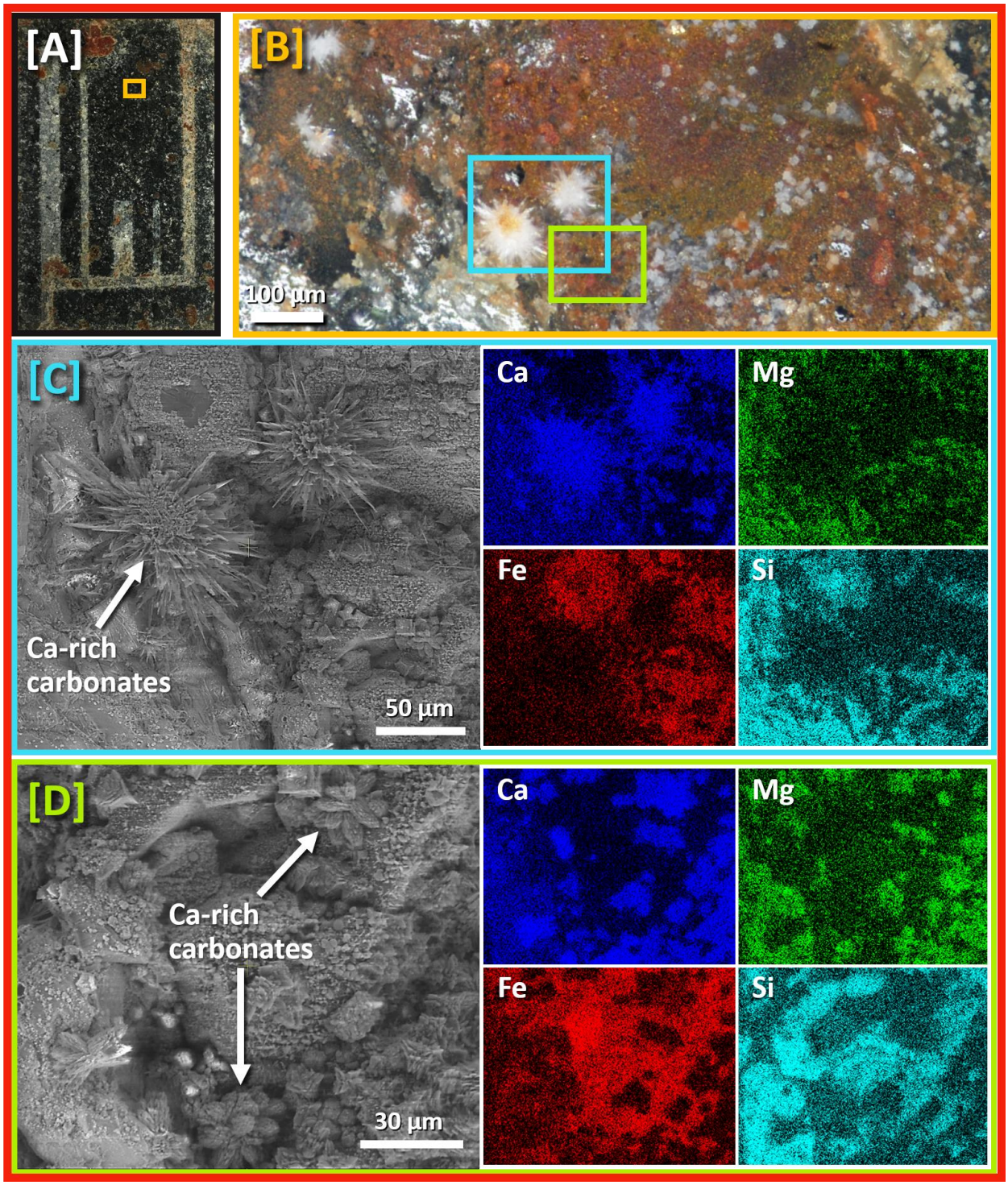

Figure C21. Ca-rich carbonates of varying morphologies on an unmilled region of the milled half of the core. The location boxed in [A] is magnified in [B] an optical microscope image revealing yellow-red Fe-oxide layers with several prominent individual white crystals, which were identified as Ca-rich carbonates with EDS mapping [C and D] and point analysis along with Raman spectroscopy (not shown).

C5. Additional Results: HB-150C

At the same concentration of $NaHCO_3$ (0.64 M), increasing the temperature to 150°C produced another increase in secondary alteration (Figure C22). Fracture aperture maps also revealed a greater reduction in total fracture volume due to secondary precipitation (Figure C23).

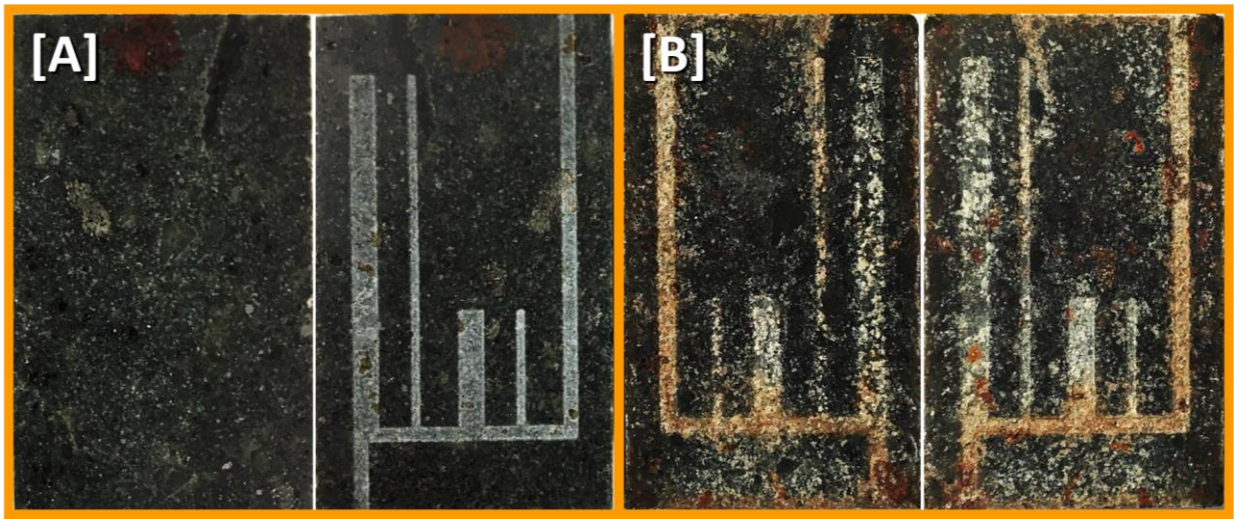

Figure C22. Comparison of (A) pre- and (B) post-reaction saw-cut basalt surfaces for HB-150C. In each image, the polished side of the core is on the left and the milled side on the right.

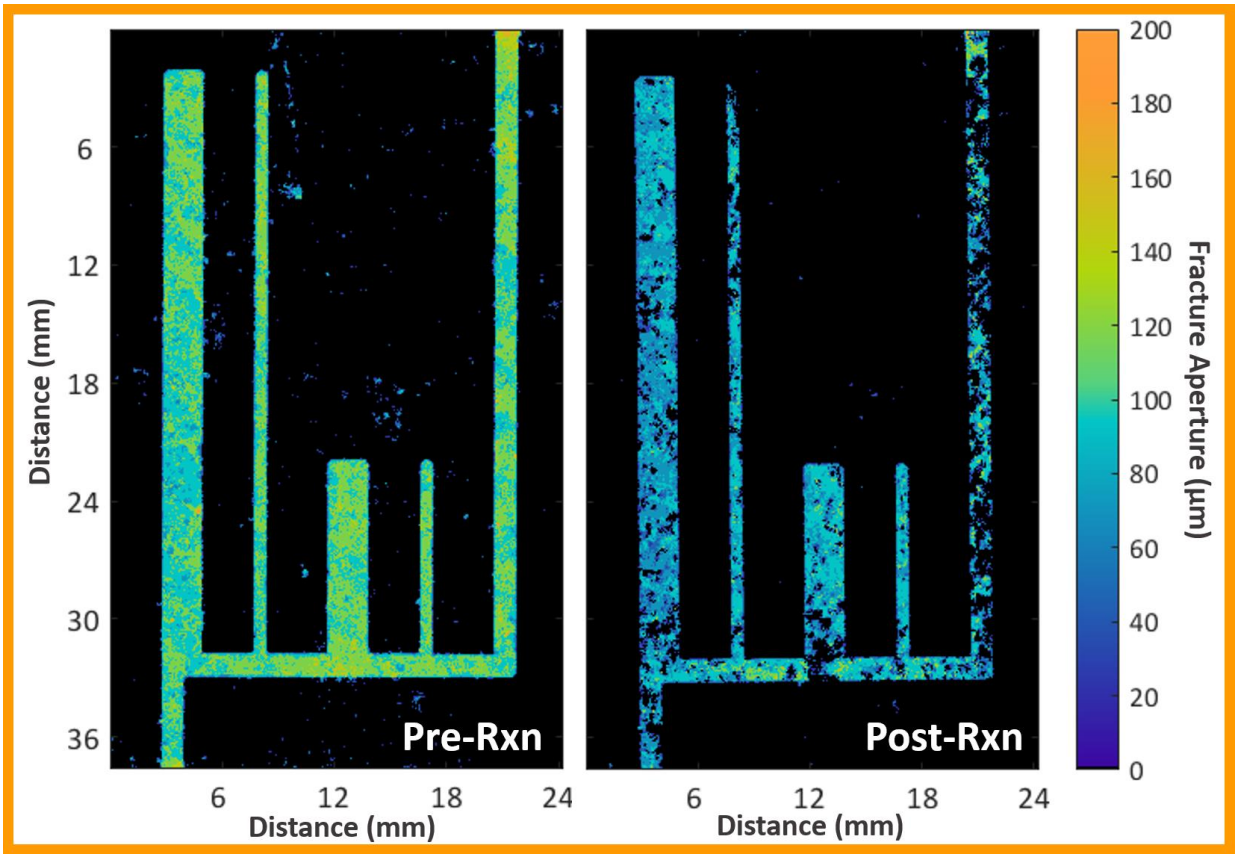

Figure C23. Fracture aperture maps for HB-150C based on segmentation of pre- and post-reaction xCT scans. Dark regions in post-reaction fractures indicate aperture reduction from secondary precipitation.

Changes in fracture volume were again calculated as a function of distance into the dead-end fractures (Figure C24), revealing similar trends as HB-100C. Fracture bridging generally increased with diffusion distance in the long narrow fracture. In the long wide fracture, the extent of precipitate bridging reached a maximum in two locations: near the base of the fracture adjacent to the main flow path and in the middle.

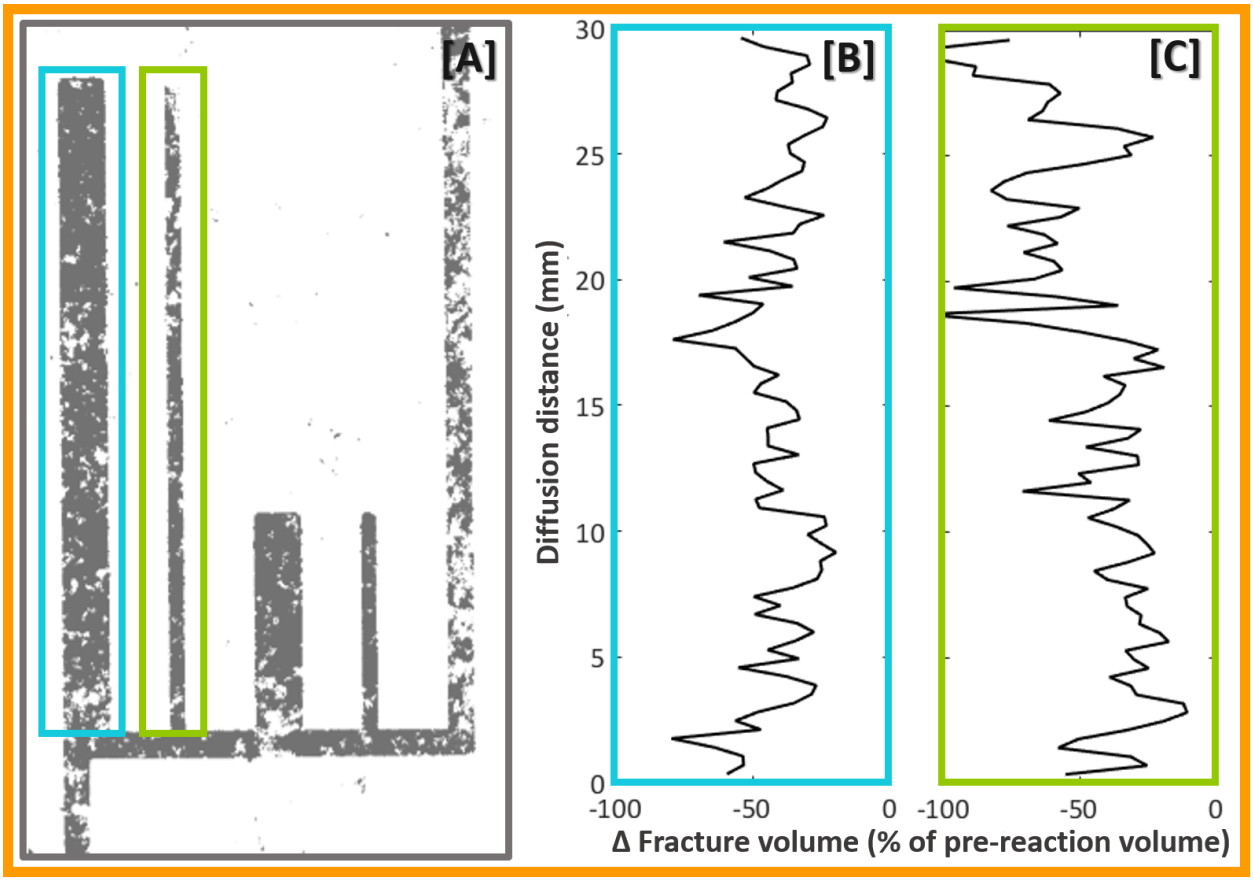

Figure C24. Fracture volume changes as a function of diffusion distance for HB-150C. [A] Binary post-reaction aperture map, where white regions within the fractures correspond to complete fracture closure (i.e., bridging) due to precipitation. In each scan, fracture volumes were also calculated along the width of the fractures in 235-µm depth increments moving from the main flow path into the fracture. The changes in volume between pre- and post-reaction scans were then calculated as a function of distance into the long [B] wide and [D] narrow dead-end fractures.

As noted in Chapter 3 (Section 3.3.4), some carbonate crystals were found in the main advection-dominated flow path of HB-150C in addition to the diffusion-dominated regions. An example of carbonate crystals found on Fe-oxide coatings in the milled channel is provided in Figure C25. xCT data showing fracture filling with precipitates near the inlet, which were primarily clays and Fe-oxides, is also included.

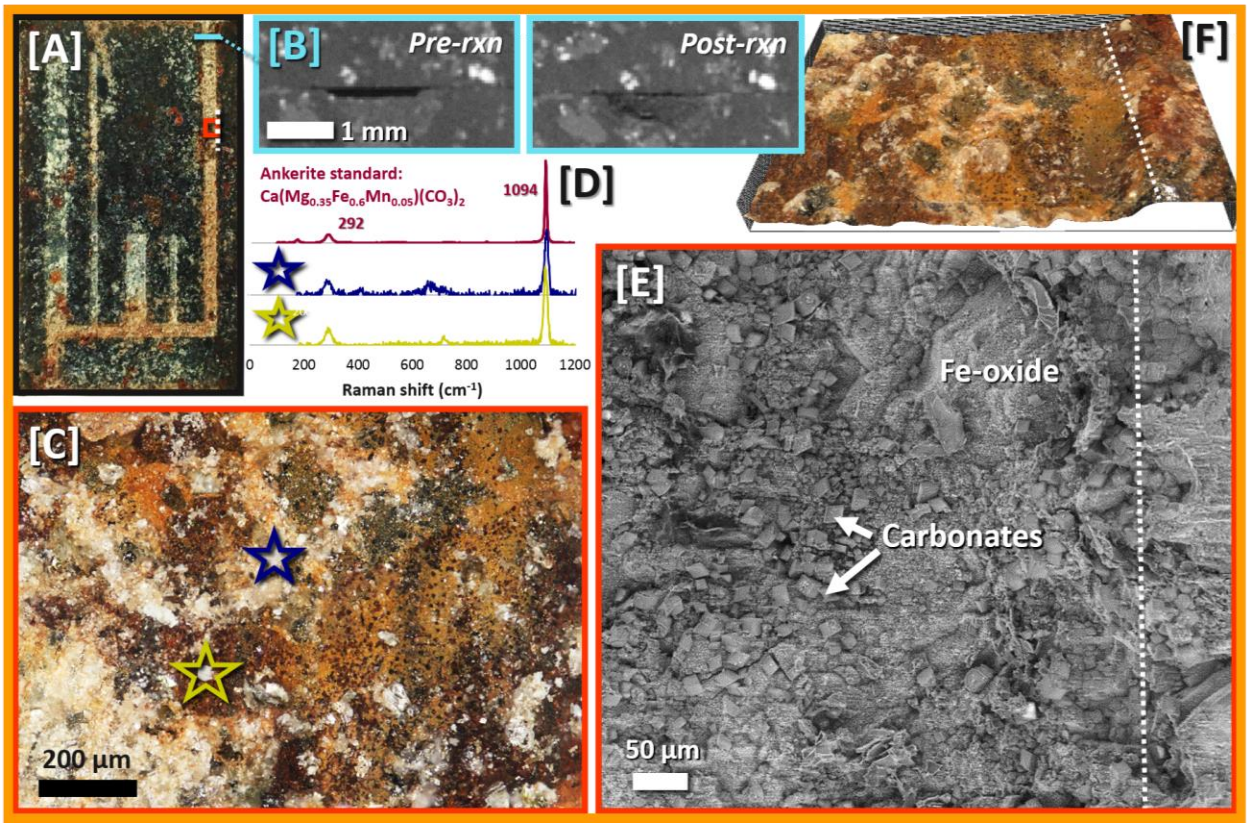

Figure C25. Precipitation in two locations [A] along the main flow path of HB-150C. [B] Cross-sectional pre- and post-reaction xCT images showing where the flow path had filled with precipitates near the inlet. [C] Optical microscope image showing white carbonates forming on orange-red Fe-oxide coatings further down the flow path, which had Raman spectra characteristic of ankerite [D]. SEM [E] and 3-D optical microscope [F] imaging along the edge of this region further illustrate the carbonates forming on the milled surface as small (<20 µm) rhombohedral crystals.

White carbonates were also found associated with Fe-oxides near the outlet of the milled channel (Figure C26), where precipitation also filled the milled space in post-reaction xCT scans.

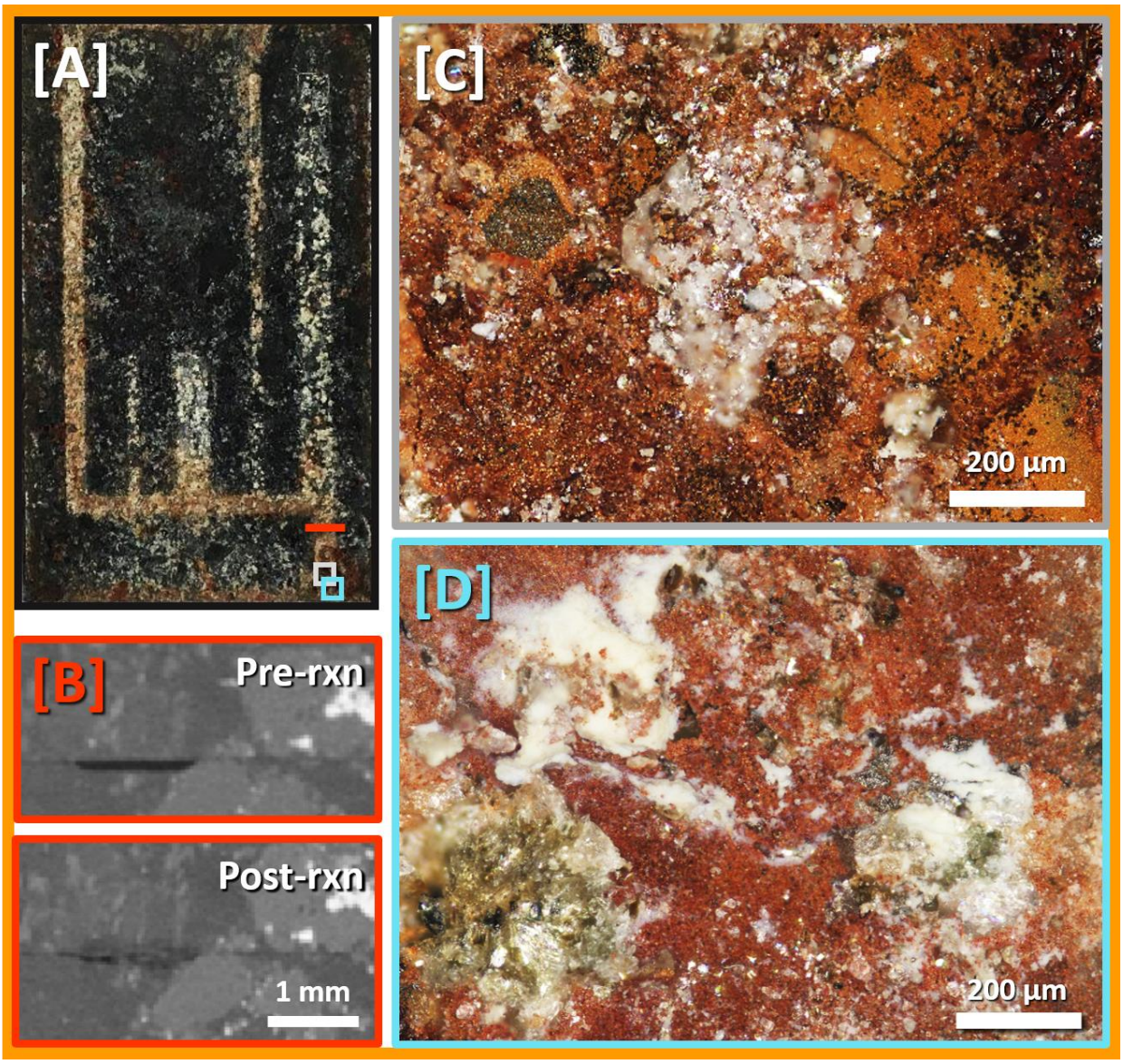

Figure C26. Carbonates near the outlet of the main flow path. [A] marks locations where the unmilled side of the milled path was [B] filled with precipitates in the post-reaction xCT scan and [C-D] coated with Fe-oxides and various carbonates.

Post-reaction xCT scans also evidenced precipitates filling the milled dead-end fractures. Figure C27 highlights carbonates (identified with SEM and Raman spectroscopy) bridging the end of the long and narrow dead-end fracture. Strongly localized carbonates were again observed in HB-150C, but only on the unmilled surfaces of the saw-cut cores (Figure C28).

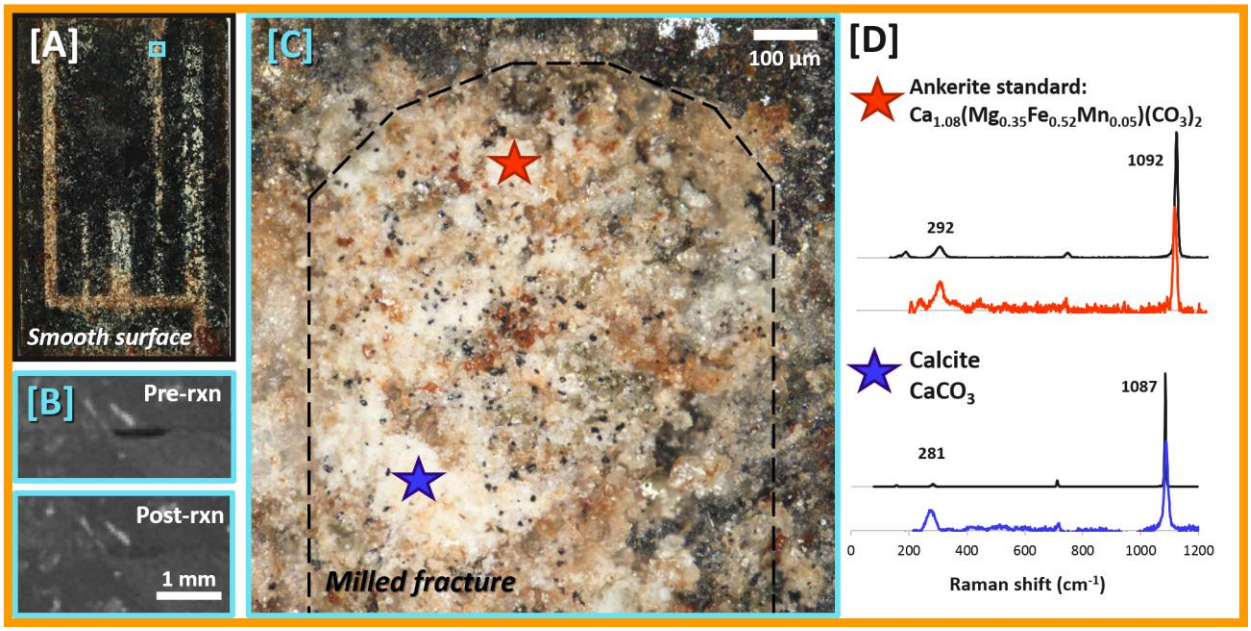

Figure C27. Carbonates filling the end of the long and narrow dead-end fracture [A], evidenced with cross-sectional xCT scans [B], an optical microscope image showing carbonates attached to the unmilled surface at the fracture tip, and [C] Raman spectroscopy exemplifying different crystals.

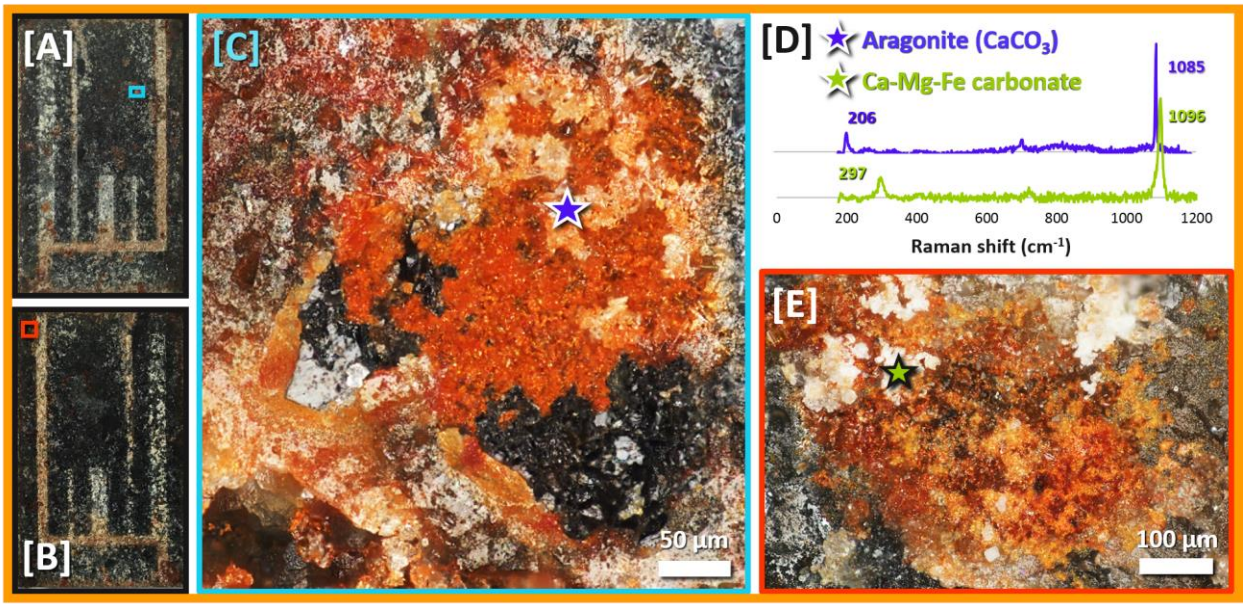

Figure C28. Localized carbonates forming on the [A] milled and [B] unmilled core surfaces in HB-150C, identified with [D] Raman spectroscopy. [C] Small aragonite crystals formed on orange and black Fe-oxide coatings near the main flow path of the milled side. [E] Ca-Mg-Fe-bearing carbonates, also associated with Fe-oxides, that precipitated on the smooth (unmilled) side of the core.

REFERENCES

(1) Steefel, C. I.; Appelo, C. A. J.; Arora, B.; Jacques, D.; Kalbacher, T.; Kolditz, O.; Lagneau, V.; Lichtner, P. C.; Mayer, K. U.; Meeussen, J. C. L.; Molins, S.; Moulton, D.; Shao, H.; Šimůnek, J.; Spycher, N.; Yabusaki, S. B.; Yeh, G. T. Reactive Transport Codes for Subsurface Environmental Simulation. *Comput. Geosci.* **2015**, *19* (3), 445–478. https://doi.org/10.1007/s10596-014-9443-x.

(2) Menefee, A. H.; Li, P.; Giammar, D. E.; Ellis, B. R. Roles of Transport Limitations and Mineral Heterogeneity in Carbonation of Fractured Basalts. *Environ. Sci. Technol.* **2017**, *51* (16), 9352–9362. https://doi.org/10.1021/acs.est.7b00326.

(3) Adeoye, J. T.; Menefee, A. H.; Xiong, W.; Wells, R. K.; Skemer, P.; Giammar, D. E.; Ellis, B. R. Effect of Transport Limitations and Fluid Properties on Reaction Products in Fractures of Unaltered and Serpentinized Basalt Exposed to High P CO2 Fluids. *Int. J. Greenh. Gas Control* **2017**, *63*, 310–320. https://doi.org/10.1016/j.ijggc.2017.06.003.

(4) Cadogan, S. P.; Maitland, G. C.; Trusler, J. P. M. Diffusion Coefficients of CO_2 and N_2 in Water at Temperatures between 298.15 K and 423.15 K at Pressures up to 45 MPa. *J. Chem. Eng. Data* **2014**, *59* (2), 519–525. https://doi.org/10.1021/je401008s.

(5) Duan, Z.; Sun, R. An Improved Model Calculating CO_2 Solubility in Pure Water and Aqueous NaCl Solutions from 273 to 533 K and from 0 to 2000 Bar. *Chem. Geol.* **2003**, *193*, 257–271.

(6) Palandri, J. L.; Kharaka, Y. K. *A Compilation of Rate Parameters of Water-Mineral Interaction Kinetics for Application to Geochemical Modeling*; DTIC Document, 2004.

(7) Knauss, K. G.; Johnson, J. W.; Steefel, C. I. Evaluation of the Impact of CO_2, Co-Contaminant Gas, Aqueous Fluid and Reservoir Rock Interactions on the Geologic Sequestration of CO_2. *Chem. Geol.* **2005**, *217* (3–4), 339–350. https://doi.org/10.1016/j.chemgeo.2004.12.017.

(8) Teir, S.; Revitzer, H.; Eloneva, S.; Fogelholm, C.-J.; Zevenhoven, R. Dissolution of Natural Serpentinite in Mineral and Organic Acids. *Int. J. Miner. Process.* **2007**, *83* (1–2), 36–46. https://doi.org/10.1016/j.minpro.2007.04.001.

(9) Orlando, A.; Borrini, D.; Marini, L. Dissolution and Carbonation of a Serpentinite: Inferences from Acid Attack and High P–T Experiments Performed in Aqueous Solutions at Variable Salinity. *Appl. Geochem.* **2011**, *26* (8), 1569–1583. https://doi.org/10.1016/j.apgeochem.2011.06.023.

(10) Pokrovsky, O. S.; Golubev, S. V.; Schott, J. Dissolution Kinetics of Calcite, Dolomite and Magnesite at 25 °C and 0 to 50 Atm PCO_2. *Chem. Geol.* **2005**, *217* (3–4), 239–255. https://doi.org/10.1016/j.chemgeo.2004.12.012.

(11) Golubev, S. V.; Bénézeth, P.; Schott, J.; Dandurand, J. L.; Castillo, A. Siderite Dissolution Kinetics in Acidic Aqueous Solutions from 25 to 100 °C and 0 to 50 Atm PCO_2. *Chem. Geol.* **2009**, *265* (1–2), 13–19. https://doi.org/10.1016/j.chemgeo.2008.12.031.

(12) Pokrovsky, O. S.; Schott, J. Surface Chemistry and Dissolution Kinetics of Divalent Metal Carbonates. *Environ. Sci. Technol.* **2002**, *36* (3), 426–432. https://doi.org/10.1021/es010925u.

(13) Carroll, S. A.; McNab, W. W.; Dai, Z.; Torres, S. C. Reactivity of Mount Simon Sandstone and the Eau Claire Shale under CO_2 Storage Conditions. *Environ. Sci. Technol.* **2013**, *47* (1), 252–261. https://doi.org/10.1021/es301269k.

(14) Tester, J. W.; Worley, W. G.; Robinson, B. A.; Grigsby, C. O.; Feerer, J. L. Correlating Quartz Dissolution Kinetics in Pure Water from 25 to 625C. *Geochem. Cosmochim. Acta* **1994**, *58* (11), 2407–2420.

(15) Huertas, F. J.; Chou, L.; Wollast, R. Mechanism of Kaolinite Dissolution at Room Temperature and Pressure Part II: Kinetic Study. *Geochim. Cosmochim. Acta* **1999**, *63* (19), 3261–3275.

(16) Dogan, A. U.; Dogan, M.; Onal, M.; Sarikaya, Y.; Aburub, A.; Wurster, D. E. Baseline Studies of the Clay Minerals Society Source Clays: Specific Surface Area by the Brunauer Emmett Teller (BET) Method. *Clays Clay Miner.* **2006**, *54* (1), 62–66.

(17) Fontes, M. P. F.; Weed, S. B. Phosphate Adsorption by Clays from Brazilian Oxisols: Relationships with Specific Surface Area and Mineralogy. *Geoderma* **1996**, *72* (1–2), 37–51.

(18) Zimmer, K.; Zhang, Y.; Lu, P.; Chen, Y.; Zhang, G.; Dalkilic, M.; Zhu, C. SUPCRTBL: A Revised and Extended Thermodynamic Dataset and Software Package of SUPCRT92. *Comput. Geosci.* **2016**, *90*, 97–111. https://doi.org/10.1016/j.cageo.2016.02.013.

(19) Johnson, J. W.; Oelkers, E. H.; Helgeson, H. C. SUPCRT92: A Software Package for Calculating the Standard Molal Thermodynamic Properties of Minerals, Gases, Aqueous Species, and Reactions from 1 to 5000 Bar and 0 to 1000 C. *Comput. Geosci.* **1992**, *18* (7), 899–947.

(20) Murray, J. W. Deposition of Calcite and Aragonite in Caves. *J. Geol.* **1954**, *62* (5), 481–492.

(21) Stockmann, G. J.; Wolff-Boenisch, D.; Gislason, S. R.; Oelkers, E. H. Do Carbonate Precipitates Affect Dissolution Kinetics? 1: Basaltic Glass. *Chem. Geol.* **2011**, *284* (3–4), 306–316. https://doi.org/10.1016/j.chemgeo.2011.03.010.

(22) Stockmann, G. J.; Wolff-Boenisch, D.; Gislason, S. R.; Oelkers, E. H. Do Carbonate Precipitates Affect Dissolution Kinetics? *Chem. Geol.* **2013**, *337–338*, 56–66. https://doi.org/10.1016/j.chemgeo.2012.11.014.

APPENDIX D

Supporting Information for Chapter 4

D1. DTG RESULTS FOR PB-2

DTG curves for each of the samples analyzed from PB-2 are provided below (Figures D2-D10). Reference DTG curves for the unreacted samples (i.e., forsterite or wollastonite powders as received) are also included. As discussed in Chapter 4, one sample was taken from the shorter packed beds and two samples were taken from the longer beds (one from the upper half and one from the lower half). Note that only one sample was obtained from the fourth longer bed (Figure D10) because there was not sufficient sample material to run two TGA tests. For clarity, the samples represented in Figures D2-D10 are denoted in the schematic (Figure D1) below.

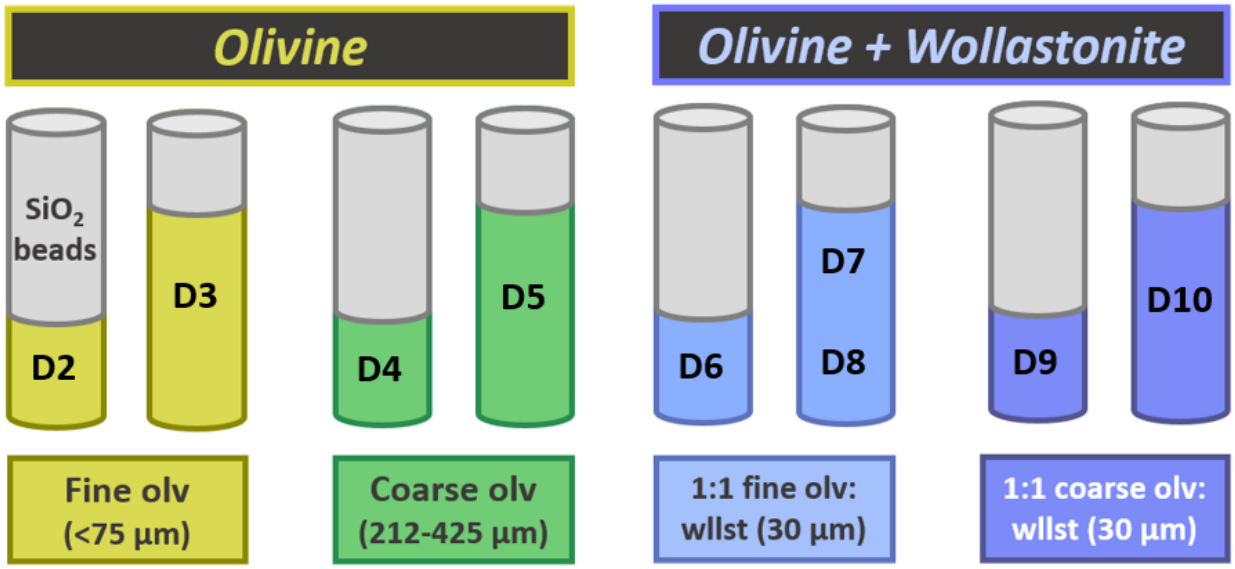

Figure D1. Schematic overview of the locations of DTG measurements presented in this section. Note that in Figures D3 and D5, DTG curves for samples taken from the upper and lower halves of the packed beds are presented on the same graph.

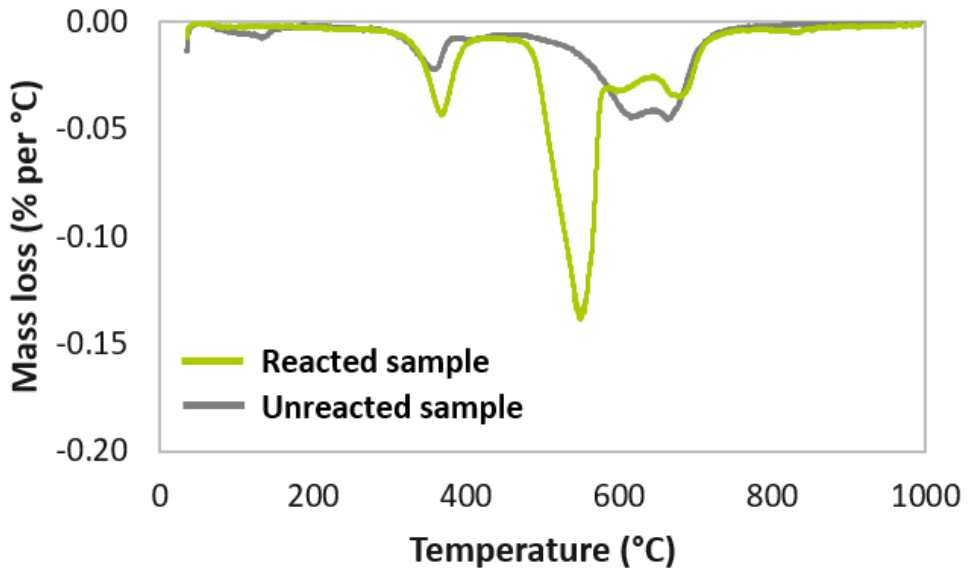

Figure D2. DTG curve for the reacted powders in the shorter fine olivine packed bed, compared to the unreacted fine-grained olivine powders.

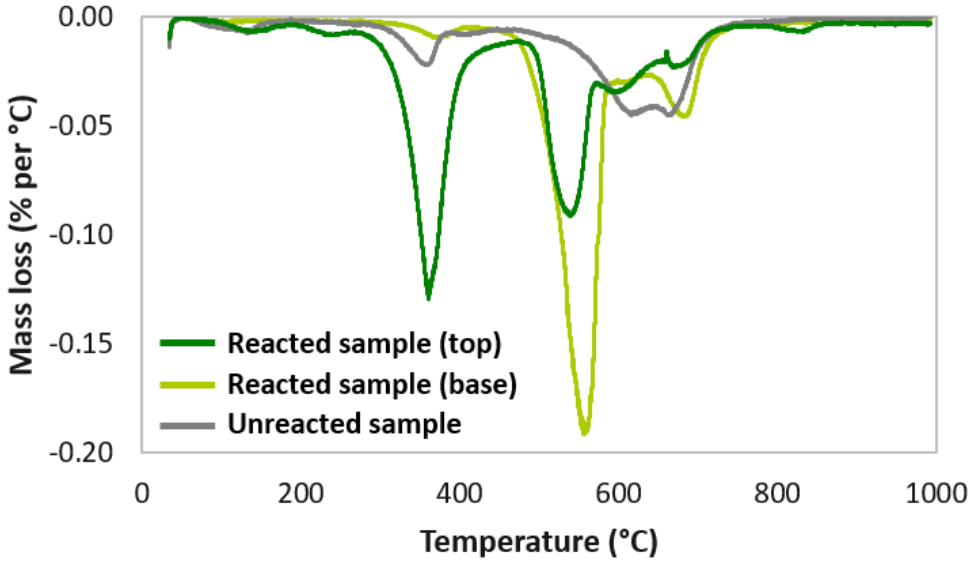

Figure D3. DTG curves for samples taken from the upper (top) and lower (base) halves of the longer fine-grained olivine packed bed.

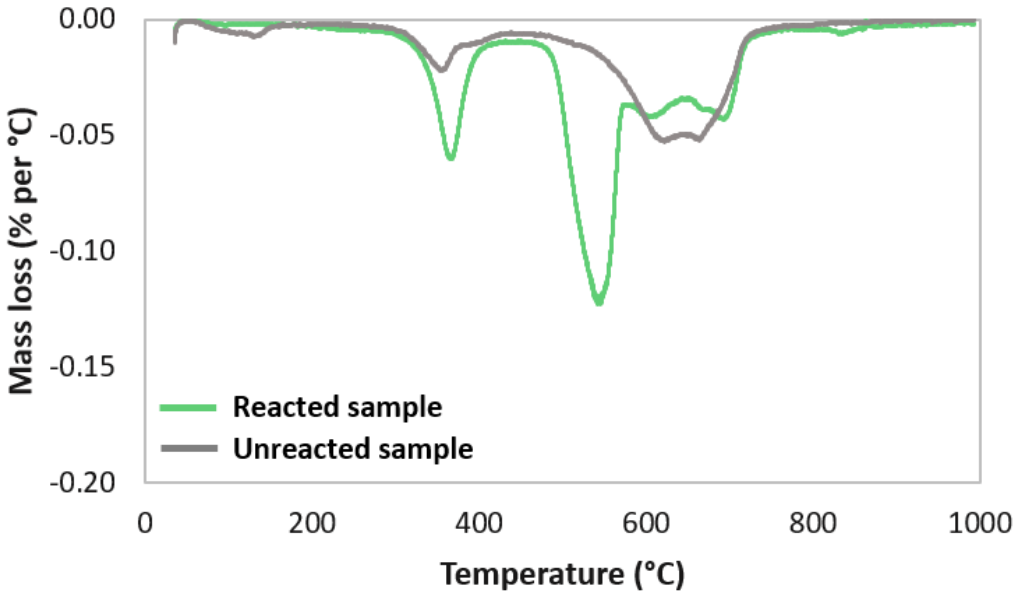

Figure D4. DTG curve and standard for the shorter coarse-grained olivine bed compared with unreacted coarse-grained olivine powders.

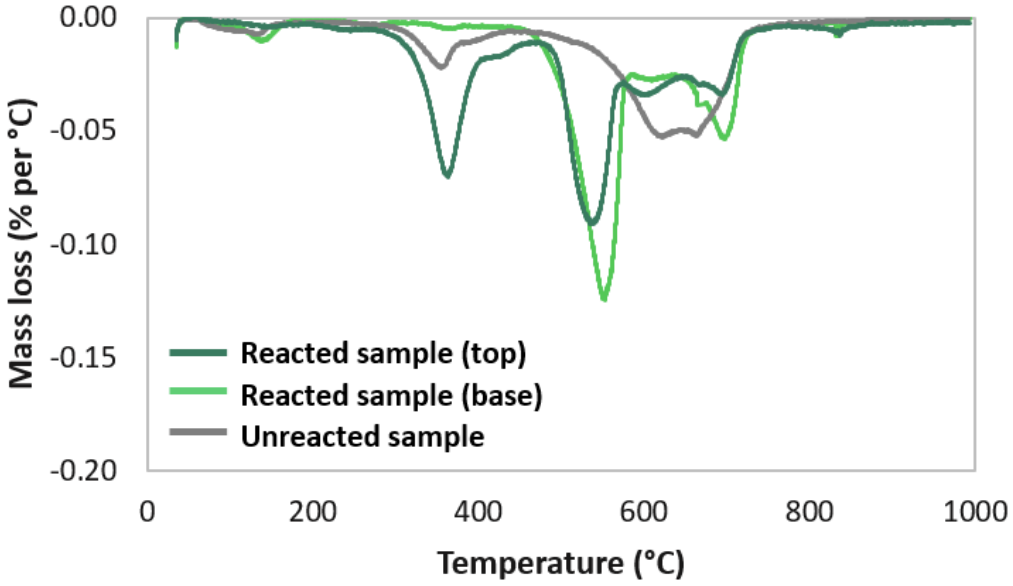

Figure D5. DTG curves for samples taken from the upper (top) and lower (base) halves of the longer coarse-grained olivine packed bed.

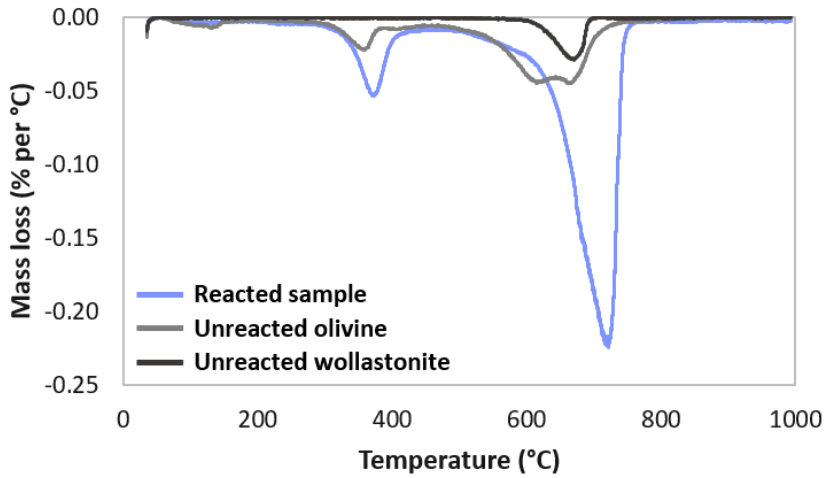

Figure D6. DTG curve for the reacted sample from the shorter mixed fine-grained olivine and wollastonite bed, compared to unreacted fine-grained olivine and wollastonite.

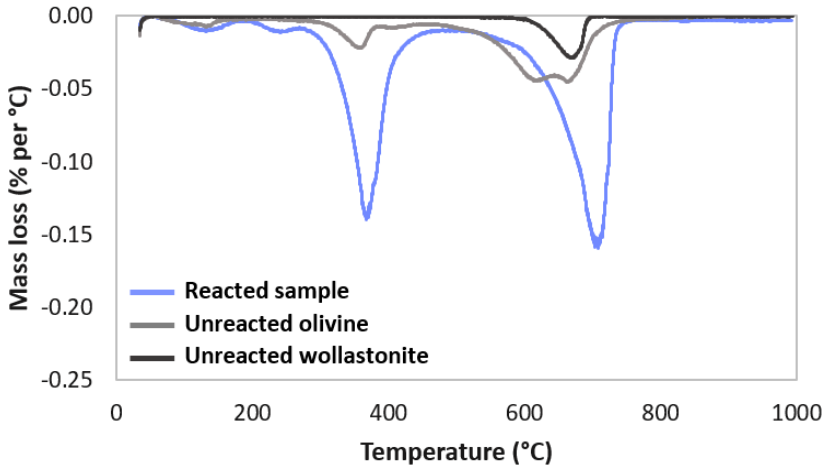

Figure D7. Reacted sample from the top half of the longer mixed fine-grained olivine and wollastonite packed bed, compared with unreacted olivine and wollastonite.

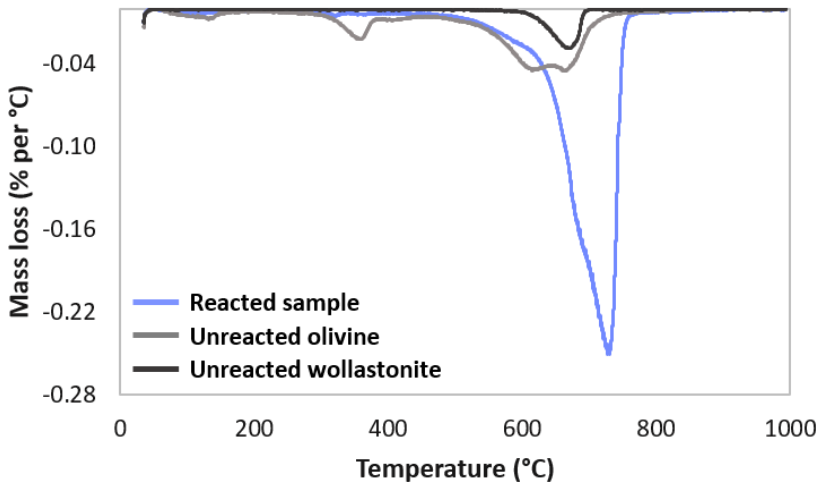

Figure D8. Reacted sample from the lower half of the longer mixed fine-grained olivine and wollastonite packed bed, compared with unreacted olivine and wollastonite.

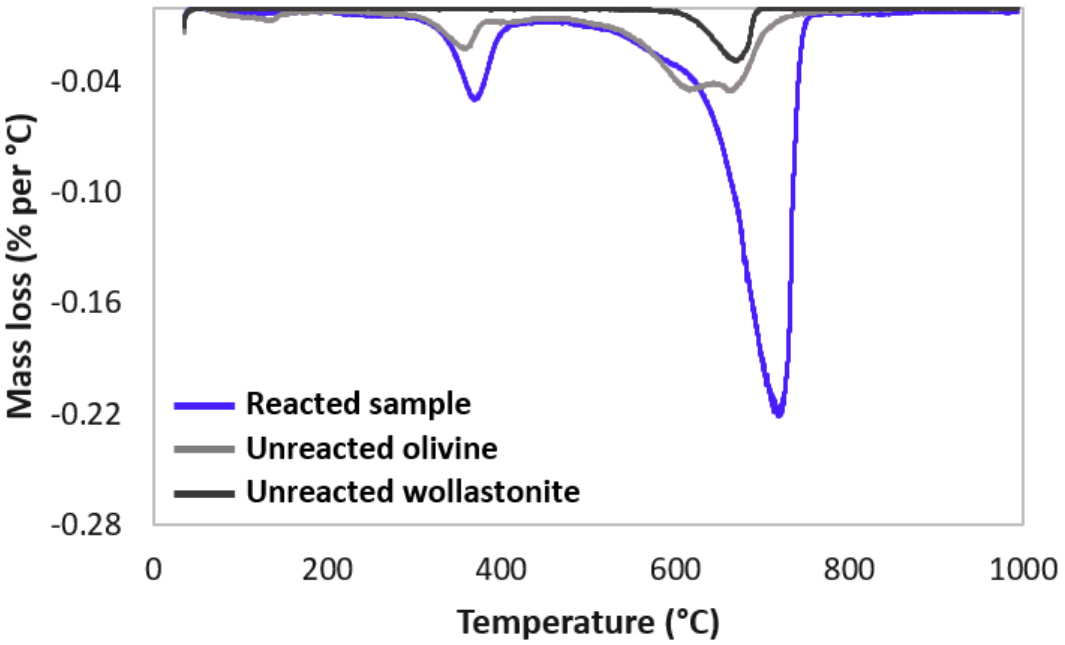

Figure D9. DTG curve for the reacted sample from the shorter mixed coarse-grained olivine and wollastonite bed, compared to unreacted fine-grained olivine and wollastonite.

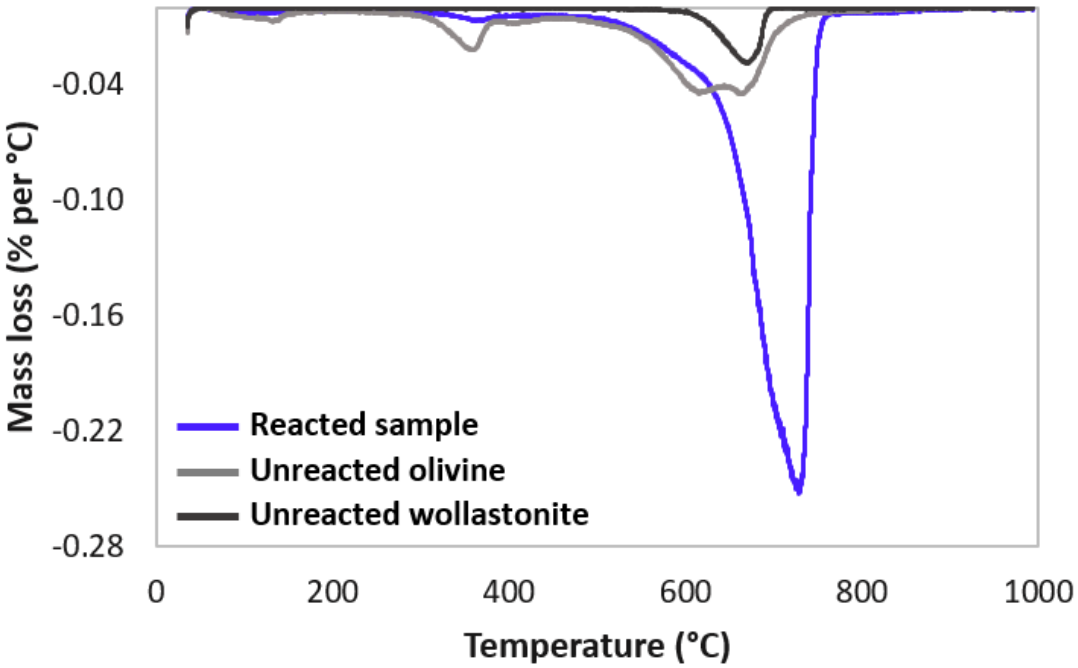

Figure D10. DTG curve for the reacted sample from the longer mixed coarse-grained olivine and wollastonite bed, compared to unreacted fine-grained olivine and wollastonite. As noted in Chapter 4, only enough material for one TGA run was recoverable from this packed bed, precluding separate measurements for the upper and lower halves.

D2. Additional xCT Results

Comparisons of processed pre- and post-reaction xCT scans for both experiments are provided in this section. As noted in Chapter 4, the scans from PB-1 were segmented to quantify changes in void space, but the scans from PB-2 could not be meaningfully segmented due to limited contrast between the starting minerals and reaction products along with the fact that most of the porosity was sub voxel resolution.

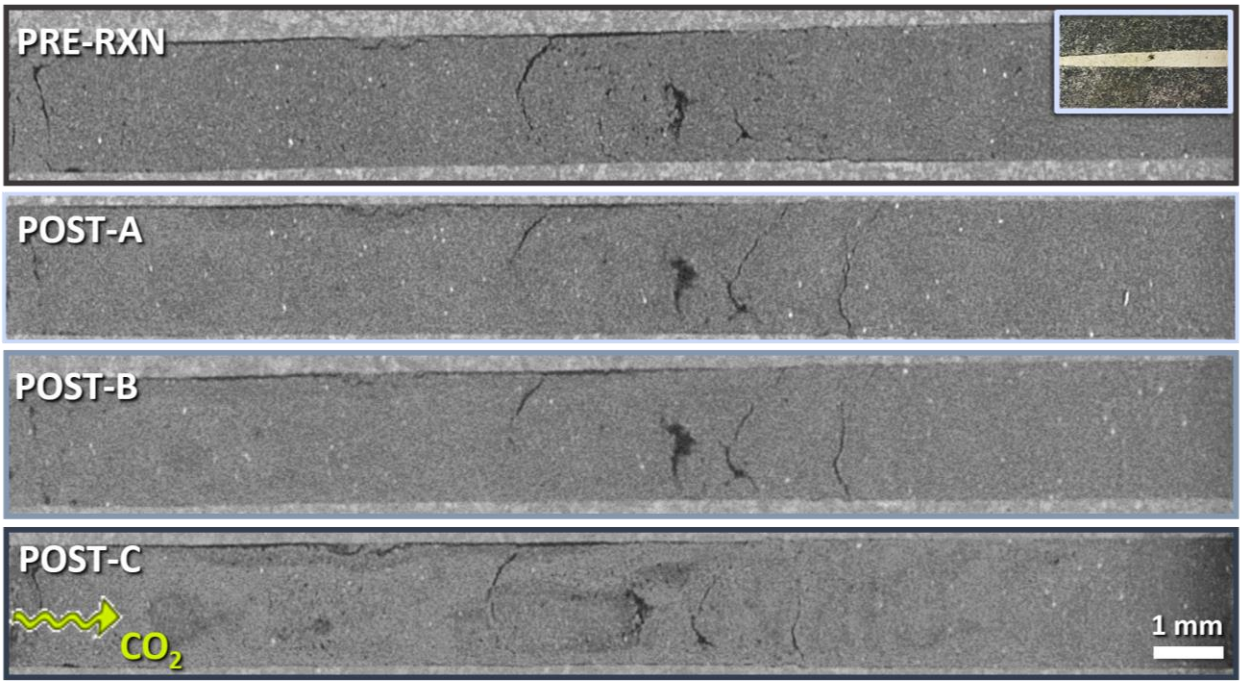

Figure D11. Cross sections taken through the center of the packed bed in PB-1 (shown in the inset at the upper right-hand corner) at each stage of the experiment. Refer to Section 4.2.2 (Chapter 4) for experimental details. The source of initial CO_2 exposure in the packed beds is on the lefthand side of the cross-sections, as illustrated in the lower panel.

While the scans from PB-2 could not be meaningfully segmented, comparisons of packed beds pre- and post-reaction (Figure D12) evidenced changes in solid phase density (corresponding to changes in grayscale coloration) attributable to reactions induced by CO_2-acidified fluids that resulted in the hydration and carbonation products identified in Chapter 4.

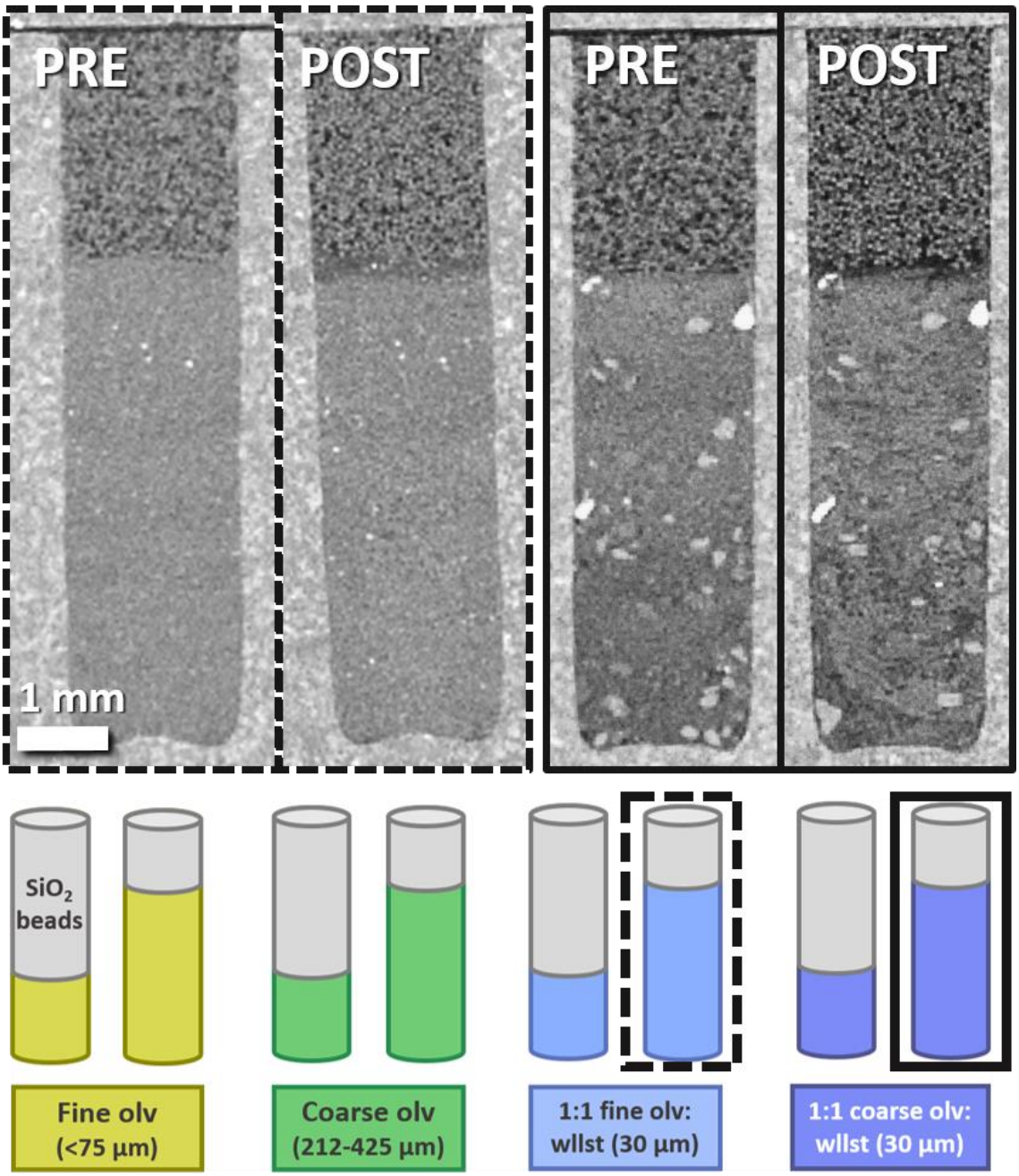

Figure D12. Comparison of pre- and post-reaction xCT scans for longer mixed beds with wollastonite and fine-grained olivine (left) or coarse-grained olivine (right), as denoted in the lower schematic. The 2D sections shown were taken through the center of the packed beds, parallel to the direction of flow.

D3. Additional SEM/BSE Results

Example BSE images from the reacted packed olivine/wollastonite bed in PB-1 are included in Figure D13 below. EDS maps are excluded because the reacting (olivine and wollastonite) and precipitating phases were so small that contrast in key elements (Ca, Mg, Si) was limited. However, as documented in Chapter 4, TGA revealed that significant (>50%) carbonation occurred throughout the packed bed and most carbonates were identified as $CaCO_3$, both in the form of calcite and aragonite, via Rama spectroscopy. Some Mg-bearing Ca-carbonates were also identified, primarily near the inlet of the packed bed.

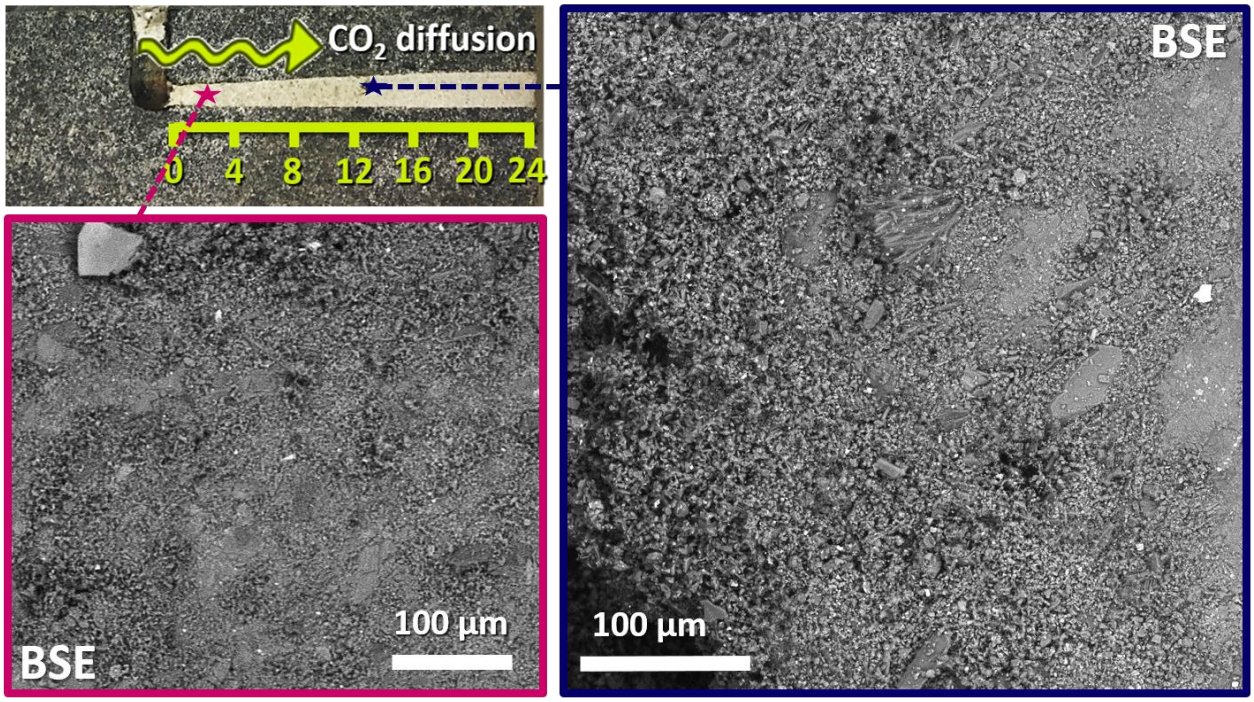

Figure D13. BSE images taken near the inlet and center of the packed bed in PB-1, which contained mixed wollastonite and fine-grained olivine. While SEM/EDS resolution was insufficient for mineral identification, most reaction products were identified as Ca-carbonates with TGA and Raman spectroscopy.

Figure D14 below includes SEM images from the deeper mixed wollastonite/coarse-grained olivine packed bed in PB-2 that highlight wispy Mg-silicate alteration products that formed during the experiment. These reaction products exhibit morphologies similar to chrysotile, an Mg-rich serpentine ($Mg_3(Si_2O_5)(OH)_4$) and naturally occurring form of asbestos. While many of these regions exhibited Raman peaks characteristic of Mg-serpentine, the precipitates were not explicitly identified because they formed as narrow fibers on the surface that were subject to background fluorescence and difficult to parse from underlying minerals with more defined crystal structures.

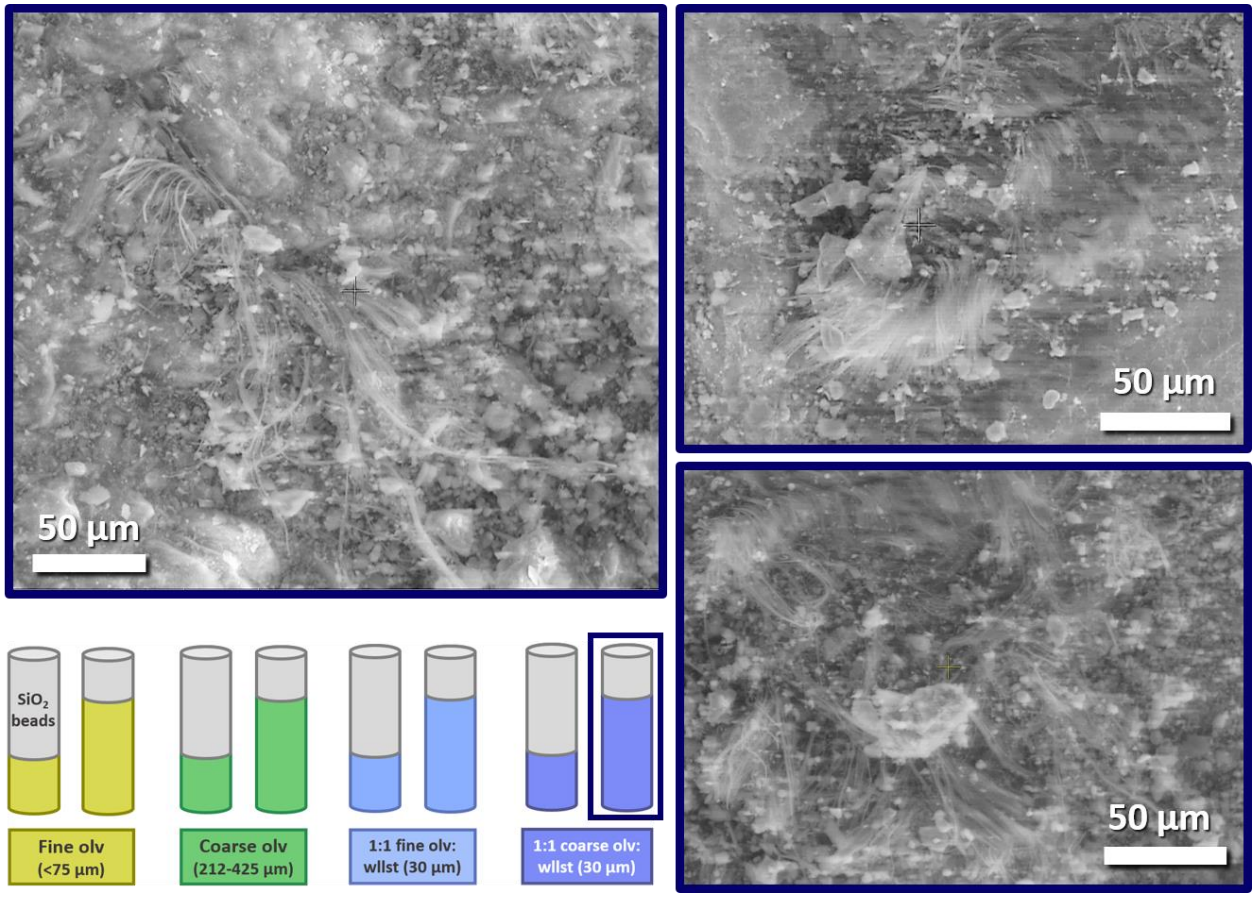

Figure D14. Additional SEM results from PB-2, highlighting fibrous Mg-rich silicate alteration products with morphologies and Raman spectra characteristic of Mg-rich serpentine. SEM images were taken from the deeper packed bed with mixed wollastonite and coarse-grained olivine, as denoted by the schematic in the lower left. EDS maps are excluded as they did not distinguish differences in key element (Mg, Si) abundances between the alteration products and underlying silicate minerals.

D4. Additional Modeling Results

As discussed in Section 4.3.3 of Chapter 4, additional simulations were run using the same conditions as the models created for the mixed wollastonite and coarse-grained olivine beds in PB-2, but with a coarser wollastonite with a specific surface area of 0.0069 m^2/g (compared to 0.69 m^2/g in the original models that simulated experimental conditions). Results comparing volume fractions of primary (forsterite and wollastonite) and secondary (antigorite and calcite) minerals throughout the modeled packed bed are presented in Figure D15 below. Note that dashed lines represent primary (i.e., dissolving) minerals while solid lines represent secondary (i.e., precipitating) minerals. The results indicate that past a depth of ~3 mm, most of the initial wollastonite was converted to calcite during the simulation.

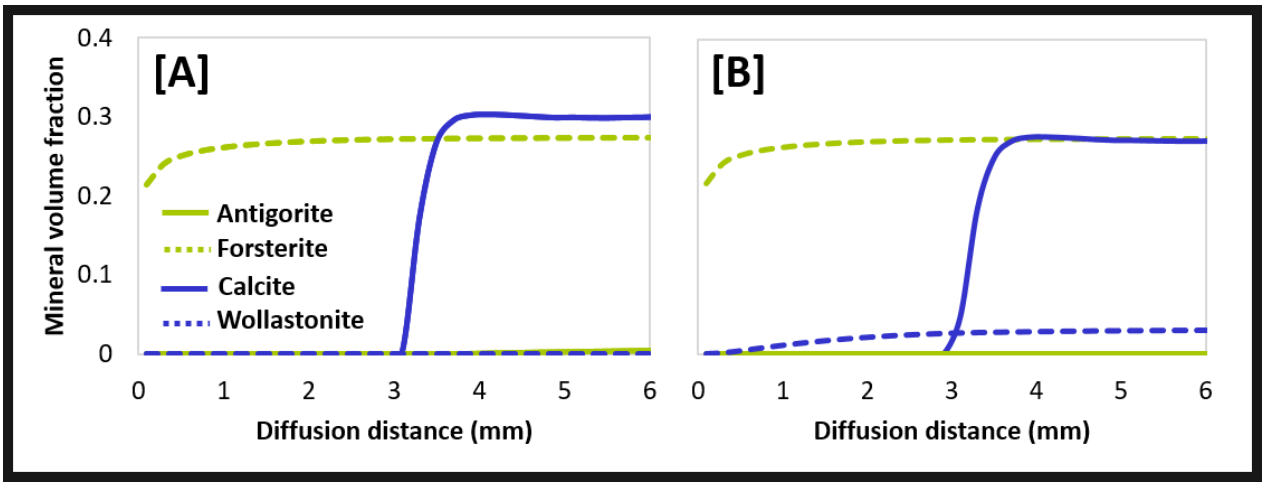

Figure D15. Reactive transport model predictions of mineral volume fractions as a function of diffusion distance into equivalent packed beds containing [A] fine-grained wollastonite with coarse-grained olivine (1:1 mixture) and [B] coarse-grained wollastonite and olivine in a 1:1 mixture. Dashed lines indicate primary (i.e. dissolving) minerals while solid lines represent secondary (i.e. precipitating) phases.

D5. Effluent Chemistry Results

Effluent samples were taken regularly throughout the PB-1 and PB-2 experiments to monitor changes in fluid chemistry through ICP-MS, but the results were not ultimately useful in these experiments due to dissolution of both the basalt matrix and reactive powders in the packed beds. Measurements for the major cations (Ca, Mg, Fe) are included in Figure D16 below.

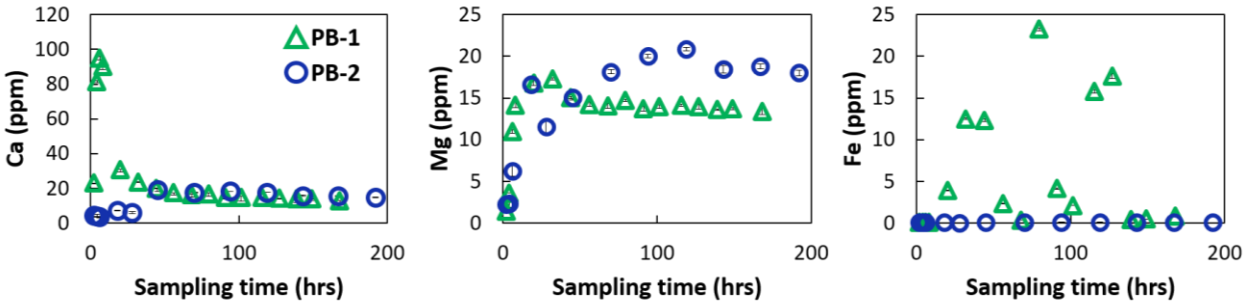

Figure D16. Effluent chemistry results for major cations (Ca, Mg, Fe) for PB-1 and PB-2.

D6. Preliminary Packed Bed Experiment

The design of the cores and experimental procedures for PB-1 and PB-2 were motivated by a preceding test where holes were similarly drilled into one half of a flood basalt core, but were completely filled with reactive powders. Two holes were wet-packed with fine-grained (<75 µm) forsterite and four with wollastonite, as illustrated in Figure D17. To start the experiment, DI water was first equilibrated with CO_2 at 100°C and 10 MPa. The CO_2-acidified fluid was then injected through the core at a constant rate of 1 mL/hr for 3 weeks under the same temperature and pressure conditions, maintaining a confining pressure of 20 MPa. Pre- and post-reaction xCT scans were collected (Figure D17c) and the reacted core was opened and analyzed via optical microscopy (Figure D17b). Effluent samples were collected in regular intervals (~ every 8 hours) for the duration of the 3-week test and analyzed via ICP-MS (Figure D18).

The xCT scans evidenced significant loss of material within the packed beds (Figure D17c), likely due to the rapid dissolution of the fine-grained powders upon exposure to CO_2-acidified fluid. Optical microscopy indicated that most of the remaining material had been carbonated, but the space left by dissolution more than accommodated any potential volume expansion that would have occurred within the beds. This result prompted the addition of non-reactive silica beads to the upper portions of the packed beds in the experiments documented in Chapter 4 to prevent channelization in the packed beds.

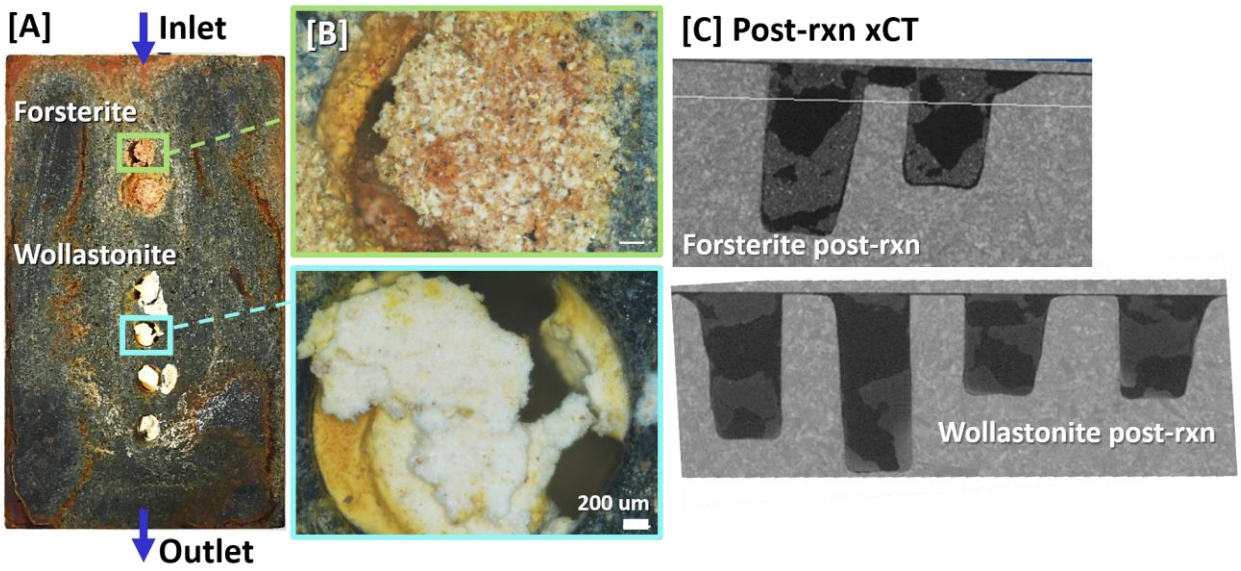

Figure D17. Select results from preliminary packed bed experiment. [A] Reacted packed bed half of the core, featuring two packed forsterite and two packed wollastonite beds. [B] Optical microscopy images illustrate precipitation as well as dissolution in the backed beds, which is also evident in [C] xCT scans of the reacted sample that show significant dissolution and channeling occurred within the beds.

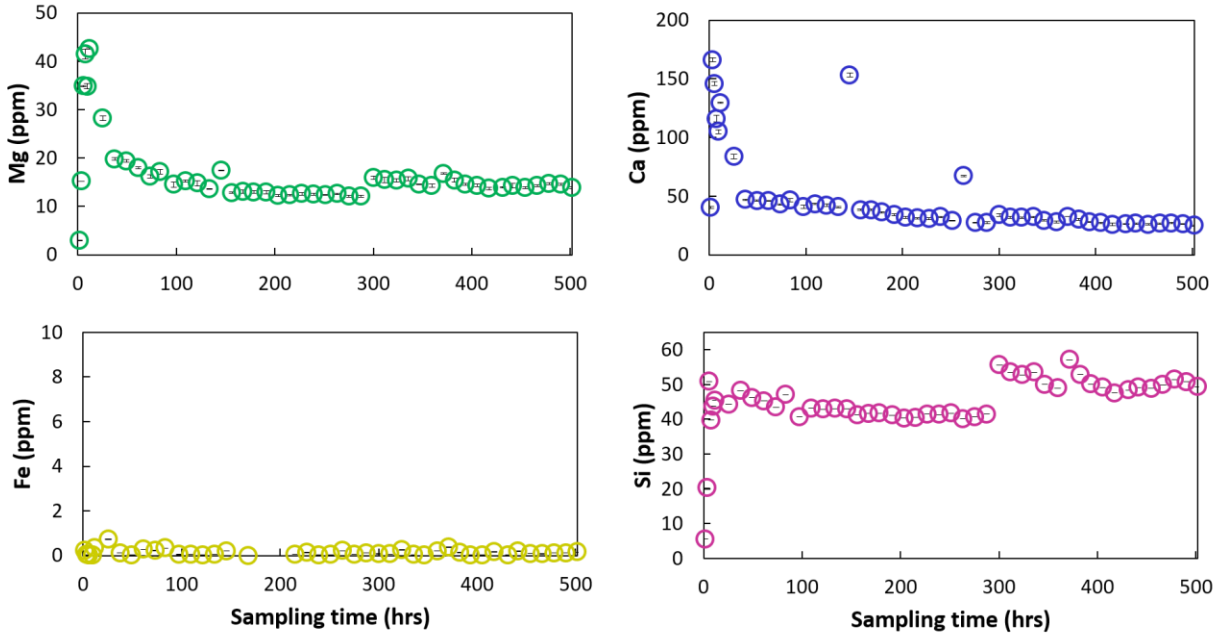

Figure D18. Effluent chemistry results for major cations (Ca, Mg, Fe) and Si from the preliminary packed bed experiment, measured via ICP-MS.

APPENDIX E

Supporting Information for Chapter 5

This appendix documents experiments preceding those presented in Chapter 5 that helped in defining the objectives and methods of this study. These results have not been published.

E1. MARBLE EXPERIMENTS

As discussed in Chapter 5 (Section 5.2.1), preliminary batch experiments were carried out to evaluate the most reactive combinations of fluids and geologic materials. Marble consisting of ~100% calcite exhibited significant coverage of secondary precipitates when reacted with 2,000 ppm $BaCl_2$ and was used in initial core flooding experiments. In the first test (MB-1), a marble core (1.5" length by 1" diameter) was saw-cut lengthwise and one half was laser-etched with a diamond-shaped flow path 100 μm deep and 3 mm wide to create a single central 'asperity' (Figure E1). This surface was mated to a non-reactive polycarbonate half-core in order to isolate geochemical reactions on a single fracture plane. The core was secured in the triaxial core holder described in Section 5.2.3 and a 2,000 ppm $BaCl_2$ solution was injected at 6 mL/hr for 5 hours under 3.5 MPa confining stress. At the end of the test, the core was removed and the halves were separated for post-reaction SEM imaging of the marble fracture surface. Continuous radiography focused on the plane of contact between the two core halves did not evidence mineral dissolution or precipitation, but BSE and EDS analyses revealed that small (<20 μm) barium carbonate crystals had formed in some regions of the etched flow paths. These precipitates were concentrated in corners where flow velocity slowed and exhibited similar morphologies to $BaCO_3$ crystals observed in the initial batch experiments. Representative BSE images are provided in Figure E1.

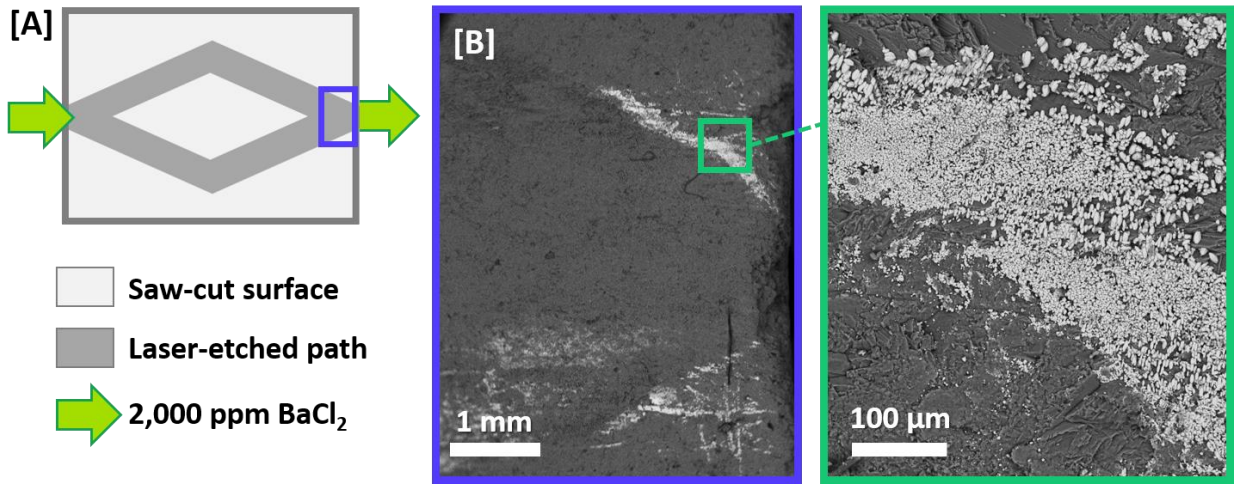

Figure E1. [A] Schematic overview of MB-1 flow-through experiment, where 2,000 ppm $BaCl_2$ was injected through a core consisting of a marble half laser-etched with the pattern shown above and a solid polycarbonate half. [B] Representative BSE images of the fracture surface post-reaction, revealing small $BaCO_3$ crystals that formed along the edges of the etched flow path.

Following this test, a second marble experiment (MB-2) was designed to create more low-flow regions with longer residence times that could encourage precipitate nucleation and growth. In this experiment, a marble half-core was laser-etched with a single primary flow path connected to six dead-end fractures (Figure E2). The channels were narrower (0.5 mm wide) than those in MB-1 to increase the rock:fluid ratio, but were etched deep enough (~500 µm) to be resolved in x-ray radiographs. This etched surface was mated to another marble core half instead of a polycarbonate core in order to increase the amount of reactive surface area in the flow channels. It was also hypothesized that calcite dissolution was a limiting factor for $BaCO_3$ precipitation in MB-1, so the 2,000 ppm $BaCl_2$ solution was saturated with CO_2 prior to injection to promote acid-driven dissolution. However, lowering the pH likely inhibited precipitation, as no $BaCO_3$ crystals were observed in either the *in situ* radiographs or post-reaction SEM analysis of the fracture surfaces.

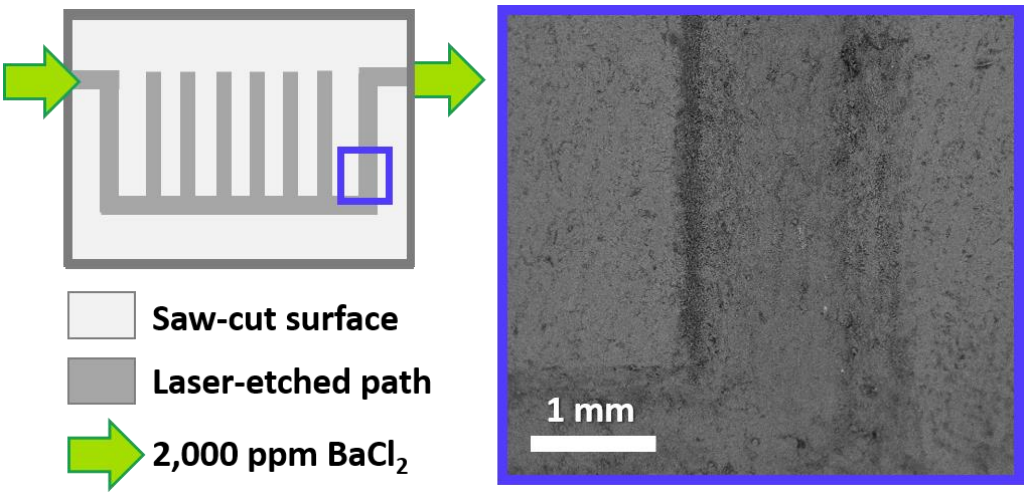

Figure E2. Schematic of the laser-etched marble core half used in the MB-2 flow-through experiment along with a representative SEM image revealing a lack of precipitation in the etched channel.

Given the limited extent of precipitation observed in the flow-through experiments, a triaxial direct shear experiment was designed to test the influence of fracture activation on geochemical reactivity. A whole marble core (1" diameter) was trimmed to 1" length and saw-cut in half lengthwise. This core was then positioned with the mated surfaces oriented perpendicular to the shear platens in the triaxial core holder (Section 5.2.3) such that shear would occur perpendicular to the saw-cut fracture plane. A 2,000 ppm $BaCl_2$ solution (without CO_2) was again used as a working fluid. The core was sheared under 3.5 MPa confining stress per the procedures outlined in Section 5.2 of the dissertation. No evidence of dissolution or precipitation was observed in the real-time x-ray radiographs focused on the shear plane, the post-reaction CT scan, or in post-reaction SEM analysis of the fracture surfaces.

E2. DOLOMITE SHEAR EXPERIMENT

The limited reactivity observed in the marble experiments motivated subsequent experiments with less consolidated geologic materials and more reactive fluids. First, a whole dolomite-rich core (1" diameter by 1" length) was directly sheared under 3.5 MPa confining stress using a much higher concentration of 18 weight % (180,000 ppm) $BaCl_2$ in the pore fluid. While no reactions were observed directly in the x-ray radiographs aligned with the shear plane, reconstructed xCT scans evidenced thin coatings of precipitates on several regions of the fracture surfaces (Figure E3). BSE and EDS analysis confirmed that small needle-like $BaCO_3$ crystals had formed on fracture surfaces (Figure E4). Considering that dolomite has a lower reaction rate than calcite, the presence of visible precipitation in this dolomite test (using 180,000 ppm $BaCl_2$) compared with little to no precipitation in the experiments on calcite-rich marble (using 2,000 ppm $BaCl_2$) indicate that the higher level of $BaCl_2$ in the pore fluid was a significant factor in promoting precipitation.

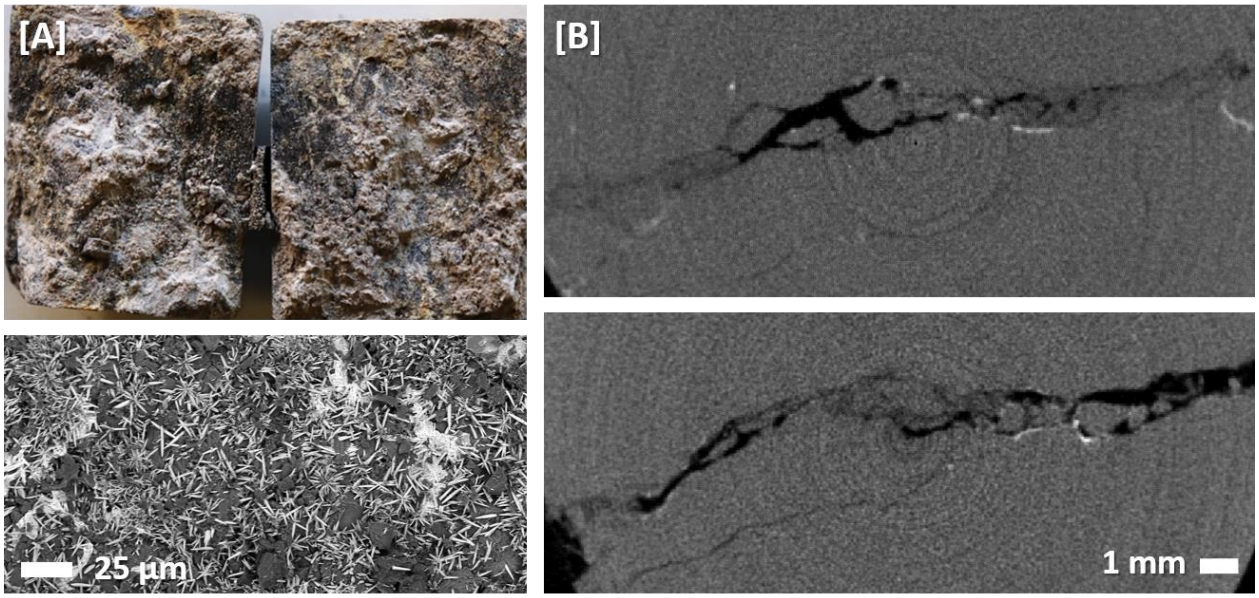

Figure E3. [A] Post-shearing, the fracture surfaces of the dolomite core evidenced white precipitates, which were identified as BaCO3 crystals (representative BSE image included below with additional images in Figure E4). [B] xCT scans also revealed dense precipitates (white regions) forming in the fracture.

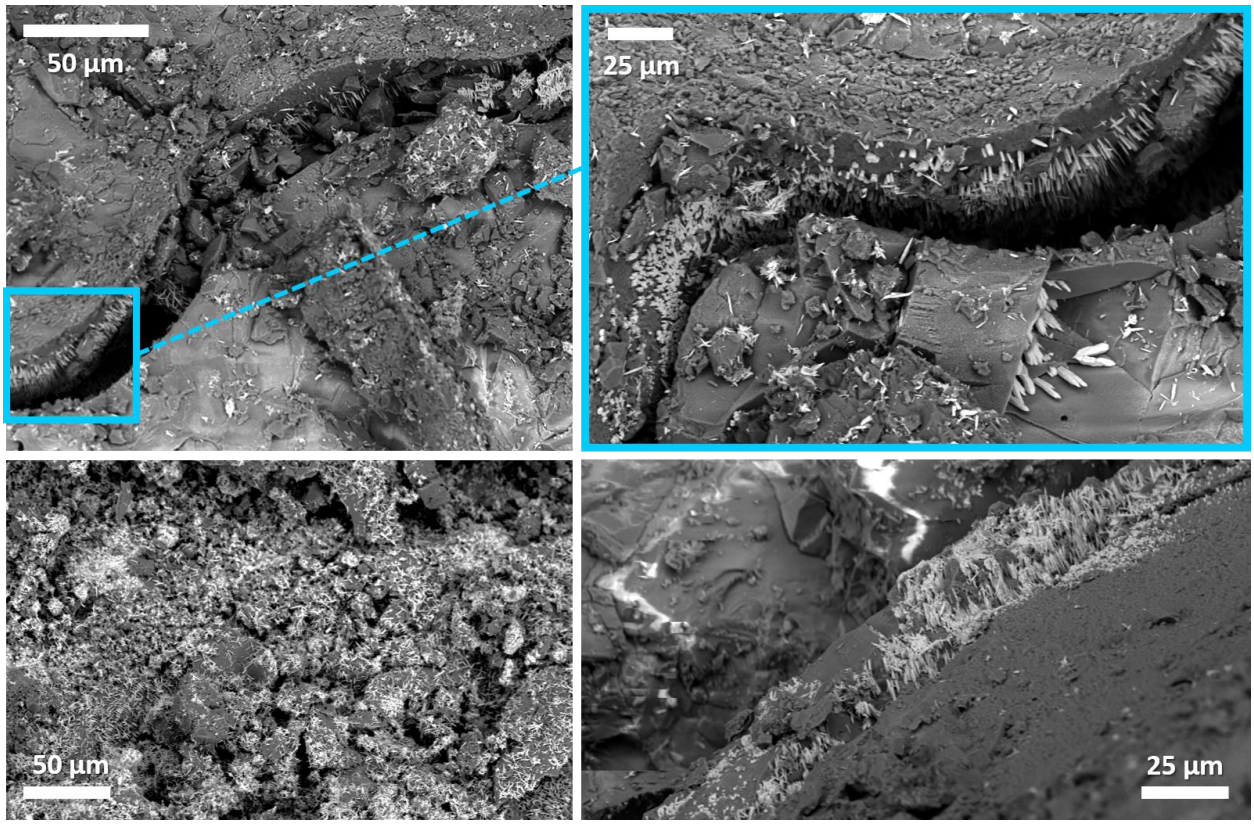

Figure E4. Example SEM images from the dolomite shear experiment revealing small needle-like $BaCO_3$ crystals that formed on shear fracture surfaces as a result of interactions between the $BaCl_2$-rich pore fluid and carbonate minerals in the host rock.

APPENDIX F

Additional Unpublished Experiments

This appendix documents additional experiments that were conducted over the course of this dissertation but not included in published work.

F1. COLORADO BASALT EXPERIMENT AT NETL

An additional experiment with a Colorado basalt, using the same core design as the experiments conducted in Chapter 3, was conducted within the industrial xCT scanner at the National Energy Technology Lab (Morgantown, WV). The sample contained a notable calcite vein (identified via Raman spectroscopy) that ran diagonally across the saw-cut surface. This test (LB-20C for clarity) was intended to be a replicate of the LB-100C experiment in Chapter 3 with the added component of 4D imaging, but was ultimately conducted at ambient temperature (~20°C) due to complications in heating the system. In attempt to compensate for the anticipated reduction in mineral reactivity, the test was run for a longer time frame of 18 days. CO_2-acidified fluid containing 6.3 mM $NaHCO_3$ was injected at a constant rate of 1 mL/hr, with intermittent effluent samples taken from a micro-metering valve downstream of the reactor. A pore pressure of 10 MPa was maintained with a syringe pump downstream of the valve and core, while confining stress was maintained at 20 MPa. Complete xCT scans were taken approximately every 24 hours to capture potential reaction products in real time, in addition to "dry" scans (i.e., outside of the reactor) that were taken pre- and post-reaction. Scans were reconstructed using proprietary software (Northstar Imaging) and processed with ImageJ.

Effluent data for major cations are included in Figure F1, with data from LB-100C included for reference. As expected, the trends for major divalent cations were markedly different from experiments conducted at higher temperature, which were characterized by rapid initial spikes in concentration followed by a decline to a quasi steady-state (Chapters 2 and 3). In LB-20C, the initial rise in concentration lagged, with most ion concentrations increasing after 60-80 hours of CO_2-acidfiied fluid flow. Silica was notably lower than LB-100C, consistent with previous comparisons between experiments at 45 and 100°C (Chapter 2) that indicated dissolution became

more incongruent (i.e., less stoichiometric) at lower temperatures. Iron release exhibited cyclical trend in both tests but concentrations were much higher in LB-20C, rising to around 7 ppm compared to <1 ppm in LB-100C. After ~80 hours, Ca concentrations were also higher in LB-20C, but this is likely due to contributions from the pre-existing calcite vein that intersected the flow path in LB-20C rather than greater dissolution of Ca-bearing silicates.

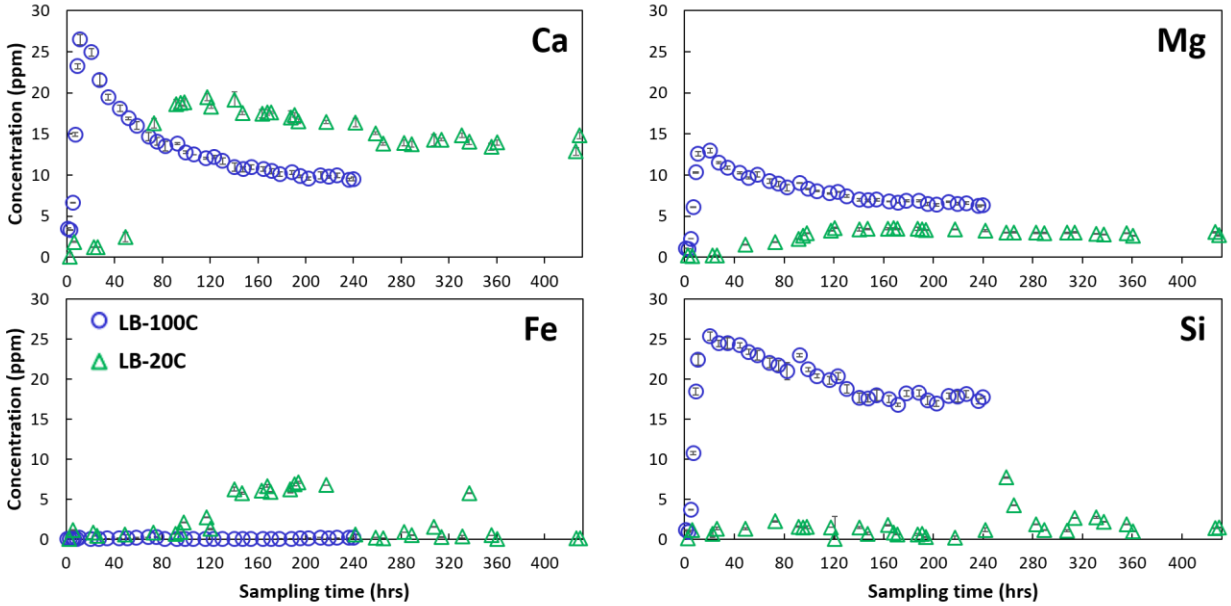

Figure F1. Effluent chemistry results for LB-100C "replicate" experiment conducted at NETL. Data for LB-100C, conducted at higher temperature over a shorter time frame (Chapter 3), are included for reference.

As in the experiments conducted in Chapter 3, no measurable permeability changes occurred during this test. While some of the fractures appeared partially filled in xCT scans, primarily after 328 hours, this material was later determined to be basalt fragments that had been mobilized by dissolution. A few isolated carbonates, similar to the crystals that formed in LB-100C, were identified on the fracture surfaces through analysis with Raman spectroscopy and SEM. In contrast to the higher temperature experiments, red coatings (i.e. iron oxides) were notably absent in LB-20C. In combination, the results indicate that the reduction in kinetic reaction rates at lower temperature may have inhibited both dissolution and precipitation. However, the fact that substantial carbonation occurred at the pilot site in the CarbFix project, where the target reservoir was at a similar temperature (~20°C) suggests that temperature may not be inhibitory over longer time frames, particularly if rocks are abundant in reactive Ca-bearing minerals.

F2. Colorado Basalt Static Experiment

In addition to the core flooding experiments conducted in Chapter 2, a static experiment was conducted on a Colorado basalt. The core was saw-cut lengthwise, but one half was roughened with sandpaper instead of milled with a fracture pattern. After placing the core in the biaxial core flooding system (100°C; pore pressure of 10 MPa; confining pressure of 20 MPa), CO_2-acidified ultrapure water was injected to saturate the core and simulate "reservoirs" of fluid within spacers on either end of the core. Flow was then stopped and the core was left under the same temperature and pressure conditions for 3 weeks. However, no precipitates were identified in post-reaction analyses with optical microscopy and Raman spectroscopy.

F3. Grand Ronde Basalt Experiments

One flow experiment was conducted on a core plug from the Grand Ronde basalt formation, which contained large mm- to cm-scale vesicles and consisted primarily of plagioclase, pyroxene, and Si-rich glass. Additional information on sample composition is provided in the published sample library that also documents the cores used in Chapters 2 and 3.[1] Prior batch experiments with these cores resulted in carbonates forming within the vesicles, even when they appeared disconnected from the source of CO_2-acidified fluid.[2] The experiment conducted here involved alternating periods of constant flow and static conditions, which was intended to induce dissolution followed by longer residence times to promote carbonate precipitation. The core was saw-cut lengthwise and one half was lightly roughened with sandpaper (Figure F2). No fractures were milled as the interest was in carbonating the large vugs and vesicles, many of which were directly connected to the saw-cut fracture. The two halves of the core were secured in chemical-resistant heat-shrink tubing and placed in the biaxial core holder (Appendix A). CO_2-acidified fluid (ultrapure water with 6.3 mM $NaHCO_3$) was first injected at a constant rate of 1 mL/hr for 3 days under 100°C and 10 MPa. Effluent samples were collected hourly for the first 8 hours and once every 8-10 hours for the remainder of the 3 days. Flow was then stopped and the core was left under static conditions at the same temperature and pressure for 6 weeks. During this time, flow was briefly re-initiated once a week (i.e., CO_2-acidified fluid was injected for enough time to 'flush' once through the core) to replenish CO_2. An effluent sample was taken during each 'flush' of CO_2-acidified fluid (i.e. once a week) for the duration of the experiment.

Figure F2. Grand Ronde core sample, illustrating the abundance of large vesicles.

Select effluent chemistry results for the first 80 hours of the experiment, where samples were taken in ~8 hour intervals, are presented in Figure F3. Dissolved Si concentrations were much higher than prior tests with the flood and Colorado basalts, likely due to the abundance of Si-rich glass in the Grand Ronde.

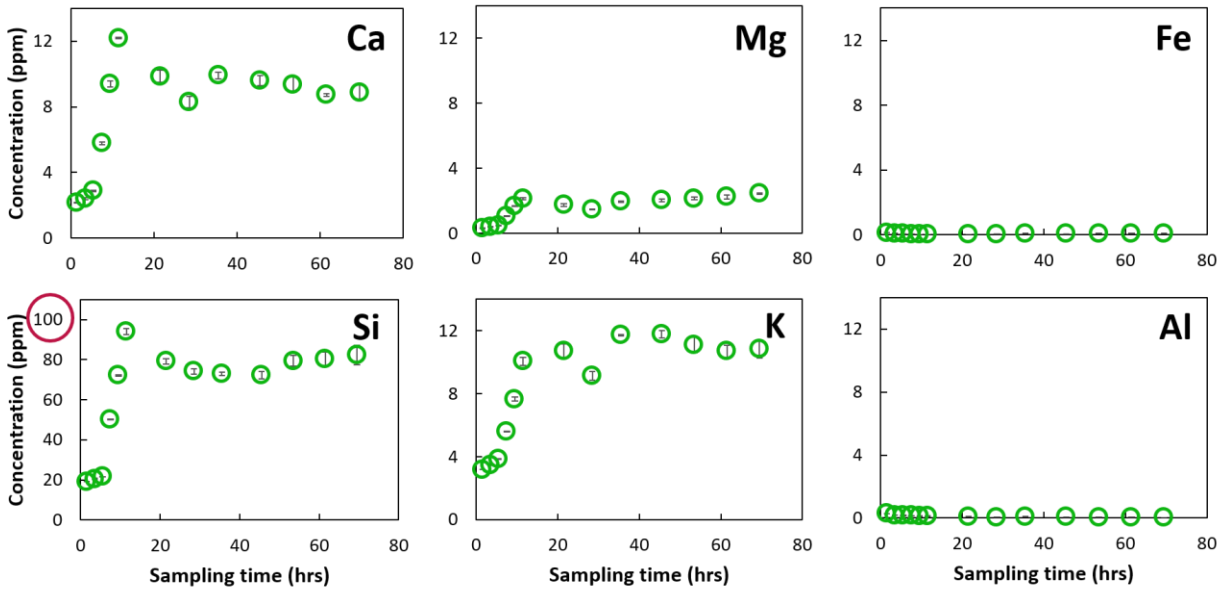

Figure F3. Abridged effluent chemistry results from Grand Ronde flow experiment, highlighting trends over the first ~80 hours of flow where effluent samples were collected in regular ~8 hour intervals. Note that the concentration axis is much higher for Si; the other cations were intentionally not scaled to this same level so that trends would be evident. Fe and Al concentrations were consistently below 1 ppm.

Full effluent data collected over the entire 6-week experiment are included in Figure F4. Note that after ~80 hours (the data presented in Figure 3), samples were only collected once a week when CO_2-acidified fluid flow was re-initiated. While concentrations of the predominant carbonate-forming cations (Ca and Mg) appeared to level off to a quasi steady-state in the initial flow-through portion of the experiment (Figure F3), they increased continuously over the following 6 weeks of alternating flow and static conditions. However, limited carbonation occurred as discussed below. Concentrations of Si and K also increased steadily over most of the experiment, likely due to the dissolution of the silica-rich matrix and glass (which comprised 25% of the bulk sample composition), but levelled off between 600-800 hours.

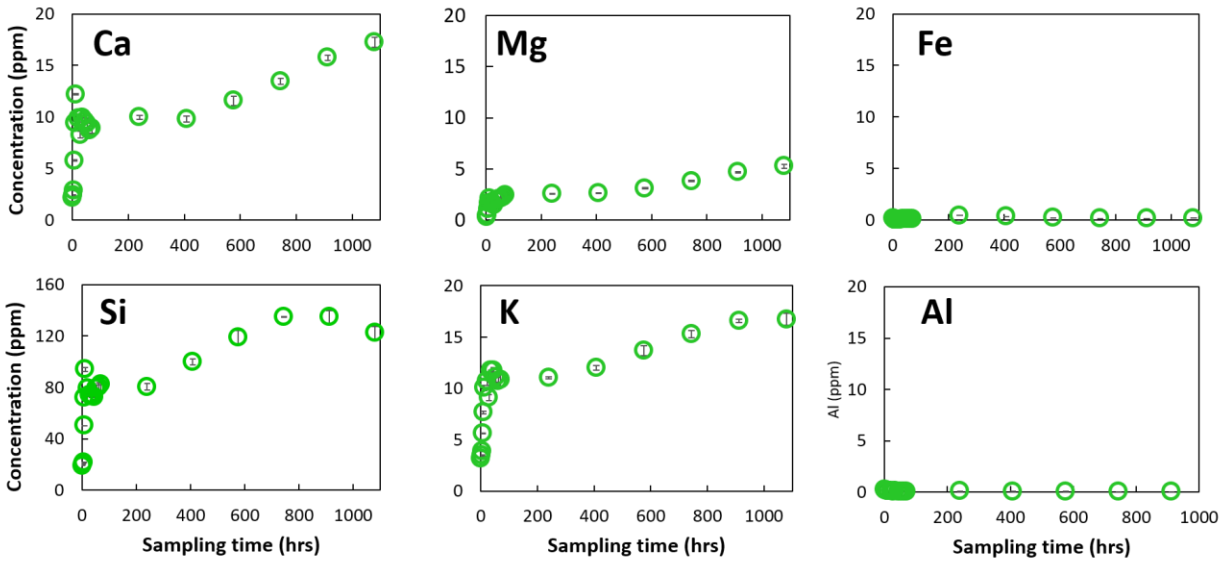

Figure F4. Full effluent chemistry results from Grand Ronde flow experiment. Note that the concentration axis is again much higher for Si and the rest of the data were not scaled to the same magnitude so that trends would be clear. After ~80 hours, samples were only collected ~once per week when flow was re-initiated.

No evidence of carbonation was observed in the xCT scans, but a few small isolated carbonates were observed on surfaces with post-reaction optical microscopy and SEM. However, the xCT scans did reveal that significant crushing of the basalt matrix occurred, which filled some of the vesicles (Figure F5). This likely resulted from the lower tensile strength of the Grand Ronde core relative to the flood and Colorado basalts, which made it susceptible to damage under high confining stress. Due to these limitations, no additional flow experiments were conducted with Grand Ronde basalt cores.

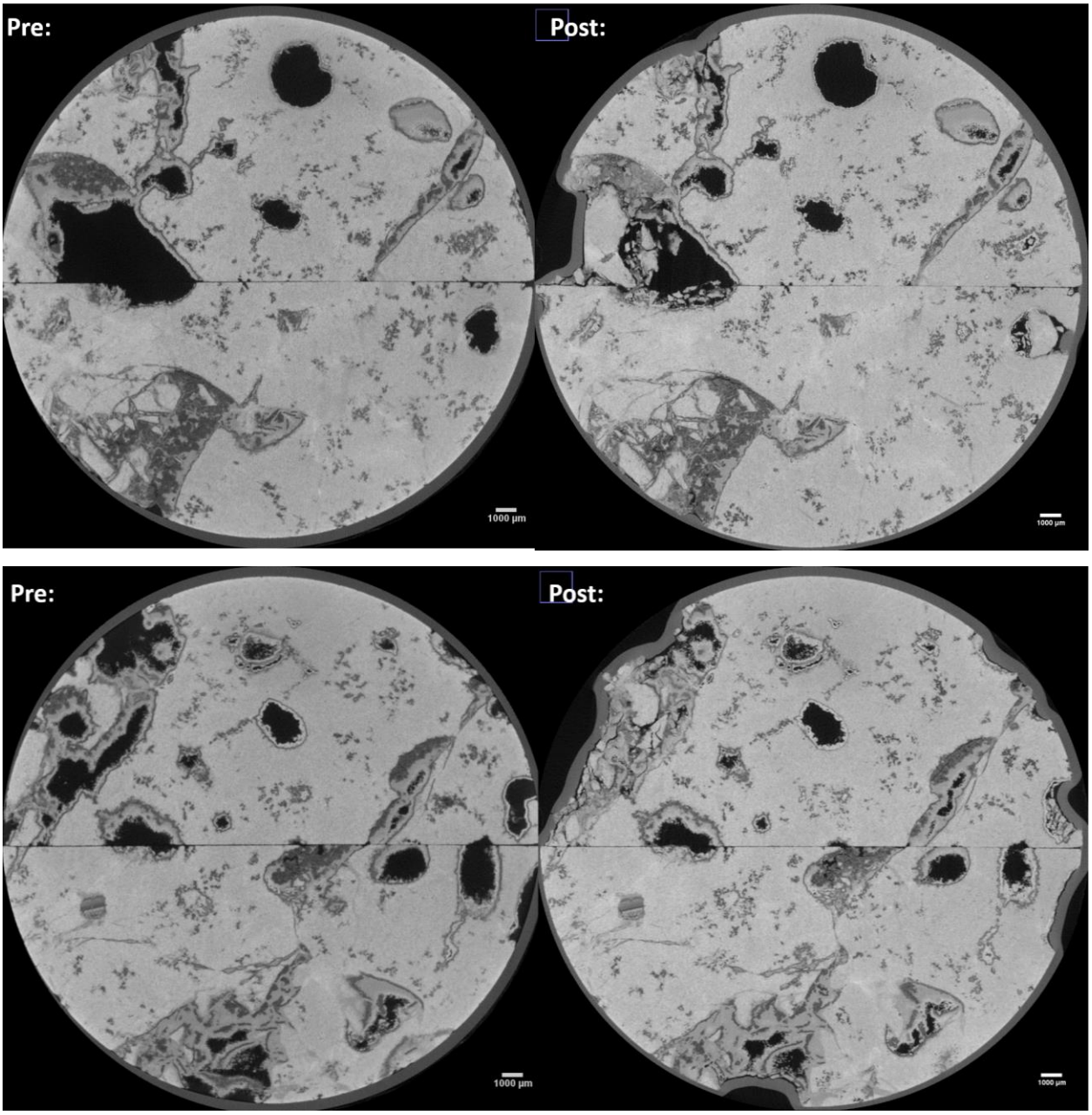

Figure F5. Representative xCT images evidencing crushing of the Grand Ronde sample under confining pressure. The top slices were taken ~9.8 mm from the fracture inlet while the lower slices were ~12 mm in.

REFERENCES

(1) Wells, R.; Giammar, D.; Skemer, P. *Sample Library of Natural and Artificial Basalts*; 2016.

(2) Xiong, W.; Wells, R. K.; Horner, J. A.; Schaef, H. T.; Skemer, P. A.; Giammar, D. E. CO_2 Mineral Sequestration in Naturally Porous Basalt. *Environ. Sci. Technol. Lett.* **2018**, *5* (3), 142–147. https://doi.org/10.1021/acs.estlett.8b00047.

APPENDIX G

References to Published Work

Additional publications that were not documented in this dissertation are included here for reference. The most relevant involved carbonation of serpentinized basalt and flood basalt cores (from the same bulk samples as those used in Chapter 2) under static conditions. The 1D reactive transport modeling, xCT segmentation, and discussion that was completed for this manuscript was omitted from the dissertation for clarity, but the work is published in:

Xiong, W.; Wells, R.K.; **Menefee, A.H.**; Skemer, P.; Ellis, B.R.; Giammar, D.E. CO_2 Mineral Trapping in Fractured Basalt. *Int. J. Greenh. Gas Control* **2017**, *66*, 204–217

The following are additional papers related to carbon sequestration and low-carbon energy production that were completed over the course of this PhD:

Menefee, A.H.; Ellis, B.R. Regional-scale greenhouse gas utilization strategies for enhanced shale oil recovery and carbon management. *Energy & Fuels* **2020,** *34*(5), 6136-6147

Menefee, A.H.; Ellis, B.R. Wastewater management strategies for sustained shale gas production. *Environ. Res. Lett.* **2020,** *15* (2), 024001

Bielicki, J.M.; Langenfeld, J.K.; Tao, Z.; Middleton, R.S.; **Menefee, A.H.**; Clarens, A.F. The geospatial and economic viability of CO_2 storage in hydrocarbon depleted fractured shale formations. *International Journal of Greenhouse Gas Control* **2018**, *75*, 8–23

Wilkins, R.; **Menefee, A.H.**; Clarens, A.F. Environmental life cycle analysis of water and CO_2-based fracturing fluids used in unconventional gas production. *Environmental Science & Technology* **2016**, *50*(23), 13134-13141